PHYSICS OF LAYERED MICRO-FLOWS

A THESIS

submitted by

JASON RYAN PICARDO

for the award of the degree

of

DOCTOR OF PHILOSOPHY

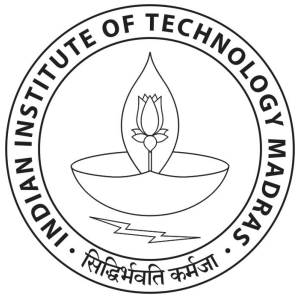

DEPARTMENT OF CHEMICAL ENGINEERING
INDIAN INSTITUTE OF TECHNOLOGY MADRAS.

March 2017

DEDICATION

This thesis is dedicated to

Jaysankar E. Variyar

a teacher, mentor and friend,

who

introduced me to the delights of scientific inquiry

and taught me to compute with care.

QUOTATIONS

“The scientist does not study nature because it is useful to do so. He studies it because he takes pleasure in it, and he takes pleasure in it because it is beautiful. If nature were not beautiful it would not be worth knowing, and life would not be worth living."

– H. Poincare, *Science and Method (1914)*

“The reduction of a colorful variety of phenomena to a general and simple principle, or, as the Greeks would have put it, the reduction of the many to the one, is precisely what we mean by ’understanding’. The ability to predict is often the consequence of understanding, of having the right concepts, but is not identical with understanding."

– W. Heisenberg, *Physics and Beyond (1971)*

“Simple (mathematical) models can be invaluable without being "right," in an engineering sense. Indeed, by such lights, all the best models are wrong. But they are fruitfully wrong. They are illuminating abstractions. I think it was Picasso who said, "Art is a lie that helps us see the truth." So it is with many simple beautiful models... because they capture qualitative behaviors of overarching interest"

– J. M. Epstein, *Why model? (2008)*

THESIS CERTIFICATE

This is to certify that the thesis titled, **"Physics of Layered Micro-Flows"**, submitted by **Jason Ryan Picardo**, to the Indian Institute of Technology, Madras, for the award of the degree of **Doctor of Philosophy**, is a bona fide record of the research work done by him under my supervision. The contents of this thesis, in full or in parts, have not been submitted to any other Institute or University for the award of any degree or diploma.

Prof. S. Pushpavanam
Research Guide
Professor
Dept. of Chemical Engineering
IIT-Madras, 600 036

Place: Chennai

Date: 15 March 2017

ACKNOWLEDGEMENTS

"...just like in every art an appropriate way to become an applied mathematician is to become part of a good school, i.e. to work for some time in a team under the guidance of a genuine master. Knowledge, experience and inspiration come from constant discussions on scientific and non-scientific matters, not only with the master gender but also with colleagues and other members of the team. Conversations about music, literature, history, visual art etc. are as important in the process of education as are scientific debates."

– G.I. Barenblatt, *Scaling (2003)*

I strongly identify with these words of Barenblatt, after spending four years in the company of Prof. Pushpavanam and my colleagues in the Pushpavanam Research League (PRL). I had joint the PhD program with the goal of learning how to understand, explain and predict natural phenomena, using mathematics. Thus, I was drawn towards several different topics and wished to read and understand as much as I could. In this journey I could not have had a more supportive and understanding mentor, than Prof. Pushpavanam. He encouraged me to pursue my ideas, no matter where they lead, and taught me that patience, perseverance and hard work unlocks the most forbidding doors, albeit in rather unexpected ways. I have enjoyed every moment of my time under his guidance and wish that we remain colleagues and friends in the future.

The last year of my PhD was spent, away from IIT Madras, at the University of Florida (USA) with Prof. Ranga Narayanan. This year was the perfect end to my graduate life. Things had come full circle, as it was Ranga's lectures on Interfacial Instabilities that had captivated me when I was a final year undergraduate. Watching him extract deep physical insights, using elegant mathematical analysis, without recourse to a computer, was spellbinding. Thus, I was extremely happy to have the opportunity to work with him. I have learned much from him about the beauty of fluid mechanics, Art and Life. Among the chief highlights of my trip are the long Saturday afternoon derivation sessions and the burritos that followed. I am grateful to Dr. Georg Dietze for his warm hospitality during my stay at Lab. FAST (Orsay, France). It was a pleasure to meet all the faculty at FAST. I especially enjoyed my discussions with Georg, over lunch and before the chalk board, and hope to have the opportunity to work with him in the future.

I also enjoyed the company of my colleagues and friends in Florida – Kevin, John, Xin, Anirudh, CC, Jean, Areej, Adrian, Natya and Priyanka and wish them the very best

in their future careers. I am thankful for having met Amazing Alexander, and for the wonderful time we shared as apartment-mates. His passion, work ethic and ability to quickly grasp advanced concepts are remarkable. Often, during our long discussions, I would forget that he was just starting out in engineering as a freshman! My friendship with Akanksha was one of the best things I found in Florida. Working at the Marsten Library would not have been nearly as enjoyable without her company, despite Marsten's excellent ambiance, writing boards and Starbucks coffee.

I have benefited immensely from the many spontaneous conversations with my friends and scientific peers – Dipin, Danny, Babita, Anil, Avinash, Shekhar, Dinesh, Piyush, Radhakrishna, Swaminath, Vijayanand, Sangeeth and Malayaja. Dipin and I learned the basics of fluid mechanics together through many long hours of reading and discussion. Our conversations would go on though the night into the early hours of the morning, and would end with breakfast (very late dinner?) and an eventual drop into sleep mode. My conversations with Danny, however, took place mostly during normal waking hours and often over a plate of delicious food. These were among the best times of my PhD. Whenever I was stuck on a problem and needed inspiration, I would seek them out, and invariably leave a few hours later, refreshed, invigorated and buzzing. The thrill and joy of PhD life was most tangible when in their company.

I also enjoyed the many nights spent discussing stability, and spectral methods of all varieties, with Dinesh, over cups of delicious 'chai' (tea). It has been a pleasure to be a part of his journey, from a young graduate freshman to a passionate and promising researcher. Piyush came to our lab as a second year undergraduate student, with a keen mind and an even sharper wit. He left an exceptional young scholar, with three international papers under his belt. I am grateful to him for the exciting and fun time we had, working together. Swaminath (Swami) joint IIT-Madras (ChemE) along with me and Danny. Although he spent most of these years at the Physics building, we did manage to bump into each other quite often. These encounters were always fun, invigorating and informative. Swami's enthusiasm for science is infectious, and, because of his expertise in molecular physics, he always brought a new perspective to our discussions. I met Sangeeth towards the end of my PhD. Despite this, I have had many delightful conversations with him on fluid mechanics and the philosophy of science. His eye for detail is astounding and his patience and perseverance while exploring a phenomenon is truly inspirational. Babita has been a part of my journey since the very beginning, even before I decided to do a PhD. She has been a kid sister to me, through the ups and downs of the past years, complete with an inexplicable knack for finding the more effective ways to bug me!

My research work has benefited significantly from collaborations with members of our lab. Again, frequent discussions with them have been both enjoyable and enriching.

I extend my heartfelt thanks to Dipin, Anil, Avinash, Shekhar, Sundari, Radhakrishna and Sneha. We have shared many memorable moments, from serious discussions at lab meetings to playful pranks, parties and treats. The atmosphere in the lab has been positive, upbeat and congenial. Even as the old guard has begun to retire, the latest additions to the lab have taken over the responsibility for maintaining this happy state of affairs. I am glad to have had the opportunity to know them, especially Akash, Krishnaveni, Sai, Krishna, Roshan and Aditi. In addition, I have enjoyed the company of the bright young undergraduate students who came to our lab for internships and projects, and I thank them all for choosing to work with me. In short, I am grateful to all the aforementioned people, and the rest of my colleagues in the lab, for their support, encouragement, friendship and tolerance of my many idiosyncrasies.

During the initial years of my PhD, I benefited immensely from the excellent courses taught by the faculty of the Chemical Engg. and Physics departments – Professors R. Ravi, S. Pushpavanam, S. Jayanti, Arul Lakshminarayanan, M. Gopalakrishnan. Prof. R. Ravi has had a particularly profound impact on my understanding and general appreciation of continuum mechanics and linear operator theory. His courses, being the best I have ever attended, showed me the beauty inherent in these subjects. He taught me to appreciate the importance of precision, clarity and elegance, be it in a mathematical demonstration or in the mathematization of "intuitive" conceptual ideas.

I am grateful to Prof. Raghunathan Rengaswamy for his support, advice and friendship. The other members of my DC committee - Professors A. Deshpande, R. Sujith and N. Vasa have also been very supportive throughout my PhD, and I thank them for the interest they showed in my work and progress. A special thanks goes out to the administrative staff of the Chemical Engg. office, as well as of the Academic department, especially Mrs. Regina, Mrs. Saraswati and Mr Ravi. I am also thankful to the HOD's of the department, Prof. Sai and Prof. Kannan, as well as the Dean (Academic Research) and the Director.

I have received much encouragement and affection from my extended family and friends during these years. They have been very kind and understanding, especially regarding my strange schedule and poor communication habits. I am deeply grateful to my parents and brother for their constant support and love. Knowing that I have their total support, and the backing of their prayers, has given me the confidence to set out on uncertain paths without hesitation.

Finally, I must confess that all the work in this thesis, as in every other endeavor of my life, has been carried out as a humble offering of thanks and praise to God – *"In His time, He makes all things beautiful"*.

ABSTRACT

KEYWORDS: two-phase flow, mass transfer, multi-scale averaging, hydrodynamic instabilities, Dean vortices, microchannels

In this thesis, we study the transport of momentum and mass in two-phase layered (stratified) flows, in microchannels, with the aim of developing a theoretical understanding of the governing physical mechanisms. These flows are encountered in several microfluidic applications, which often involve transport of a solute from one phase to the other, e.g. solvent extraction and phase transfer catalysis. These applications will benefit from design and operating protocols that enhance the rate of inter-phase mass transfer. Here, we propose several such strategies, based on a detailed analysis of the physics of these flows.

Two classes of problems are investigated:

- *Mass transport of a solute between immiscible fluid layers, flowing in straight microchannels.* Here, coupling between momentum and mass transport can lead to new physical phenomena, and significantly impact the performance of these channels as mass transfer devices.
- *Vortices in layered flow of immiscible fluids through curved channels.* Here, we investigate the three-dimensional circulatory flow that arises in curved channels, due to the action of centrifugal forces. Special attention is paid to the structure of the vortices and their dependence on system parameters. A detailed understanding of these flows will aid in the design of microchannels with curved sections that enhance intra-fluid mixing and mass transfer.

Chapters 2 to 4 belong to the first category. In Ch. 2, we analyze the influence of fluid and solute properties on the rate and extent of mass transfer between layered fluids. These parameters can impact mass transfer either directly, by modifying the rate of diffusion in each phase, or indirectly through its affect on the flow field. A reduced order model, derived systematically using multi-scale averaging techniques, is used to study this system across a wide range of the multi-dimensional parameter space. In Ch. 3, the influence of the relative flow direction of the two phases is considered; i.e. we investigate the extent to which operating in counter-current flow increases mass transport. These two chapters demonstrate the significant, and often non-intuitive, influence of the unidirectional two-phase flow field on transverse mass transport. On the other hand, solutal diffusion across the fluids can in turn have a dramatic effect on the flow, if the solute is a soluble surfactant. This situation is investigated in Ch. 4, where the action of solutal-Marangoni

stresses on a deformable interface are taken into account. We find that the base unidirectional flow becomes unstable, even under creeping flow conditions, and gives rise to a new dynamic flow state.

Ch. 5 and Ch. 6 are concerned with layered flow in curved channels. When the channel has a bounded cross-section, such as a rectangle, the centrifugal forces are distributed non-uniformly because of no-slip conditions at the wall. This mandates a three-dimensional circulatory flow state at any finite Reynolds number. This case is studied in Ch. 5. When the height of the rectangular channel is increased, however, the magnitude of the vortices decreases, until they vanish completely in the limit of an infinitely tall curved channel. Instead, arrays of vortices can arise via a centrifugal instability, similar to the classic Taylor-Couette instability. This problem is addressed in Ch. 6, with a focus on determining the critical conditions for instability and the associated vortex patterns.

The results of every chapter suggest a different strategy for enhancing mass transfer in layered micro-flows, without compromising the integrity of the inter-fluid interface. These strategies stem from an increased understanding of the physics of layered micro-flows and the two-way coupling between momentum and mass transport. These results, both quantitative and qualitative, are expected to aid in the design of efficient micro-devices, while paving the way for future experimental and numerical studies on transport phenomena in layered fluids.

TABLE OF CONTENTS

LIST OF TABLES

LIST OF FIGURES

CHAPTER 1

Introduction

The pursuit of science has often been compared to the scaling of mountains, high and not so high. But who amongst us can hope, even in imagination, to scale the Everest and reach its summit when the sky is blue and the air is still, and in the stillness of the air survey the entire Himalayan range in the dazzling white of the snow stretching to infinity? None of us can hope for a comparable vision of Nature and the universe around us, but there is nothing mean or lowly in standing in the valley below and waiting for the sun to rise over Kanchenjunga.

– S. Chandrasekhar

1.1 Layered two-phase flows in microchannels

Layered (or stratified) two-phase flow of immiscible liquids has been the subject of several investigations, including theory, experiments and simulations (Charles and Lilleleht, 1965; Boomkamp and Miesen, 1996; Valluri *et al.*, 2010; Barmak *et al.*, 2016). Here, two immiscible liquids flow alongside one another, with a clearly defined inter-fluid interface. These flows find applications in several technological processes, spanning a wide range of length and time scales. At the macro-scale, the stability of layered flow plays a crucial role in the lubricated transport of a viscous liquid by a less viscous one, e.g. transport of oil using water, and rinsing of equipment in the food industry (Valluri *et al.*, 2010; Barmak *et al.*, 2016). Slower layered flows, at smaller scales, are encountered in extrusion processes and fabrication of laminated materials and multi-layer coatings (Pozrikidis, 2004). At the even smaller scale of micro-meters, layered flows have recently gained attention as effective systems for carrying out mass transfer limited processes, such as liquid-liquid extraction (Assmann *et al.*, 2013; Picardo *et al.*, 2015). In this thesis, we focus on this relatively unexplored micro-scale regime, where capillary forces dominate gravity, solutes diffuse rapidly (diffusion time is $O(10)$ s), and inertia is held in check by viscous forces (Re ranges from $O(1)$ to $O(100)$).

Due to the small dimensions of microchannels ($O(10^1)$ – $O(10^2)$ μm), liquid-liquid flows in rigid microchannels are laminar. Nevertheless, two-phase micro-flows can exhibit complex dynamical flow regimes, due to nonlinear capillary forces that act at the

deformable inter-fluid interface. The interaction of capillary, inertial and viscous forces result in a rich variety of flow states that undergo transitions/bifurcations as flow parameters are varied. The relative magnitude of these forces can be expressed in terms of two dimensionless groups, Reynolds number (Re) and Capillary number $(Ca = u_c\mu/\gamma)$, which are ratios of inertial to viscous forces and viscous to capillary forces respectively. Here l_c and u_c are characteristic length and velocity scales, ρ and μ are a representative density and viscosity respectively, and γ is the interfacial tension. The Weber number $(We = ReCa)$, expressing the ratio of inertial to capillary forces, is often used in place of either Re or Ca in the literature. Gravity does not play a significant role in deciding the stratification of liquids in microchannels, because capillary forces dominate buoyancy $(l_c^2(\rho_1 - \rho_2)g/\gamma \ll 1)$. Several experimental studies have mapped out various steady and dynamic flow states as a function of fluid flow rates. These include drop and slug flow, steady layered flow (stratified and core-annular), wavy interface flow and fully dispersed flow (Zhao *et al.*, 2006; Fries *et al.*, 2008; Cubaud and Mason, 2008; Kashid *et al.*, 2011).

Two-phase micro-flows are typically set up by pumping two immiscible liquids (such as water and toluene), using syringe pumps, into two separate branches of a microchannel. The phases are brought into contact at a T or Y shaped junction (Zhao *et al.*, 2006; Fries *et al.*, 2008; Znidarsic-Plazl and Plazl, 2007; Cubaud and Mason, 2008), the latter being more effective at producing layered flow. At low flow rates, capillary forces are dominant ($We \approx O(10^{-6})$ – $O(10^{-1})$, $Ca \approx O(10^{-4})$ – $O(10^{-1})$) and cause one of the liquids to break up into drops, depending on relative flow rates and wall-wetting properties. This leads to a dynamic drop or slug flow regime. At higher flow rates, both viscous stresses and inertia enable the liquids to stream past the junction without rupturing the inter-fluid interface ($We \approx O(10^{-1})$ – $O(1)$, $Ca \approx O(10^{-1})$ – $O(1)$). The resulting flow is steady and layered, with a stationary interface. Fig. 1.1 presents some micro-graphs of two-phase layered micro-flows.

This layered flow regime is observed over quite a wide range of flow rates (Znidarsic-Plazl and Plazl, 2007; Fries *et al.*, 2008), provided the flow rate ratio is not too far from unity. As an example, Fries *et al.* (2008) obtained layered flow (cf. Fig. 1.1(ii)) in the range of 100-150 μL min^{-1}, for a water-toluene combination, in a channel of width 300 μm and height 150 μm. Layered flow eventually becomes unstable at large flow rates ($We \approx O(10^1)$ – $O(10^2)$, $Ca \approx O(10^1)$) and gives way to dynamic and disordered regimes, in which the interface develops waves that ultimately breakup and result in fully dispersed flow (Zhao *et al.*, 2006).

Two-phase micro-flows offer several advantages for carrying out separations and reactions. These include small diffusion path lengths, large interfacial area per unit volume and low inventories (beneficial when dealing with exothermic processes or hazardous substances (Hotokezaka *et al.*, 2005)). An added advantage of the layered flow configu-

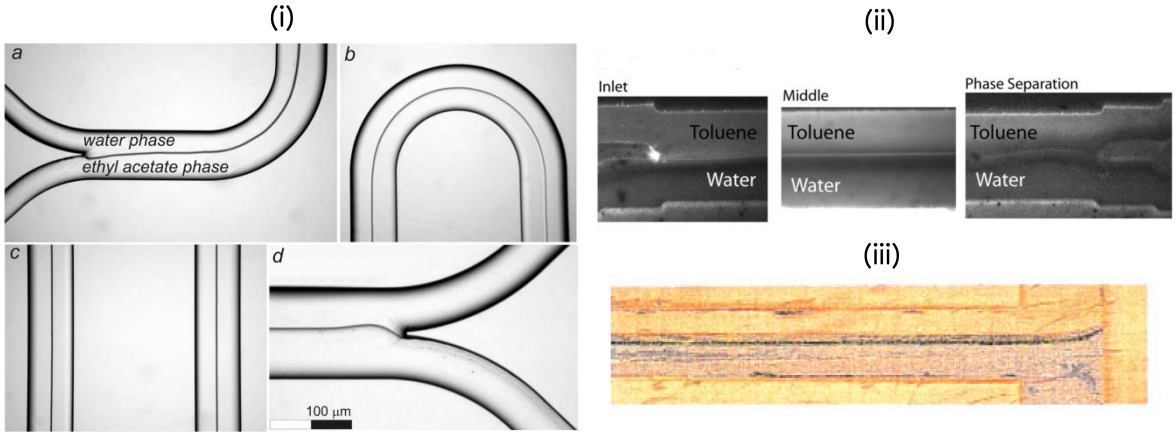

Figure 1.1: Experimental observations of layered two-phase flow in microchannels (i)Ethyl-acetate (21μL min^{-1}) and water (10μL min^{-1}) in a channel of width 220 μm and height 50 μm. (a) entrance, (b) curved part, (c) flat part and (d) exit of the microreactor (Znidarsic-Plazl and Plazl, 2007). (ii) Toluene (80μL min^{-1}) and water (80μL min^{-1}) in a channel of width 300 μm and height 180 μm (Fries *et al.*, 2008). (iii) Kerosene (3 mL min^{-1}) and water (2.65 mL min^{-1}) in a channel of width 600 μm and height 300 μm (Zhao *et al.*, 2006).

ration is that it allows the fluids to be separated at the outlet easily. Among applications of layered micro-flows that have been successfully demonstrated are liquid-liquid extraction (Assmann *et al.*, 2013; Fries *et al.*, 2008; Okubo *et al.*, 2008; Znidarsic-Plazl and Plazl, 2007), separation of biomolecules (Huang *et al.*, 2013), reactive extraction and phase transfer catalysis (wherein a catalyst facilitates the transport of a reactant and product species between immiscible liquids (Aljbour *et al.*, 2010; Šinkovec *et al.*, 2013)).

All the applications mentioned above involve diffusion of a solute from one phase (carrier) to the other (solvent). This can give rise to new physical phenomena, involving a two-way coupling between momentum and mass transport. The flow field controls the diffusion path length and the residence time of each fluid in the channel. Inversely, variations in solute concentration can generate gradients of interfacial tension that modify the flow, provided the solute is a soluble surfactant. Another interesting physical situation commonly encountered in these applications is the flow of layered fluids through curved channels. Curved and serpentine sections are often included in microchannels to reduce the size of microchips (cf. Fig. 1.1(i) from Znidarsic-Plazl and Plazl (2007)) and to improve mixing (Carlo, 2009; Gelfgat *et al.*, 2003). While the effects of centrifugal force on single phase flow are extensively documented (Berger *et al.*, 1983; Carlo, 2009; Vashisth *et al.*, 2008), its influence on the flow and stability of immiscible fluid layers is largely unknown. This thesis treats both these relatively unexplored aspects of layered micro-flows – solutal diffusion and centrifugal effects – with a focus on gaining fundamental understanding of these technologically relevant flows.

1.2 What, why and how

The objective of this thesis is two-fold: firstly, to develop an illuminating theoretical description of inter-phase diffusion and centrifugal effects in layered micro-flows; secondly, to investigate strategies for enhancing inter-phase mass transfer without destabilizing the inter-fluid interface. These two objectives are complementary, since an in-depth understanding of the system enables us to anticipate its response to modifications in design, fluid properties and operating parameters. Such insight is essential for designing and operating robust, high performance micro devices.

The simplest approach to improve mass transfer is to vary adjustable parameters, such as flow rates, channel dimensions and fluid properties (if alternative solvent liquids are available). A mathematical model is ideally suited to this purpose. However, the equations governing diffusive transport of a solute, in steady layered flow, involve coupled partial differential equations in two spatial dimensions (at least). These are tedious to solve repeatedly for a large range of parameter values, as is required for optimization. To overcome this issue, we develop a low dimensional model, or averaged model, that accounts for the essential physical processes while greatly reducing computational cost (cf. Chapter 2). This is done systematically using the Lyapunov-Schmidt reduction technique, which has been applied successfully to many single phase problems (Balakotaiah and Chakraborty, 2003; Ratnakar *et al.*, 2012). This reduced model enables us to explore the system's behaviour across the high dimensional parameter space, and understand how parameters affect mass transfer by modifying the flow field and concentration gradients within the fluids.

A common and traditional strategy for improving mass transfer in two-phase systems is to operate in counter-current flow, rather than co-current. The average departure from equilibrium is typically higher in counter-current systems, where the fluids flow in opposite directions. Unfortunately, it is quite difficult to obtain counter-current flow in microchannels (Aota *et al.*, 2007), and specially designed channels with fluid specific wall properties are required. This extra investment is justified only if the benefit provided by counter-current flow is significant. To identify conditions under which this is true, we develop and analyze mathematical models of both flow configurations (cf. Chapter 3). Since this comparison is relevant to many separation processes, we attempt to identify its generic features that extend beyond microfluidic extraction.

As long as the flow is unidirectional, mass transfer can only occur by transverse molecular diffusion. Therefore, mass transfer will be significantly enhanced if a transverse component of velocity can be induced within each fluid. Such a flow may be spontaneously generated if the diffusing solute is a soluble surfactant. An example of such a system is acetone diffusing between water and toluene (Javed *et al.*, 1989). Variations

in solute concentration along the interface will generate gradients of interfacial tension, which in turn give rise to Marangoni stresses. Although these stresses are weak in comparison to the applied pressure gradient (Picardo *et al.*, 2015), they may destabilize the base steady flow and give rise to a dynamic flow state. We investigate this possibility by carrying out a linear stability analysis for arbitrary wavelength perturbations (cf. Chapter 4). We focus on understanding the nature of the instability modes and their influence on the inter-fluid interface. The ultimate goal is to identify conditions under which the system selects an instability mode that generates a transverse flow in each fluid, while leaving the interface stationary.

In the absence of a favorable instability, circulations must be induced by external forces. Curved channels make this possible, by subjecting the fluids to a transverse centrifugal force that generates a secondary circulatory flow (Dean, 1927). We analyze these vortex flows in detail using perturbation methods and numerical simulations (cf. Chapter 5). The aim is to determine all possible vortex patterns and their corresponding magnitudes. Attention is paid to the interaction of the circulatory flows in the two fluids, which are intimately coupled via interfacial viscous stresses.

In laterally stratified flow (with a vertical interface), the interfacial area per unit volume for mass transfer can be increased by increasing the height of the channel. Unfortunately, this decreases the strength of circulatory flow in rectangular curved channels. In fact, in the limit of an infinitely tall channel, the flow is unidirectional. However, if the flow rates are sufficiently high, strong vortical flows are generated due to a centrifugal instability, as demonstrated by Dean (1928*b*) for single phase flow. Such an instability could lead to high mass transfer rates in tall microchannels, by combining the benefits of circulatory flows and a high specific interfacial area. For simplicity, we analyze the case of an infinitely tall channel, with emphasis on those instability modes that do not disturb the interface (cf. Chapter 6).

Apart from mass transfer based applications of layered micro-flows, a considerable portion of this work is also motivated by a desire to understand instabilities and pattern formation in two-phase systems. Multiple instability mechanisms operate simultaneously in these systems, both in the fluid domains and at the interface (Govindarajan and Sahu, 2014). Layered flows provide an ideal setting in which to study these complex phenomena, without the additional burden of complicated boundary geometry and background flows. Here we analyze previously unreported instabilities, which arise due to solutal-Marangoni effects (Chapter 4) and centrifugal forces (Chapter 6). Both cases raise the uncommon possibility of destabilizing layered flow, at low Re, without disrupting the interface. The study on solutal-Marangoni instabilities is particularly interesting, as it connects the extensive literature on solutal-Marangoni convection in stationary fluid layers (Schwarzenberger *et al.*, 2014) with that on the stability of layered Poiseuille flows

(Govindarajan and Sahu, 2014).

1.3 Organization and content

This thesis is organized into five main chapters, each of which may be read independently of the others. Each chapter opens with an introduction that reviews the relevant literature and highlights the scientific and practical significance of the specific problem considered therein. The mathematical notation is chapter specific and symbols are defined as they arise within each chapter. The concluding section at the end of every chapter summarizes the results, discusses their significance and highlights promising areas for future work. In addition, an overall summary of the thesis work is presented in the Epilogue. Here, the relevance of the results to layered micro-flows is discussed from a unified perspective. The five appendices included at the end of the thesis contain mathematical derivations and formulas, discussions of numerical methods and their implementation, and additional comments and explanations.

The key results contained in chapters 2 to 6 are summarized in the following paragraphs.

Chapter 2: Averaging of Transport and Reactions in Layered Flows

In this chapter, we develop low dimensional models to describe steady state mass transfer and reactions in two-phase stratified flow in microchannels. The partial differential equations that consider the effect of axial convection, transverse diffusion and reaction are averaged in the transverse direction using the Lyapunov-Schmidt method. The resulting reduced order model describes the evolution of the cup-mixing average and cross-section average concentrations along the axial direction. Two different reduced models are obtained: a One Equation Averaged model (OEA) in which we average across both fluids simultaneously, and a Two Equation Averaged model (TEA) in which we average across each fluid *separately*. The OEA model cannot capture the initial mass transfer between the phases when they first come into contact at the inlet of the channel. It can only be used when there is a deviation from equilibrium due to a reaction. The TEA model overcomes this limitation and is able to describe mass transfer between the phases right from the inlet of the channel. It accurately predicts extraction and reactive extraction with slow reactions. However, if the reaction is fast, the TEA model does not perform as well, and the OEA model is preferable. Some applications of the TEA model are presented. It leads to closed form expressions for the overall mass transfer coefficient in terms of the properties of the fluids and their holdups. An analytical solution of the TEA model is derived for the case of non-reactive extraction and used to identify the operating conditions

for high extraction performance. Finally, the TEA model is applied to investigate how the yield in competitive-consecutive reactions can be improved by exploiting the mass transfer resistance between the two phases.

Chapter 3: Selecting between Co-Current and Counter-Current Flow

Counter-current flow always results in higher overall mass transfer that co-current flow, under similar operating conditions. However, because it is challenging to implement counter-current flow in a microchannel, the improvement in mass transfer must be substantial to justify its selection over co-current flow. In this chapter, we use simplified mathematical models to identify the range of fluid properties and operating conditions for which counter-current flow is a truly attractive proposition. An analytical solution, based on the theory of Sturm-Liouville linear operators, is obtained for the case of co-current flow. The counter-current model belongs to the class of two-way diffusion equations for which a novel semi-analytical solution is presented. Analysis of the predictions of the models shows that the relative extraction performance is governed by a general principle of *maximum gain at mediocre performance* (MGMP). According to MGMP, the relative improvement of counter-current operation is low when the fluid properties and operating conditions (parameter values) either strongly promote, or oppose extraction. Instead, the improvement in performance is greatest for conditions that correspond to an intermediate extent of extraction.

Chapter 4: Solutal-Marangoni Instability of Layered Micro-Flows

In this chapter, the instability of layered two-phase flows caused by the presence of a soluble surfactant (or a surface active solute) is studied. The fluids have different viscosities, but are density matched to focus on Marangoni effects. The fluids flow between two flat plates, which are maintained at different solute concentrations. This establishes a constant flux of solute from one fluid to the other in the base state. A linear stability analysis is performed, using a combination of asymptotic and numerical methods. In the creeping flow regime, Marangoni stresses destabilize the flow, provided a concentration gradient is maintained across the fluids. One long wave and two short wave Marangoni instability modes arise, in different regions of parameter space. A well-defined condition for the long wave instability is determined in terms of the viscosity and thickness ratios of the fluids, and the direction of mass transfer. On increasing the Reynolds number, the long wave viscosity-induced interfacial instability comes into play. This mode is shown to either suppress or enhance the Marangoni instability, depending on the viscosity and thickness ratios.

Energy budget calculations are carried out to gain insight into the origins of the long

wave and short wave Marangoni instabilities. We find that the former is caused by interface deformation while the latter is associated with convection by the disturbance flow. Consequently, even when the interface is non-deforming (in the large interfacial tension limit), the flow can become unstable to short wave disturbances. This implies that mass transport between the phases could be enhanced, without disturbing the inter-fluid interface, by exciting the appropriate short-wave instability. Apart from its relevance to mass transfer in microchannels, this analysis is also applicable to the thermocapillary problem of layered flow between heated plates.

Chapter 5: Steady Layered Flow through Curved Microchannels

In this chapter, we study the laterally layered (stratified), fully developed flow of two viscous immiscible fluids in a curved channel, of rectangular cross-section. We focus on understanding the circulatory flow in each fluid, the shape of the deformed interface, the modified axial velocity profile and the modified flow rates. Using the method of domain perturbations, we obtain an analytical solution for the limit of small curvature ratios (ratio of the channel's width to its radius of curvature) and low Reynolds numbers. The flow field consists of helical vortices within each fluid, that are induced by centrifugal forces. The fluids have a tendency to flow in opposite directions on either side of the interface. However, depending on the properties of the fluids and their holdups (volume fractions), one of the fluids dominates the flow and causes the other to reverse its direction of circulation. This inter-fluid competition results in five different vortex patterns. Using the analytical solution, we study the effect of each parameter on the flow pattern and construct flow regime maps in parameter space. The strength of the circulatory flow, in each fluid, is found to peak at specific optimum values of the aspect ratio of the channel. We show that the interface is deformed by normal stresses associated with the centrifugal force and the circulatory flow; it bulges outward along the horizontal centerline. This deformation increases with the Reynolds number (higher centrifugal forces) and the Capillary number (lower interfacial tension forces). The axial velocity profile and the flow rates are found to be significantly different in a curved channel, compared to a straight channel. This modification is related to effects of the curved geometry (geometric effect), as well as the circulatory flow (inertial effect). The asymptotic solution is compared with numerical simulations, and found to be accurate for the range of Reynolds numbers and curvature ratios typically encountered in microchannels.

Chapter 6: Centrifugal Instability of Layered Flows

The centrifugal instability of layered two-phase flow in an infinitely tall curved channel is investigated, in this chapter. The fluids are laterally stratified between cylindrical walls

of infinite extent. We focus on the limiting case of small Capillary numbers (relatively high surface tension), wherein interfacial deformation and associated interfacial instabilities are suppressed. The centrifugal instability, caused by unstable gradients of angular momentum, destabilizes the axisymmetric azimuthal base flow. As in the corresponding single phase problem (Dean instability), an array of vortices are formed within each fluid beyond a critical value of the Reynolds number. A numerical linear stability analysis is carried out using a recombined Chebyshev Galerkin spectral method, as well as a shooting method. Across the space of physical parameters (volume fractions, density and viscosity ratios), six critical modes corresponding to distinct secondary flows are observed. These are classified into axisymmetric stationary vortices and rotating spiral vortices (travelling waves). Each category consists of three subtypes based on the relative vortex strength in the fluids: stronger in the outer fluid, stronger in the inner fluid and comparable strength in both fluids. The critical mode switches amongst these six types as parameters are varied. The outer fluid is found to be more unstable than the inner fluid, even if the fluids have equal physical properties. This is explained using Rayleigh's criterion for inviscid flows. Consequently, the arrangement of fluids has a significant impact on stability. Instability and vortex motion is promoted if the fluid with a higher density, a lower viscosity and a larger volume fraction is placed on the outer side of the channel. These results imply that although the base flow in tall curved channels is nearly uni-directional, strong circulatory flows can still be generated by exploiting the centrifugal instability. Hence, tall curved channels could make excellent mass transfer devices, by combining a large interfacial area with good intra-fluid mixing.

CHAPTER 2

Averaging of Transport and Reactions in Layered Flows

"Why is it possible to encapsulate the complicated deep structure of matter? The answer is that matter ordinarily relaxes to a stable internal state with high energetic or entropic barriers to excitation of all but a few degrees of freedom. We can focus our attention on those few effective degrees of freedom; the rest just supply the stage for the actors."

– F. Wilczek, *Whence the Force: Culture Shock*

2.1 Introduction

In this first chapter, we begin our study of layered flows with an analysis of diffusion and reaction of a solute between co-flowing fluid layers in a straight channel. This is the basic process underlying many applications of layered micro-flows, including extraction (Assmann *et al.*, 2013; Huang *et al.*, 2013; Priest *et al.*, 2012) and phase transfer catalysis (Aljbour *et al.*, 2010). Consequently, many experiments have been conducted, to measure the rate and extent of mass transfer in these flows (Assmann *et al.*, 2013; Fries *et al.*, 2008; Znidarsic-Plazl and Plazl, 2007; Kashid *et al.*, 2011; Aljbour *et al.*, 2010). In addition, mathematical models of varying degrees of complexity have been developed to describe these systems. Fries *et al.* (2008), Znidarsic-Plazl and Plazl (2007) and Šinkovec *et al.* (2013) have performed CFD simulations and found good agreement with experimental data. Simpler models have been developed by Pushpavanam and coworkers, to investigate the underlying physics of extraction in layered flows (Picardo *et al.*, 2015). They have analyzed the influence of the channel geometry (Picardo *et al.*, 2015), axial velocity profile (Malengier *et al.*, 2012) and the flow regime (laterally layered or core-annular) (Vir *et al.*, 2014*a*) on extraction performance.

The models used to describe these systems consist of partial differential equations (PDEs) for each phase. The key physical processes to be modeled include transverse diffusion, axial convection and possibly reactions. These models must generally be solved numerically. They contain a large number of parameters, all of which can affect the system performance. Thus analysis of the system across parameter space and optimization become quite tedious.

Here, we aim to overcome this computational limitation by deriving a reduced order model or averaged model of the system. This model would describe the evolution of the transversely averaged concentration along the length of the channel. In many applications, it is the averaged quantities that are of relevance for analysis and optimization. Such a model can reduce computation time and may also lead to new insights into the governing physics.

Over the past fifteen years, Balakotaiah and coworkers have developed a powerful technique for averaging partial differential equations of the convection-diffusion-reaction type (Chakraborty and Balakotaiah, 2002, 2003, 2005; Balakotaiah and Chakraborty, 2003; Balakotaiah and Ratnakar, 2010). They have applied the *Lyapunov-Schmidt* (LS) reduction technique from bifurcation theory to average the equations when transverse diffusion is relatively fast in comparison with axial convection and reaction. The reduction is made possible by the existence of a low dimensional *slow invariant manifold* (SIM) in solution space, along which the system evolves slowly. Due to much faster dissipative processes (transverse diffusion in this case), the system, starting from an arbitrary initial state, collapses rapidly onto the SIM. Thereafter, it evolves along the SIM. It is this slow evolution, involving only a few active degrees of freedom, that we seek to describe by a reduced order model or averaged model. The LS reduction is one method to obtain such a low-dimensional model. Two other prominent techniques that have been used to successfully average equations on long thin domains are the *slow-manifold reduction* (Roberts, 2015) and the *weighted-residual integral boundary layer* method (Ruyer-Quil and Manneville, 2000; Kalliadasis *et al.*, 2012; Dietze and Ruyer-Quil, 2013). These two methods have been extensively applied to free-surface flows of thin liquid films. The LS method, on the other hand, has been applied mainly to reaction-diffusion convection problems, where it leads to a particularly insightful and useful parameterization of the SIM (Balakotaiah and Ratnakar, 2010).

Balakotaiah and coworkers have used the LS reduction to obtain averaged equations for many single fluid flow systems and have studied Taylor-Aris dispersion (Ratnakar and Balakotaiah, 2011; Balakotaiah, 2004; Balakotaiah and Ratnakar, 2010) and homogeneous and heterogeneous reactions in tubular reactors (Balakotaiah and Chakraborty, 2003; Chakraborty and Balakotaiah, 2002, 2003). They have also applied this technique to other systems, including supported catalysts (Ratnakar and Balakotaiah, 2014) and IC engines (Kumar *et al.*, 2011). The averaged equations consist of one evolution equation for the cup-mixing averaged concentration mode and another local equation that accounts for the difference between the cup-mixing and cross-section averaged concentrations. These two averages are different because transverse diffusion is not instantaneous. Heuristically derived simple models, such as the ideal Plug Flow Reactor do not account for the finite rate of transverse mixing and hence are inaccurate and cannot describe important physical effects, such as Taylor-Aris dispersion.

In this chapter, we apply the LS reduction to two-phase layered flow that involves mass transfer and reactions. Two different reduced order models are derived. The first model is called the One Equation Averaged model (OEA). In this case, we apply the LS technique to both phases simultaneously. Mathematically, the PDEs are formulated as a single operator equation in a direct sum space and then reduced. This approach was used by Ratnakar *et al.* (2012) to develop an averaged model for a monolith catalytic reactor that consists of a core fluid phase and an annular solid catalyst. The OEA model is found to have an important drawback - it is unable to describe mass transfer in the absence of a reaction. To overcome this limitation, we adopt a novel approach in which the LS technique is applied to each fluid separately, using a homotopy parameter. This leads to two averaged evolution equations – one for each fluid. This model is called the Two Equation Averaged (TEA) model.

In this work, we focus on the steady state behavior of the system. We analyze the case of solvent extraction, without any reaction, as well as reactive extraction, wherein a reaction occurs in the solvent.

This chapter is organized as follows. In the first half, we derive the averaged models and in the second half we present some applications of the TEA model. We first present the governing PDEs for the problem of interest in Sec. 2.2. Then we derive the OEA model and compare its predictions with simulations of the full PDE model, as well as a simple heuristic plug flow model (Sec. 2.3). Having identified the drawbacks of the OEA model, we proceed to derive the TEA model (Sec. 2.4). The two models are then compared with each other and with the full PDE model. The second half of the chapter begins with an analysis of mass transfer between the fluids and its dependence on fluid properties and holdups (volume fractions) (Sec. 2.5). Next, an analytical solution of the TEA model is derived for extraction, without a reaction (Sec. 2.6). These results are used to identify rules for selecting a solvent, and the corresponding holdup, that increases extraction performance. Lastly, we investigate the possibility of using the mass transfer resistance between layered fluids to increase product yield in a system of competitive-consecutive reactions (Sec. 2.7). We conclude with a summary and discussion of the key results (Sec. 2.8).

2.2 Detailed PDE Model

Transport phenomena in layered flow through microchannels can be effectively studied by considering the simpler problem of layered flow between two infinite flat plates, as depicted in Fig. 2.1. This geometric simplification has been shown to result in an accurate model for rectangular channels with the wider side aligned along the inter-fluid interface (Vir *et al.*, 2014*a*; Picardo *et al.*, 2015). It also works reasonably well for square channels.

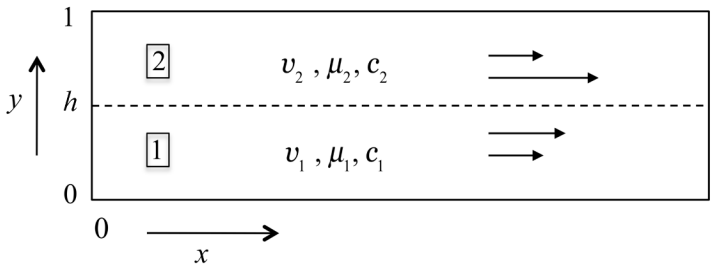

Figure 2.1: Schematic of two-phase layered flow between flat plates: a simplified model for layered flow in rectangular microchannels. The interface between the fluids is located at *h*. In extraction, phase 1 is the carrier fluid, which enters the channel with solute, and phase 2 is the solvent fluid. In reactive extraction, a reaction occurs in phase 2.

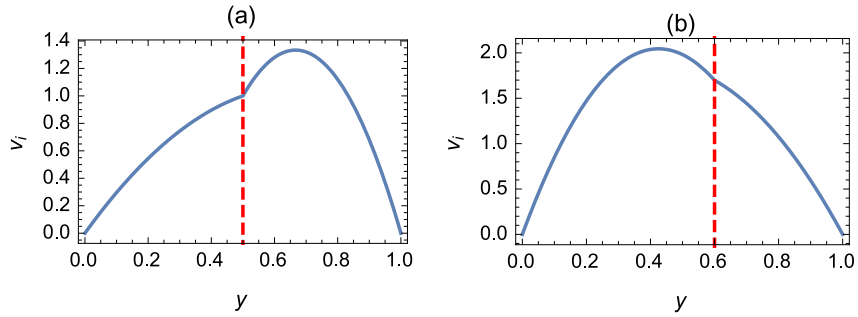

Figure 2.2: Velocity profiles for different viscosity ratios (μ_{12}) and holdups of phase 1 (h): (a) $\mu_{12} = 3, h = 0.5$ and (b) $\mu_{12} = 1/2, h = 0.6$. The interface is marked by a vertical dashed line.

In this model, the interface is considered to be flat and located at a fractional distance h from the bottom plate. The holdup (volume fraction) of phase 1 is given by h and that of phase 2 by $(1 - h)$. Pressure driven, unidirectional fully developed steady flow is assumed. The axial velocity varies in the transverse direction, in accordance with the momentum balance equations. The boundary conditions for the axial velocity field are no-slip at the walls and continuity of velocity and continuity of tangential shear stresses at the interface. The non-dimensional velocity field in each fluid (v_1, v_2), scaled by the respective average velocity, is given by (Vir *et al.*, 2014*b*):

$$v_i = A_i y^2 + B_i y + C_i \tag{2.1}$$

A_i, B_i and C_i are constants that depend on the holdup of phase 1 (h) and on the ratio of the viscosities of fluid 1 to fluid 2 (μ_{12}) (cf. (E.1) in Appendix E.1). Typical velocity profiles are depicted in Fig. 2.2, for different viscosity ratios and holdups.

In this chapter, we mainly focus on extraction and reactive extraction. Phase 1 $(0 \leq y < h)$ is considered to be the carrier phase that enters the channel with dissolved solute. Phase 2 $(h \leq y \leq 1)$ is the solvent phase, into which the solute is transfered by diffusion, where it possibly undergoes a reaction of the type $A \rightarrow$ products. The non-dimensional partial differential equations governing the concentration of the solute

(c_i) are given below.

$$\frac{\partial^2 c_1}{\partial y^2} = p v_1 \frac{\partial c_1}{\partial x} \tag{2.2a}$$

$$\frac{1}{D_{12}} \frac{\partial^2 c_2}{\partial y^2} = p \frac{v_2}{\omega} \frac{\partial c_2}{\partial x} - pDa\, r\,(c_2) \tag{2.2b}$$

The concentration at the inlet of the channel is an input to the problem:

$$c_1 = \frac{c_{1,in}}{\hat{c}_{1,in}} \quad \text{and} \quad c_2 = \frac{c_{2,in}}{\hat{c}_{1,in}} \quad \text{at} \quad x = 0 \tag{2.3}$$

Here, the concentration variables have been scaled with the mixing cup average concentration (cf. (2.13a)) of the carrier phase at the inlet of the channel ($\hat{c}_{1,in}$). The dimensionless parameters are the ratio of average fluid velocities (ω), ratio of diffusivities (D_{12}), the Damhkohler number (Da) and the transverse Peclet number (p):

$$\omega = \frac{\bar{v}_1}{\bar{v}_2}, \quad D_{12} = \frac{D_1}{D_2}, \quad Da = \frac{R\left(\hat{c}_{1,in}\right) L}{\hat{c}_{1,in} \bar{v}_1}, \quad p = \frac{\bar{v}_1 H^2}{D_1 L} \tag{2.4}$$

Here, D_i denotes the diffusivity of the solute in each fluid and $\bar{v}_i$ denotes the dimensional average velocity of each fluid. The ratio of average velocities (ω) is a function of μ_{12} and h, as given in (E.2) of Appendix E.1. R is the dimensional rate of reaction while r is the non-dimensional rate expression given by $\frac{R\left(c_2\, \hat{c}_{1,in}\right)}{R\left(\hat{c}_{1,in}\right)}$. (e.g. for an n$^{\text{th}}$ order reaction of the solute we have $r = -c_2^n$). L is the length of the channel. In this model, the channel is assumed to be sufficiently long so that axial diffusion is negligible in comparison with convection ($\frac{\bar{v}_i L}{D_i} \gg 1$).

Equations (2.2) are subject to no-flux boundary conditions at the walls. At the interface, continuity of flux must be satisfied. In addition, we assume that the two phases are in equilibrium at the interface.

$$\frac{\partial c_1}{\partial y} = 0 \quad \text{at} \quad y = 0 \tag{2.5a}$$

$$\frac{\partial c_2}{\partial y} = 0 \quad \text{at} \quad y = 1 \tag{2.5b}$$

$$D_{12} \frac{\partial c_1}{\partial y} = \frac{\partial c_2}{\partial y} \quad \text{at} \quad y = h \tag{2.5c}$$

$$c_1 = K c_2 \quad \text{at} \quad y = h \tag{2.5d}$$

Here, K is a constant distribution coefficient. If $K < 1$ then phase 2 (solvent) has a higher concentration at equilibrium, and is said to have a greater affinity for the solute.

2.3 One Equation Averaged (OEA) Model

In this section, we average across the entire channel, i.e. across both fluids simultaneously, using the Lyapunov-Schmidt (LS) reduction. The LS reduction is described in detail by Golubitsky and Schaeffer (1984), in the context of bifurcation theory. Balakotaiah and co-workers have explained how to use the LS reduction for order reduction of partial differential equations that describe convection, diffusion and reaction (Chakraborty and Balakotaiah, 2002, 2003). Ratnakar *et al.* (2012) have derived reduced models for a catalytic monolith reactor, consisting of a core flowing fluid phase and an annular stationary catalytic solid. They applied the LS technique to average across both phases together. We follow a similar approach in this section.

2.3.1 Derivation

Equations (2.2) can be written in linear operator form as follows:

$$\mathbf{L}c - p\mathbf{N}(c) = 0 \tag{2.6a}$$

where

$$\mathbf{L}c = \frac{1}{D_r}\frac{\partial^2 c}{\partial y^2} \tag{2.6b}$$

$$c = \begin{cases} c_1 & 0 \leq y < h \\ c_2 & h \leq y < 1 \end{cases} \tag{2.6c}$$

$$D_r = \begin{cases} 1 & 0 \leq y < h \\ D_{12} & h \leq y < 1 \end{cases} \tag{2.6d}$$

$$\mathbf{N}(c) = \begin{cases} v_1 \frac{\partial c_1}{\partial x} - v_1 \frac{c_{1,in}}{\hat{c}_{1,in}} \delta(x) & 0 \leq y < h \\ \frac{v_2}{\omega}\frac{\partial c_2}{\partial x} - Da\, r(c_2) - \frac{v_2}{\omega}\frac{c_{2,in}}{\hat{c}_{1,in}}\delta(x) & h \leq y < 1 \end{cases} \tag{2.6e}$$

The inlet conditions (2.3) are included in (2.6e) using Dirac delta functions $\delta(x)$. (2.3) is recovered on integrating (2.6) in x from 0^- to 0^+, while the differential equations (2.2) are obtained for $x > 0$. Writing the inlet conditions in this manner enables us to systematically derive the inlet conditions for the averaged model, as demonstrated by Balakotaiah and coworkers (Balakotaiah and Ratnakar, 2010).

Equations (2.6b) to (2.6d) define a linear operator $\mathbf{L}$ operating on functions c, which belong to the subspace of $\mathcal{L}_2(0,1)$ that satisfies (2.5a)-(2.5d). This operator is self adjoint under the following inner product (Ramkrishna and Amundson, 1974):

$$\langle u \cdot w \rangle = \int_0^h u_1 w_1 dy + K \int_h^1 u_2 w_2 dy \tag{2.7}$$

When $p = 0$, (2.6a) reduces to $\mathbf{L}c = 0$. The operator $\mathbf{L}$ has a nullspace ψ given by:

$$\psi = \begin{cases} \frac{K}{E} & 0 \leq y < h \\ \\ \frac{1}{E} & h \leq y < 1 \end{cases} \tag{2.8a}$$

where

$$E = \left(K^2 h + K\left(1-h\right)\right)^{1/2} \tag{2.8b}$$

Here, ψ has been normalized so that $\langle \psi \cdot \psi \rangle = 1$.

The first step of the LS procedure, is to decompose the domain space into orthogonal subspaces given by ker($\mathbf{L}$) and $\mathrm{ker}(\mathbf{L})^{\perp}$:

$$c(x,y) = \phi(x)\psi + \tilde{c}(x,y) \tag{2.9a}$$

where

$$\phi = \langle c \cdot \psi \rangle \quad \text{and} \quad \langle \tilde{\mathrm{c}} \cdot \psi \rangle = 0 \tag{2.9b}$$

The co-domain is also decomposed into orthogonal subspaces given by range($\mathbf{L}$) and $\mathrm{range}(\mathbf{L})^{\perp}$. Since $\mathbf{L}$ is self-adjoint, $\mathrm{range}(\mathbf{L})^{\perp}$ = ker($\mathbf{L}$). Projecting (2.6a) onto ker($\mathbf{L}$), i.e. onto ψ, effectively averages the governing PDEs (2.2a) and (2.2b) across both fluids:

$$\left\langle \left(\mathbf{L}c - p\mathbf{N}\left(c\right)\right) \cdot \psi \right\rangle = 0 \tag{2.10}$$

Substituting from (2.6)-(2.8) in (2.10) yields

$$\int_0^h \frac{\partial^2 c_1}{\partial y^2} dy + \int_h^1 \frac{1}{D_{12}} \frac{\partial^2 c_2}{\partial y^2} dy - \int_0^h \left(p v_1 \frac{\partial c_1}{\partial x} - p v_1 \frac{c_{1,in}}{\hat{c}_{1,in}} \delta\left(x\right) \right) dy$$
$$- \int_h^1 \left(p \frac{v_2}{\omega} \frac{\partial c_2}{\partial x} - p \frac{v_2}{\omega} \frac{c_{2,in}}{\hat{c}_{1,in}} \delta\left(x\right) - pDa\, r\left(c_2\right) \right) dy = 0 \tag{2.11}$$

Using the boundary conditions (2.5a) - (2.5d), we obtain:

$$\int_0^h \left(v_1 \frac{\partial c_1}{\partial x} - v_1 \frac{c_{1,in}}{\hat{c}_{1,in}} \delta(x) \right) dy + \int_h^1 \left(\frac{v_2}{\omega} \frac{\partial c_2}{\partial x} - \frac{v_2}{\omega} \frac{c_{2,in}}{\hat{c}_{1,in}} \delta(x) \right) dy = \int_h^1 Dar(c_2)\, dy \tag{2.12}$$

This equation can be expressed in terms of physically relevant cup mixing ($\hat{c}_1$, $\hat{c}_2$) and cross-section ($\bar{c}_1$, $\bar{c}_2$) averages. These quantities are defined as follows:

$$\hat{c}_1 = \frac{\int_0^h v_1 c_1 dy}{\int_0^h v_1 dy} = \frac{1}{h} \int_0^h v_1 c_1 dy \quad \text{and} \quad \hat{c}_2 = \frac{\int_h^1 v_2 c_2 dy}{\int_h^1 v_2 dy} = \frac{1}{(1-h)} \int_h^1 v_2 c_2 dy \tag{2.13a}$$

$$\bar{c}_1 = \frac{1}{h} \int_0^h c_1 dy \quad \text{and} \quad \bar{c}_2 = \frac{1}{(1-h)} \int_h^1 c_2 dy \tag{2.13b}$$

where we have used the fact that $\int_0^h v_1 dy = h$ and $\int_h^1 v_2 dy = (1-h)$, due to non-dimensionalization. The reaction term in (2.12) can be simplified, when p is small. In this case, fast transverse mixing causes the deviation of c_2 from its cross-section averaged value $\bar{c}_2$ to be small. Thus we may expand $r(c_2)$ in a Taylor series about $\bar{c}_2$. Making these substitutions in (2.12) we obtain:

$$h \left(\frac{d\hat{c}_1}{dx} - \delta(x) \right) + \frac{(1-h)}{\omega} \left(\frac{d\hat{c}_2}{dx} - \frac{\hat{c}_{2,in}}{\hat{c}_{1,in}} \delta(x) \right) = Da\, r(\bar{c}_2)(1-h) + O\left((c_2 - \bar{c}_2)^2 \right) \tag{2.14}$$

This is the global equation, which governs the evolution of the averaged concentrations along the length of the channel. To close the averaged model, we must have an equation that relates the average concentration of phase 1 to that of phase 2. In addition, we need relations between the cup-mixing average and cross-section average concentrations in each fluid. These relationships can be derived only after determining $\tilde{c}$, which accounts for the variation of the concentration field in the transverse direction (cf. (2.9a)).

The equations for $\tilde{c}$ are obtained by projecting (2.6a) onto range($\mathbf{L}$) or equivalently onto $\ker(\mathbf{L})^{\perp}$:

$$\mathbf{L}c - p\mathbf{N}(c) - \Big\langle \big(\mathbf{L}c - p\mathbf{N}(c) \big) \cdot \psi \Big\rangle \psi = 0 \tag{2.15}$$

Substituting from (2.6) - (2.9) in (2.15) yields

$$\frac{\partial^2 \tilde{c}_1}{\partial y^2} = p\left[\frac{d\phi}{dx}\frac{K}{E}\left(v_1(y) - \left(\frac{K}{E}\right)^2 - \frac{K}{\omega E^2}\right) + \left(\frac{K}{E}\right)^2 \left(Dar\left(\bar{c}_2\right)(1-h) + O\left(\left(c_2 - \bar{c}_2\right)^2\right)\right) + v_1(y)\frac{\partial \tilde{c}_1}{\partial x} - \left(\frac{K}{E}\right)^2 \frac{d}{dx}\left(\int_0^h v_1 \tilde{c}_1 dy + \frac{1}{\omega}\int_h^1 v_2 \tilde{c}_2 dy\right) - \left\{v_1(y)\frac{c_{1,in}}{\hat{c}_{1,in}} - \left(h + \frac{(1-h)}{\omega}\frac{\hat{c}_{2,in}}{\hat{c}_{1,in}}\right)\left(\frac{K}{E}\right)^2\right\}\delta(x)\right] \quad (2.16a)$$

$$\frac{\partial^2 \tilde{c}_2}{\partial y^2} = pD_{12}\left[\frac{d\phi}{dx}\frac{1}{E}\left(\frac{v_2(y)}{\omega} - \left(\frac{K}{E}\right)^2 - \frac{K}{\omega E^2}\right) - Da\left(r\left(\bar{c}_2\right) + r'\left(\bar{c}_2\right)\left(c_2 - \bar{c}_2\right) + O\left(\left(c_2 - \bar{c}_2\right)^2\right)\right) + \frac{K}{E^2}\left(Dar\left(\bar{c}_2\right)(1-h) + O\left(\left(c_2 - \bar{c}_2\right)^2\right)\right) + \frac{v_2(y)}{\omega}\frac{\partial \tilde{c}_1}{\partial x} - \frac{K}{E^2}\frac{d}{dx}\left(\int_0^h v_1 \tilde{c}_1 dy + \frac{1}{\omega}\int_h^1 v_2 \tilde{c}_2 dy\right) - \left\{\frac{v_2(y)}{\omega}\frac{c_{2,in}}{\hat{c}_{1,in}} - \left(h + \frac{(1-h)}{\omega}\frac{\hat{c}_{2,in}}{\hat{c}_{1,in}}\right)\frac{K}{E^2}\right\}\delta(x)\right] \quad (2.16b)$$

Equations (2.16a) and (2.16b) specify the transverse concentration variations ($\tilde{c}$) in terms of the average modes ϕ and $\bar{c}_2$. Here we obtain an asymptotic solution for small p by expanding $\tilde{c}$ as a perturbation expansion in p:

$$\tilde{c}_1 = \tilde{c}_{1,0} + p\tilde{c}_{1,1} + O(p^2) \quad (2.17a)$$

$$\tilde{c}_2 = \tilde{c}_{2,0} + p\tilde{c}_{2,1} + O(p^2) \quad (2.17b)$$

Substituting (2.17) into (2.16a) and (2.16b), and applying the orthogonality condition (2.9b), we find that $\tilde{c}_{1,0} = \tilde{c}_{2,0} = 0$. This corresponds to the case of perfect transverse mixing.

At $O(p)$, we obtain:

$$\frac{\partial^2 \tilde{c}_{1,1}}{\partial y^2} = \frac{d\varphi}{dx}\frac{K}{E}\left(v_1(y) - \left(\frac{K}{E}\right)^2 - \frac{K}{\omega E^2}\right) + \left(\frac{K}{E}\right)^2 Da\, r(\bar{c}_2)(1-h) - \left\{v_1(y)\frac{c_{1,in}}{\hat{c}_{1,in}} - \left(h + \frac{(1-h)}{\omega}\frac{\hat{c}_{2,in}}{\hat{c}_{1,in}}\right)\left(\frac{K}{E}\right)^2\right\}\delta(x) \quad (2.18a)$$

$$\frac{\partial^2 \tilde{c}_{2,1}}{\partial y^2} = D_{12}\left[\frac{d\varphi}{dx}\frac{1}{E}\left(\frac{v_2(y)}{\omega} - \left(\frac{K}{E}\right)^2 - \frac{K}{\omega E^2}\right) - Da\, r(\bar{c}_2) + \frac{K}{E^2}Da\, r(\bar{c}_2)(1-h) - \left\{\frac{v_2(y)}{\omega}\frac{c_{2,in}}{\hat{c}_{1,in}} - \left(h + \frac{(1-h)}{\omega}\frac{\hat{c}_{2,in}}{\hat{c}_{1,in}}\right)\frac{K}{E^2}\right\}\delta(x)\right] \quad (2.18b)$$

Note that we have assumed Da to be $O(1)$, i.e. the time scale of reaction is comparable to the time scale of convection.

We can further simplify (2.18a) and (2.18b) by using the relation between $\frac{d\varphi}{dx}$ and $\bar{c}_2$, obtained by substituting (2.9) into the averaged equation (2.14):

$$\left(\frac{K}{E}h + \frac{1}{\omega E}(1-h)\right)\frac{d\phi}{dx} = Da\, r(\bar{c}_2)(1-h) + \left(h + \frac{(1-h)}{\omega}\frac{\hat{c}_{2,in}}{\hat{c}_{1,in}}\right)\delta(x) + O(p) \quad (2.19)$$

Using (2.19) to replace $\frac{d\varphi}{dx}$ in (2.18a) and (2.18b), and retaining terms to $O(p)$, we obtain

$$\frac{\partial^2 \tilde{c}_{1,1}}{\partial y^2} = Da\, r(\bar{c}_2)\frac{v_1(y)(1-h)}{\left(h + \frac{(1-h)}{\omega K}\right)} - \delta(x)\, v_1(y)\left[\frac{c_{1,in}}{\hat{c}_{1,in}} - \frac{h + \frac{(1-h)}{\omega}\frac{\hat{c}_{2,in}}{\hat{c}_{1,in}}}{h + \frac{(1-h)}{\omega K}}\right] \quad (2.20a)$$

$$\frac{\partial^2 \tilde{c}_{2,1}}{\partial y^2} = D_{12}\, Da\, r(\bar{c}_2)\left(\frac{v_2(y)(1-h)}{\omega K h + (1-h)} - 1\right) - D_{12}\,\delta(x)\frac{v_2(y)}{\omega}\left[\frac{c_{2,in}}{\hat{c}_{1,in}} - \frac{h + \frac{(1-h)}{\omega}\frac{\hat{c}_{2,in}}{\hat{c}_{1,in}}}{hK + \frac{(1-h)}{\omega}}\right] \quad (2.20b)$$

These equations are subject to the boundary conditions given in (2.5). In addition, the solution must satisfy the orthogonality condition (2.9b). The solvability of these equations is guaranteed by the manner in which the domain and co-domain are decomposed in the Lyapunov-Schmidt procedure. The solution is of the following form:

$$\tilde{c}_{1,1} = f_1(y)\, Da\, r(\bar{c}_2) + d_1(y)\,\delta(x) \quad (2.21a)$$

$$\tilde{c}_{2,1} = f_2(y)\, D_{12} Da\, r(\bar{c}_2) + d_2(y)\, D_{12}\,\delta(x) \quad (2.21b)$$

Now, substituting (2.21) into (2.9), we obtain a low dimensional slow invariant manifold

in solution space (accurate to $O(pDa)$) that is parameterized by ϕ and $\bar{c}_2$.

$$c_1 = \frac{K}{E}\phi + pDa\, r\left(\bar{c}_2\right) f_1\left(y\right) + p\delta\left(x\right) d_1\left(y\right) \tag{2.22a}$$

$$c_2 = \frac{1}{E}\phi + pDa\, r\left(\bar{c}_2\right) D_{12} f_2\left(y\right) + pD_{12}\,\delta\left(x\right) d_2\left(y\right) \tag{2.22b}$$

Starting from arbitrary inlet conditions, the concentration rapidly relaxes to this manifold due to relatively fast transverse diffusion (small p). After collapsing onto the manifold, the system's evolution along x is governed by the averaged equation (2.14).

In order to close the averaged model, we substitute (2.22) into (2.13a) and (2.13b) and derive the following relationships between the cross-section and cup-mixing averages (to $O(p)$):

$$\hat{c}_1 - \bar{c}_1 = pDa\, r\left(\bar{c}_2\right)\left(\hat{f}_1 - \bar{f}_1\right) + p\delta\left(x\right)\left(\hat{d}_1 - \bar{d}_1\right) \tag{2.23a}$$

$$\hat{c}_2 - \bar{c}_2 = pDaD_{12}\, r\left(\bar{c}_2\right)\left(\hat{f}_2 - \bar{f}_2\right) + pD_{12}\,\delta\left(x\right)\left(\hat{d}_2 - \bar{d}_2\right) \tag{2.23b}$$

$$\bar{c}_1 - K\bar{c}_2 = pDa\, r\left(\bar{c}_2\right)\left(\bar{f}_1 - KD_{12}\bar{f}_2\right) + p\delta\left(x\right)\left(\bar{d}_1 - KD_{12}\bar{d}_2\right) \tag{2.23c}$$

Here $\hat{f}_i$, $\hat{d}_i$ and $\bar{f}_i$, $\bar{d}_i$ are cup-mixing and cross-section averages of $f_i(y)$, $d_i(y)$.

Now, dropping the $\delta\left(x\right)$ terms, we obtain the reduced order OEA model for $x > 0$ as follows:

$$h\frac{d\hat{c}_1}{dx} + \frac{(1-h)}{\omega}\frac{d\hat{c}_2}{dx} = Dar\left(\bar{c}_2\right)(1-h) \tag{2.24a}$$

$$\hat{c}_1 - \bar{c}_1 = pDa\, r\left(\bar{c}_2\right)\left(\hat{f}_1 - \bar{f}_1\right) \tag{2.24b}$$

$$\hat{c}_2 - \bar{c}_2 = pDaD_{12}\, r\left(\bar{c}_2\right)\left(\hat{f}_2 - \bar{f}_2\right) \tag{2.24c}$$

$$\bar{c}_1 - K\bar{c}_2 = pDa\, r\left(\bar{c}_2\right)\left(\bar{f}_1 - KD_{12}\bar{f}_2\right) \tag{2.24d}$$

The expressions for f_i are given in appendix E.1.

To obtain the inlet condition for the averaged model, we use the relations in (2.23) to write the averaged equation (2.14) entirely in terms of $\bar{c}_2$. The resulting equation is integrated in x from 0^- to 0^+ to yield the inlet condition (Balakotaiah and Ratnakar, 2010). The calculation is straightforward, and we omit the details for the sake of brevity. The final inlet condition to $O(p)$ is:

$$h\hat{c}_1 + \frac{(1-h)}{\omega}\hat{c}_2 = h + \frac{(1-h)}{\omega}\frac{\hat{c}_{2,in}}{\hat{c}_{1,in}} \quad \text{at} \quad x = 0 \tag{2.24e}$$

The source terms ($d_i\delta\left(x\right)$) do not contribute to the inlet condition. This is because after substitution into (2.14), $\delta\left(x\right)$ is transformed to $\delta'\left(x\right)$ and does not contribute to the integral in x from 0^- to 0^+. The inlet condition (2.24e) ensures that the total input of solute

in the averaged model is the same as that in the PDE model.

This reduced model consists of one averaged mass balance equation (2.24a), which describes the evolution of the cup mixing averaged concentrations along the channel length. Equations (2.24b) and (2.24c) account for the difference between the cup-mixing and cross-section average concentrations in each phase. This difference arises due to the interplay between the reaction and the non-uniform velocity profile, which results in varying residence times along the cross-section. Also intra-fluid diffusive mixing is not instantaneous ($p \neq 0$) but proceeds at a finite rate and hence cannot completely homogenize the concentration in each phase. Equation (2.24d) accounts for the departure from equilibrium maintained between the two phases due to the reaction in phase 2.

It is possible to systematically derive the model to higher orders in p. However, we do not pursue this here, because our goal is to obtain a relatively simple reduced order model. Also the major features of the system, and all the physical parameters, are captured at $O(p)$.

In the following subsection we compare the predictions of the OEA model with the full PDE model. We also compare its performance to that of a simple heuristic plug flow model.

2.3.2 Comparison of the OEA model with the PDE model and a Simple Heuristic model

Apart from comparing the OEA model with the full PDE model, it is also instructive to analyze how much better it performs in comparison to a simpler model that is derived heuristically. If we assume the fluids to be perfectly mixed, i.e. the cup-mixing and cross-section averages to be equal, and the two phases to be in equilibrium, then a mass balance directly leads to the following model:

$$\left(hK + \frac{(1-h)}{\omega}\right)\frac{d\hat{c}_2}{dx} = Dar\left(\hat{c}_2\right)(1-h) \tag{2.25a}$$

$$\hat{c}_1 = K\hat{c}_2 \tag{2.25b}$$

Note that the OEA model reduces to this simple heuristic (SH) plug-flow model when $p \to 0$. Thus we expect the improvement in accuracy of the OEA model over the SH model to increase as p increases. Since the reduced model was derived for small p, we expect quantitative accuracy for $p \leq 1$ and qualitative agreement, possibly, with the full PDE model for larger $p > 1$.

Fig. 2.3 presents predictions of the three models – full PDE, OEA and SH – for different values of p and Da, for the case of $\mu_{12} = 1/2$, $D_{12} = 3$, $K = 2$, $h = 0.4$. The

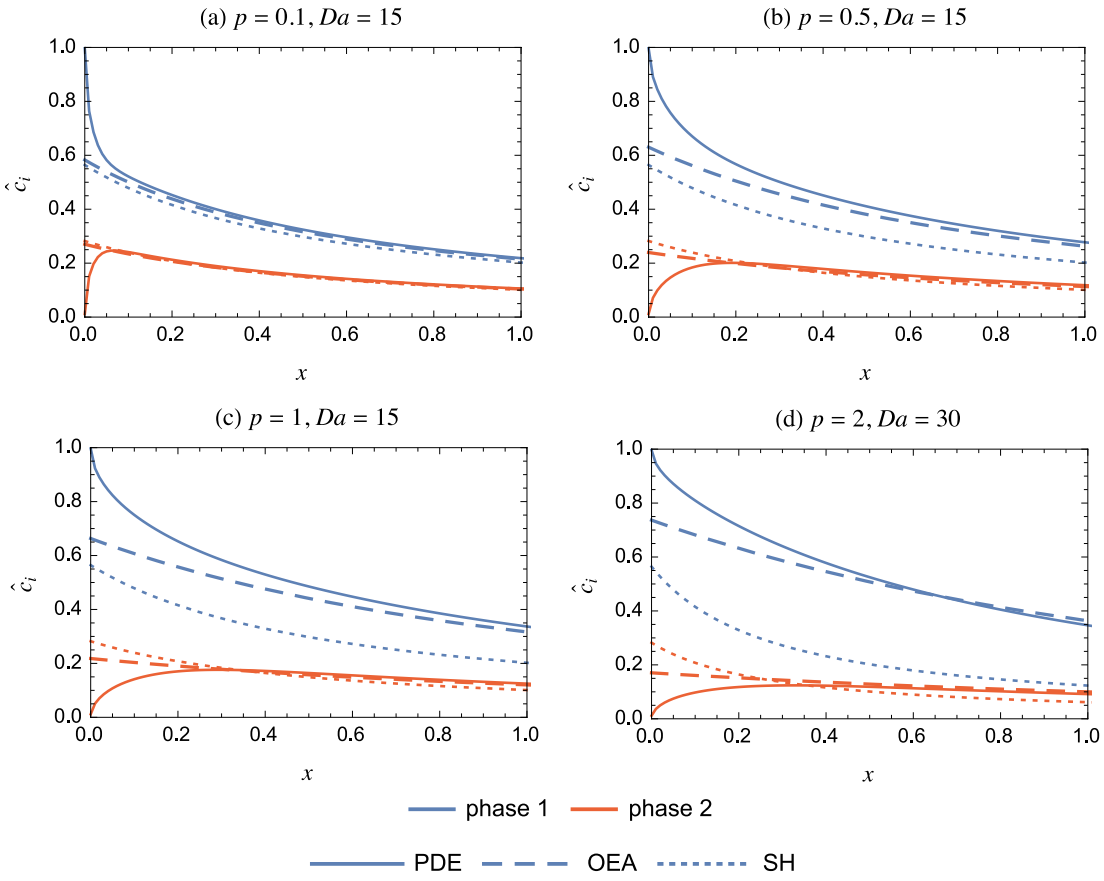

Figure 2.3: Comparison of the one equation averaged (OEA) model (2.24) with the full PDE model (2.2) - (2.5) and the simple heuristic (SH) model (2.25), for different values of p and Da. At the inlet ($x = 0$), $\hat{c}_{1,in} = 1$ and $\hat{c}_{2,in} = 0$. Parameter values: $\mu_{12} = 1/2$, $D_{12} = 3$, $K = 2$, $h = 0.4$.

reaction is assumed to be second order: $r(\bar{c}_2) = -(\bar{c}_2)^2$. At the inlet, phase 2 (solvent) is taken to be pure ($\hat{c}_{2,in} = 0$). At low values of p (Fig. 2.3a), the predictions of all three models nearly coincide. So there is no advantage of using the OEA model over the SH model. However, as p increases (compare Figs. 2.3a - 2.3c) the predictions of the Lyapunov-Schmidt averaged OEA model are much better than the SH model. Although the derivation was carried out for small p, the OEA model predicts the *outlet concentration* well even for p greater than unity.

Fig. 2.3 shows that the predictions of the OEA model differ from that of the full PDE model, in the initial portion of the channel. At the inlet, the concentrations in the two phases do not lie on the slow invariant manifold (2.22). As they flow through the channel, rapid transverse diffusion causes the concentrations to relax to this slow manifold. As p increases, the diffusion time scale increases relative to convection, and the initial length required for the concentrations to fall onto the slow invariant manifold increases. Therefore, the predictions of the full PDE model matches the OEA after a greater distance along the channel, when p is larger.

These results show clearly that the initial mass transfer between the phases that occurs near the inlet of the channel is not captured by the OEA model. Only the subsequent mass transfer that is sustained by the reaction is captured. Therefore, the OEA model cannot be used to model extraction without a reaction. This shortcoming of the OEA model is apparent from the model equations (2.24). When $Da = 0$, equations (2.24) merely predict the final equilibrium concentrations, without giving any information about the evolution along the channel length. Thus, averaging across both fluids simultaneously has resulted in a loss of information regarding the flux of solute between the phases in the absence of a reaction. In the following section, we seek to overcome this drawback by averaging across each fluid separately and obtaining an explicit low dimensional approximation for the inter-fluid solute flux.

2.4 Two Equation Averaged (TEA) Model

In this section, we will apply the Lyapunov-Schmidt method to each fluid domain separately, and obtain two averaged equations to describe the evolution of the mixing cup concentrations in the two fluids. Our objective is to describe the mass transfer that occurs between the phases in the absence of a reaction.

2.4.1 Derivation

In the derivation of the OEA model, the LS reduction was based on the null space obtained in the limit of $p \to 0$. This null space consisted of uniform concentrations in each phase, related to each other by the equilibrium relationship (2.5d). In order to average each phase separately, we must carry out the LS reduction of a different base state, in which an independent null space is obtained for each fluid. To accomplish this, we embed the problem into a family of problems parameterized by α, as follows:

For phase 1:

$$\frac{\partial^2 c_1}{\partial y^2} = pv_1 \frac{\partial c_1}{\partial x} - pv_1 \frac{c_{1,in}}{\hat{c}_{1,in}} \delta(x) \tag{2.26a}$$

$$\frac{\partial c_1}{\partial y} = 0 \quad \text{at} \quad y = 0 \tag{2.26b}$$

$$-\frac{\partial c_1}{\partial y} = \alpha J(x) \quad \text{at} \quad y = h \tag{2.26c}$$

For phase 2:

$$\frac{1}{D_{12}} \frac{\partial^2 c_2}{\partial y^2} = p\frac{v_2}{\omega} \frac{\partial c_2}{\partial x} - p\frac{v_2}{\omega} \frac{c_{2,in}}{\hat{c}_{1,in}} \delta(x) - Dar(c_2) \tag{2.27a}$$

$$\frac{\partial c_2}{\partial y} = 0 \quad \text{at} \quad y = 1 \tag{2.27b}$$

$$-\frac{1}{D_{12}} \frac{\partial c_2}{\partial y} = \alpha J(x) \quad \text{at} \quad y = h \tag{2.27c}$$

Here, $J(x)$ is the inter-fluid flux.. It has been multiplied by the parameter α. The original problem ((2.2) and (2.5)) is recovered from (2.26) and (2.27) on setting $\alpha = 1$ and using the the equilibrium condition (2.5d) to determine $J(x)$.

In the derivation that follows, we consider the base state in the limit of $\alpha \to 0$ and $p \to 0$. In this limit, the equations for the two phases decouple and result in an independent null space in each fluid. The LS reduction is carried out, to first order in α and p, for each fluid separately. We then set $\alpha = 1$ to obtain two reduced equations for the averaged concentration in each fluid, in terms of the inter-fluid flux $J(x)$. The flux is determined by requiring the low dimensional manifold solutions to satisfy the equilibrium condition (2.5d). This last step couples the variation of the concentrations in the two fluids, while accounting for local equilibrium at the interface.

The introduction of an artificial small parameter, to provide a convenient base state for constructing an asymptotic solution, is a well known technique (Bender and Orszag, 1999). It has recently been applied for obtaining low dimensional models via center manifold reduction (Roberts, 2015). The effectiveness of this reduction procedure will

be evaluated a posteriori by comparison with the full PDE model.

Beginning with phase 1, we find that, in the limit of $p \to 0$ and $\alpha \to 0$, (2.26) reduces to $\mathbf{L}_1 c_1 = \frac{\partial^2 c_1}{\partial y^2} = 0$. The linear operator $\mathbf{L}_1$ is self adjoint under the inner product $\langle u \cdot w \rangle_1 = \frac{1}{h} \int_0^h uwdy$. The normalized basis for ker($\mathbf{L}_1$) is 1. Decomposing c_1 into ker($\mathbf{L}_1$) and $\ker(\mathbf{L}_1)^\perp$ yields:

$$c_1(x,y) = \langle c_1 \cdot 1 \rangle_1 (1) + \tilde{c}_1 = \bar{c}_1(x) + \tilde{c}_1(x,y) \tag{2.28a}$$

$$\langle \tilde{c}_1 \cdot 1 \rangle_1 = 0 \tag{2.28b}$$

The equations for phase 2 (2.27) reduce to $\mathbf{L}_2 c_2 = \frac{\partial^2 c_2}{\partial y^2} = 0$ when $p \to 0$ and $\alpha \to 0$. $\mathbf{L}_2$ is also self adjoint and has a nullspace with normalized basis equal to unity. The inner product in this case is defined as: $\langle u \cdot w \rangle_2 = \frac{1}{1-h} \int_h^1 uwdy$. Decomposing c_2 into ker($\mathbf{L}_2$) and $\ker(\mathbf{L}_2)^\perp$ yields:

$$c_2(x,y) = \langle c_2 \cdot 1 \rangle_2 (1) + \tilde{c}_2 = \bar{c}_2(x) + \tilde{c}_2(x,y) \tag{2.29a}$$

$$\langle \tilde{c}_2 \cdot 1 \rangle_2 = 0 \tag{2.29b}$$

Here $\bar{c}_1$ and $\bar{c}_2$ are the cross-section average concentrations in phase 1 and phase 2 respectively (cf. (2.13b)).

The next step is to project (2.26) onto ker($\mathbf{L}_1$) and (2.27) onto ker($\mathbf{L}_2$). Using the boundary conditions (2.26b), (2.26c) and (2.27b), (2.27c) we obtain two averaged equations that describe the evolution along x of the cup-mixing average concentration (cf. (2.13a)) in each fluid :

$$p\frac{d\hat{c}_1}{dx} - p\delta(x) = \frac{-\alpha J(x)}{h} \tag{2.30a}$$

$$\frac{p}{\omega}\left(\frac{d\hat{c}_2}{dx} - \frac{\hat{c}_{2,in}}{\hat{c}_{1,in}}\delta(x)\right) = \frac{\alpha J(x)}{(1-h)} + pDar(\bar{c}_2) + O\left(\tilde{c}_2^2\right) \tag{2.30b}$$

Here, we have expanded $r(c_2)$ in a Taylor series about $\bar{c}_2$, as was done in the derivation of the OEA model.

To close the averaged model, we need to identify $J(x)$ and relate the cup-mixing average concentrations to the cross-section averages. This is achieved by solving the equations obtained from the projections of (2.26) onto $\ker(\mathbf{L}_1)^\perp$ and (2.27) onto $\ker(\mathbf{L}_2)^\perp$, to first order in p and α.

Focusing first on phase 1, we obtain the following equation for $\tilde{c}_1$:

$$\frac{\partial^2 \tilde{c}_1}{\partial y^2} = p v_1(y) \frac{\partial}{\partial x}(\bar{c}_1 + \tilde{c}_1) - \alpha \frac{J(x)}{h} - \frac{p}{h} \int_0^h v_1(y) \frac{\partial}{\partial x}(\bar{c}_1 + \tilde{c}_1)\, dy - p\delta(x) \left[v_1(y) \frac{c_{1,in}}{\hat{c}_{1,in}} - 1 \right] \quad (2.31)$$

At zeroth order ($p = 0,\ \alpha = 0$), this equation results in $\tilde{c}_1 = 0$, because $\langle \tilde{c}_1 \cdot 1 \rangle_1 = 0$. At first order in p and α, we obtain the following equation for $\tilde{c}_1$:

$$\frac{\partial^2 \tilde{c}_1}{\partial y^2} = p\left(v_1(y) - 1\right) \frac{\partial \bar{c}_1}{\partial x} - \alpha \frac{J(x)}{h} - p\delta(x) \left[v_1(y) \frac{c_{1,in}}{\hat{c}_{1,in}} - 1 \right] \quad (2.32)$$

Substituting (2.28) in (2.30a), we obtain $p\frac{\partial \bar{c}_1}{\partial x} = -\alpha \frac{J(x)}{h} + p\delta(x)$ to leading order. Substituting this result in (2.32) yields:

$$\frac{\partial^2 \tilde{c}_1}{\partial y^2} = -\alpha \frac{J(x)}{h} v_1(y) - p\delta(x) v_1(y) \left[\frac{c_{1,in}}{\hat{c}_{1,in}} - 1 \right] \quad (2.33)$$

Proceeding in a similar manner for phase 2, we obtain $\tilde{c}_2 = 0$ at $O(1)$ and the following equation for $\tilde{c}_2$ at first order:

$$\frac{1}{D_{12}} \frac{\partial^2 \tilde{c}_2}{\partial y^2} = \alpha \frac{J(x)}{(1-h)} v_2(y) + pDa\, r(\bar{c}_2)\left(v_2(y) - 1\right) - p\delta(x) \frac{v_2(y)}{\omega} \left[\frac{c_{2,in} - \hat{c}_{2,in}}{\hat{c}_{1,in}} \right] \quad (2.34)$$

Solving (2.33) and (2.34), subject to boundary conditions (2.26b), (2.26c) and (2.27b), (2.27c) and the orthogonality conditions in (2.28b) and (2.29b), we obtain:

$$\tilde{c}_1 = s_1(y)\, \alpha J(x) + e_1(y)\, p\delta(x) \quad (2.35a)$$

$$\tilde{c}_2 = s_2(y)\, D_{12} \alpha J(x) + q_2(y)\, D_{12} pDa\, r(\bar{c}_2) + e_2(y)\, D_{12}\, p\delta(x) \quad (2.35b)$$

Substituting these solutions into (2.28a) and (2.29a), and setting $\alpha = 1$, we obtain two low dimensional manifolds parameterized by $\bar{c}_1$ and $\bar{c}_2$:

$$c_1 = \bar{c}_1 + s_1(y)\, J(x) + e_1(y)\, p\delta(x) \quad (2.36a)$$

$$c_2 = \bar{c}_2 + s_2(y)\, D_{12} J(x) + q_2(y)\, D_{12} pDa\, r(\bar{c}_2) + e_2(y)\, pD_{12}\, \delta(x) \quad (2.36b)$$

The cup-mixing and the cross-section average concentrations in the two fluids can now be related by substituting (2.36) in (2.13a) and (2.13b).

$$\hat{c}_1 - \bar{c}_1 = \hat{s}_1 J(x) + p\hat{e}_1 \delta(x) \quad (2.37a)$$

$$\hat{c}_2 - \bar{c}_2 = D_{12}\hat{s}_2 J(x) + pDaD_{12}\,\hat{q}_2 r(\bar{c}_2) + pD_{12}\,\hat{e}_2\delta(x) \tag{2.37b}$$

Here $\hat{s}_i$, $\hat{e}_i$, $\hat{q}_2$, are the mixing-cup averages of s_i, e_i, q_2.

The flux $J(x)$ is identified by requiring the manifold (2.36) to satisfy the equilibrium condition $c_1 = Kc_2$ at the interface (2.5d). This yields:

$$J(x) = \frac{(\bar{c}_1 - K\bar{c}_2) - pDaD_{12}K\,r(\bar{c}_2)\,q_2(h) + \big(e_1(h) - KD_{12}e_2(h)\big)p\delta(x)}{KD_{12}s_2(h) - s_1(h)} \tag{2.38}$$

Now we can obtain the inlet conditions for $\hat{c}_1$ and $\hat{c}_2$. First, we use (2.37) and (2.38) to rewrite (2.30) in terms of $\bar{c}_1$ and $\bar{c}_2$ only. Then integrating in x from 0^- to 0^+, we obtain the following inlet conditions (to $O(p)$):

$$\hat{c}_1 = 1 - \left[\frac{e_1(h) - KD_{12}e_2(h)}{KD_{12}s_2(h) - s_1(h)}\right] \quad \text{at} \quad x = 0 \tag{2.39a}$$

$$\hat{c}_2 = \frac{\hat{c}_{2,in}}{\hat{c}_{1,in}} + \frac{\omega}{(1-h)}\left[\frac{e_1(h) - KD_{12}e_2(h)}{KD_{12}s_2(h) - s_1(h)}\right] \quad \text{at} \quad x = 0 \tag{2.39b}$$

The source terms (involving $e_i\delta(x)$) modify the inlet condition at $O(1)$, through the inter-fluid flux (2.38). The source terms do not contribute at higher orders of p because $\delta(x)$ is transformed to $\delta'(x)$ on substituting into the averaged equation. The $O(1)$ modification accounts for transverse variations in the inlet concentrations. If the inlet concentrations are uniform across the cross-section, then $e_1 = e_2 = 0$. We assume this to be the case, in this work. The inlet condition then reduces to:

$$\hat{c}_1 = 1 \quad \text{and} \quad \hat{c}_2 = \frac{\hat{c}_{2,in}}{\hat{c}_{1,in}} \quad \text{at} \quad x = 0 \tag{2.40}$$

Note that, for the case of uniform inlet concentrations, the inlet cup-mixing average concentrations of the TEA model are identical to the inlet cup-mixing average concentration of the full PDE model. This is not the case in the OEA model, where only the total amount of solute entering the channel is the same (cf. (2.24e)).

Having obtained the inlet conditions, we drop the $\delta(x)$ terms to obtain the two equation averaged (TEA) model for $x > 0$:

$$p\frac{d\hat{c}_1}{dx} = \frac{-J(x)}{h} \tag{2.41a}$$

$$\hat{c}_1 - \bar{c}_1 = \hat{s}_1 J(x) \tag{2.41b}$$

$$\frac{p}{\omega}\frac{d\hat{c}_2}{dx} = \frac{J(x)}{(1-h)} + pDar(\bar{c}_2) \tag{2.41c}$$

$$\hat{c}_2 - \bar{c}_2 = D_{12}\hat{s}_2 J(x) + pDaD_{12}\hat{q}_2 r(\bar{c}_2) \tag{2.41d}$$

$$J(x) = \frac{(\bar{c}_1 - K\bar{c}_2)}{D_{12}Ks_2(h) - s_1(h)} - pDa\, r(\bar{c}_2)\, \frac{D_{12}Kq_2(h)}{D_{12}Ks_2(h) - s_1(h)} \tag{2.41e}$$

Expressions for s_i and q_2 are given in Appendix E.1.

Equations (2.41a) to (2.41e) define the TEA model. This model consists of two differential equations for the evolution of the cup-mixing average concentrations along the channel. Two more equations account for the difference between the cup-mixing and the cross-section averages (due to the finite rate of transverse diffusion). The last equation gives an expression for the flux between the fluids.

The flux $J(x)$ is composed of two terms (cf. (2.41e)). The first is due to the departure of the concentration in the two fluids from equilibrium. Note that *this term is non-zero even in the absence of a reaction*, implying that this averaged model can be used to study non-reactive extraction. The second term is a correction to the flux due to a chemical reaction. The magnitude of this terms depends on pDa.

We can identify the coefficient of $(\bar{c} - K\bar{c}_2)$ in (2.41e) as a Sherwood number (Sh_b). This is a dimensionless number given by ($\frac{k_b L}{D_1}$) where k_b is an overall mass transfer coefficient based on the cross-section average concentrations in the two phases (Cussler, 2009).

$$\mathrm{Sh}_b = \left[D_{12}Ks_2(h) - s_1(h)\right]^{-1} \tag{2.42}$$

By studying the variation of Sh_b, we can easily ascertain the influence of various fluid and flow parameters on the rate of inter-phase mass transfer. This is done in Sec. 2.5.

In the following subsection, we compare the TEA model with the full PDE model and the previously derived OEA model.

2.4.2 Comparison of the TEA model with the PDE model and the OEA model

The OEA model, develop in Sec. 2.3, was unable to capture the variation of the average concentration near the inlet of the channel. Also, it did not yield useful results for the case of extraction without a reaction. With the aim of overcoming these limitations, the TEA model was formulated in Sec. 2.4.1. Now, we will evaluate the accuracy of the TEA model by comparing its predictions with simulations of the PDE model and the OEA model.

Fig. 2.4 presents a comparison of the predictions of the TEA, OEA and full PDE models. The simulations are carried out for the same case as Fig. 2.3: second order reaction, with pure solvent (phase 2) at the inlet. The results show that the TEA model predicts the average concentrations much better than the OEA model, when Da is relatively small

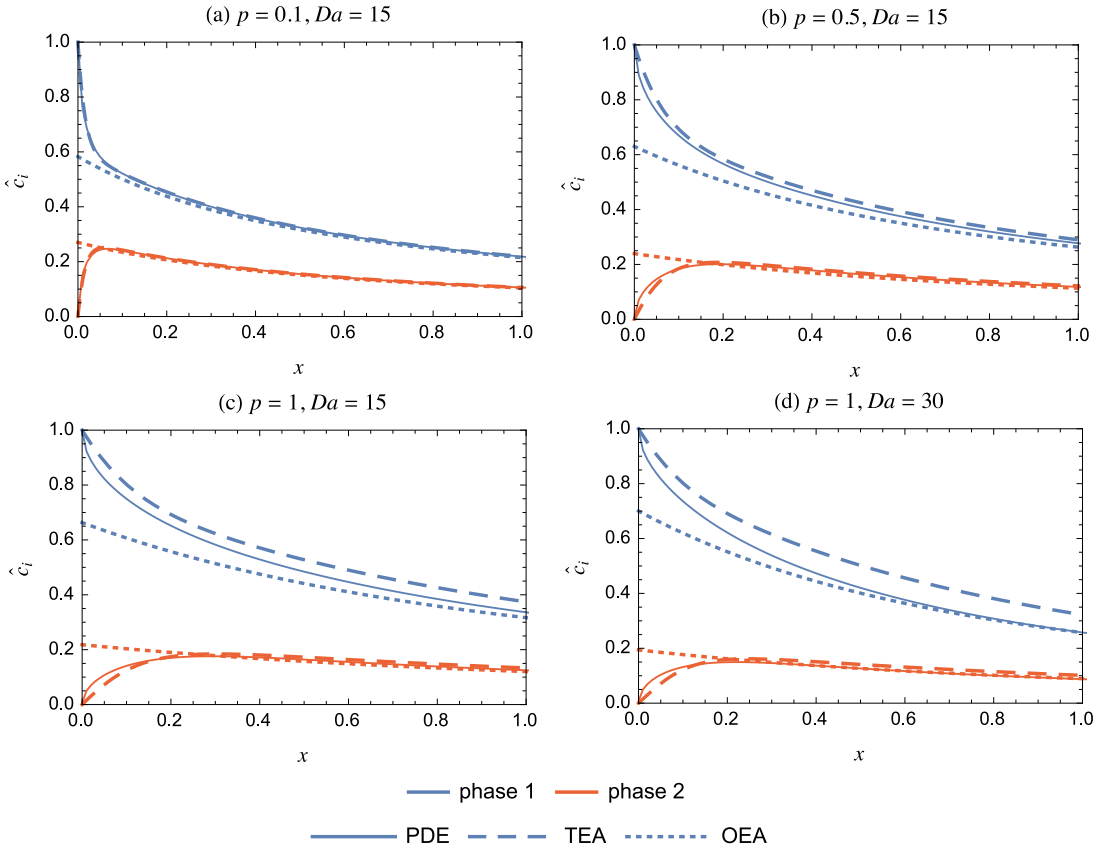

Figure 2.4: Comparison of the two equation averaged (TEA) model (2.41) with the full PDE model (2.2) - (2.5) and the one equation averaged (OEA) model (2.24) for the case of second order reaction in phase 2. The variation of the cup-mixing average concentration along the length of the channel is plotted. Different values of p and Da are considered. At the inlet $(x = 0)$, $\hat{c}_{1,in} = 1$ and $\hat{c}_{2,in} = 0$. Parameter values: $\mu_{12} = 1/2$, $D_{12} = 3$, $K = 2$, $h = 0.4$

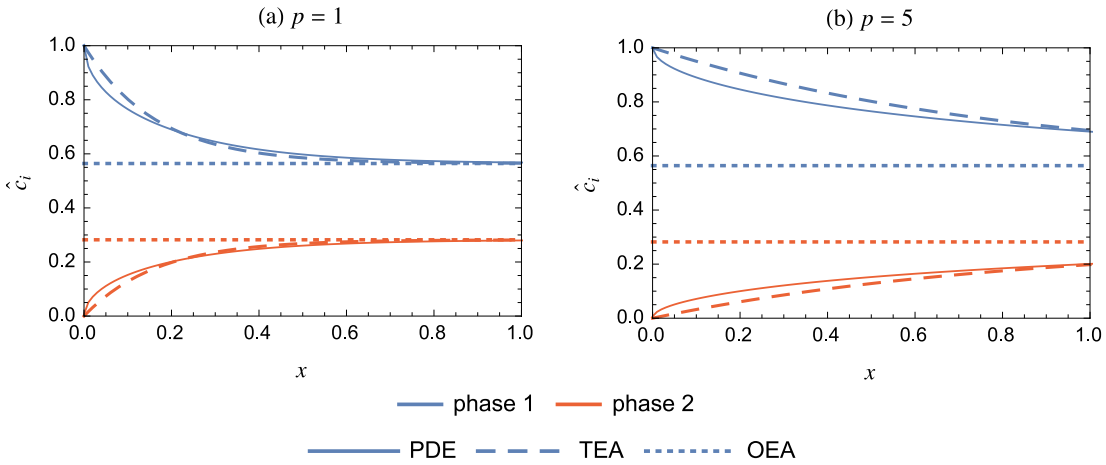

Figure 2.5: Comparison of the two equation averaged (TEA) model (2.41) with the full PDE model (2.2) - (2.5) and the one equation averaged (OEA) model (2.24) for the case of extraction (without a reaction). The variation of the cup-mixing average concentration along the length of the channel is plotted. Different values of p are considered. The concentration in phase 1 (carrier) is always greater than that in phase 2 (solvent). Parameter values: $\mu_{12} = 1/2$, $D_{12} = 3$, $K = 2$, $h = 0.4$

(Figs. 2.4a-2.4c). This improvement is pronounced near the inlet; the TEA model captures the variation of the average concentrations right from the entrance of the channel. Clearly, for small Da, the TEA model based on averaging the two fluids separately is superior to the OEA model, which averages across both fluids.

The predictions of the TEA model deteriorate, however, as Da is increased and the OEA model performs better, as seen in Fig. 2.4d. This was found to be the case in other comparisons as well, which were carried out for a range of parameter values. Thus, when modeling reactive extraction, the TEA model should be used unless Da is large ($Da < 1$).

The primary objective of developing the TEA model was to predict extraction, without any reaction. Comparisons of the two averaged models with simulations of the full PDEs, for the case of non-reactive extraction, are shown in Fig. 2.5. The parameter values are the same as in Fig. 2.4. Here, the TEA model performs remarkably well in comparison with the OEA model, which only predicts the equilibrium concentrations. The TEA model is able to capture the system's approach to equilibrium along the length of the channel. Extraction will be analyzed in greater detail using the TEA model in Sec. 2.6.

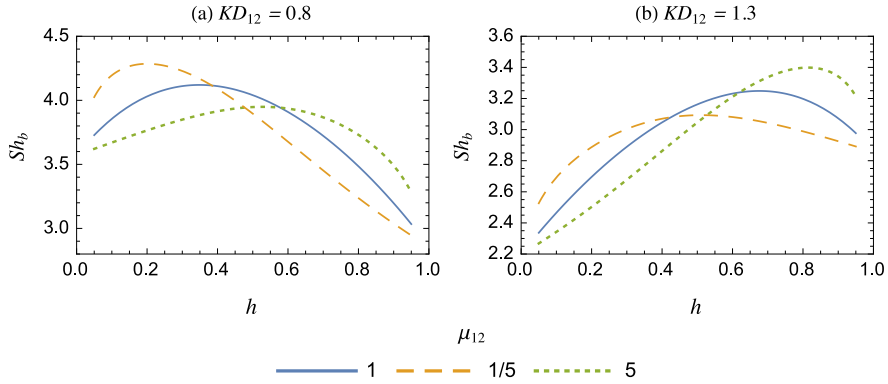

Figure 2.6: Variation of the Sherwood number (Sh_b) with the holdup (h), for different values of mu_{12} and (KD_{12}). Sh_b is a non-dimensional inter-phase mass transfer coefficient, and its variations is indicative of the influence of fluid and flow parameters on the rate of mass transfer.

2.5 Effect of holdup and fluid properties on mass transfer: Variation of the Sherwood number

An explicit low-dimensional approximation for the flux between the two fluids $J(x)$ was obtained while deriving the TEA model (cf. (2.41e)). In the absence of a reaction or when pDa is small, the flux depends primarily on the difference between the cross-section average concentrations and on the Sherwood number: $J(x) \sim Sh_b(\bar{c}_1 - K\bar{c}_2)$. The Sherwood number ($Sh_b$) depends on the holdup (h), the viscosity ratio (μ_{12}) and the product (KD_{12}) (Sh_b does not depend on K and D_{12} separately, as is clear from (2.42)). In this section, we analyze the variation of Sh_b with these parameters, to identify their effect on inter-fluid mass transfer. In particular, we wish to identify the holdup (h), which will maximize Sh_b for a specific fluid-solute combination.

Fig. 2.6 depicts the dependence of Sh_b on the holdup (h), for different values of μ_{12} and (KD_{12}). The variation is non-monotonic for the cases shown in Fig. 2.6 and Sh_b attains a maximum value at a holdup, which we call h_{max}. The value of h_{max} is affected considerably by changes in μ_{12} and (KD_{12}). Comparing the curves for different viscosity ratios, we infer that Sh_b is greater when the more viscous fluid occupies a larger portion of the channel. h_{max} is very sensitive to the value of (KD_{12}). For values not close to unity, the variation of Sh_b becomes monotonic as h_{max} shifts out of the physically relevant range (0,1). When the value of h_{max} approaches zero or one, Sh_b becomes a monotonically decreasing or increasing function of h respectively.

Contours of h_{max} are plotted in Fig. 2.7 as a function of μ_{12} and (KD_{12}). The variation of h_{max} clearly shows that Sh_b is larger when the fluid with higher viscosity, higher diffusivity and more affinity for the solute occupies a larger portion of the channel. (The fluid with a higher concentration in equilibrium relationship $c_1 = Kc_2$ is said to have

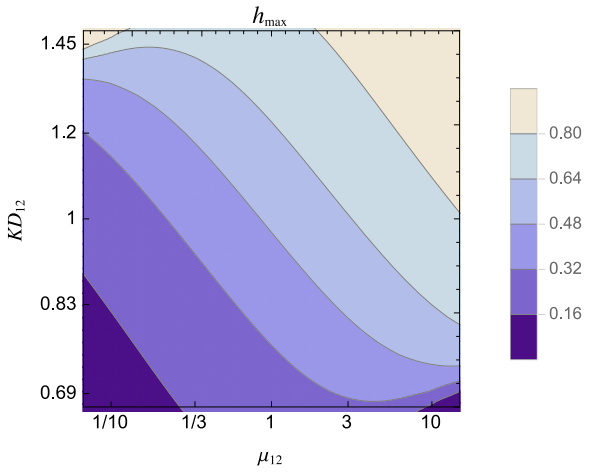

Figure 2.7: Contours of h_{max} as a function of μ_{12} and (KD_{12}). h_{max} is the value of the holdup (h) at which Sh_b attains its maximum value. When the value of h_{max} approaches zero or one, Sh_b becomes a monotonically decreasing or increasing function of h respectively.

more affinity for the solute.) For example, when $\mu_{12} > 1$ and $(KD_{12}) > 1$, we find that $h_{max} > 0.5$.

Using these results, the layered flow micro channel can be operated at a holdup that enhances the rate of mass transfer between the fluids. In some applications, it may be desirable to decrease the rate of mass transfer by increasing the net mass transfer resistance. We discuss such an application in Sec. 2.7.

2.6 Analysis of Extraction using the TEA model

In this section we shall apply the TEA model to study extraction, without a reaction. Our aim is to use the averaged model to obtain insights into the affect of parameters on the extent of extraction, determined by the equilibrium concentrations, and the rate at which the equilibrium is attained. This information will be useful for optimizing the performance of microchannel extraction systems.

The TEA model can be simplified for the case of extraction by setting $r(\bar{c}_2) = 0$ in (2.41). The simplified equations are analytically solvable. First, the algebraic equations (2.41b), (2.41d) and (2.41e) are solved to obtain the following expressions for $\bar{c}_1$ and $\bar{c}_2$, in terms of $\hat{c}_1$ and $\hat{c}_2$:

$$\bar{c}_1 = \frac{\left(D_{12}Ks_2(h) - s_1(h) - D_{12}K\hat{s}_2\right)\hat{c}_1 + \hat{s}_1 K\hat{c}_2}{\left(D_{12}Ks_2(h) - s_1(h)\right) - \left(D_{12}K\hat{s}_2 - \hat{s}_1\right)} \tag{2.43a}$$

$$\bar{c}_2 = \frac{-D_{12}\hat{s}_2\hat{c}_1 + \left(D_{12}Ks_2(h) - s_1(h) + \hat{s}_1\right)\hat{c}_2}{\left(D_{12}Ks_2(h) - s_1(h)\right) - \left(D_{12}K\hat{s}_2 - \hat{s}_1\right)} \tag{2.43b}$$

Substituting these expressions into (2.41a) and (2.41c) yields a system of two differential equations for $\hat{c}_1$ and $\hat{c}_1$, the solution to which is given below:

$$\hat{c}_1 = \frac{K}{1+h\left(K\omega-1\right)}\left[h\omega + \frac{\hat{c}_{2,in}}{\hat{c}_{1,in}}\left(1-h\right)\left(1-\exp\left(-\lambda\frac{x}{p}\right)\right) + \frac{\left(1-h\right)}{K}\exp\left(-\lambda\frac{x}{p}\right)\right] \tag{2.44a}$$

$$\hat{c}_2 = \frac{1}{1+h\left(K\omega-1\right)}\left[\left(1-\exp\left(-\lambda\frac{x}{p}\right)\right)h\omega + \frac{\hat{c}_{2,in}}{\hat{c}_{1,in}}\left\{1-h\left(1-K\omega\exp\left(-\lambda\frac{x}{p}\right)\right)\right\}\right] \tag{2.44b}$$

where

$$\lambda = \frac{1+h\left(K\omega-1\right)}{h\left(1-h\right)\left[\left(D_{12}Ks_2\left(h\right)-s_1\left(h\right)\right)-\left(D_{12}K\hat{s}_2-\hat{s}_1\right)\right]} \tag{2.44c}$$

This solution has been derived for the general case wherein both phase 1 and phase 2 may contain solute at the inlet of the channel. However, in extraction it is common to have a pure solvent entering the channel (phase 2). We assume this to be the case in the remainder of this section, and use the solution above with $\hat{c}_{2,in} = 0$.

Comparison of the analytical solution (2.44) with simulations of the PDE model are presented in Fig. 2.8, for different parameter values. The match is quite good.

The analytical solution of the TEA model enables us to efficiently analyze the system's behavior across parameter space. We focus here on the extent of extraction and the rate at which extraction progresses along the channel. The maximum extraction that is possible depends on the equilibrium concentrations in the two phases, which are attained as $\frac{x}{p} \to \infty$ or $p \to 0$. The rate at which the equilibrium is reached, as fluid flows along the channel, is determined by the decay rate $\frac{\lambda}{p}$.

To quantify the extent of extraction we use the extraction ratio (ER), defined as the ratio of the mass of solute transfered to the solvent (phase 2) to the mass that enters the channel in the carrier (phase 1). For the case of a *pure solvent*, we have $ER = \frac{(\hat{c}_2)(1-h)}{(\hat{c}_1)(h)}$. The maximum possible ER for a given system is attained at equilibrium, i.e. as $p \to 0$. Using (2.44), we obtain:

$$ER^{\text{eq}} = \lim_{p\to 0}\left(\frac{\hat{c}_2}{\hat{c}_1}\right)\frac{1-h}{h} = \frac{\omega\left(1-h\right)}{1+h\left(K\omega-1\right)} \tag{2.45}$$

Here we see that ER^{eq} depends on h, μ_{12} and K, but not on D_{12}. λ on the other hand is affected by all four parameters. We now study how the extent of extraction and the rate of approach to equilibrium changes as the holdup is varied, for different fluid properties.

Fig. 2.9 shows the variation of λ and ER^{eq} with the holdup of the carrier (h) for different fluid properties. ER^{eq} is seen to have maximum value ($ER^{\text{eq}}_{\max}$) at a particular value of the holdup ($h_{\max}$). Interestingly, even when the fluids have identical properties,

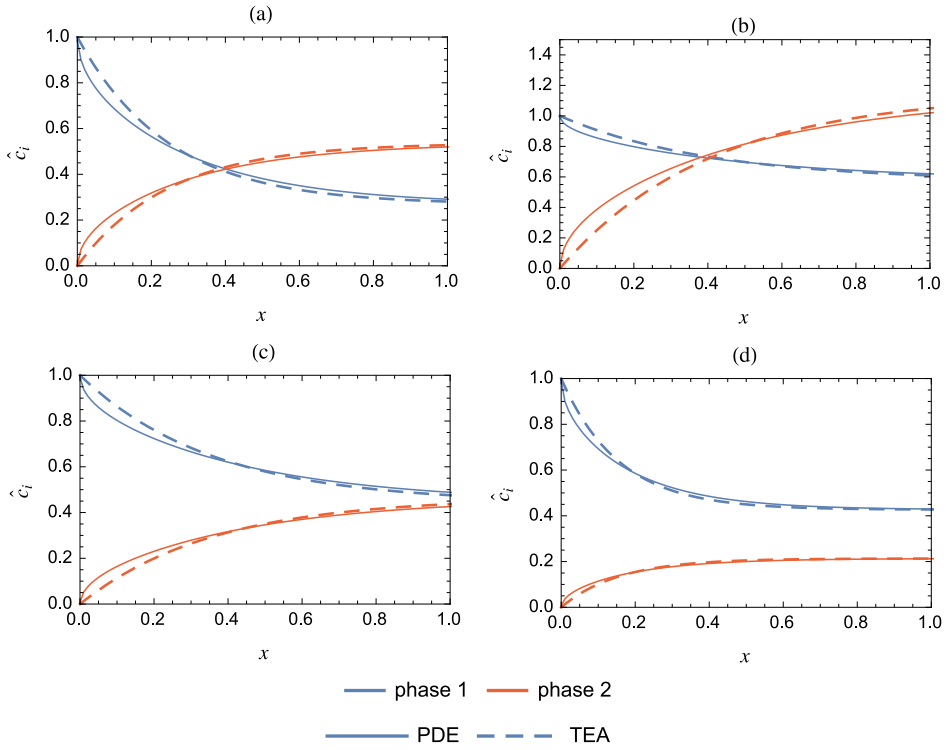

Figure 2.8: Comparison of the analytical solution of the TEA model for the case of extraction without a reaction with the full PDE model. The solvent (phase 2) enters the channel without any solute. Parameter values: (a) $D_{12} = 1/3$, $h = 0.5$, $\mu_{12} = 3$, $K = 1/2$; (b) $D_{12} = 3$, $h = 0.7$, $\mu_{12} = 3$, $K = 1/2$; (c) $D_{12} = 1.2$, $h = 0.5$, $\mu_{12} = 2$, $K = 0.95$; (d) $D_{12} = 1/3$, $h = 0.3$, $\mu_{12} = 1/3$, $K = 2$. In all cases, $p = 5$.

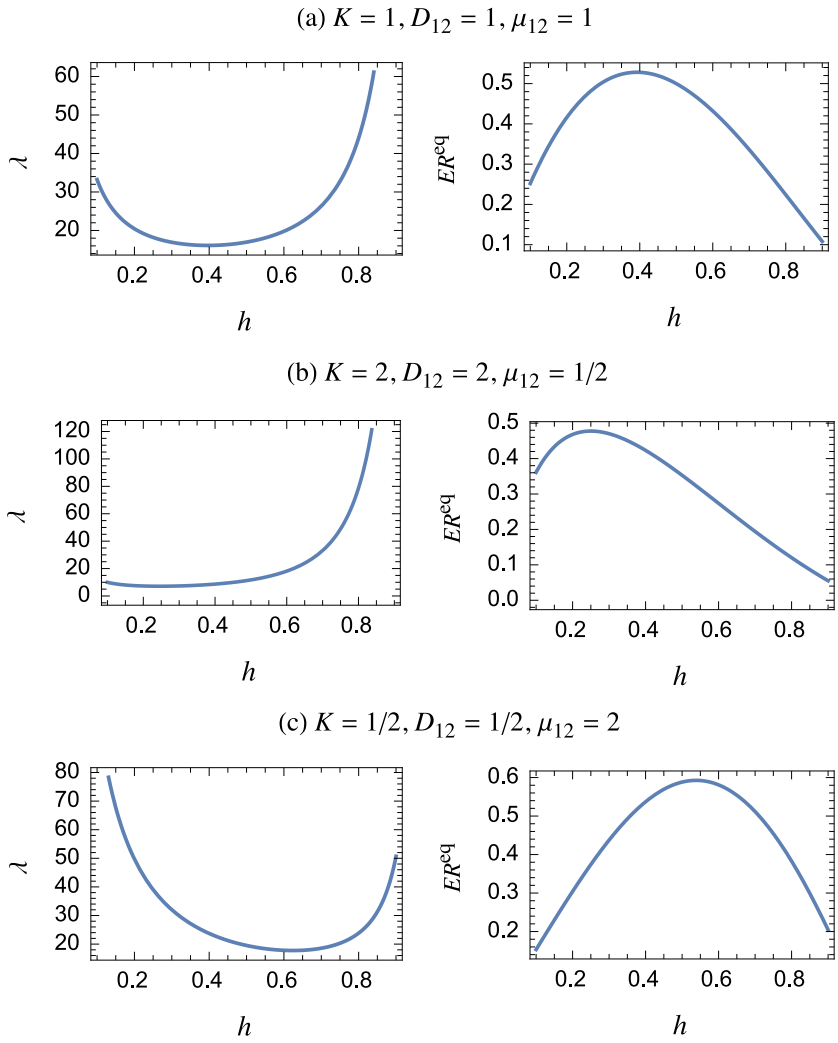

Figure 2.9: Variation of λ and ER^{eq} with the holdup of the carrier phase (h), for different fluid properties. These quantities indicate the rate at which equilibrium is attained and the extent of extraction at equilibrium respectively.

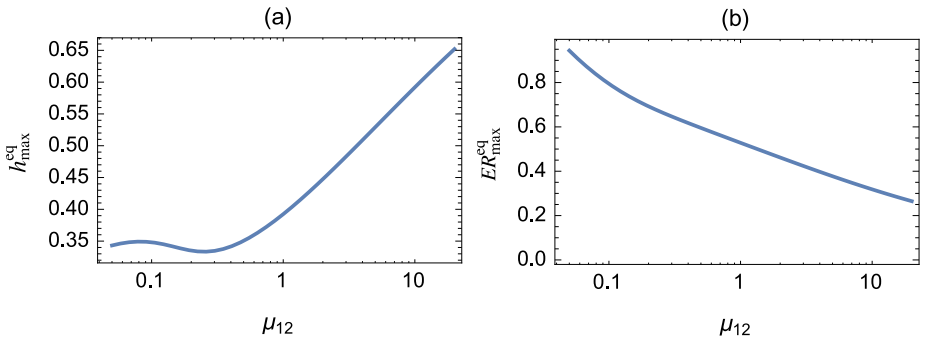

Figure 2.10: Variation of the maximum extraction attainable at equilibrium (ER^{eq}_{max}) and the corresponding value of the holdup (h^{eq}_{max}) with the viscosity ratio (μ_{12}). The distribution coefficient K is kept constant at a value of 1.

the maximum ER^{eq} does not occur at $h = 0.5$ (Fig. 2.9a). Rather, the maximum occurs at $h = 0.39$, i.e. when the carrier fluid (phase 1) has a lower holdup than the solvent (phase 2). The corresponding diffusion path length is smaller in the carrier phase. This result implies that *extraction is promoted when the solute bearing carrier phase has a slightly lower mass transfer resistance than the solvent phase.*

A striking result, observable in all cases in Fig. 2.9, is that for the holdup at which ER^{eq} peaks, λ is relatively small and ofter very near its minimum value. Thus, *there is an inherent trade-off between the extent and rate of extraction.* When the extent of extraction at equilibrium is maximized (by adjusting the holdup), then the rate at which equilibrium is attained is very slow, i.e. the channel length required for equilibrium becomes large.

To gain insight into the effects of μ_{12} and K on the extent of extraction, we compute the maximum ER^{eq} (called ER^{eq}_{max}) and the corresponding value of h (called h^{eq}_{max}) for different values of μ_{12} and K. Fig. 2.10 depicts the variation of these quantities with μ_{12}, while Fig. 2.11 shows the effect of varying K. These results indicate that t*he maximum attainable extraction is greater when the solvent is more viscous than the carrier fluid ($\mu_{12} < 1$) and when it has a greater affinity for the solute ($K < 1$).* The value of h^{eq}_{max} is seen to vary considerably with μ_{12} and K in Figs. 2.10 and 2.11. Therefore, after selecting a solvent, it is important to calculate h^{eq}_{max} and to operate at this holdup, in order to maximize the extent of extraction.

Finally, we consider the effect of the solute's diffusivities in the two fluids. The diffusivity ratio (D_{12}) does not affect the extent of extraction (ER^{eq}) but it does affect the approach to equilibrium (λ). This effect is illustrated in Fig. 2.12, which plots the variation of λ and ER^{eq} with the holdup, for two different diffusivity ratios. This figure shows that *equilibrium is attained faster when the diffusivity of the solute is greater in the solvent ($D_{12} < 1$).* However, the maximum ER^{eq} still occurs near the minimum of λ.

The results of this section provide guidance for selecting a solvent for extraction and

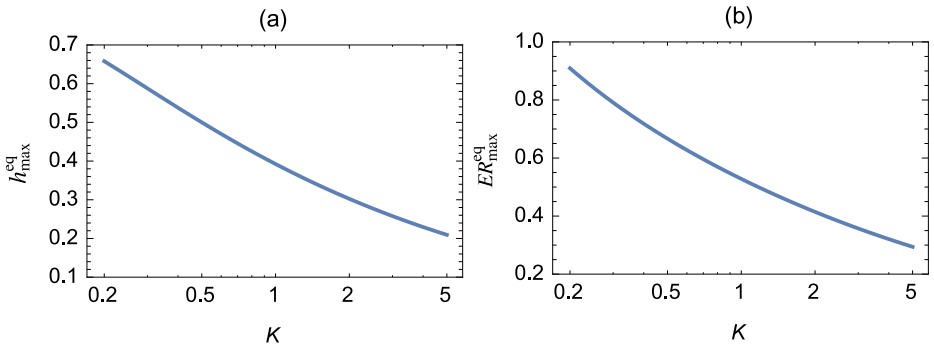

Figure 2.11: Variation of the maximum extraction attainable at equilibrium (ER^{eq}_{max}) and the corresponding value of the holdup (h^{eq}_{max}) with the distribution coefficient K. The viscosity ratio (μ_{12}) is kept constant at a value of 1.

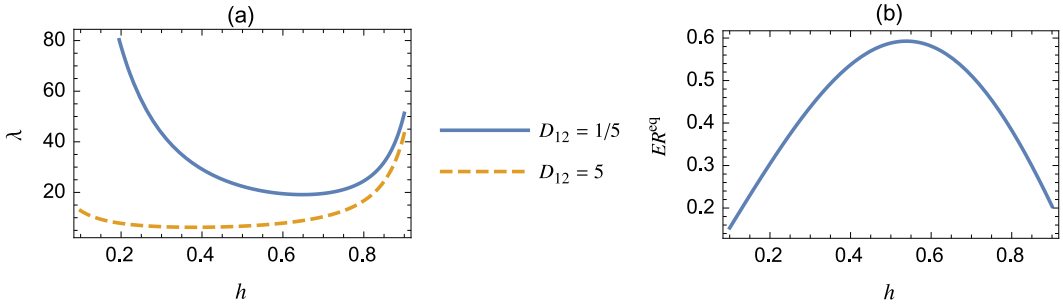

Figure 2.12: Influence of the diffusivity ratio (D_{12}) on the rate of extraction (λ) and the extent of extraction attained at equilibrium (ER^{eq}). The variation of λ and ER^{eq} with the holdup (h) is plotted for two different diffusivity ratios (D_{12}). While ER^{eq} is unaffected by changes in D_{12}, λ increases as the diffusivity of the solvent (phase 2) increases. Other parameter values: $K = 1/2$ and $\mu_{12} = 2$.

for deciding the holdup (or flow rate ratio) at which the layered-flow microchannel should be operated. Extraction will be better when the solvent has a higher solute diffusivity and higher viscosity than the carrier fluid. These requirements for a good solvent are not intuitively obvious and would have been difficult to identify without the TEA reduced order model. The third criteria, which is more intuitive, requires the solvent to have a greater affinity for the solute. Once the solvent is selected, the holdups can be chosen using plots like Fig. 2.9. The extent of extraction will be maximum if the holdup of the carrier phase is set as $h^{eq}_{\max}$.

2.7 Improving the yield of competitive consecutive reactions: insights from the TEA model

In this section, we investigate the possibility of increasing the yield of a desired product that is formed by a two step competitive-consecutive reaction system, using two-phase layered flow. The model reactions are given below:

$$\begin{aligned} A + B &\xrightarrow{k_1} C \\ C + B &\xrightarrow{k_2} D \end{aligned} \tag{2.46}$$

Here, D is the desired product. A and B are the reactants and C is an intermediate. k_1 and k_2 are the reaction rate constants of the reactions whose rates are given by $k_1 c_A c_B$ and $k_2 c_C c_B$. If the first reaction is much faster than the second ($k_1 \gg k_2$), then all the B is consumed by the first reaction and a very small amount of B is available to react with C. The outcome is a large amount of intermediate and a very small amount of the desired product, i.e. the yield of D is very low. (The yield of D is defined as ratio of the moles of D formed to the moles of B input to the reactor.) This reaction system is a model for the class of competitive-consecutive reactions, which are often encountered in industry where increasing the yield of the desired product is of prime importance.

Chakraborty and Balakotaiah (2002) have studied these reactions in a homogeneous tubular reactor using a LS reduced order model. They showed how mixing limitations in the transverse direction affects the yield in single phase flow. In this section, we consider the possibility of increasing the yield of D by using mass transfer resistance in two-phase flow to slow down the progress of the first reaction. This may be accomplished by feeding A into the reactor in phase 1 (carrier fluid) and B in phase 2 (reacting phase). To react with B, A must first diffuse into phase 2. Thus mass transfer resistance can slow down the consumption of B in the first reaction and allow more of B to react with C and form the desired product. We assume that C, B and D are all confined to phase 2 and only A can be exchanged between the two fluids.

In Sec. 2.5, we showed that the mass transfer resistance depends on the fluid properties and the holdups. Therefore, there is a possibility of further increasing the yield by appropriate selection of the carrier fluid for A and its holdup (phase 1).

We will use the TEA model to predict the system's behavior and investigate the effect of parameter variations on the yield of D. The extension of the TEA model to multiple reactions is straightforward: the steps outlined in Sec. 2.4.1 should be followed for each reactant, using appropriate reaction rate expressions. The final reduced order model is given below:

$$p\frac{d\hat{c}_A^{(1)}}{dx} = \frac{-J_A}{h} \tag{2.47a}$$

$$\hat{c}_A^{(1)} - \bar{c}_A^{(1)} = \hat{s}_1 J_A \tag{2.47b}$$

$$\frac{p}{\omega}\frac{d\hat{c}_A^{(2)}}{dx} = \frac{J_A}{(1-h)} - pDa_1\bar{c}_A^{(2)}\bar{c}_B \tag{2.47c}$$

$$\hat{c}_A^{(2)} - \bar{c}_A^{(2)} = D_{12,A}\hat{s}_2 J_A - pDa_1 D_{12,A}\hat{q}_2\bar{c}_A^{(2)}\bar{c}_B \tag{2.47d}$$

$$J_A = \frac{\left(\bar{c}_A^{(1)} - K_A\bar{c}_A^{(2)}\right)}{D_{12,A}K_A s_2(h) - s_1(h)} + pDa_1\bar{c}_A^{(2)}\bar{c}_B\frac{D_{12,A}K_A q_2(h)}{D_{12,A}K_A s_2(h) - s_1(h)} \tag{2.47e}$$

$$\frac{1}{\omega}\frac{d\hat{c}_B}{dx} = -Da_1\left(\frac{\hat{c}_{A,in}^{(1)}}{\hat{c}_{B,in}}\right)\bar{c}_A^{(2)}\bar{c}_B - Da_2\bar{c}_C\bar{c}_B \tag{2.47f}$$

$$\hat{c}_B - \bar{c}_B = -pD_{AB}\hat{q}_2\left(Da_1\left(\frac{\hat{c}_{A,in}^{(1)}}{\hat{c}_{B,in}}\right)\bar{c}_A^{(2)}\bar{c}_B + Da_2\bar{c}_C\bar{c}_B\right) \tag{2.47g}$$

$$\frac{1}{\omega}\frac{d\hat{c}_C}{dx} = +Da_1\left(\frac{\hat{c}_{A,in}^{(1)}}{\hat{c}_{B,in}}\right)\bar{c}_A^{(2)}\bar{c}_B - Da_2\bar{c}_C\bar{c}_B \tag{2.47h}$$

$$\hat{c}_C - \bar{c}_C = pD_{AC}\hat{q}_2\left(Da_1\left(\frac{\hat{c}_{A,in}^{(1)}}{\hat{c}_{B,in}}\right)\bar{c}_A^{(2)}\bar{c}_B - Da_2\bar{c}_C\bar{c}_B\right) \tag{2.47i}$$

$$\frac{1}{\omega}\frac{d\hat{c}_D}{dx} = Da_2\bar{c}_C\bar{c}_B \tag{2.47j}$$

$$\hat{c}_D - \bar{c}_D = pD_{AD}\hat{q}_2 Da_2\bar{c}_C\bar{c}_B \tag{2.47k}$$

The inlet conditions at $x = 0$ are :

$$\hat{c}_A^{(1)} = 1, \;\; \hat{c}_A^{(2)} = 0, \;\; \hat{c}_B = 1, \;\; \hat{c}_C = 0, \;\; \hat{c}_D = 0 \tag{2.47l}$$

Here, $c_A^{(1)}$ and $c_A^{(2)}$ denotes the concentration of A in phase 1 and phase 2 respectively. $\hat{c}_B$, $\hat{c}_C$ and $\hat{c}_D$ denote the concentrations of B, C, and D in phase 2 respectively. The concentrations of A in both phases have been scaled with the mixing-cup average of the

concentration of A that enters the channel in phase 1 ($\hat{c}^{(1)}_{A,in}$). The concentrations of B, C and D in phase 2 have been scaled with the mixing-cup average concentration of B, entering the channel in phase 2 ($\hat{c}_{B,in}$). $D_{12,A}$ is the ratio of the diffusivity of A in phase 1 to that in phase 2. D_{AB}, D_{AC}, D_{AD} are the ratios of the diffusivity of A in phase 1 to the diffusivity of B, C and D in phase 2 respectively. Da_1 and Da_2 are Damkohler numbers given by $k_i \hat{c}_{B,in}(L/\bar{v}_1)$ $(i = 1, 2)$. The expressions for s_1, s_2 and q_2 are the same as those used in Sec. 2.4 and are given in Appendix E.1.

Results of simulations of this averaged model (cf. (2.47)) are presented in Fig. 2.13 for the case of $Da_1 = 50, Da_2 = 5$. Two different cases are considered with different fluid properties and holdup. In both cases, $p = 0.5$ and all the diffusivities are taken to be equal for simplicity. Equal number of moles of A and B are fed into the reactor. This figure also shows the predictions obtained by solving the governing PDEs. The TEA model matches well with the full PDE model and is clearly able to predict the system's behavior.

The amount of D formed is very different for the two cases presented in Fig. 2.13. This shows that the yield of D is very sensitive to the fluid properties and holdup of phase 1. Varying these parameters affects the mass transfer resistance and thereby modifies the net rate of progress of the first reaction. The parameter values that lead to higher mass transfer resistance will result in a higher yield of D.

The yield of D (Y_D) is plotted as a function of the holdup (h) of phase 1 in Fig. 2.14, considering different fluid properties. The other parameters are the same as in Fig. 2.13. The yield for the case of single phase flow is also indicated in this figure. The results clearly show that increasing the holdup of the carrier phase (phase 1) increases the yield of D (except when h nears unity). This is because the path length for diffusion from the carrier phase (phase 1) to the reacting phase (phase 2) increases as h increases. Consequently, the rate of transport of A into the reacting phase decreases. Another reason for the increase in the yield of D with h (phase 2) is that the flow rate of the carrier phase increases as its holdup (h) is increased. Since the input number of moles of A is fixed, the concentration of A in the entering carrier phase will be lower. This results in a smaller driving force for mass transfer of A to the reacting phase.

Comparing the three curves in Fig 2.14, we find that the yield of D is higher when the carrier (phase 1) has a greater affinity for A ($K > 1$) than the reacting phase. In this case, more A is retained in the carrier phase than the reacting phase, which allows B to react with C to form more D. Fig. 2.14 also shows that a less viscous carrier fluid promotes the yield of D. When the viscosity of the carrier fluid is lower, its flow rate will be higher, which as explained above results in a smaller driving force for mass transfer.

These results show that the yield of the desired product can be significantly increased when A is supplied through a second carrier fluid, instead of supplying it along with

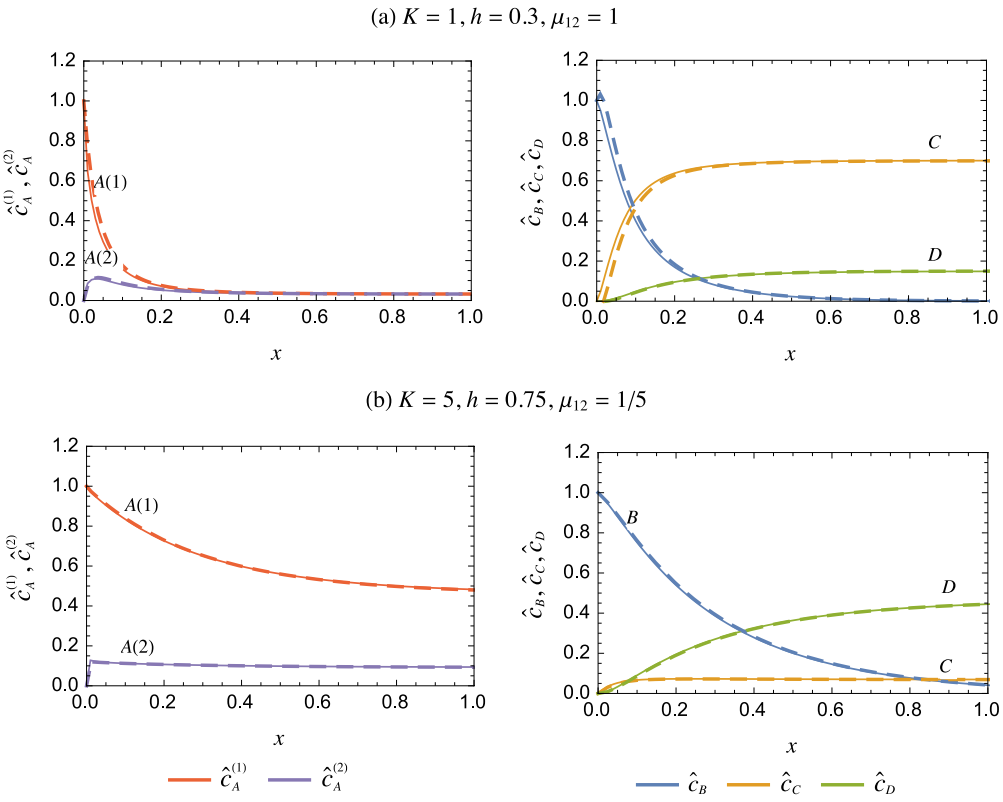

Figure 2.13: Comparison of the TEA model (2.47) for the competitive-consecutive reaction system (2.46) with simulations of the corresponding PDEs. The cup-mixing average concentration profiles of various species are plotted along the reactor length. Solid lines are simulations of the governing PDEs while dashed lines are the simulations of the TEA reduced order model. Parameter values: $Da_1 = 50, Da_2 = 5, p = 0.5, D_{12,A} = D_{AB} = D_{AC} = D_{AD} = 1$. Equal number of moles of A and B are fed into the reactor.

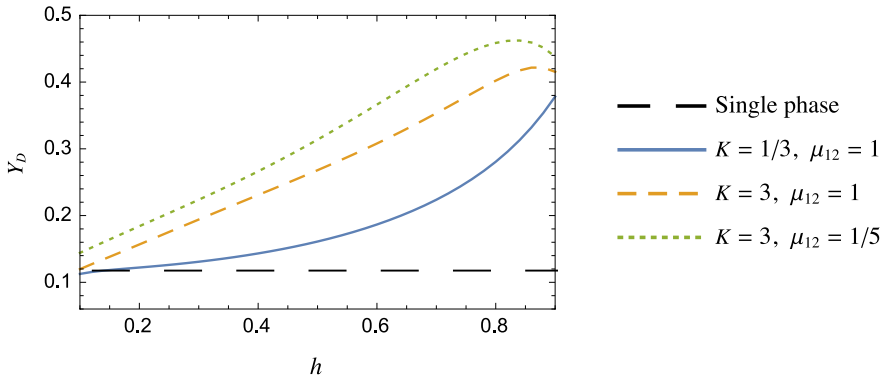

Figure 2.14: Yield of D as a function of the holdup (h) for different fluid properties. The yield in the case of single phase flow is indicated by the horizontal dashed line for the sake of comparison. Common parameter values: $Da_1 = 50, Da_2 = 5, p = 0.5, D_{12,A} = D_{AB} = D_{AC} = D_{AD} = 1$. Equal number of moles of A and B are fed into the reactor.

B in the same fluid. This layered flow system ensures a controlled slow input of A into the reacting phase, which allows enough time for B to react with C and form the desired product D. This basic concept can be applied to other problems, such as runaway reactions. In this case, restricting the availability of one of the reactants by supplying it in a second fluid will reduce the rate of heat generation in a manner similar to a semi-batch reactor.

2.8 Concluding Remarks

In this chapter, two reduced order models were derived to describe mass transfer and reactions in two-phase layered flows. These models were derived assuming transverse diffusion to be fast compared to convection, i.e. for small Peclet number (p). Yet, they remain quantitatively accurate for p upto unity and capture the qualitative behavior of the system for p moderately greater than unity. These models will reduce computation time and aid in optimization, parameter identification, model based control and analysis of the system across the multidimensional parameter space.

The OEA model consists of a single ordinary differential equation (ODE) that describes the evolution of the average concentrations of both fluids along the channel. The model includes three algebraic equations that account for the difference between the cup-mixing average and the cross-section average concentration in each fluid and the concentration difference between the fluids. This model cannot predict mass transfer in the absence of a reaction – it only predicts the final equilibrium concentrations. The model can only capture the deviation from equilibrium brought about by a reaction. Even in these cases, the model cannot predict the concentration near the inlet of the reactor, where the phases first come into contact. On the positive side, the concentration at the outlet of the reactor is predicted accurately over a large range of Da, if p is small ($p \leq 1$).

The TEA model is a major improvement over the OEA model. It consists of two ordinary differential equations for the evolution of the cup-mixing average concentration – one for each fluid. These ODEs are accompanied by algebraic equations that relate the cup-mixing averages, the cross-section averages and the flux between the fluids. This model captures the mass transfer between the phases in the absence of reactions, right from the inlet of the channel. Thus, it gives very good predictions for extraction. It also works well when a reaction is present, unless the reaction is very fast and Da is large.

The TEA model provides closed form expressions for the Sherwood number (based on an overall mass transfer coefficient). Studying its dependence on system parameters revealed that *inter-fluid flux is promoted when the fluid with higher holdup (volume fraction) has a higher viscosity, a higher solute diffusivity and more affinity for the solute*.

The TEA model was solved analytically for the case of extraction without a reaction. Analysis of the solution showed that the extent of extraction is higher when the solvent phase has a higher viscosity, a higher solute diffusivity and more affinity for the solute than the carrier phase. *The holdup of the carrier phase that maximizes the extent of extraction at equilibrium was shown to correspond to a very slow approach to equilibrium.* Thus a trade-off between these two factors must be made when deciding the holdup.

Finally, the TEA model was used to study consecutive-competitive reactions in layered flow. We found that the yield of the desired product can be significantly increased by using inter-phase mass transfer resistance to slow down the formation of the intermediate species. This results in increased formation of the desired product.

The example of competitive-consecutive reactions demonstrates that the TEA averaged model may be easily extended to systems with multiple species, involving interfacial transport and multiple reactions. An important avenue for future work is the development of averaged models for practically important layered flow microsystems, involving surface and bulk reactions. An example of such a system is phase transfer catalysis in microchannels (Aljbour *et al.*, 2010; Šinkovec *et al.*, 2013).

Using the TEA model, one can identify the system parameters (flow rates and solvents) that maximize extraction performance in *co-current* layered flows. However, even better performance may be obtained by operating in a counter-current flow instead of a co-current flow. The reason this is not common practice is that obtaining counter-current flow in microchannels is difficult, requiring fluid specific channel modifications. In Chapter 3, we compare the performance of both systems across parameter space, to determine whether the gain in performance is sufficient to justify this extra investment.

CHAPTER 3

Selecting between Co-Current and Counter-Current Flow

A double minded man (is) unstable in all his ways

– James 1:8, KJV

3.1 Introduction

In separation operations, like solvent extraction, the driving force for interphase mass transfer is given by the difference of the solute concentrations in each phase from the values at thermodynamic equilibrium. In this context the configuration of the flow, whether co-current or counter-current, assumes significance. In the co-current mode, the two liquid phases flow in the same direction and the concentration in each phase monotonically approaches the equilibrium value. Therefore the driving force decreases along the length of the channel. On the other hand, in the counter-current mode, the two phases flow in opposite directions. At the solvent inlet, pure solvent is brought into contact with the exiting depleted carrier stream. At the opposite end, the entering concentrated carrier phase meets with the exiting enriched solvent. In this counter-current flow configuration, the two streams are always away from equilibrium throughout the channel. The overall driving force for mass transfer is consequently greater in counter-current flow. Hence, with all other system properties being the same, a counter-current extraction process always outperforms a co-current process (Treybal, 1980). However, this performance improvement can be significant or marginal depending on the parameters of the system, such as the relative affinity of the solute for the solvent phase, fluid flow rates and channel size.

In microchannels, the higher efficiency of counter-current flow is offset by the difficulty of establishing such a flow regime. Gravity and inertia cannot be exploited to establish counter-current flow, as is done in macro systems. At the micro scale, interfacial and viscous forces play a dominant role. These forces ensure stable layered flow over a wide range of operating conditions. Co-current layered flow arises naturally in pressure driven flow through a microchannel with a Y-junction inlet. This flow system

has been investigated extensively (Hotokezaka *et al.*, 2005; Fries *et al.*, 2008; Znidarsic-Plazl and Plazl, 2007; Okubo *et al.*, 2008). On the other hand, layered counter-current flow requires the hydrodynamic driving force to act in opposite directions in each phase. Aota *et al.* (2007) have achieved counter-current flow for an aqueous-organic fluid pair by making one wall hydrophobic and the other hydrophilic.

Due to the relative difficulty in implementing counter-current flow in microchannels, the choice between the two flow configurations in a non-obvious one. The extraction performance gain must be significant to justify the selection of counter-current flow over co-current. The relative extraction performance will vary with the equilibrium and transport properties of the fluids, their relative flow rates and the geometric features of the microchannel. Investigating these extraction systems experimentally over a wide range of parameters is challenging, especially for the counter-current system. Therefore, it is important to identify the regions of the parameter space that correspond to a significant performance gain. Experiments and detailed calculations can then be made within this restricted subset of parameter values. This information can be obtained with the help of simplified mathematical models.

In Ch. 2, we used an averaging strategy to reduce computation costs while retaining the ability to describe intricate physical effects, such as the influence of the velocity profile on mass transfer. In this section, we are primarily concerned with the influence of the relative flow direction of the two phases, on extraction performance. Therefore, we significantly simplify the PDE model used in Sec. 2.2, by assuming a plug flow velocity profile within each fluid. This enables us to obtain analytical and semi-analytical solutions, which greatly aid in carrying out a thorough comparison of the two systems across the high dimensional parameter space.

The organization of this chapter is as follows. The mathematical models used in this work are presented in Sec. 3.2. These partial differential equations have been recently analyzed in the context of extraction by Malengier *et al.* (2012). In Sec. 3.3, we present an analytical solution for the co-current equations based on the theory of Sturm-Liouville linear operators. The counter-current model belongs to the class of two way diffusion equations and is mathematically more challenging. Such equations arise in various fields of study and an analytical solution is available (Fisch and Kruskal, 1980; Beals, 1981). However, in this chapter, a novel semi-analytical solution strategy is adopted, which is closely related to the physics of the mass transfer process. This is presented in Sec. 3.4.

In Sec. 3.5, we define metrics to quantify the mass transfer performance of both systems. The ability of the simple model to describe the essential behavior of extraction systems is confirmed in Sec. 3.6, by a comparison with detailed simulations and experimental results from the literature. In Sec. 3.7, we demonstrate that, while the model contains 5 parameters, the relative extraction performance depends on only 4 of these.

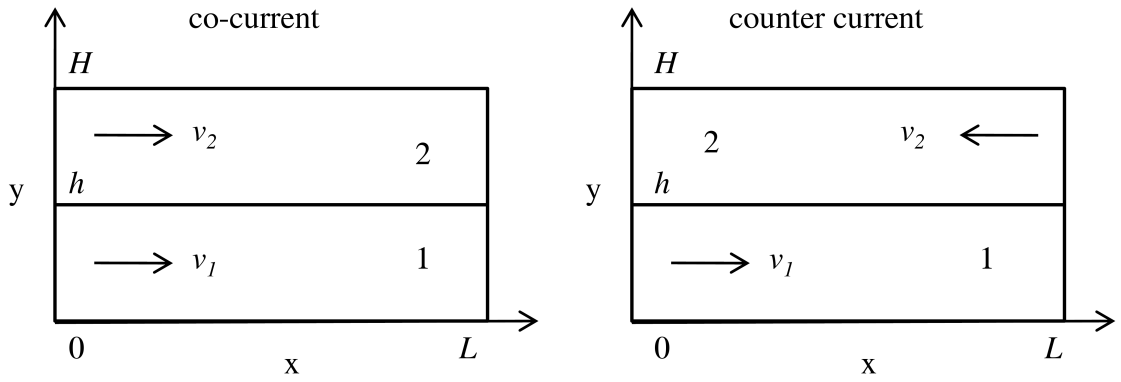

Figure 3.1: Schematic of simplified co-current and counter-current flow systems. The interface is located at a position h within the channel of width H and length L. Phases 1 and 2 correspond to the carrier and solvent phases respectively, which flow with constant velocities v_1 and v_2.

This reduction in the number of independent parameters is extremely helpful in the subsequent investigation of the influence of parameters on relative extraction performance. This is done in terms of a relative extraction ratio in Sec. 3.8. A general principle is identified, namely “maximum gain at mediocre performance", which can aid the engineer/experimentalist in selecting between co-current and counter-current configurations. The results are summarized and discussed in Sec. 3.9.

3.2 Simple model for extraction in microchannels

Consider layered flow of the carrier and solvent phases in a microchannel with a uniformly flat interface of contact. For the sake of simplicity, we consider only plug flow velocity profiles. The model is restricted to two spatial dimensions by neglecting any variations in the direction perpendicular to the flow and parallel to the interface/walls. Further, diffusion in the direction of the flow is neglected in comparison with convection. A schematic of this system for co-current and counter-current flow is depicted in Fig. 3.1.

A differential mass balance of the solute species in each phase yields the following partial differential equations.

$$v_1 \frac{\partial c_1}{\partial x} = D_1 \frac{\partial^2 c_1}{\partial y^2} \qquad 0 \leq y \leq h \tag{3.1a}$$

$$v_2 \frac{\partial c_2}{\partial x} = D_2 \frac{\partial^2 c_2}{\partial y^2} \qquad h < y \leq H \tag{3.1b}$$

Here c_i denotes the concentration of the solute in each phase and D_i is the diffusivity of the solute in each phase. v_i are the constant phase velocities. h represents the location of the interface and H is the channel width. i = 1 denotes the carrier phase while i = 2 denotes the solvent phase.

These equations are subject to four boundary conditions and two initial conditions. At the walls we have the no-flux conditions:

$$\left.\frac{\partial c_1}{\partial y}\right|_{y=0} = 0, \qquad \left.\frac{\partial c_2}{\partial y}\right|_{y=H} = 0 \tag{3.2}$$

A balance of material flux across the interface yields the following condition at $y = h$:

$$D_1 \frac{\partial c_1}{\partial y} = D_2 \frac{\partial c_2}{\partial y} \tag{3.3}$$

At the interface the two phases are assumed to be in local thermodynamic equilibrium. This yields (at $y = h$):

$$c_1 = K c_2 \tag{3.4}$$

where K is a constant equilibrium coefficient.

For co-current flow, the initial concentration of the solute in both phases is specified at $x = 0$. For counter-current flow, the initial concentration of the carrier phase (C_{in}) is specified at $x = 0$ and that of the solvent phase at $x = L$. The inlet solvent stream is assumed to be pure, without any solute. This yields for co-current flow:

$$c_1(0, y) = C_{in} \qquad 0 \leq y \leq h \tag{3.5a}$$

$$c_2(0, y) = 0 \qquad h < y \leq H \tag{3.5b}$$

and for counter-current flow:

$$c_1(0, y) = C_{in} \qquad 0 \leq y \leq h \tag{3.6a}$$

$$c_2(L, y) = 0 \qquad h < y \leq H \tag{3.6b}$$

Equations (3.1) to (3.4) along with (3.5) or (3.6) constitute the simplified mathematical model for the co-current or counter-current extraction system respectively. The co-current problem is a purely initial value problem in the x coordinate. A solution for a large channel length can be used to determine the performance for all intermediate channel lengths as well. On the other hand, the split initial conditions of the counter-current problem require it to be solved separately for each value of the channel length; it is a boundary value problem in both the x and y coordinates. The solution methodologies for the two problems, described in sections 3.3 and 3.4, are therefore quite different.

3.3 Analytical solution of the co-current model

The model equations for co-current flow ((3.1) to (3.4) and (3.5)) are non-dimensionalized with the characteristic scales of the channel length (L) and width (H) and the initial concentration of the carrier phase (C_{in}).

$$x^* = \frac{x}{L}, \quad y^* = \frac{y}{H}, \quad {h_r}^* = \frac{h}{H}, \quad {c_i}^* = \frac{c_i}{C_{in}} \tag{3.7}$$

The asterisk indicates dimensionless variables. The dimensionless Peclet numbers and the diffusivity ratio (β) are defined as

$$Pe_1 = \frac{v_1 H^2}{D_1 L}, \quad Pe_2 = \frac{v_2 H^2}{D_2 L}, \quad \beta = \frac{D_1}{D_2} \tag{3.8}$$

From this point forward we work only in dimensionless variables and drop the asterisk for convenience. The co-current model equations in dimensionless form are given below.

$$\frac{\partial c_1}{\partial x} = \frac{1}{Pe_1}\frac{\partial^2 c_1}{\partial y^2} \qquad 0 \le y \le h_r \tag{3.9a}$$

$$\frac{\partial c_2}{\partial x} = \frac{1}{Pe_2}\frac{\partial^2 c_2}{\partial y^2} \qquad h_r < y \le 1 \tag{3.9b}$$

$$\left.\frac{\partial c_1}{\partial y}\right|_{y=0} = 0, \qquad \left.\frac{\partial c_2}{\partial y}\right|_{y=1} = 0 \tag{3.10a}$$

$$\beta\frac{\partial c_1}{\partial y} = \frac{\partial c_2}{\partial y} \qquad \text{at} \quad y = h_r \tag{3.10b}$$

$$c_1 = K c_2 \qquad \text{at} \quad y = h_r \tag{3.10c}$$

$$c_1(0, y) = 1 \qquad 0 \le y \le h_r \tag{3.10d}$$

$$c_2(0, y) = 0 \qquad h_r < y \le 1 \tag{3.10e}$$

Based on the theory of Sturm-Liouville operators (Ramkrishna and Amundson, 1974, 1985) an analytical solution in the form of a series of orthonormal eigen functions is obtained. Malengier *et al.* (2012) present a solution for the special case of equal liquid velocities. Here we extend this solution to the general case of unequal velocities by suitably redefining the inner product. The details are given in Appendix A. The final

solution of the co-current concentration field follows:

$$
\begin{aligned}
c\left(x,y\right) &= \left\{ \begin{array}{ll} c_1\left(x,y\right) & 0 \leq y \leq h_r \\ c_2\left(x,y\right) & h_r < y \leq 1 \end{array} \right\} \\
&= \left\{ \begin{array}{c} 1 \\ 1/K \end{array} \right\} \frac{h_r}{h_r + \left(Pe_2/Pe_1\right)\frac{\left(1-h_r\right)}{\beta K}} \\
&+ \sum_{n=1}^{\infty} \left[b_n \frac{\sin\left(\lambda_n \sqrt{Pe_1} h_r\right)}{\lambda_n \sqrt{Pe_1}} e^{-\lambda_n^2 x} \left\{ \begin{array}{c} b_n \cos\left(\lambda_n \sqrt{Pe_1} y\right) \\ d_n \cos\left(\lambda_n \sqrt{Pe_2}\left(1-y\right)\right) \end{array} \right\} \right]
\end{aligned}
\tag{3.11}
$$

Here, λ_n are eigenvalues, which are roots of the characteristic equation (A.7). b_n and d_n are parameter dependent constants, given by (A.9) (cf. Appendix A).

3.4 Semi-analytical solution of the counter-current model

The counter-current model is given by equations (3.1) to (3.4) and (3.6). This model has been studied previously in various asymptotic regimes (Fitt *et al.*, 1985; Hagan and Ockendon, 1991). These equations belong to the category of 'two-way diffusion equations'. Since the flow is in opposite directions in each phase, the equations cannot be cast into the standard Sturm-Liouville form. Nevertheless a series solution has been obtained in terms of two sets of eigenfunctions corresponding to the two fluid sub-domains (Fisch and Kruskal, 1980). The eigenfunctions in the carrier phase decay along the channel length while eigenfunctions in the solvent phase grow in magnitude. These eigenfunctions have been shown to be complete in their respective fluid sub-domains (Beals, 1981). Unfortunately the eigenfunctions are not orthogonal. Therefore the coefficients of the eigenfunctions in the series solution must be computed numerically by a least squares procedure for a given initial condition (Fisch and Kruskal, 1980). Further the calculation of the eigenfunctions is complicated by the degeneracy of the zero eigenvalue. These difficulties motivate us to develop a new strategy for the solution of two-way diffusion equations, which is based on a simpler mathematical formalism. An additional advantage of this method lies in the close relationship between the calculation procedure and the physics of the extraction problem. An overview of the method follows after which the procedure is described in detail.

The two coupled partial differential equations (3.1) are decomposed into two separate equations by introducing an auxiliary function $f(x)$, which describes the concentration at the interface. Both of these equations are standard non-homogeneous Sturm-Liouville equations and are easily solved in their respective domains. To complete the solution, the interface concentration $f(x)$ must be determined. This is done by enforcing the equal

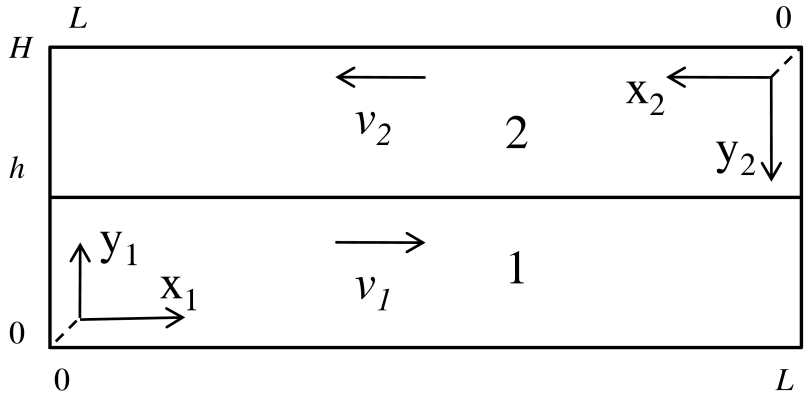

Figure 3.2: Schematic of the coordinate systems defined for each phase separately. The sub-domains 1 and 2 correspond to the carrier and solvent phases respectively, which flow in a counter-current manner. The axes are displaced for visual clarity. The true origin locations are at the domain vertices and are indicated by dashed lines.

flux condition (3.3) at the interface. This last step is carried out numerically, resulting in a semi-analytical solution of the counter-current extraction problem. This solution procedure is described below in detail.

First, two new Cartesian coordinate axes are introduced for each fluid sub-domain. Each pair of axes has the horizontal axis oriented along the respective flow direction and the vertical axis points towards the center of the channel. A schematic of the co-ordinate system is presented in Fig. 3.2. The dimensionless variables used in this section are different from those used in the co-current case (Sec. 3.3). These are defined below with an asterisk, which is later dropped for convenience.

$$y_1^* = \frac{y_1}{H}, \quad y_2^* = \frac{y_2}{(H-h)}, \quad x_i^* = \frac{x_i}{L}, \quad {c_i}^* = \frac{c_i}{C_{in}} \tag{3.12}$$

$$Pe_1 = \frac{v_1 h^2}{D_1 L}, \quad Pe_2 = \frac{v_2 (H-h)^2}{D_2 L}, \quad \beta = \frac{D_1}{D_2} \tag{3.13}$$

Equations (3.1)-(3.4) and (3.6) are presented below in terms of the new co-ordinate systems (x_1, y_1) and (x_2, y_2). Here, $i = 1$ corresponds to the carrier phase and $i = 2$ corresponds to the solvent phase.

$$\frac{\partial c_i}{\partial x_i} = \frac{1}{Pe_i} \frac{\partial^2 c_i}{\partial y_i^2} \qquad \begin{matrix} 0 < y_i < 1 \\ 0 < x_i < 1 \end{matrix} \tag{3.14a}$$

$$\left. \frac{\partial c_i}{\partial y_i} \right|_{y_i = 0} = 0 \tag{3.14b}$$

$$c_1 \left(x_1 = 0, y_1 \right) = 1 \tag{3.14c}$$

$$c_2 \left(x_2 = 0, y_2 \right) = 0 \tag{3.14d}$$

Instead of applying the boundary conditions in (3.3) and (3.4), which couple the equations for the carrier and solvent phases, the concentration at the interface in each domain is described in terms of an auxiliary function $f(x_1)$. Thus the equations for $i = 1, 2$ are decoupled and two independent equations with non-homogeneous Dirichlet boundary conditions at the interface $(y_i = 1)$ are obtained:

$$c_1\left(x_1, y_1 = 1\right) = f_1(x_1) = Kf(x_1) \tag{3.15a}$$

$$c_2\left(x_2, y_2 = 1\right) = f_2(x_2) = f(1 - x_2) \tag{3.15b}$$

Here $x_1 = 1 - x_2$. These new interface conditions, in terms of $f(x_1)$, inherently satisfy the thermodynamic equilibrium condition (3.4). Thus, only the equal flux condition (3.3) is left to be satisfied. This condition will be used to determine the auxiliary function $f(x_1)$ after the decoupled equations in (3.14)-(3.15) are solved.

Both the equations in (3.14a) are instances of the following general non-homogeneous partial differential equation.

$$\frac{\partial u}{\partial x} = \frac{1}{P}\frac{\partial^2 u}{\partial y^2} \tag{3.16a}$$

$$\left.\frac{\partial u}{\partial y}\right|_{y=0} = 0 \tag{3.16b}$$

$$u\left(x, 1\right) = p\left(x\right) \tag{3.16c}$$

$$u\left(0, y\right) = u_0 \tag{3.16d}$$

here x and y are general independent variables and not the co-ordinates in Fig. 3.1.

We now construct a solution to this general equation, which may then be applied to obtain solutions for (3.14) - (3.15). The solution $u(x, y)$ is constructed as a superposition of two functions $u_a(x, y)$ and $u_b(y)$. We require $u_a(x, y)$ to satisfy (3.16) but with homogeneous boundary conditions. $u_b(y)$ is a linear function that is superposed to account for the forcing from the non-homogeneous boundary conditions. Thus, $u_b(y)$ is required to satisfy the following:

$$\frac{\partial^2 u_b}{\partial y^2} = 0, \quad \left.\frac{\partial u_b}{\partial y}\right|_{y=0} = 0, \quad u_b\left(x, 1\right) = p\left(x\right) \tag{3.17}$$

Solving (3.17) yields $u_b = p(x)$. Substituting $u = u_a + u_b = u_a + p(x)$ in (3.16), we obtain

$$\frac{\partial u_a}{\partial x} = \frac{1}{P}\frac{\partial^2 u_a}{\partial y^2} - \frac{dp}{dx} \tag{3.18a}$$

$$\left.\frac{\partial u_a}{\partial y}\right|_{y=0} = 0 \tag{3.18b}$$

$$u_a\left(x, 1\right) = 0 \tag{3.18c}$$

$$u_a\left(0, y_1\right) = u_0 - p(0) \tag{3.18d}$$

A solution can be obtained as a convergent infinite series in a manner similar to the solution of the co-current problem detailed in Appendix A. The major difference lies in the non-homogenous term, which however does not present any difficulty to the eigen-function expansion method (Ramkrishna and Amundson 1985). The final solution for u obtained after combining u_a and u_b is

$$u = p\left(x\right) + \sum_{n=0}^{\infty} \left[\frac{4(-1)^n}{\pi\left(2n+1\right)} \cos\left(\left(2n+1\right)\frac{\pi}{2} y\right) \times \left\{ \left(1 - p\left(0\right)\right) \exp\left(-\lambda_n^2 x\right) - \int_0^x \frac{dp\left(m\right)}{dm} \exp\left(-\lambda_n^2\left(x - m\right)\right) dm \right\} \right] \tag{3.19}$$

where $\lambda_n = \left(2n+1\right)\pi \Big/ \left(2\sqrt{P}\right)$.

From (3.19), the solutions for c_1 and c_2 in (3.14) can be directly obtained as

$$c_1\left(x_1, y_1\right) = Kf\left(x_1\right) + \sum_{n=0}^{\infty} \left[\frac{4(-1)^n}{\pi\left(2n+1\right)} \cos\left(\left(2n+1\right)\frac{\pi}{2} y_1\right) \times \left\{ \left(1 - Kf\left(0\right)\right) \exp\left(-\lambda_{1,n}^2 x_1\right) - K \int_0^{x_1} \frac{df\left(m\right)}{dm} \exp\left(-\lambda_{1,n}^2\left(x_1 - m\right)\right) dm \right\} \right] \tag{3.20a}$$

$$c_2\left(x_2, y_2\right) = f\left(1 - x_2\right) + \sum_{n=0}^{\infty} \left[\frac{4(-1)^n}{\pi\left(2n+1\right)} \cos\left(\left(2n+1\right)\frac{\pi}{2} y_2\right) \times \left\{ -f\left(1\right) \exp\left(-\lambda_{2,n}^2 x_2\right) - \int_0^{x_2} \frac{df\left(1-m\right)}{dm} \exp\left(-\lambda_{2,n}^2\left(x_2 - m\right)\right) dm \right\} \right] \tag{3.20b}$$

where $\lambda_{1,n} = \left(2n+1\right)\pi \Big/ \left(2\sqrt{Pe_1}\right)$, $\lambda_{2,n} = \left(2n+1\right)\pi \Big/ \left(2\sqrt{Pe_2}\right)$

Equation (3.20) will be the solution of the concentration field provided $f(x_1)$ satisfies the equal flux condition at the interface (3.3). This condition in terms of the new co-ordinate systems (Fig. 3.2) is

$$\beta \frac{\partial c_1\left(x_1, y_1\right)}{\partial y_1}\bigg|_{y_1=1} + \left(\frac{h}{H-h}\right) \frac{\partial c_2\left(x_2, y_2\right)}{\partial y_2}\bigg|_{y_2=1} = 0 \quad \text{with} \quad x_1 = 1 - x_2 \tag{3.21}$$

The derivatives in (3.21) can be analytically calculated in terms of $f(x_1)$ from the so-

lutions for c_1 and c_2 in (3.20). Equation (3.21) provides an independent condition to determine the auxiliary function. This final calculation bears a close relationship to the extraction process as it basically accounts for the transfer of mass from one phase to the other. For an arbitrary function $f(x_1)$, the concentration fields calculated from (3.20) will lead to unequal fluxes across the interface. But the physical process requires these fluxes to be equal, since mass cannot accumulate at the interface. There is a unique function $f(x_1)$ that satisfies this condition and leads to the unique solution of the counter-current concentration field, determined by (3.20). The last step is executed numerically as described below.

The domain is discretized using N nodes along the x_1 coordinate direction, into $N-1$ intervals. The function $f(x_1)$ is approximated as a piecewise linear function over these intervals. Hence, the function derivative $df(x_1)/dy$ is piecewise constant in each interval (k) and is given by

$$\frac{df\,(x_1)}{dx_1} = -\frac{df\,(1-x_2)}{dx_2} = \bar{f}_k \quad \text{where} \quad \begin{array}{l} x_1^k < x_1 < x_1^{k+1}\ ,\ 1 \le k \le N-1 \\ x_1 = 1 - x_2 \end{array} \tag{3.22}$$

Apart from the $N-1$ unknown derivative values, the value of $f(0) = f_0$ is also an unknown. Thus there are a total of N unknowns to be determined.

Under this numerical approximation each integral in (3.20) becomes a finite sum and (3.21) results in a linear algebraic equation with N unknowns. This equation is applied at each of the N nodes to give a closed system of N linear algebraic equations. This system has a unique solution, and it is solved to obtain the discretized $f(x_1)$. The equation to be applied at each node q $(1 \le q \le N)$ is given in (3.23). Here, the superscript indices on the x coordinate variables (x_1 and x_2) refer to the node index.

$$\begin{aligned}
&2\beta \sum_{n=0}^{\infty} \left(\exp\left(-\lambda_{1,n}^2 x_1^q\right)\right) = \\
&f_o \left[2\beta K \sum_{n=0}^{\infty} \left(\exp\left(-\lambda_{1,n}^2 x_1^q\right)\right) + 2\left(\tfrac{h}{H-h}\right) \sum_{n=0}^{\infty} \left(\exp\left(-\lambda_{2,n}^2 x_2^r\right)\right)\right] \\
&+ \sum_{i=1}^{q-1} \bar{f}_i \left[\begin{array}{l} \sum_{n=0}^{\infty} \frac{2K\beta}{\lambda_{1,n}^2} \left\{ \exp\left(-\lambda_{1,n}^2 \left(x_1^q - x_1^{i+1}\right)\right) - \exp\left(-\lambda_{1,n}^2 \left(x_1^q - x_1^i\right)\right)\right\} \\ \quad + \ 2\left(\tfrac{h}{H-h}\right)\left(x_1^{i+1} - x_1^i\right) \sum_{n=0}^{\infty} \left(\exp\left(-\lambda_{2,n}^2 x_2^r\right)\right) \end{array} \right] \\
&+ \sum_{j=1}^{r-1} \bar{f}_{N-j} \left[\begin{array}{l} -\sum_{n=0}^{\infty} \frac{2}{\lambda_{2,n}^2} \left(\tfrac{h}{H-h}\right) \left\{ \exp\left(-\lambda_{2,n}^2 \left(x_2^r - x_2^{j+1}\right)\right) - \exp\left(-\lambda_{2,n}^2 \left(x_2^r - x_2^j\right)\right)\right\} \\ \quad +2\left(\tfrac{h}{H-h}\right)\left(x_2^{j+1} - x_2^j\right) \sum_{n=0}^{\infty} \left(\exp\left(-\lambda_{2,n}^2 x_2^r\right)\right) \end{array} \right]
\end{aligned} \tag{3.23}$$

where $r = N - q + 1$

A large number of terms must be considered in the eigenfunction expansions (3.20) to obtain a converged solution near the horizontal boundaries. This is because the inlet conditions (3.6) at $x_1 = 0, 1$ do not satisfy the equilibrium condition at the interface (3.4). This mismatch causes oscillations in the numerical solution close to the horizontal boundaries (Gibbs phenomena). However, the region of Gibbs oscillations decreases as more terms are included in the eigenfunction expansions. In this work the first 501 terms $(0 \leq n \leq 500)$ are used, because they are sufficient for obtaining a smooth converged solution over more than 99% of the horizontal domain. We use an unequally spaced mesh of grid points with a finer grid near the ends of the channel where there are sharp gradients in concentration. In all our calculations, 1800 nodes are found to be sufficient for a converged solution. Half of these nodes are located in the first and last 10% of the length of the channel.

3.5 Definition of extraction performance metrics

In this section we define some key metrics that shall be used in the remainder of this study. The extraction ratio (ER), defined below, is used to quantify the extractor performance.

$$\mathrm{ER} = \frac{\overline{C}_{2,out} v_2 \left(H - h\right)}{\overline{C}_{1,in} v_1 h} \tag{3.24}$$

$\overline{C}_{1,in}$ is the average concentration of the carrier stream at the inlet and $\overline{C}_{2,out}$ is the average concentration of the solvent stream at its outlet. ER represents the fraction of the total solute input in the carrier phase that is removed by the solvent. This performance metric focuses on the purification of the carrier phase, which is the goal in most applications. ER has been used in several studies to quantify the extent of extraction in microchannels (Okubo *et al.*, 2008; Malengier *et al.*, 2012; Malengier and Pushpavanam, 2012).

The relative performance improvement of the counter-current extraction system over the co-current system is quantified via a relative extraction ratio (RER)

$$\mathrm{RER} = \frac{\mathrm{ER}_{\mathrm{counter}} - \mathrm{ER}_{\mathrm{co}}}{\mathrm{ER}_{\mathrm{co}}} \tag{3.25}$$

The RER will be strictly positive, as counter-current flow always performs better than co-current flow. However only a substantial improvement will merit the selection of counter-current operation. Studying the dependence of RER on the system parameters will help to identify regions where it is desirable to operate in counter-current flow. While other metrics, such as number of equivalent stages, have been used in the extraction literature, the RER provides a direct and clear measure of the relative performance of counter-

current and co-current systems. One significant advantage of using RER is demonstrated in Sec. 3.7, where the number of independent parameters affecting the relative extraction performance is reduced from five to four.

3.6 Verification of the qualitative predictions of the simple model

In this section the predictions of the proposed simplified model are compared with published experimental results and detailed simulations. The goal is to ensure that the model captures important physical phenomena as well as the effect of parameter variations on extraction performance. The focus of the comparison is on qualitative trends. A certain quantitative discrepancy is to be expected due to the simplifying assumptions of the present model. Here, only results for the co-current model are verified, for which there is sufficient literature available. Since the physics is essentially the same in the counter-current system, a verification of the co-current predictions should be sufficient for the purpose of this study.

Fig. 3.3a presents a comparison with the experiments and simulations of Znidarsic-Plazl and Plazl (2007). Here, the outlet concentrations of the carrier phase and the solvent phase are plotted against the flow rate of the carrier phase. The carrier phase concentration is normalized with its concentration at the inlet. The solvent concentration is normalized with its value at saturation. Another comparison with the work of Okubo *et al.* (2008) is presented in Fig. 3.3b. Here, the extraction ratio (ER) is plotted as a function of the total flow rate of both phases. In both studies (Znidarsic-Plazl and Plazl, 2007; Okubo *et al.*, 2008), numerical simulations based on a detailed model of the extraction process are carried out. These simulations show a very good match with the experiments (Fig. 3.3, compare dashed lines with circular markers). In this work we use a simplified model of the extraction process. The results of the simple model are plotted as solid lines in Fig. 3.3.

In the detailed model used by Znidarsic-Plazl and Plazl (2007) and Okubo *et al.* (2008), the laminar fully developed flow field in a rectangular duct is considered and the 3-D species conservation equation is solved numerically. The channel geometry used in the simulations has a finite height and width, which introduces wall effects into the calculations. These computationally intensive simulations also consider diffusion in all directions. In contrast, the simplified model in this study approximates the velocity field in each phase by a uniform plug flow profile. The velocity is constant in each phase and represents the average flow in that phase. In general the two velocities can have different values. The dimensionality of the problem is reduced by considering flow between two

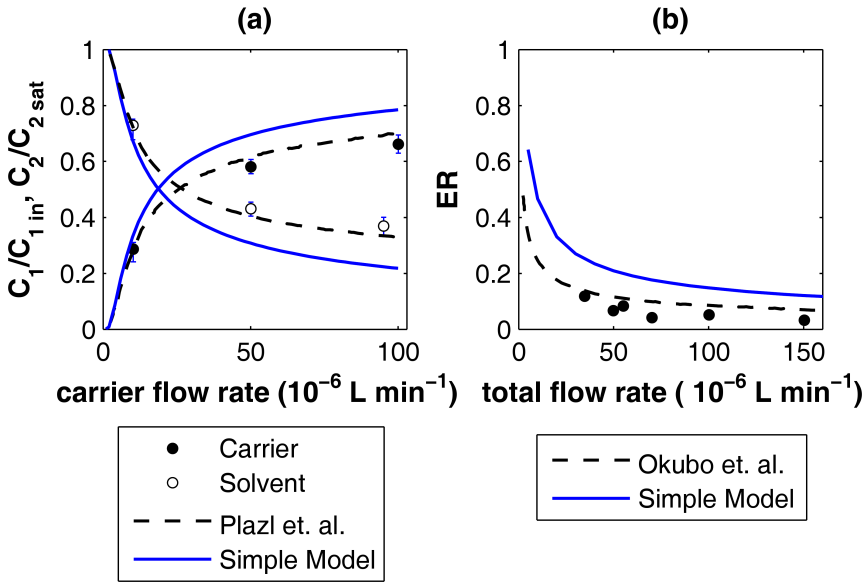

Figure 3.3: Comparison of the results of the model presented in this chapter with the experiments and simulations of Znidarsic-Plazl and Plazl (2007) and Okubo *et al.* (2008). Experimental data is represented as circular markers. The dashed lines represent simulations in the original work. The results of the present work are represented by solid lines.

infinite parallel plates (wall effects are neglected). Further, diffusion in the axial direction is neglected in comparison to axial convective transport.

Given the many simplifications made in the present model, the predictions agree remarkably well with the literature. All qualitative trends are described faithfully (Fig. 3.3) and the quantitative mismatch is uniform without any abrupt variations. The discrepancy between the simple model and the experiments are due to the simplifying assumptions described above. The predictions may be improved by systematically relaxing these assumptions. However, the primary aim of this work is to study the variation of RER across the parameter space in order to identify the regions in which it is high. This requires that the qualitative predictions of the model, especially as regards the effects of parameter variations, be accurate. In this section, the simple model has been shown to be suitable for this task.

The main advantage of using a simple model, which retains only the essential physics, lies in its relatively simple mathematical formulation. This in turn allows an analytical/semi-analytical solution of the equations. These solutions are free from convergence issues for all parameter values. Thus they can be used for investigating the effect of wide variations in parameter values. Moreover, a considerable reduction in computation time is achieved compared to full numerical solutions, especially in the case of the counter-current problem.

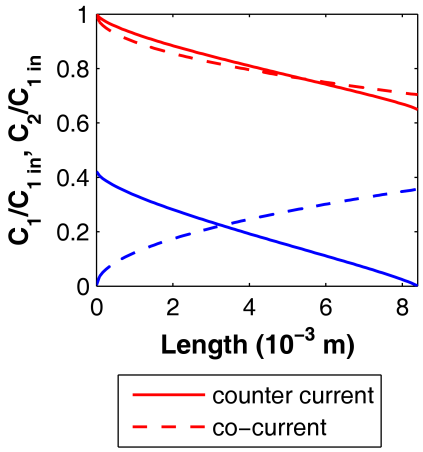

Figure 3.4: Average concentration profiles in co-current and counter-current flow through a microchannel for typical parameter values. $H = 4 \times 10^{-4}$ m, $h = 2 \times 10^{-4}$ m , $L = 0.0084$ m, $u_1 = 0.0857\ \mathrm{m\,s^{-1}}$, $u_2 = 0.0714\ \mathrm{m\,s^{-1}}$, $D_1 = 7.4 \times 10^{-8}\ \mathrm{m^2 s^{-1}}$, $D_2 = 3.7 \times 10^{-8}\ \mathrm{m^2 s^{-1}}$, K = 0.4 (h_r = 1/2, β = 2, Pe_1 = 5.5157, Pe_2 = 9.1929)

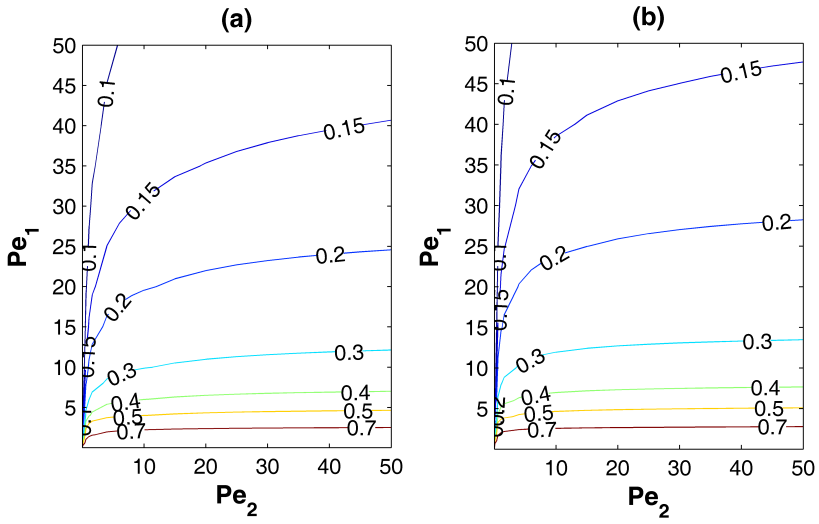

Figure 3.5: Contours of ER in the $Pe_1 - Pe_2$ parameter plane (cf. (3.13)). (a) co-current (b) counter-current. $K = 1/5$, $h_r = 1/2$ and $\beta = 1$

3.7 Typical concentration profiles and the influence of Peclet numbers

The concentration field depends on five dimensionless parameters. These are the Peclet numbers of the two phases Pe_1 and Pe_2, the ratio of diffusivities β, the fractional width of the carrier phase h_r (h/H) and the equilibrium constant K. The Peclet numbers contain information of the flow conditions. The definition of the Peclet numbers given in (3.13) are used in the remainder of this work.

Average concentration profiles for the co-current and counter-current systems, for a typical case, are presented in Fig. 3.4. In the co-current flow system, the average concentration in each phase steadily approaches the equilibrium state along the channel length.

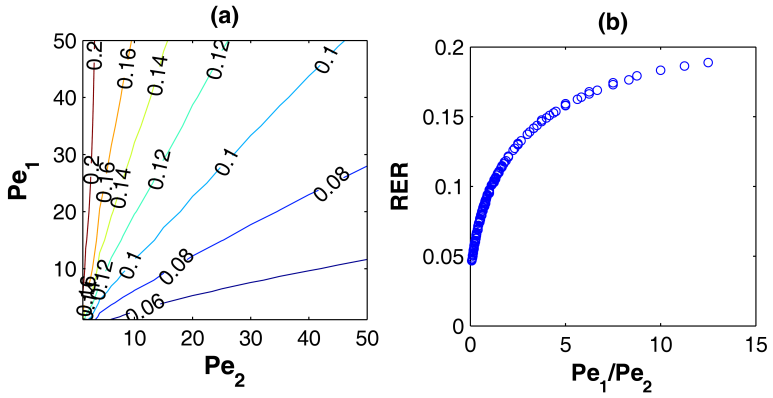

Figure 3.6: (a) Contours of RER in the $Pe_1 - Pe_2$ parameter plane (cf. (3.13)). (b) Scatter plot of RER and the Peclet number ratio (Pe_1/Pe_2) for the data in Fig. 3.6a. Parameter values: $K = 1/5$, $h_r = 1/2$ and $\beta = 1$.

Thus the concentration difference decreases monotonically along the channel. On the other hand, in the counter-current system, a nearly uniform concentration difference is maintained between both phases. The overall average driving force is higher in counter-current flow. This is confirmed by the lower outlet concentration of the carrier phase in this case.

The extraction performance is quantified in terms of the extraction ratio (ER) defined in Sec. 3.5. We now analyze the effect of the flow conditions on the ER by varying the Peclet numbers. The results for the case of $K = 1/5$, $h_r = 1/2$ and $\beta = 1$ are presented as contour plots in Fig. 3.5. The ER is seen to increase monotonically with decreasing Pe_1 for both counter-current and co-current systems. At low values of Pe_1, the velocity of the carrier phase is low and it has a high residence time within the channel. Thus a larger amount of solute is extracted from the carrier phase leading to a higher ER. On the other hand, decreasing Pe_2 gradually reduces the amount of solute extracted by the solvent phase (low ER).

In order to compare the performance of the co-current and counter-current systems, we now study the relative extraction ratio (RER, defined in Sec. 3.5) at various Peclet numbers. The results for the case under consideration ($K = 1/5$, $h_r = 1/2$ and $\beta = 1$) are presented in Fig. 3.6a. The contours are nearly straight lines that pass through the origin of the plot (small deviations from linearity may be attributed to numerical errors in the counter-current calculation). This clearly indicates that while the ER is dependent on Pe_1 and Pe_2 individually, the RER depends only on the ratio of the Peclet numbers Pe_1/Pe_2. To confirm this important result, the ratio Pe_1/Pe_2 is computed for each of the 196 data points in Fig. 3.6a and plotted as a scatter plot of RER against Pe_1/Pe_2. All the 196 data points fall on a single curve (Fig. 3.6b), which confirms the unique dependence of RER on the Peclet number ratio. This remains true for all values of K, h_r and β. This fact greatly aids our analysis, as the effective parameter space for studying the variation of RER is now reduced by one dimension – it consists of only K, h_r, β and Pe_1/Pe_2.

3.8 Relative improvement of counter-current operation: Maximum Gain at Mediocre Performance

Based on the results of Sec. 3.7, RER can be considered as a single valued function of four dimensionless parameters - K, h_r, β and Pe_1/Pe_2. In this section, the variation of RER with Pe_1/Pe_2 is studied for different values of K, h_r, β. Based on the results, we propose a general principle that governs the variation of RER in the four dimensional parameter space. This principle is '*maximum gain at mediocre performance*'. Henceforth, for convenience, we shall use the acronym MGMP to refer to this principle. According to MGMP, the relative improvement of counter-current operation is low (low value of RER) when the fluid properties and operating conditions (parameter values) either strongly promote or oppose extraction. Under these conditions, both co-current and counter-current systems perform well (high values of ER) or poorly (low values of ER), respectively. The relative improvement (RER) is low in either case. Instead, *the improvement in performance is greatest for conditions that result in an intermediate level of extraction performance for both systems*.

The principle of MGMP is illustrated in Fig. 3.7 where the variation of ER and RER with Pe_1/Pe_2 is depicted for the case of $K = 1$, $\beta = 1$ and $h_r = 1/2$. As demonstrated in Sec. 3.7, the extraction performance is poor at high values of Pe_1. Thus at high values of Pe_1/Pe_2 the performance is poor for both counter-current and co-current extraction systems, while it is very good at low Pe_1/Pe_2. At both these extremes the relative improvement of counter-current flow (RER) tails off in a symmetric manner to low values of about 12%. The case of intermediate performance (ER) occurs at intermediate values of all the parameters, i.e. Pe_1/Pe_2 = 1, $K = 1$ and $\beta = 1$ when $h_r = 1/2$. It is for these parameter values that RER attains a maximum value (approximately 55 %) and counter-current operation is most beneficial. This illustrates the principle of MGMP.

We now study the effect of the equilibrium constant (K) on RER. In Fig. 3.8, the variation of RER with Pe_1/Pe_2 for various values of K is presented. β and h_r are kept at the same constant values of 1 and 1/2 respectively. Consider the variation of RER with K at a constant $Pe_1/Pe_2 = 1$. The values of K chosen in Fig. 3.8 are evenly spaced about $K = 1$ on a geometric scale. Their corresponding curves intersect at $Pe_1/Pe_2 = 1$. This indicates that RER decreases symmetrically as K is displaced away from unity, towards higher or lower values. A high value of K implies that the solute has a greater affinity for the carrier phase. Hence the extraction performance will be poor. Conversely, low values of K will result in higher extraction from the carrier phase. Thus the maximum value of RER at $K = 1$ corresponds to an average performance level for both co-current and counter-current flow. This is again in agreement with the principle of MGMP.

A comparison of the cases for $K = 2.5$ and $K = 1$ makes it clear that the maximum in

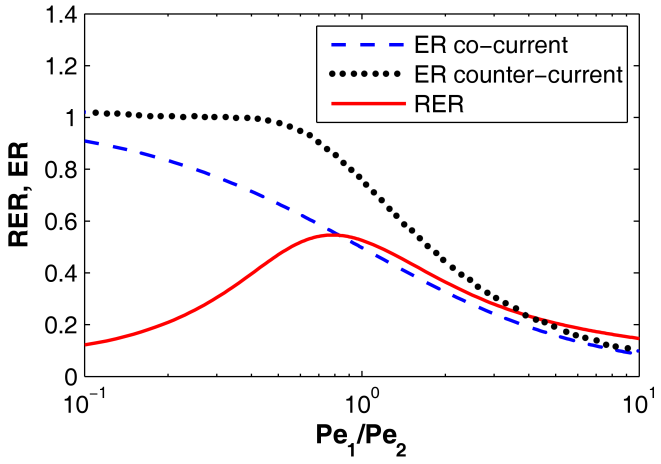

Figure 3.7: Illustration of the principle of *maximum gain at mediocre performance* (MGMP). ER for co-current and counter-current systems are plotted along with RER as a function of the ratio of Peclet numbers Pe_1/Pe_2. The other parameters are fixed at $K = 1/5$, $h_r = 1/2$ and $\beta = 1$.

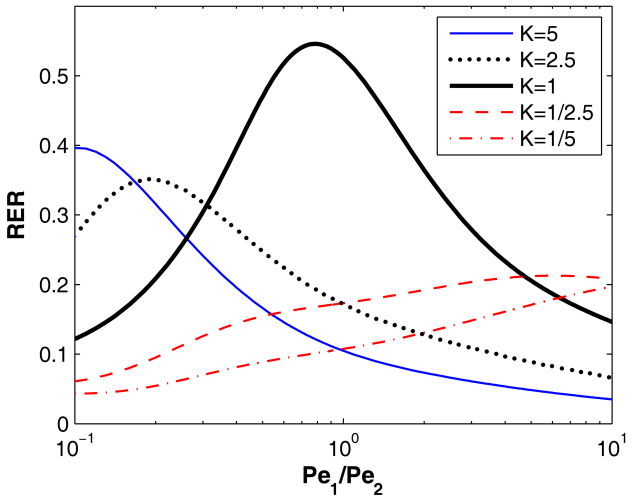

Figure 3.8: Effect of the equilibrium coefficient (K) on the improvement in extraction performance offered by operating in counter-current flow instead of co-current. The variation of RER with Pe_1/Pe_2 is plotted for various values of the K. Other parameters are fixed at $\beta = 1$ and $h_r = 1/2$.

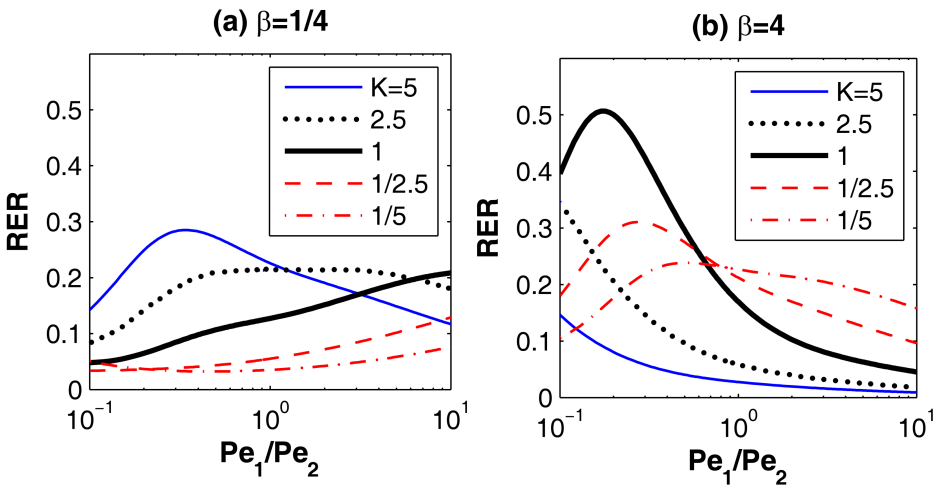

Figure 3.9: Effect of the diffusivity ratio on the improvement in extraction performance offered by operating in counter-current flow instead of co-current. The variation of RER with Pe_1/Pe_2 is plotted for various values of K, and for for two values of the diffusivity ratio: (a) $\beta = 1/4$ (b) $\beta = 4$. In both cases h_r = 1/2.

RER shifts to lower values of Pe_1/Pe_2 when K is increased. This can also be explained by MGMP. An increase in K above unity implies a greater affinity of the solute for the carrier phase. This results in a decrease in the extraction performance of both co-current and counter-current systems. To achieve intermediate performance, Pe_1/Pe_2 must be decreased below unity (Section 7). Therefore, according to MGMP, the maximum in RER must shift to $Pe_1/Pe_2 < 1$ when $K > 1$. Based on a similar argument, one may anticipate a shift in the maximum of RER to values of $Pe_1/Pe_2 > 1$ when $K < 1$. This shift is clear in Fig. 3.8.

The effect of relative solute diffusivities (β) is studied by computing RER - Pe_1/Pe_2 profiles for β values of 1/4 and 4. These curves are presented in Fig. 3.9. From this figure it can be seen that a larger diffusivity of the carrier phase ($\beta > 1$, c.f. Fig. 3.9b) leads to a higher relative performance of counter-current flow under two conditions: (i) the solute should have a higher affinity for the solvent i.e. $K < 1$. For example, the curve for $K = 1/5$ in Fig. 3.9b ($\beta > 1$) has higher RER values than the corresponding curve in Fig. 3.9a ($\beta < 1$). (ii) the carrier phase must have a lower velocity than the solvent phase ($Pe_1/Pe_2 < 1$ at fixed h_r). For example compare the curves for $K = 1$ in Fig. 3.9b and Fig. 3.9a. RER for $\beta = 4$ (Fig. 3.9b) is higher (lower) than RER for $\beta = 1/4$ (Fig. 3.9a) when Pe_1/Pe_2 is less (greater) than unity. For parameter values that do not satisfy the above two conditions, a lower diffusivity of the carrier phase ($\beta < 1$) results in a higher RER.

In all the aforementioned cases, h_r = 1/2 and the interface is located at the center of the channel. This allows the two phases to be separated easily at a Y-junction outlet (Znidarsic-Plazl and Plazl, 2007). Hence, it is the preferred configuration in applications. Nevertheless, we also study the effect of interface position on RER. Results are presented

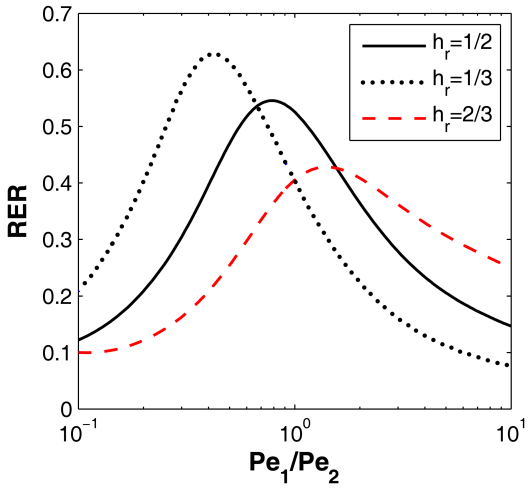

Figure 3.10: Effect of carrier phase volume fraction (h_r) on the improvement in extraction performance offered by operating in counter-current flow instead of co-current. The variation of RER with Pe_1/Pe_2 is plotted for various values of the volume fraction (or fractional width) of the carrier phase (h_r). Other parameters are fixed at K = 1 and $\beta = 1$.

for two other interface positions (with $K = 1$ and $\beta = 1$) in Fig. 3.10. Consider the case of $h_r = 2/3$ for which the carrier phase occupies a larger part of the channel. This configuration has a higher RER if the Peclet number of the carrier phase is greater than that of the solvent phase ($Pe_1/Pe_2 > 1$). However, if the solvent phase has a greater Peclet number ($Pe_1/Pe_2 < 1$), then smaller volume fractions of the carrier phase result in higher RER. If the Peclet numbers are nearly equal then the interface should be located at the center of the channel in order to gain maximum benefit from counter-current flow.

The results of this section have demonstrated that under *no condition* will counter-current systems perform well while co-current systems perform poorly (or vice-versa). In other words, parameter values for the maximum or minimum extraction performance coincide for both systems. The relative improvement due to counter-current flow is low at both these extremes, but peaks under conditions that correspond to intermediate performance levels for both systems (MGMP).

In a practical design problem, the diffusivity ratio (β) and the equilibrium constant (K) are fixed properties of the solute and fluids. On the other hand, the volume fraction (h_r) and the ratio of Peclet numbers (Pe_1/Pe_2) can be experimentally controlled by changing the fluid flow rates. So for any particular solute-fluid system, the results of this section are helpful in identifying the range of Peclet ratios at which substantial extraction improvement can be achieved by counter-current operation. It should be noted that Pe_1/Pe_2 and h_r cannot be varied independently. The relationship between these quantities depends on the viscosities of the fluids and the means of driving flow (e.g. pressure driven or electro-osmotic). To determine this relationship, the appropriate set of momentum equations and boundary conditions must be solved to obtain the fully developed velocity profile. (The velocity field for pressure driven layered flow is given in (2.1)

and (E.1).) The average velocities of each phase may then be determined as functions of h_r and used to obtain the relationship between Pe_1/Pe_2 and h_r.

3.9 Concluding Remarks

Micro systems pose unique challenges and paradigms that are applicable at the macro scale must be re-examined. Counter-current operation is widely preferred in large scale interfacial mass transfer units (Treybal 1980). However, due to design and operational difficulties, the choice between co-current and counter-current flow is a non-trivial one in microchannels. The relative improvement of counter-current operation must therefore be significant to justify its selection over co-current operation. In this chapter, we have identified the operating conditions and the fluid properties for which counter-current operation is most beneficial. This has been achieved by using simple models to carry out a thorough investigation of the effect of the physical parameters on the relative extraction performance.

A straight forward analytical solution has been obtained for the co-current model. The counter-current model is mathematically more challenging and a novel semi-analytical solution strategy has been developed. This method of solution can be applied to similar 'two way diffusion' type problems arising in other fields of study (e.g. particle scattering). The corresponding computations are relatively less intensive and free from convergence issues and thus a detailed study of the parameter space is possible.

This study reveals a general principle that governs the relative improvement in performance achievable by using a counter-current flow configuration rather than co-current. This is the principle of *maximum gain at mediocre performance* (MGMP), according to which *the relative increase in extraction due to counter-current operation is maximum at parameter values for which both systems perform at a mediocre level.* This translates into a limited range of operating conditions and fluid properties for which counter-current operation is a truly attractive option. For some fluid systems (e.g. low β and K values) the improvement is relatively low. In such cases, co-current flow may be the operating mode of choice due to ease of design and operation. Apart from quantitative results, the principle of MGMP provides qualitative information even before any calculations or experiments are done. For e.g., if $h_r \approx 1/2$, $\beta \approx 1$ and $K > 1$, then one can expect high performance improvement for $Pe_1/Pe_2 < 1$ (cf. Fig. 3.8).

With the aid of the quantitative results presented here, along with the intuitive guidance of the principle of MGMP, the range of parameters for study can be significantly reduced. Detailed numerical calculations and experiments may be performed within this restricted range of parameter values to obtain the most useful results for a limited set

of experiments/ calculations. In addition, the principle of MGMP provides a rationale for organizing and interpreting results of a comparison between co-current and counter-current mass transfer systems, in general.

CHAPTER 4

Solutal Marangoni Instability of Layered Micro-Flows

"Galileo made a great advance in the understanding of motion when he discovered the principle of inertia: if an object is left alone, is not disturbed, it continues to move with a constant velocity in a straight line if it was originally moving, or it continues to stand still if it was just standing still. Of course this never appears to be the case in nature, for if we slide a block across a table it stops, but that is because it is not left to itself – it is rubbing against the table. It required a certain imagination to find the right rule, and that imagination was supplied by Galileo."

– R. Feynman, *Feynman Lectures on Physics, Vol I*

4.1 Introduction

In the previous two chapters (Ch. 2 and Ch. 3), the layered flow field was assumed to be insensitive to the presence of a diffusing solute. This is a reasonable approximation, when the variations in density and viscosity produced by the solute are small, especially when the difference in the properties of the pure immiscible fluids is much larger. However, even small concentration variations may have a significant effect on the flow, when the solute is a soluble surfactant. In such cases, variations in solute concentration along the interface will result in gradients of interfacial tension that produce surface forces, called solutal Marangoni stresses. These stresses could significantly impact the flow and modify (enhance?) the rate of mass transfer. Examples of such solute/fluid-fluid systems, encountered in extraction processes, are acetone/water-toluene (Javed *et al.*, 1989), Butyric acid/water-toluene (Sternling and Scriven, 1959) and oxyethylated alcohols/water-heptane (Tadmouri *et al.*, 2010). Several phase transfer catalysts also act as soluble surfactants and modify the interfacial tension of the interfluid interface (Dutta and Patil, 1993).

There are two fundamentally different routes through which Marangoni stresses may impact mass transfer in these flows. The first is due to the fact that the concentration at the interface generally varies significantly along the microchannel. The two phases enter the channel with a significant concentration difference and leave the channel close

to or at equilibrium. Marangoni stresses due to this axial concentration gradient will certainly modify the steady state flow of the system. However, in a recent study, we have shown that this effect is not strong enough to impact the primary pressure driven flow, for practical fluid solute systems (Picardo *et al.*, 2015). The *base steady state* flow remains almost the same as that in the absence of the solute.

The second route through which Marangoni stresses can impact mass transfer is by generating a hydrodynamic instability that leads to a new dynamic flow state. It is the aim of this work to establish if such an instability is possible, to determine the stability threshold, and to understand the nature of the instability modes. Towards this end, we study a model problem that is closely related to the extraction system, but in which the base steady flow is fully developed and free from Marangoni stresses. Specifically, we consider layered flow between two infinite flat plates, which are maintained at different solute concentrations. The concentration gradient maintained across the fluids sustains mass transfer between the phases. The corresponding base steady flow is fully developed and unidirectional. We analyze the stability of this flow to infinitesimal perturbations via a classic normal mode analysis.

There is good reason to expect a Marangoni instability in this flow, on the basis of past work on the stability of stationary fluid layers sustaining mass transfer of a soluble surfactant. First analyzed by Sternling and Scriven (1959), this stationary *solutal Marangoni* instability is the subject of a large body of literature. Much of this work is surveyed in the reviews by (Schwarzenberger *et al.*, 2014; Kovalchuk and Vollhardt, 2006). The stability is affected by the fluid and solute properties as well as the direction of mass transfer. The existence of a finite concentration gradient across the fluids is a necessary condition for instability of the stationary fluid layers. Whether this remains a necessary condition when pressure driven flow is imposed is a question that we aim to answer in this chapter.

A rather disjoint, though equally large body of literature exists on the stability of two-phase layered Poiseuille flow (Boomkamp and Miesen, 1996; Govindarajan and Sahu, 2014; Barmak *et al.*, 2016). In the absence of surfactants (but in the presence of interfacial tension), this flow is unstable to long wave and short wave interfacial instabilities, that arise from the viscosity contrast between the fluids (viscosity-induced modes) (Boomkamp and Miesen, 1996; Govindarajan and Sahu, 2014). Both these modes can occur at arbitrarily small Reynolds numbers (but not in creeping flow). However, the short wave mode is suppressed by interfacial tension, and therefore does not play a prominent role in the microscale regime where capillary forces are dominant. On the other hand, interfacial tension is not as effective at stabilizing the long wavelength interfacial mode. Thus, it remains relevant even as the channel dimensions are decreased. This mode was first identified by Yih (1967), and we shall henceforth refer to it as the Yih-instability or the (long wave) viscosity-induced instability.

The viscosity-induced interfacial modes require finite fluid inertia for instability, and therefore are stable in the creeping flow regime. At the other extreme of large Reynolds numbers, the shear mode becomes unstable (Boomkamp and Miesen, 1996; Yiantsios and Higgins, 1988). This mode takes the form of Tollmein-Schilichting waves and is induced by Reynolds stresses near the walls. The shear instability is unimportant at the low Reynolds numbers encountered in milli and micro channels.

Studies on the effects of surfactants on two-phase layered flow are largely limited to the case of insoluble surfactants. Frenkel and Halpern (Frenkel and Halpern, 2002; Halpern and Frenkel, 2003) first demonstrated that the otherwise stable creeping flow becomes unstable on introducing an insoluble surfactant. Further studies have explored the influence of inertia on this instability (Blyth and Pozrikidis, 2004*a*; Frenkel and Halpern, 2005) and its nonlinear evolution (Blyth and Pozrikidis, 2004*b*; Wei, 2005; Blyth *et al.*, 2007; Samanta, 2013). From the perspective of this literature, the present study extends current understanding of surfactant effects to the case of soluble surfactants.

A few studies that consider the influence of shear flow on the solutal Marangoni instability have been carried out. Sun and Fahmy (2006) have analyzed the instability caused by mass transfer in gas-liquid Poiseuille flow. Zaisha *et al.* (2008) have carried out DNS simulations for the case of liquid-liquid Couette flow. Both studies are restricted to the case of a non-deforming interface. However, interfacial deformation has a profound impact on the solutal Marangoni instability when Poiseuille flow is present, as shown in this chapter. Very recently You *et al.* (2014) have presented stability results for the solutal Marangoni instability in Poisuelle flow. However, a key term that accounts for interfacial concentration gradients due to interface deformation is absent in their model. Here, we show that this term plays an important role in the Marangoni instability and cannot be ignored unless the interface is flat.

We make certain assumptions that simplify the system while retaining its essential features. We consider two dimensional Poiseuille flow between flat walls of two immiscible, incompressible Newtonian fluids. The concentrations of the solute at the two walls are maintained at two different constant values. The channel width is assumed to be sufficiently small for buoyancy effects to be neglected in comparison with Marangoni effects. This occurs when the velocity scale of natural convection induced flow ($\beta_D \Delta C g d^2/\mu$) to Marangoni stress induced flow ($\beta \Delta C d/l_c \mu$) is small ($dgl_c\beta_D/\beta \ll 1$), for each fluid. Here, μ and d are the fluid's viscosity and channel width respectively. β_D and β are measures of the sensitivity of density and interfacial tension to solute concentration respectively. ΔC is the concentration difference applied across the plates and l_c is the longitudinal length scale of streamwise variations in concentration. As buoyancy effects are unimportant in this regime, we simplify the model by assuming the densities of the fluids to be equal and independent of concentration.

We also make certain simplifying assumptions regarding the properties of the soluble surfactant. A linear dependence of interfacial tension on concentration is considered. The rate of solute adsorption/desorption to/from the interface is assumed to be instantaneous in comparison with transport processes on the interface and in the bulk. Under these conditions, the interface solute concentration will be in equilibrium with the bulk concentration in the adjacent fluid, on either side of the interface. The model can then be written entirely in terms of bulk phase concentrations. It consists of a solute transport equation in each fluid and two interface boundary conditions that enforce equality of flux and local equilibrium at the interface (Picardo *et al.*, 2015).

Apart from model simplification, an additional advantage of assuming the aforementioned solute properties is that the results and conclusions of this study can be directly applied to thermocapillary instabilities, which arise due to variations of temperature. In the thermal analogue of this problem, the walls are maintained at different temperatures and heat transfer occurs between the fluids. Marangoni stresses are generated due to the dependence of interfacial tension on temperature. The corresponding governing equations are identical to those considered in this chapter, provided an appropriate interchange of physical quantities is made (e.g. replacing the solute diffusion coefficients by thermal diffusion coefficients of the fluids). Scriven and Sternling (1964) were among the first to study the thermocapillary instability in stationary fluid layers. Gumerman and Homsy (1974) have studied the stability of layered *Couette* flow between heated plates, simultaneously considering bouyancy and thermocapillary effects. However, the parameter space was not fully explored, as only a few specific fluid systems were analyzed. A detailed asymptotic analysis of thermocapillary instability in Couette flow was carried out by Wei (2006) for the case of one fluid layer being much thinner than the other (thin-layer limit).

The outline of this chapter is as follows. The governing equations are presented in Sec. 4.2. The steady base state concentration and velocity fields are presented in Sec. 4.3. Brief descriptions of the linear stability analysis and energy budget calculation are presented in Sec. 4.4 and Sec. 4.5. An asymptotic analysis for long wave disturbances is carried out in Sec. 4.6. The results of numerical calculations for all wave numbers are discussed next. Sec. 4.8 to Sec. 4.11 consider the limit of creeping flow, wherein Marangoni effects are the only possible source of instability (the viscosity induced mode is stable for creeping flow). In Sec. 4.8 three different types of instability modes - one long wave and two short wave - are identified. Mode switching between the two short wave modes is studied in Sec. 4.9. The results therein reveal a key qualitative difference between the two short wave modes. The transition from long waves to short waves is analyzed in Sec. 4.10. These numerical results along with the long wave analysis of Sec. 4.6 points to a well defined transition boundary in parameter space. Sec. 4.11 investigates whether a finite concentration difference across the fluids is a necessary condition for the Marangoni

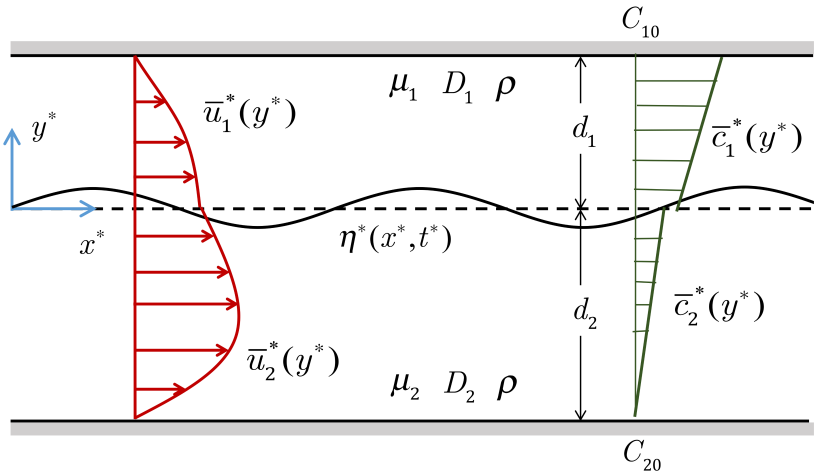

Figure 4.1: Schematic of the system under study: layered flow between flat plates with transverse diffusion of a soluble surfactant. The concentrations at the two plates are maintained at constant values of C_{10} and C_{20}. The deformable interface is located at $y^* = \eta^*(x^*, t^*)$. The dashed line at $y^* = 0$ corresponds to the undeformed interface in the base state. $\bar{u}_i^*$ and $\bar{c}_i^*$ are the velocity and concentration fields in the base state. The concentration field obeys the linear equilibrium condition $\bar{c}_1^* = K\bar{c}_2^*$ at the interface. Since K can differ from unity, the concentration field can be discontinuous at the interface in general. Both fluids have a density ρ, while μ_i and D_i are the viscosities and solute diffusivities respectively.

instability. The analysis is extended beyond the creeping flow limit to small but finite Reynolds numbers in Sec. 4.12. This introduces the viscosity-induced mode in addition to the three previous Marangoni modes. The influence of inertia on the Marangoni modes, as well as the effect of a soluble surfactant on the long wave viscosity-induced mode are studied in this section. In Sec. 4.13 we compare our results with previous work by Wei (2006) and You *et al.* (2014). The key results and conclusions of this chapter are summarized in Sec. 4.14, along with some suggestions for future work.

4.2 Governing Equations

A schematic of the 2D flow system being investigated is shown in Fig. 4.1. Two immiscible, incompressible viscous fluids with equal densities flow side-by-side between two infinite parallel plates separated by $d_1 + d_2$. The liquid-liquid interface is located at $y^* = 0$ (superscript '$*$' indicates that the quantity is dimensional). The flow is driven by an imposed pressure gradient parallel to the x^*-axis. Concentrations at the top and bottom plates are maintained at C_{10} and C_{20}, respectively.

Choosing the interfacial velocity (U_0), the thickness of the top fluid layer (d_1) and the concentration at the top plate (C_{10}) as the characteristic velocity, length and concentration scales, the dimensionless coordinate directions (x, y), streamwise velocity (u_j'),

transverse velocity (v_j'), pressure (p_j') and concentration (c_j') fields are defined as

$$(x, y) = \frac{(x^*, y^*)}{d_1},\ (u_j', v_j') = \frac{(u_j^*, v_j^*)}{U_0},\ p_j' = \frac{p_j^*}{\mu_j U_0/d_1},\ c_j' = \frac{c_j^*}{C_{10}} \tag{4.1}$$

The subscript j takes the values 1 and 2 to denote the top and bottom fluids, respectively. The dimensionless governing equations, viz. the continuity equation, Navier-Stokes equation and the species transport equation, are given by

$$\boldsymbol{\nabla} \cdot \boldsymbol{v}_j' = 0 \tag{4.2a}$$

$$\frac{Re}{m_j}\left(\frac{\partial \boldsymbol{v}_j'}{\partial t} + \boldsymbol{v}_j' \cdot \boldsymbol{\nabla}\boldsymbol{v}_j'\right) = -\boldsymbol{\nabla} p_j' + \nabla^2 \boldsymbol{v}_j' \tag{4.2b}$$

$$\frac{\partial c_j'}{\partial t} + \boldsymbol{v}_j' \cdot \boldsymbol{\nabla} c_j' = \frac{D_{r,j}}{Pe}\nabla^2 c_j' \tag{4.2c}$$

with $j = 1$, $m_1 = 1$, $D_{r,1} = 1$ for fluid 1 and $j = 2$, $m_2 = m = \mu_2/\mu_1$, $D_{r,2} = D_r = D_2/D_1$ for fluid 2. Here,

$$\boldsymbol{\nabla} = \left(\frac{\partial}{\partial x},\ \frac{\partial}{\partial y}\right);\ \boldsymbol{v}_j' = (u_j',\ v_j');\ Re = \frac{\rho U_0 d_1}{\mu_1},\ Pe = \frac{U_0 d_1}{D_1} \tag{4.3}$$

The dimensionless parameters Re, Pe, m and D_r represent the Reynolds number, Péclet number, ratio of dynamic viscosities and molecular diffusivities, respectively. All physical properties are assumed to be constant with the exception of interfacial tension, which depends on the concentration of the solute at the interface.

In general, a separate solute balance equation must be written at the interface, which accounts for changes in interface concentration due to surface convection and diffusion along the interface, as well as adsorption/desorption (Leal, 2007). However, if the rates of adsorption and desorption are very high, then the interface concentration may be assumed to be in equilibrium with the concentration in the adjacent fluid on either side of the interface. Under these conditions, the interface solute balance reduces to two boundary conditions at the interface, $y = \eta'(x, t)$, which require the diffusive flux to be continuous and the bulk concentrations to be in equilibrium. For dilute solutions these boundary conditions read as (Picardo *et al.*, 2015):

$$-\eta_x' c_{1,x}' + c_{1,y}' = D_r(-\eta_x' c_{2,x}' + c_{2,y}') \tag{4.4}$$

$$c_1' = K c_2' \tag{4.5}$$

Here subscripts x and y indicate partial differentiation and K is the distribution coefficient. Note that the unit normal to the interface is given by $(\boldsymbol{e}_y - \eta_x' \boldsymbol{e}_x)(1 + (\eta_x')^2)^{-1/2}$, while the unit tangent is given by $(\eta_x' \boldsymbol{e}_y + \boldsymbol{e}_x)(1 + (\eta_x')^2)^{-1/2}$. Here $\boldsymbol{e}_y$ and $\boldsymbol{e}_x$ are unit vectors in the y and x directions respectively.

The value of interfacial tension is calculated using the bulk concentration at the interface. Assuming a linear dependence of interfacial tension on solute concentration, we have:

$$\sigma^* = \sigma_0(1 - \beta C_{10}(c_1' - c_r')) \tag{4.6}$$

where $\beta = -(d\sigma^*/dc_1^*)/\sigma_0$ and σ_0 is the interfacial tension when the solute concentration at the interface equals the reference value $C_{10}c_r'$. A positive value of β implies that interfacial tension decreases with increasing solute concentration. Due to the linear equilibrium relationship (4.5), either c_1' or c_2' can be used to express the dependency of interfacial tension on concentration (Sternling and Scriven, 1959).

The variation of interfacial tension causes tangential Marangoni stresses at the interface, which are balanced by shear stresses. Using relation (4.6), the tangential stress balance at the interface reads:

$$\frac{1}{\left(1+(\eta_x')^2\right)^{1/2}}\left[\!\left[2\eta_x' m_j\left(v_{j,y}'-u_{j,x}'\right)+\left(1-(\eta_x')^2\right)m_j\left(u_{j,y}'+v_{j,x}'\right)\right]\!\right]_2^1-\frac{Ma}{Pe}\left(c_{1,x}'+\eta_x' c_{1,y}'\right)=0 \tag{4.7}$$

where the jump operator is defined as $[\![g_j]\!]_2^1 = g_1 - g_2$. Ma is the Marangoni number, given by $\sigma_0\beta C_{10}d_1/D_1\mu_1$. We have not included the concentration difference between the plates in the Marangoni number, to allow for the possibility that the interface sensitivity parameter (β) and the concentration difference (represented by $\gamma = C_{20}/C_{10}$) may have independent effects on the system's stability.

A similar description of solutal Marangoni effects has been used by Sternling and Scriven (1959) and Smith (1966) to study instabilities in stationary layered fluids. The two terms multiplied by Ma in (4.7) derive from the surface gradient of the solute concentration ($\boldsymbol{\nabla}_s c_1$). They account for variations of interfacial tension due to a non-uniform distribution of the solute along the interface. The first term represents concentration perturbations caused by the disturbance flow. The second term accounts for concentration variations that arise along a deformed interface, when the base concentration varies transversely. This latter term is absent in the analysis of You *et al.* (2014).

Interfacial tension also exerts normal stresses that tend to maintain a flat interface. This effect is included in the normal stress balance at the interface, which reads:

$$\left(1+(\eta_x')^2\right)\left(mp_2'-p_1'\right)+2\left[\!\left[(\eta_x')^2 m_j u_{j,x}'+\eta_x' m_j\left(u_{j,y}'+v_{j,x}'\right)+m_j v_{j,y}'\right]\!\right]_2^1 = -\frac{1}{Ca}\left(\frac{\sigma^*}{\sigma_0}\right)\frac{\eta_{xx}'}{\left(1+(\eta_x')^2\right)^{1/2}} \tag{4.8}$$

$Ca = \mu U_0/\sigma_0$ is the dimensionless Capillary number, which represents the relative importance of capillary forces in comparison to viscous forces. Note that because the characteristic scale for pressure in each fluid contains the respective fluid's viscosity (cf.

(4.1)), the dimensionless pressure is discontinuous across the interface even when the interface is flat with $v_i' = 0$ ($mp_2' = p_1'$ in this case).

The remaining boundary conditions at the interface are the equality of velocities and the kinematic condition:

$$\boldsymbol{v}_1' = \boldsymbol{v}_2' \tag{4.9}$$

$$\eta_t' + u_1'\eta_x' = v_1' \tag{4.10}$$

At the bounding plates, no-slip and no-penetration conditions are applied on the velocity field and Dirichlet conditions on the concentration field:

$$u_1' = v_1' = 0;\ c_1' = 1 \quad \text{at} \quad y = 1 \tag{4.11}$$

$$u_2' = v_2' = 0;\ c_2' = \frac{C_{20}}{C_{10}} = \gamma \quad \text{at} \quad y = -n \tag{4.12}$$

where $n = d_2/d_1$ is the ratio of thickness of fluid layers.

Equations (4.2–4.10) govern the behavior of the layered flow system, accounting for inter-phase mass transfer of a soluble surfactant and associated Marangoni stresses. These equations extend the model used by Sternling and Scriven (1959) to the case of layered Poiseuille flow. In this simplified model, the dissipative effect of surface viscosity is neglected in comparison with that of bulk viscosity. Studies on stationary fluid layers have found that surface viscosity has a stabilizing influence, but does not significantly modify the key features of the stationary Marangoni instability (Hennenberg *et al.*, 1977; Kovalchuk and Vollhardt, 2006). The model also neglects dynamic transport of the solute in the interface Gibbs adsorption layer. This idealization corresponds to the limit of instantaneous adsorption/desorption of the solute to and from the interface. As a result of this assumption, the present model *cannot* be reduced to the case of an insoluble surfactant by taking the limit of zero solute diffusivity within the fluids. Insoluble surfactants are trapped at the interface and can only be transported along the interface (Frenkel and Halpern, 2002).

4.3 Base state velocity and concentration profiles

The steady base state consists of unidirectional fully developed flow with a flat inter-fluid interface. The corresponding concentration field is invariant along the flow direction. The transverse variation of the base state fields (denoted by an overbar), obtained by solving

(4.2) - (4.12) are given by:

$$\overline{u}_j = 1 + a_j y + b_j y^2, \quad \overline{v}_j = 0 \tag{4.13a}$$

$$\overline{c}_j = s_j y + t_j, \quad \text{for } j = 1, 2 \tag{4.13b}$$

$$\text{with } a_1 = \frac{m - n^2}{n(n+1)};\ b_1 = -\frac{m+n}{n(n+1)};\ a_2 = \frac{a_1}{m};\ b_2 = \frac{b_1}{m};$$
$$s_1 = \frac{D_r(1-\gamma K)}{D_r + Kn};\ t_1 = \frac{K(n + D_r\gamma)}{D_r + Kn};\ s_2 = \frac{s_1}{D_r};\ t_2 = \frac{t_1}{K}$$

The piecewise linear base concentration field has different slopes in each fluid, which depend on the diffusivity ratio and thickness ratio. The direction of mass transfer depends on γ, with $\gamma < 1/K (> 1/K)$ corresponding to mass transfer from plate 1 to plate 2 (plate 2 to plate 1). When the plates are maintained at equilibrium ($\gamma = 1/K$), the concentration is constant in each fluid and no net mass transfer occurs.

Marangoni stresses are absent in the base state since the concentration is uniform along the interface. However, a perturbation to the base flow will disturb the uniformity of the concentration profile and lead to Marangoni stresses. These stresses may cause the initial perturbation to grow, resulting in an instability.

In the next section we analyze the stability of this base state to infinitesimally small perturbations.

4.4 Linearized equations

Infinitesimally small perturbations (denoted by a hat) are imposed on the base state (4.13) as follows:

$$u_j' = \overline{u}_j(y) + \widehat{u}_j(x,y,t), \quad v_j' = \widehat{v}_j(x,y,t), \quad p_j' = \overline{p}_j(x) + \widehat{p}_j(x,y,t)$$
$$c_j' = \overline{c}_j(y) + \widehat{c}_j(x,y,t), \quad \eta' = \widehat{\eta}(x,t), \quad j = 1, 2 \tag{4.14}$$

The disturbance velocity field can be expressed in terms of a disturbance streamfunction ($\widehat{\psi}_j$) as $\widehat{u}_j = \partial\widehat{\psi}_j/\partial y$ and $\widehat{v}_j = -\partial\widehat{\psi}_j/\partial x$.

We focus on a temporal stability analysis, in this work, and assume classic normal mode forms for the perturbations:

$$\begin{bmatrix}\widehat{\psi}_j & \widehat{p}_j & \widehat{c}_j & \widehat{\eta}\end{bmatrix} = \begin{bmatrix}\psi_j(y) & p_j(y) & c_j(y) & h\end{bmatrix} \exp[\mathrm{i}\alpha(x - \omega t)] + \text{c.c.} \tag{4.15}$$

where c.c. denotes the respective complex conjugate and ψ_j, p_j, c_j and h are complex amplitudes of the corresponding normal modes. The streamwise wavenumber α is real while the wave speed ω is complex ($\omega = \omega_r + i\omega_i$). The growth rate of each normal mode

is given by $\alpha\omega_i$. Hence, the system is unstable if $\omega_i > 0$ for any α.

The governing equations (4.2) are linearized about the base state (4.13) to obtain evolution equations for the disturbance fields. Applying the stream function formulation and adopting the normal mode form of perturbations, we obtain:

$$\mathrm{i}\alpha Re\big[(\overline{u}_j - \omega)(\mathcal{D}^2 - \alpha^2)\psi_j - 2b_j\psi_j\big] = m_j(\mathcal{D}^2 - \alpha^2)^2\psi_j \tag{4.16a}$$

$$\mathrm{i}\alpha Pe\big[(\overline{u}_j - \omega)c_j - s_j\psi_j\big] = D_{r,j}(\mathcal{D}^2 - \alpha^2)c_j \tag{4.16b}$$

where the operator $\mathcal{D}$ refers to differentiation with respect to y i.e. $\mathcal{D} = d/dy$. The boundary conditions at the interface are simplified for the case of small deflections ($h \ll 1$) using the domain perturbation technique (Johns and Narayanan, 2002). The resulting boundary conditions for the normal mode amplitudes are:

$$\psi_1(1) = \mathcal{D}\psi_1(1) = c_1(1) = \psi_2(-n) = \mathcal{D}\psi_2(-n) = c_2(-n) = 0 \tag{4.17a}$$

$$\mathcal{D}\psi_1(0) + ha_1 = \mathcal{D}\psi_2(0) + ha_2 \tag{4.17b}$$

$$\psi_1(0) = \psi_2(0) \tag{4.17c}$$

$$c_1(0) + hs_1 = K(c_2(0) + hs_2) \tag{4.17d}$$

$$\mathcal{D}c_1(0) = D_r\mathcal{D}c_2(0) \tag{4.17e}$$

$$(\mathcal{D}^2 + \alpha^2)\psi_1(0) - m(\mathcal{D}^2 + \alpha^2)\psi_2(0) = \mathrm{i}\alpha\frac{Ma}{Pe}(c_1(0) + hs_1) \tag{4.17f}$$

$$m\mathcal{D}^3\psi_2(0) - \mathcal{D}^3\psi_1(0) - 3\alpha^2(m\mathcal{D}\psi_2(0) - \mathcal{D}\psi_1(0)) = (1/Ca)\,\mathrm{i}\alpha^3 h \tag{4.17g}$$

$$(\omega - 1)h = \psi_1(0) \tag{4.17h}$$

Here, the reference concentration at which interfacial tension takes the value σ_0 (cf. (4.6)) is taken to be the interface concentration in the base state ($c_r' = \bar{c}_1(0) = t_1$). Note that (4.17b) and (4.17c) are obtained from the x and y components of the continuity of velocity condition (4.9), while (4.17h) is obtained from the kinematic equation (4.10).

Equations (4.16) & (4.17) constitute a linear differential eigenvalue problem with ω as the eigenvalue. For the system to be stable, the entire spectrum of eigenvalues must lie in the lower half of the complex plane ($\omega_i < 0$).

4.5 Energy budget

Energy budget calculations help to characterize instability modes and identify their sources, especially when several different instability mechanisms are present simultaneously. Following the procedure described in Boomkamp and Miesen (1996) and Lin and Chen

(1998), we take the inner product of the linearized momentum equations with the perturbation velocity vector ($\widehat{\boldsymbol{v}}_j$) and integrate across the transverse direction in each fluid. The Gauss divergence theorem is applied to the stress integrals and the entire equation is averaged over one axial wavelength $\lambda = 2\pi/\alpha$ and one time period $T = 2\pi/(\alpha\omega_R)$. This results in the following mechanical energy balance equation:

$$\sum_{j=1}^{2} KE_j = \sum_{j=1}^{2} REY_j + \sum_{j=1}^{2} DIS_j + NOR + TAN_\mu + MAS_I + MAS_F \tag{4.18}$$

where

$$KE_j = \frac{Re}{T\lambda}\int_0^T dt \int_0^\lambda dx \int_{e_j}^{f_j} dy \left[\frac{d}{dt}\left(\frac{\widehat{u}_j^2 + \widehat{v}_j^2}{2}\right)\right] \tag{4.19a}$$

$$REY_j = -\frac{Re}{T\lambda}\int_0^T dt \int_0^\lambda dx \int_{e_j}^{f_j} dy \left[\widehat{u}_j\widehat{v}_j\frac{d\overline{u}_j}{dy}\right] \tag{4.19b}$$

$$DIS_j = -\frac{m_j}{T\lambda}\int_0^T dt \int_0^\lambda dx \int_{e_j}^{f_j} dy \left[2\widehat{u}_{j,x}^2 + 2\widehat{v}_{j,y}^2 + (\widehat{u}_{j,y} + \widehat{v}_{j,x})^2\right] \tag{4.19c}$$

$$NOR = \frac{1}{T\lambda Ca}\int_0^T dt \int_0^\lambda dx \left[\widehat{v}_1\widehat{\eta}_{xx}\right]_{y=0} \tag{4.19d}$$

$$TAN_\mu = \frac{1}{T\lambda}\int_0^T dt \int_0^\lambda dx \left[(\widehat{u}_2 - \widehat{u}_1)(\widehat{u}_{1,y} + \widehat{v}_{1,x})\right]_{y=0} \tag{4.19e}$$

$$MAS_I = -\frac{1}{T\lambda}\frac{Ma}{Pe}\int_0^T dt \int_0^\lambda dx \left[\widehat{u}_2\widehat{\eta}_x\frac{d\overline{c}_1}{dy}\right]_{y=0} \tag{4.19f}$$

$$MAS_F = -\frac{1}{T\lambda}\frac{Ma}{Pe}\int_0^T dt \int_0^\lambda dx \left[\widehat{u}_2\widehat{c}_{1,x}\right]_{y=0} \tag{4.19g}$$

Here $j = 1,\ e_1 = 0,\ f_1 = 1$ for fluid 1 and $j = 2,\ e_2 = -n,\ f_2 = 0$ for fluid 2.

On the LHS of the mechanical energy balance is the sum of the disturbance kinetic energy of the two fluids. This term is positive when a finite Re flow is unstable. On the RHS are six different work terms, which either produce kinetic energy or consume it. $\sum_{j=1}^{2} REY_j$ is the total energy transfered from the base state to the disturbance flow by Reynolds stresses. This term becomes important only at relatively high Re. The next term, $\sum_{j=1}^{2} DIS_j$ is always negative (cf. (4.19c)) and represents viscous dissipation. The other four terms correspond to work done by stresses at the interface. NOR represents the contribution from normal Capillary forces while TAN_μ is associated with the viscosity difference between the fluids. When the viscosities are unequal, $\widehat{u}_2 \neq \widehat{u}_1$ (cf. (4.17b)) and this term can transfer energy to the disturbance flow. It is responsible for the viscosity-induced instability (Yih, 1967; Boomkamp and Miesen, 1996), that occurs at small but finite Re. The last two terms are associated with Marangoni stresses due to a non-uniform distribution of soluble surfactant at the interface. MAS_I accounts for concentration variations caused by interface deformation when the base concentra-

tion field varies in the transverse direction. The transverse concentration gradient causes the crest and trough of a deformed interface to have different solute concentrations, and hence different values of interfacial tension. The second Marangoni stress term - MAS_F - is caused by concentration perturbations associated with the disturbance flow. This term will be present even if the interface is flat. These two mechanisms were identified by Goussis and Kelly (1990) in the context of thermocapillary instability of a flowing heated liquid film.

Analogous to the mechanical energy equation (4.18), we derive a balance equation for a concentration energy functional in each fluid, defined as $(\widehat{c}_j)^2/2$. Because the kinetic energy is identically zero in creeping flow ($KE_j = 0$), the presence of an instability cannot be detected from the mechanical energy equation. Instead the growth of the concentration energy functional can be used to identify an instability. In addition, this equation provides insight into the growth of concentration perturbations.

This equation is derived by multiplying the linearized solute balance with $\widehat{c}_j$, integrating across the fluids and averaging over one axial wavelength $\lambda = 2\pi/\alpha$ and one time period $T = 2\pi/(\alpha\omega_R)$. Using the Gauss divergence theorem, we obtain:

$$\sum_{j=1}^{2} E_j^c = \sum_{j=1}^{2} DIF_j + \sum_{j=1}^{2} CONT_j + INT \tag{4.20}$$

where

$$E_j^c = \int_0^T dt \int_0^\lambda dx \int_{e_j}^{f_j} dy \left[\frac{d}{dt}\left(\frac{\widehat{c}_j^2}{2} \right) \right] \tag{4.21a}$$

$$DIF_j = -\frac{D_{r,j}}{Pe} \int_0^T dt \int_0^\lambda dx \int_{e_j}^{f_j} dy \left[\widehat{c}_{j,x}^2 + \widehat{c}_{j,y}^2 \right] \tag{4.21b}$$

$$CONT_j = -\int_0^T dt \int_0^\lambda dx \int_{e_j}^{f_j} dy \left[\widehat{c}_j \widehat{v}_j \frac{d\overline{c}_j}{dy} \right] \tag{4.21c}$$

$$INT = -\frac{1}{Pe} \int_0^T dt \int_0^\lambda dx \left[(\widehat{c}_1 - \widehat{c}_2)\widehat{c}_{1,y} \right]_{y=0} \tag{4.21d}$$

The dynamics of the concentration energy functional is governed by the three terms on the RHS. DIF_j term is always negative (cf. (4.21b)) and represents the damping effect of diffusion. The other two terms can cause concentration disturbances to grow. $CONT_j$ is associated with bulk convection effects in the transverse direction. This term contributes only in the presence of a finite base state concentration gradient ($d\overline{c}_j/dy \neq 0$). INT is associated with a jump in the disturbance concentration across the interface, which occurs if the solute has a greater affinity for one of the fluids ($K \neq 1$), or has a greater diffusivity in one of the fluids ($D_r \neq 1$), or both (cf. (4.17d) and (4.13b)).

These energy balance equations are used to get insight into the mechanism driving

an instability. The eigenfunctions, calculated by solving equations (4.16) and (4.17), are substituted into the energy equations. The terms with a large magnitude correspond to dominant effects. The sign of these terms show whether they are stabilizing (negative) or destabilizing (positive) influences. Therefore, identifying the largest positive work term in the energy equation helps to identify the source of the instability.

4.6 Longwave asymptotic analysis

In this section, we obtain a regular perturbation solution to the eigenvalue problem (4.16)-(4.17) in the limit of long waves ($\alpha \to 0$). In order to understand the interaction of inertial and Marangoni effects, we assume both Re and Ma to be $O(1)$. Other parameters $(m, n, k, D_r, Ca, Pe, \gamma)$ are also assumed to be $O(1)$. The solution procedure is similar to that used by Yih (1967) and Yiantsios and Higgins (1988). The dependent variables ψ_j, c_j and the eigenvalue ω are expanded as power series in α and substituted into (4.16)-(4.17). Equating terms of $O(1)$, we obtain a simplified eigenvalue problem whose solution is the zeroth order approximation to ω, ψ_j and c_j. At first order in α, an inhomogeneous linear problem is obtained, which has a solution only if the inhomogeneity has no component along the eigenvector of the zeroth order problem. Enforcing this solvability condition provides an equation for the $O(\alpha)$ correction to ω (cf. Chapter 1 of Hinch (1991)). This calculation result in the following asymptotic expression for $\alpha\omega$:

$$\begin{aligned}\alpha\omega = \alpha\Bigg[1 + \frac{2n(m-1)(m-n^2)}{m^2+4mn+6mn^2+4mn^3+n^4}\Bigg] \\ +\mathrm{i}\alpha^2\Bigg[\frac{Ma}{Pe}\frac{D_rKn^2(n+1)(n^2-m)(1-\gamma K)}{2(D_r+Kn)^2(m^2+4mn+6mn^2+4mn^3+n^4)} \\ -Re\frac{(n^2-m)(m-1)G(n,m)}{420m^2(1+n)^2(m^2+4mn+6mn^2+4mn^3+n^4)^3}\Bigg] + O(\alpha^3)\end{aligned} \tag{4.22}$$

The speed of a travelling wave mode of wavelength α is given by ω_r while its growth rate is given by $\alpha\omega_i$ (the imaginary part of (4.22)). The growth rate consists of two terms: the first is due to Marangoni effects while the second accounts for the viscosity induced mode that is active at non-zero Re. The latter term is the same as that obtained by Yiantsios and Higgins (1988) (verified by reproducing Fig. 2a of their paper). The expression for $G(n, m)$ is given in Appendix E.2. Numerical evaluation shows this function to be positive definite over a wide range of n and m, spanning $(10^{-4}, 10^4)$ in both parameters.

Let us first focus on the case of creeping flow ($Re = 0$) wherein only Marangoni effects are important. From (4.22) it is clear that long waves become unstable when

$n^2 > m$, provided mass transfer occurs from fluid 1 to fluid 2 ($\gamma < 1/K$) and interfacial tension decreases with increasing solute concentration ($Ma > 0$, i.e. $\beta > 0$). The magnitude of the growth rate is seen to increase with the sensitivity of interfacial tension to surfactant concentration (i.e. increases with Ma) and with the applied concentration difference across the plates ($1 - \gamma K$).

Switching the direction of mass transfer (i.e. having $\gamma > 1/K$) inverts the condition for long wave instability to $n^2 < m$. Thus for a given pair of fluids and thickness ratio, the direction of mass transfer decides whether a long wave instability is present or not. This relation between long wave instability and the direction of mass transfer will reverse in case the soluble surfactant has the relatively uncommon property of increasing interfacial tension by its presence at the interface ($Ma < 0$) (Harkins and Humphery, 1916; Evans, 1937; Wang and Anderko, 2013). In the remainder of this work, we assume that mass transfer occurs from phase 1 to phase 2 ($\gamma < 1/K$) and that $Ma > 0$.

In case of the thermocapillary problem, interfacial tension always decreases with increasing temperature ($Ma > 0$). Consequently, long waves will be unstable when $n^2 > m$, provided plate 1 is hotter than plate 2.

Some insight into the role of the diffusivity ratio D_r is provided by (4.22). D_r is seen to effect only the magnitude of the growth rate, but not its sign. Therefore, it plays no role in the condition for instability. This is in contrast to the case of solutal Marangoni instability in *stationary* fluid layers, wherein the system can be unstable if mass transfer occurs from the fluid of lower diffusivity to that of the higher, even though the viscosity and thickness ratios are unity ($n^2 = m = 1$) (Sternling and Scriven, 1959; Schwarzenberger *et al.*, 2014).

The maximum growth rate occurs at $D_r = Kn$. These properties correspond to a base state concentration profile in which the interface concentration is a weighted mean of the wall concentrations: $\bar{c_1}(0) = K\bar{c_2}(0)) = (C_{10} + KC_{20})/2$. In the thermocapillary problem, $K = 1$ and the base state interface temperature for maximum instability is the arithmetic mean of the wall temperatures.

When Re is non-zero, the growth rate is affected by the presence of the viscosity-induced mode that is associated with a discontinuity of the slope of the base state velocity profile at the interface (Yiantsios and Higgins, 1988; Boomkamp and Miesen, 1996). This discontinuity occurs when the viscosities are unequal ($m \neq 1$), provided the shear rate is non-zero at the interface ($n^2 \neq m$). Equation (4.22) shows that this mode can either counteract the longwave Marangoni instability or support it, depending on the viscosity ratio. For example, if $\gamma < 1/K$, $n^2 > m$ and $Ma > 0$, then the Marangoni instability is suppressed (enhanced) on increasing Re, provided $m > 1$ ($m < 1$). In such a case, the onset of long wave instability will occur only if Ma is increased beyond a non-zero critical value. This critical threshold will increase with Re. On the other hand, if $n^2 < m$

($m > 1$) then the viscosity induced mode will cause the growth rate to increase while Marangoni effects exert a stabilizing influence. A similar interaction between long wave Marangoni and viscosity-induced modes was identified in thermocapillary Couette flow by Wei (2006).

4.7 Numerical Solution

The eigenvalue problem ((4.16)-(4.17)) is solved numerically for arbitrary wavenumbers using the Chebyshev spectral collocation method described by Boomkamp *et al.* (1997). The dependent variables, ψ_j and c_j, are expressed as series expansions of Chebyshev polynomials. Equations for the coefficients of the expansions are obtained by collocation of the governing equations on the interior points of a Gauss-Lobatto grid. Boundary conditions are applied at the boundary nodes. The result is a generalized $(N \times N)$ matrix eigenvalue problem of the form $\mathbf{A}\mathbf{x} = \omega\mathbf{B}\mathbf{x}$. Here $\mathbf{x}$ is vector of N unknowns, which includes the $(N-1)/4$ coefficients in each Chebyshev polynomial expansion (for ψ_1, ψ_2, c_1 and c_2) and the amplitude of interface deformation (h). The matrix $\mathbf{B}$ is singular due to the presence of zero rows (M in number) arising from the boundary conditions that do not contain ω. Following Boomkamp *et al.* (1997), we use the corresponding M equations to solve for M unknown coefficients and replace them in the remaining $N - M$ equations. The result is a $(N - M) \times (N - M)$ generalized eigenvalue problem $\mathbf{A}'\mathbf{x}' = \omega\mathbf{B}'\mathbf{x}'$ in which $\mathbf{B}'$ is invertible. The eigenvalue spectrum is obtained using the QZ algorithm. To obtain ψ_j and c_j, the eigenvectors $\mathbf{x}'$ must be transformed back to $\mathbf{x}$.

The computation is simplified in case of creeping flow ($Re = 0$) because the momentum equations (4.16a) simplify to

$$(\mathcal{D}^2 - \alpha^2)^2\psi_j = 0, \quad \text{for } j = 1, 2 \tag{4.23}$$

These equations (4.23) can be solved analytically to yield:

$$\psi_1 = \theta_1 \cosh(\alpha y) + \theta_2 \sinh(\alpha y) + \theta_3 y \cosh(\alpha y) + \theta_4 y \sinh(\alpha y) \tag{4.24}$$

$$\psi_2 = \theta_6 \cosh(\alpha y) + \theta_7 \sinh(\alpha y) + \theta_8 y \cosh(\alpha y) + \theta_9 y \sinh(\alpha y) \tag{4.25}$$

where θ_j are arbitrary constants of integration. These expressions are substituted into the concentration equations (4.16b), which are solved by the aforementioned Chebyshev spectral method.

In the limit of $Ma \to 0$, the current system reduces to plane Poiseuille flow, the stability of which has been studied by Yiantsios and Higgins (1988). We have verified our numerical solution in this limit by comparing with their results. We have also compared

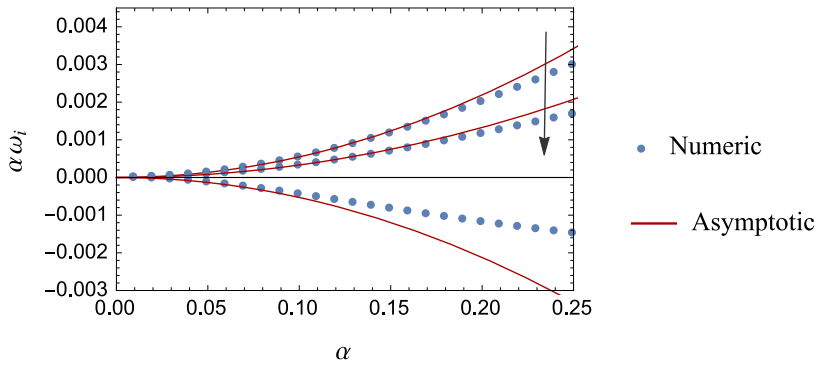

Figure 4.2: Comparison of the dispersion curve, obtained numerically using the spectral method, with the long wavelength asymptotic relation (4.22). Three cases, corresponding to Re = 0, 10, 50 are depicted. The arrow indicates the direction of increasing Re. Other parameter values: Ma = 10, Ca = 1, m = 1.5, n = 2, D_r = 0.5, K = 0.5, Pe = 2, γ = 0.5.

our numerical predictions with the long wave asymptotic expansion (4.22). The two are in good agreement in the limit of small α, as shown in Fig. 4.2. In this figure the long wave Marangoni instability is stabilized as Re is increased. This is in accordance with the prediction of (4.22) for the case of $n^2 > m$ and $m > 1$.

4.8 Instabilities in creeping flow: Long wave and short wave modes

From this section onwards, we analyze the stability of the system to perturbations of all wavelengths, using the spectral collocation method. The range of values for Ma and Pe selected for numerical calculations are appropriate to layered microchannel flows. In microchannels with dimensions of 50-200 μm, the flow rates of layered flow ranges from 20-150 μL/min (Hotokezaka *et al.*, 2005; Znidarsic-Plazl and Plazl, 2007; Fries *et al.*, 2008). Considering typical values of solute diffusivity of $O(10^{-9})$ m^2/s and liquid viscosity of $O(10^{-3})$ Pa s, we obtain Pe of $O(10^3)$ to $O(10^4)$. The magnitude of the variation of interfacial tension with concentration ($\sigma_0\beta$) is typically of $O(10^{-6})$ Nm^2/mol (Sternling and Scriven, 1959). This results in Ma of $O(10^3) - O(10^4)$. The value of Ca is varied over a wide range to uncover all instability modes of the system and understand their behaviour. Ca in microchannels however is rather small, of $O(10^{-3}) - O(10^{-1})$.

Re for layered microchannel flows ranges from $O(1) - O(10)$, which is small, but not negligible. Nevertheless, we first analyse the case of creeping flow ($Re = 0$), wherein Marangoni effects are the only source of instability. After understanding the pure Marangoni instabilities, the influence of small but finite Re is examined. We begin in this section by identifying different types of Marangoni instability modes, in the limit of creeping flow, and study their characteristic features.

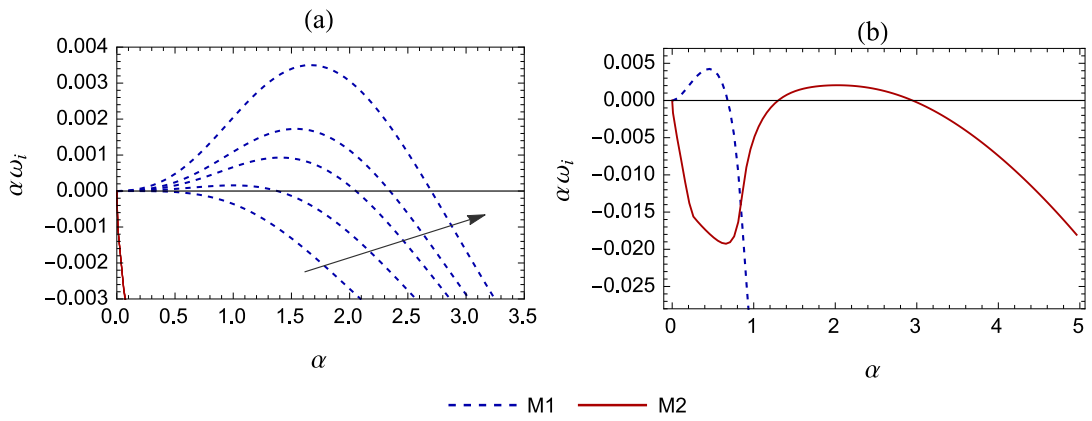

Figure 4.3: Dispersion curves for the case of $n^2 > m$, wherein long waves are unstable (a) Mode M1 manifests as a long wave instability. Dispersion curves are shown for a series of Marangoni numbers: 1, 1372.652, 3372.652, 5372.652, 11372.652. The arrow indicates the direction of increasing Ma. Other parameter values: Ca = 100, m = 1.5, n = 1.24, D_r = 0.5, K = 0.5, Pe = 2000, γ = 0.5. (b) Simultaneous instability of M1 long waves and M2 short waves. Parameter values: Ma = 10000, Ca = 1, m = 0.9, n = 1.3, D_r = 0.5, K = 1.2, Pe = 1000, γ = 0.

The numerical solution of the linear stability equations (4.16) & (4.17) yields a spectrum of eigenvalues for each wavenumber α. Of these, only two eigenvalues that have the largest and second largest imaginary parts play a role in deciding the system's stability. As α is varied these two eigenvalues trace out separate dispersion curves, which we label M1 and M2. Depending on parameter values, these two branches of eigenvalues can attain positive growth rates and render the system unstable. The real parts of the eigenvalues are always non-zero indicating that all modes have the form of travelling waves.

The asymptotic analysis for $\alpha \to 0$ in Sec. 4.6 (cf. (4.22)) revealed that the system is unstable for small α when $n^2 > m$ (provided mass transfer occurs from plate 1 to 2 or $\gamma < 1/K$). Dispersion curves for such a case are plotted in Fig. 4.3a. Five different values of Ma are considered in this figure. The M1 branch is seen to be unstable for a range of wavenumbers that extend from zero to some positive wavenumber α_0. As Ma is decreased to zero, the range of unstable wavenumbers shrinks and $\alpha_0 \to 0$. Based on these features, this mode is termed a *long wave* (LW) instability. In this figure, the M2 branch is seen to be stable for all α. This indicates that the long wave analysis of Sec. 4.6 only describes the asymptotic behavior of the M1 branch of eigenvalues and not the M2 branch.

In all our numerical calculations, the M2 branch is found to be stable for α near zero. On the other hand, it can become unstable for a range of relatively large wavenumbers that are bounded away from zero. Such a case is shown in Fig. 4.3b. In this figure, the M1 mode is unstable to long waves, while the M2 mode is unstable to *short waves* (SW).

Next, we consider the case of $n^2 < m$, for which the system is stable to long waves

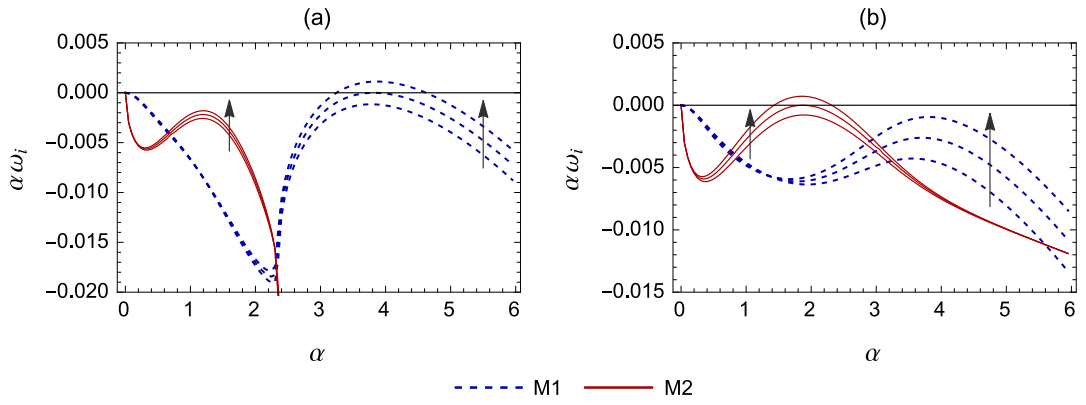

Figure 4.4: Two instability modes M1 and M2 manifest as short wave instabilities beyond a critical Marangoni number. (a) Mode M1 becomes unstable; $Ca = 10$, $Ma = 11631.21, 12231.21, 12831.21$. (b) Mode M2 becomes unstable; $Ca = 100$, $Ma = 9932.65, 10832.65, 11732.65$. Other parameter values: $m = 1.5$, $n = 1$, $D_r = 0.5$, $K = 0.5$, $Pe = 2000$, $\gamma = 0.5$. The arrow indicates the direction of increasing Ma.

($\alpha \to 0$), according to the asymptotic analysis (cf. (4.22)). In this case, only SW modes can become unstable. They can originate from either the M1 branch or the M2 branch, provided Ma is sufficiently large. Fig. 4.4a depicts a case in which the system just becomes unstable to M1 short waves, as Ma is increased. Fig. 4.4b shows the alternate case, wherein M2 short waves become unstable. As is apparent in both figures, SW modes become unstable only when Ma is increased beyond a positive critical value. Beyond this value, a range of wavenumbers, bounded away from zero, become unstable. Typically, the range of unstable wavenumbers grows as Ma is increased, as seen in Fig. 4.4.

In Figs. 4.4a and 4.4b, only one short wave mode is unstable in each case. However, the other short wave is not far from being unstable. In fact, if Ma is increased to larger values, then both short wave modes can become unstable simultaneously. An example of this is shown in Fig. 4.5a. The parameters here are the same as Fig. 4.4b, except that Ma is larger.

The dispersion curves plotted in Figs. 4.4a, 4.4b and 4.5a are useful for distinguishing the type of instability mode and for comparing their relative growth rates when Ma is super-critical. However, the condition for stability of the system is more concisely represented by a neutral stability diagram. Fig. 4.5b depicts such a diagram for the case studied in Figs. 4.4b and 4.5a. This figure is obtained by determining the value of Ma at which the growth rate of the largest eigenvalue is zero (called the marginal Marangoni number Ma_m), as a function of the wavenumber. The system is stable below this curve and unstable above it. The curve has two local minima, corresponding to the two short wave modes. The global minima of Ma_m is the critical Marangoni number (Ma_c), above which the system first becomes unstable. In Fig. 4.5b, $Ma_c = 10832.65$ and corresponds to the M2-SW mode. This implies that the M2-SW is critical at the onset of instability (as seen in Fig. 4.4b). Ma must be increased to supercritical values beyond 12500 for

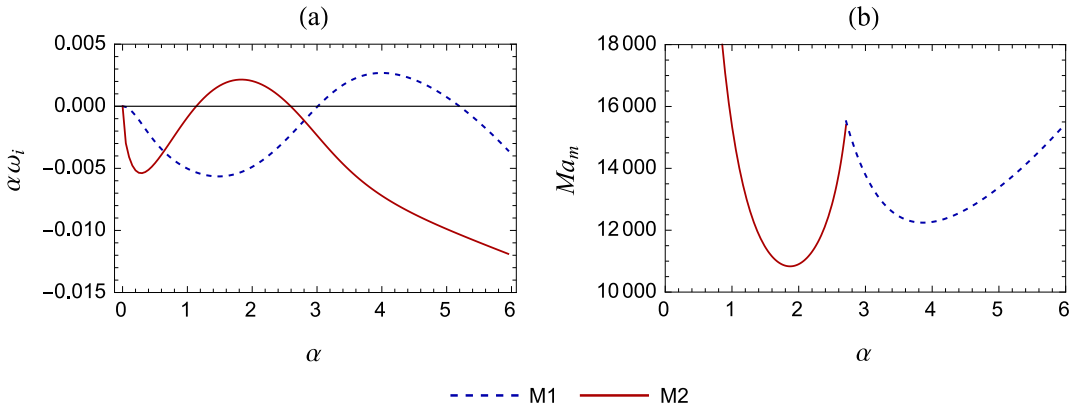

Figure 4.5: (a) Dispersion curve showing instability to both short wave modes simultaneously (Ma = 13732.65). (b) Neutral stability curve. Parameter values are given in the caption of Fig. 4.4b.

the M1-SW to become unstable as well.

The two short wave instability modes (Fig. 4.4) differ from the long wave instability (Fig. 4.3) not only in the qualitative nature of their dispersion curves, but also in their mechanical energy budgets. Tab. 4.1 presents the energy analysis for a long wave mode from Fig. 4.3 (corresponding to the fastest growing mode at $Ma = 3732.652$), the critical M1-SW mode from Fig. 4.4a and the critical M2-SW mode from Fig. 4.4b. In all cases, dissipation due to viscous forces is balanced primarily by Marangoni stress terms, affirming the fundamental association of these instabilities with solutal Marangoni forces. However, in case of long waves, MAS_I is the dominant positive work term, whereas MAS_F is the dominant positive term for both SW modes. Thus, the long wave instability is caused by concentration variations due to a deforming interface while the short wave instabilities are caused by concentration perturbations associated with the disturbance flow.

In summary, the system is susceptible to three different types of instability modes in the creeping flow limit: M1 long waves and M1 and M2 short waves. The M1 branch exhibits long waves if $n^2 > m$, and short waves otherwise. The M2 branch on the other hand only exhibits a short wave instability. However, these short wave modes can become unstable at any value of m and n, if Ma is increased sufficiently (cf. Fig. 4.3b for $n^2 > m$ and Fig. 4.4b for $n^2 < m$).

Long and short wave creeping flow instabilities also occur in the presence of an insoluble surfactant that is restricted to the inter-fluid interface (Halpern and Frenkel, 2003). However, only two instability modes are present in that case – one long wave and one short wave. Both modes belong to the same branch of eigenvalues. The dynamics are therefore richer in the present case of a soluble surfactant. The additional short wave mode from the M2 branch introduces the possibility of instability to long and short wave

Mode	α	Ma	$\sum_{j=1}^{2} DIS_j$	NOR	TAN_μ	MAS_I	MAS_F
M1-LW	1.410	3732.652	-1	-3.30×10^{-4}	-3.94×10^{-3}	1.137	-0.132
M1-SW	3.800	12231.212	-1	-1.50×10^{-12}	-7.9×10^{-4}	-0.031	1.032
M2-SW	1.851	10832.652	-1	-1.66×10^{-8}	0.105	-0.077	0.973

Table 4.1: Mechanical energy budget for LW and SW modes in Figs. 4.3 and 4.4. The values have been normalized by the magnitude of total dissipation $\sum_{j=1}^{2} DIS_j$. The LW and SW have different energy signatures with the dominant positive work term being the MAS_I in case of long waves and MAS_F in case of short waves. KE_i and REY_i are identically zero in the creeping flow limit. Parameter values are as given in the captions of Figs. 4.3 and 4.4.

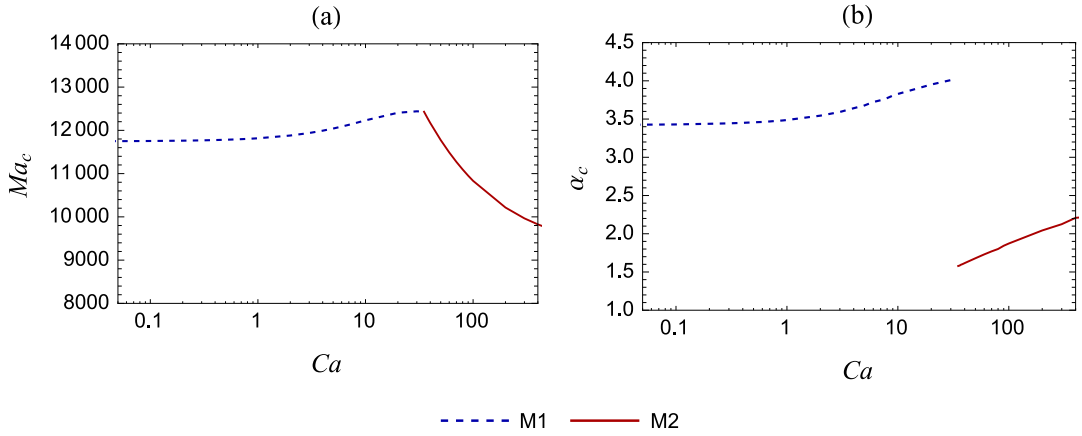

Figure 4.6: Switching between short wave modes M1 and M2 as Ca is varied. (a) Plot of the critical Marangoni number (Ma_c) (b) Plot of the critical wave number (α_c). Parameter values: n = 1, m = 1.5, D_r = 0.5, K = 0.5, Pe = 2000, γ = 0.5.

modes simultaneously (eg. Fig. 4.3b). Such a scenario is not observed when the surfactant is insoluble.

4.9 Switching between short wave modes

In this section, we focus on the M1 and M2 short wave modes, which can be simultaneously unstable when $n^2 < m$. Fig. 4.4 in Sec. 4.8 demonstrated that the M1-SW mode is critical for small Ca while the M2-SW mode is critical for large Ca ($\mu U_0/\sigma_0$). To study the transition of the critical mode with Ca, we plot the critical Marangoni number (Ma_c), at which the system first becomes unstable, and the wavenumber of the corresponding critical mode (α_c) as a function of Ca in Fig. 4.6. Here, the critical mode is seen to switch from the M1-SW mode to the M2-SW mode as Ca is increased. At the transition point, located at $Ca = 35$, both modes are critical, as shown in Fig. 4.7. Across this point there is a jump in the critical wavenumber (cf. Fig. 4.6b). This point is a codimension-two bifurcation point at which the nature of the mode at the onset of instability changes abruptly.

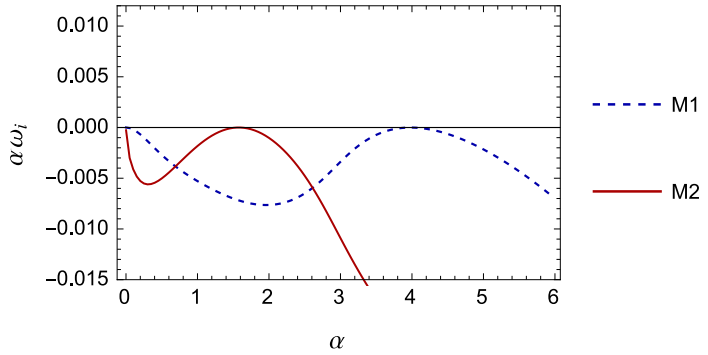

Figure 4.7: Dispersion curves at the bi-critical point corresponding to the transition from critical M1-SW modes to critical M2-SW modes (codimension two bifurcation point). Parameter values: m = 1.5, n = 1, Ca = 35, Ma = 12430.34, K = 0.5, Pe = 2000, γ = 0.5.

The transition between modes is caused by the significantly different effects of Ca on these modes, as demonstrated by Fig. 4.6. Decreasing Ca strongly stabilizes the M2-SW mode while it has only a weak influence on the M1-SW mode. In fact, as $Ca \to 0$, the M1-SW mode becomes invariant to Ca. Since large values of interfacial tension (small Ca) prevent interface deformation, Fig. 4.6 suggests that interfacial deformation plays an important role in the M2-SW mode but not in the M1-SW mode.

To verify this hypothesis, an energy budget analysis of the critical modes is carried out for each value of Ca in Fig. 4.6. The results are depicted in Figs. 4.8a and 4.8b, for the M1-SW and M2-SW critical modes respectively. The dissipation is primarily balanced by the MAS_F term, which is characteristic of both SW modes (cf. Sec. 4.8). The contribution from NOR is also insignificant in both cases. The key difference between the two modes lies in the contributions of MAS_I and TAN_μ, which are non-zero only when the interface deforms. In case of the M1-SW mode, both terms are insignificantly small. On the other hand, their values are finite for the M2-SW mode, and grow larger as the transition point $Ca = 35$ is approached. These results imply that interfacial deformation is significant in the M2-SW instability mode, but not in the M1-SW mode. Consequently, on increasing interfacial tension, the M2-SW mode is stabilized as interface deformation is suppressed, whereas the M1-SW mode remains unstable.

This difference between the two modes is explained by the impact of the disturbance flow on the motion of the interface. Each instability mode introduces vertical fluid motion, which exerts a net viscous normal stress on the interface. This is given by $2\big(v_{1,y} - m v_{2,y}\big)|_{y=0}$, to leading order. To check whether this stress supports or counteracts interface deformation, the phase difference ($\Delta\phi$) between the viscous normal stress and the velocity of the interface ($\widehat{\eta}_t$) is computed for both modes. For the case wherein both modes are critical (depicted in Fig. 4.7), we find that the viscous normal stress is almost out-of-phase with interface velocity, in case of the the critical M1-SW mode ($\Delta\phi = 0.79\pi$), but nearly in-phase in case of the critical M2-SW mode ($\Delta\phi = 0.10\pi$).

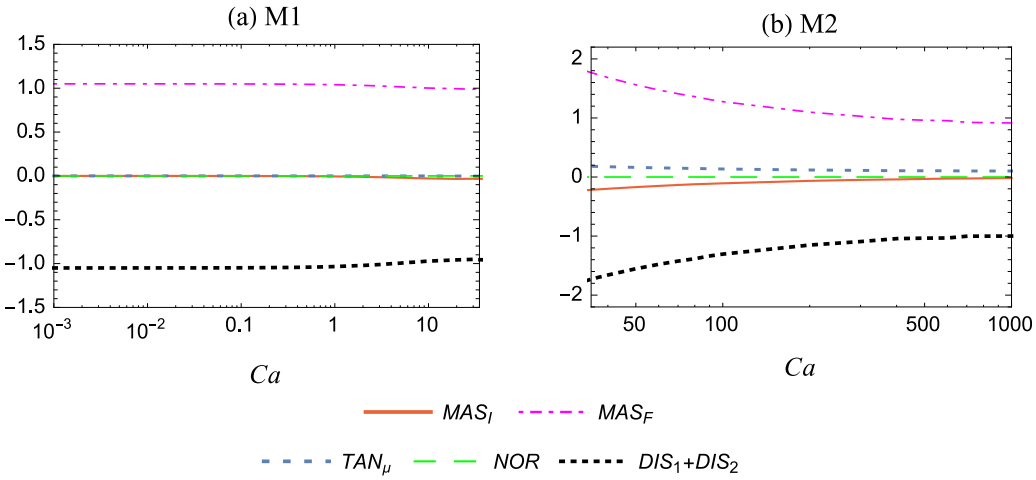

Figure 4.8: Energy budget of the critical M1 and M2 short wave modes plotted in Fig. 4.6 and Fig. 4.10b as a function of Ca. The REY_i terms are identically zero because $Re = 0$. Parameter values: n = 1, m = 1.5, D_r = 0.5, K = 0.5, Pe = 2000, γ = 0.5.

The corresponding plots of normalized viscous stress and interface velocity are presented in Fig. 4.9. This result implies that the disturbance flow of the M1-SW mode *counteracts* interface deformation by exerting a downward stress on the interface, at locations where it is rising. In contrast, the disturbance flow of the M2-SW mode *supports* interface deformation by exerting an *upward* stress at positions where the interface is rising. Therefore, the M1-SW mode manifests without significant interface deformation, while the M2-SW mode is associated with a deforming interface.

As a final point in this section, we note that the codimension two bifurcation between the short wave modes is affected by other parameter values. As an example, the influence of Pe (d_1U_0/D_1) is demonstrated in Fig. 4.10. As Pe is increased, the switching point shifts to larger values of Ca. This implies that increasing the diffusivity of the solute (decreasing Pe) increases the range of criticality of the M2-SW mode. This occurs because diffusion has a stronger stabilizing effect on the M1-SW mode due to its significantly higher wavenumber (Fig. 4.6b). A large wavenumber disturbance has rapid streamwise variations in concentration that are damped out more quickly by diffusion.

4.10 Transition from short to long waves

In Sec. 4.8, it was shown that the M1 branch of eigenvalues gives rise to a long wave instability when $n^2 > m$ and a short wave instability when $n^2 < m$. In this section we examine, via numerical calculations, the transition from short to long waves as n is increased beyond $\sqrt{m}$. We consider two examples, one for a viscosity ratio less than unity and the other for a value larger than unity.

Fig. 4.11 illustrates the transition for a case of $m = 1.5$. The critical value of the

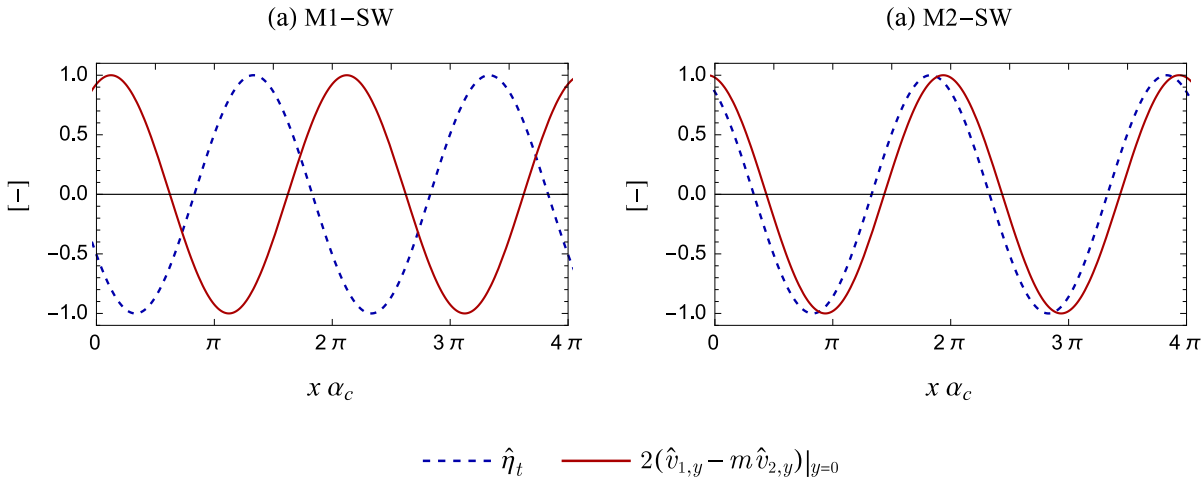

Figure 4.9: Variation of normalized viscous normal stress along the interface, plotted along with the normalized local velocity of the interface. (a) critical M1-SW mode (b) critical M2-SW mode. Viscous stresses exerted by the disturbance flow are seen to suppress interface motion in case of the M1-SW mode, but promote interface motion in case of the M2-SW mode. Parameter values are same as Fig. 4.7, which corresponds to the co-dimension two bifurcation between M1-SW and M2-SW modes.

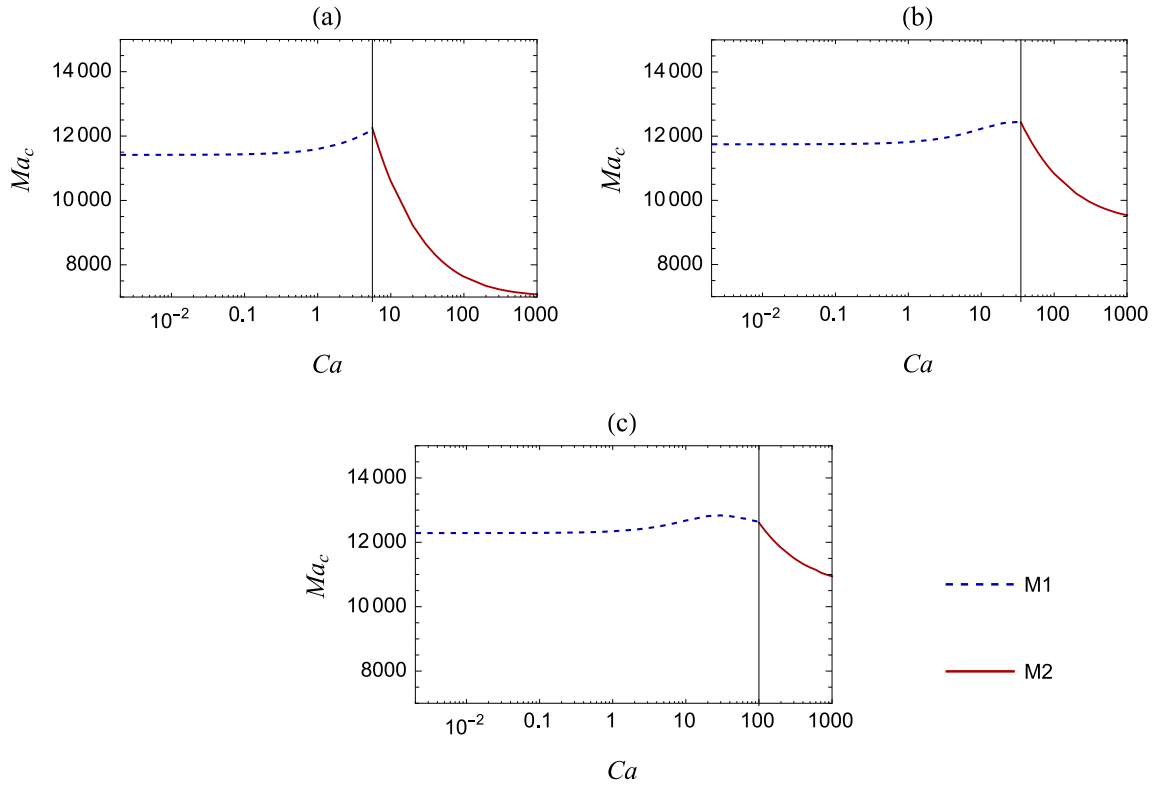

Figure 4.10: Effect of Pe on mode-switching between short wave M1 and M2 modes. (a) Pe = 1000 (b) Pe = 2000 (c) Pe = 2500 Parameter values: n = 1, m = 1.5, D_r = 0.5, K = 0.5, Pe = 2000, γ = 0.5.

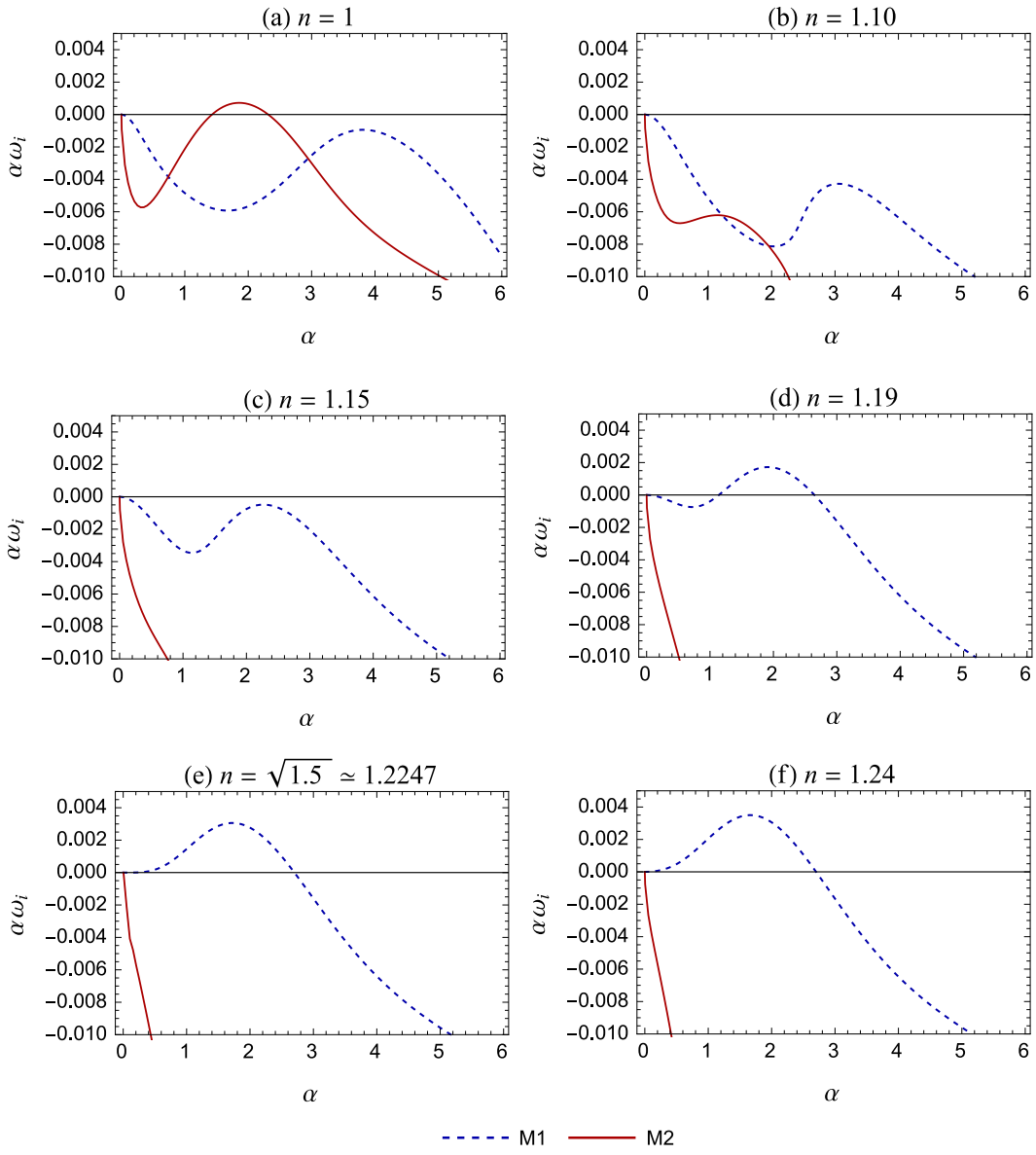

Figure 4.11: Transition from a short wave to long wave instability as n is increased beyond $\sqrt{m}$. Parameter values: m = 1.5, Ca = 100, Ma = 11732.65, D_r = 0.5, K = 0.5, Pe = 2000, γ = 0.5.

thickness ratio is $n = \sqrt{1.5} \approx 1.2247$. Six values of n from 1 to 1.24 are chosen to illustrate the transition. A sufficiently large Capillary number ($Ca = 100$) is chosen so that the M2 mode is unstable at the smallest of the selected values of n (Fig. 4.11a). The value of Ma is fixed at 11732.65 for all cases.

As n increases, with Ma constant, the M2-SW mode is strongly stabilized. The M1-SW mode is also stabilized initially (Fig. 4.11b), but is destabilized again as n is increased further (Fig. 4.11c). Simultaneously, the local maximum growth rate shifts towards longer wavelengths. At $n = 1.19$ (Fig. 4.11d) the M1 branch becomes unstable again. This mode is also of the short wave kind, but has significantly larger wavelengths than the M1-SW mode seen at $n = 1$ (cf. Fig. 4.11a). As n is increased further, the range of unstable wavenumbers of the M1 branch move closer to zero until it becomes a long

n	α	NOR	TAN_μ	MAS_I	MAS_F	$\sum_{j=1}^{2} E_j^c$
1.00	3.805	3.09×10^{-7}	-6.74×10^{-3}	-0.0213	1.0280	-0.023
1.19	1.905	-8.70×10^{-5}	5.77×10^{-3}	1.258	-0.264	0.126
1.24	1.655	-2.80×10^{-4}	3.71×10^{-3}	1.576	-0.572	0.354

Table 4.2: Energy budget for M1 short and long wave modes corresponding to the local maxima of the M1 dispersion curves in Figs. 4.11(a), 4.11(d) and 4.11(f). The mechanical energy terms have been normalized by the magnitude of total viscous dissipation, such that $\sum_{j=1}^{2} DIS_j = -1$. KE_i and REY_i are identically zero in the creeping flow limit. The stability/instability of the modes can be inferred from the evolution of the concentration energy functional $\sum_{j=1}^{2} E_j^c$. These terms have been normalized by the total amount of diffusive damping, $\sum_{j=1}^{2} DIF_j = -1$. Parameter values are given in the caption of Fig. 4.11.

wave instability (Fig. 4.11f). At the transition ($n = \sqrt{m}$, Fig. 4.11e), the M1 dispersion curve attains zero slope at the origin $\alpha = 0$, in accordance with the asymptotic expression 4.22.

In Sec. 4.8 (Tab. 4.1), it was shown that the mechanical energy budget of long wave instabilities is dominated by MAS_I while that of the short waves is dominated by MAS_F. Hence the transition from short to long waves must be accompanied by a significant change in the energy budget. This is verified in Tab. 4.2, which presents the mechanical energy-work terms for the local maximum of the M1 dispersion curve at $n = 1, 1.19 \,\text{and}\, 1.24$. While MAS_F is the dominant positive term for the M1-SW mode ($n = 1$), it decreases as n is increased and becomes negative in the case of long waves ($n = 1.24$). Instead, MAS_I becomes the dominant positive term that balances dissipation.

Interestingly, Tab. 4.2 shows that the MAS_I term is already larger than the MAS_F term at $n = 1.19$, although the M1 dispersion curve still bears the qualitative characteristics of a short wave mode. This mode, which has a relatively longer wavelength than the M1-SW mode at $n = 1$, may thus be considered as a distinct intermediate wavelength instability mode. This intermediate mode occurs for a narrow band of n values that separate the M1 short waves from the M1 long waves.

An example of the short-long wave transition when $m < 1$ is depicted in Fig. 4.12. Due to the large value of the Capillary number $Ca = 100$, the M2-SW mode is strongly unstable at $n = 0.65$. Nevertheless, as n is increased the M2-SW mode is stabilized. The M1 branch of eigenvalues, which has negative growth rates across all α for $n = 0.65$, develops a long wave instability when n exceeds $\sqrt{0.5}$ ($= 0.707$).

This section has demonstrated how the short wave instability of the M1 branch transitions to a long wave instability, as n is increased beyond $\sqrt{m}$. The M2-SW mode is generally stabilized as n is increased, provided Ma is constant. If Ma is also increased

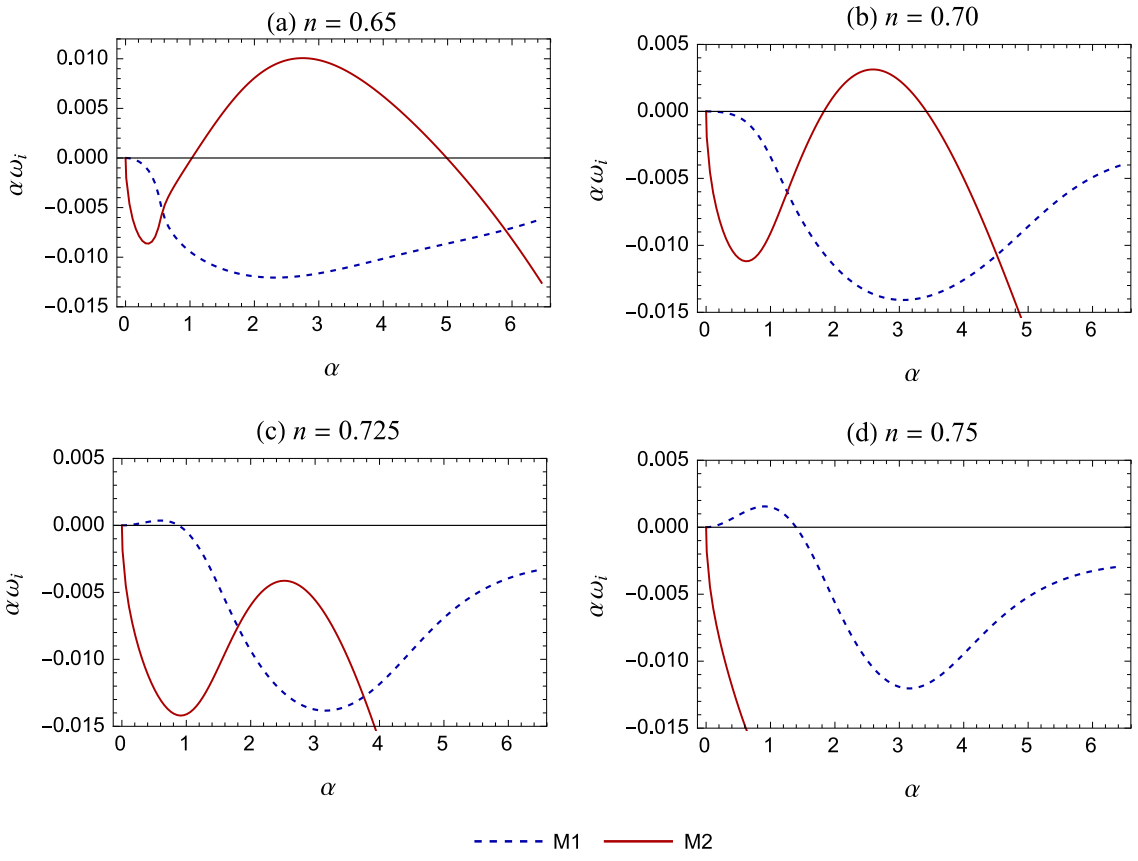

Figure 4.12: Transition from a short wave to long wave instability as n is increased beyond $\sqrt{m}$. Parameter values: $m = 0.5$, $Ca = 1000$, $Ma = 5000$, $D_r = 1$, $K = 1$, $Pe = 2000$, $\gamma = 0$.

sufficiently, then the M2-SW can remain unstable. In such a case, the system will be unstable to long and short waves simultaneously (as shown in Fig. 4.3b).

4.11 Necessity of a base state transverse concentration gradient

In this section, we investigate whether the mere presence of soluble surfactant at the interface is sufficient to cause a Marangoni instability, or whether a finite transverse concentration gradient is also required. The base state concentration field has a finite gradient if the plates are maintained at non-equilibrium concentrations ($\gamma \neq 1/K$). The long wave analysis, in Sec. 4.6, demonstrated that a finite concentration gradient is necessary for long wave Marangoni modes to be unstable. Here we check whether this remains a prerequisite for short wave Marangoni instability modes as well.

Figs. 4.13 and 4.14 demonstrate the stabilizing effect of decreasing the base concentration gradient. Each figure considers three cases, corresponding to $\gamma = 0,\ 0.5/K$, and $1/K$ (equilibrium). The parameter values in Fig. 4.13 are selected so that M1-SW and M2-SW modes are unstable in the presence of base state mass transfer ($\gamma = 0$). Fig. 4.14 corresponds to the case of unstable M1-LW and M2-SW. In both figures, the system is seen to become stable when the plates are maintained at equilibrium concentrations ($\gamma = 1/K$).

The necessity of a transverse base state concentration gradient for solutal Marangoni instability can be understood with the aid of the energy balance equations (cf. Sec. 4.5). In the mechanical energy balance (4.18), the terms contributing to the Marangoni instability are MAS_F and MAS_I. When the base state concentration gradient is zero ($d\bar{c}_j/dy = 0$), interface deformation does not generate concentration variations along the interface. Thus MAS_I is identically zero. MAS_F accounts for concentration perturbations $\widehat{c}_i$ that are coupled to the disturbance flow within the fluids. In the absence of a base state concentration gradient, convection by the disturbance flow is negligible in comparison with the stabilizing effects of diffusion and viscous dissipation. This is reflected by the vanishing of $CONT_j$ – the term that represents the contribution of convective effects to the growth of the concentration energy functional (cf. (4.20)). Thus both mechanisms for generating concentration variations along the interface are ruled out. This explains why a finite concentration gradient must exist across the phases for the solutal Marangoni instability to occur.

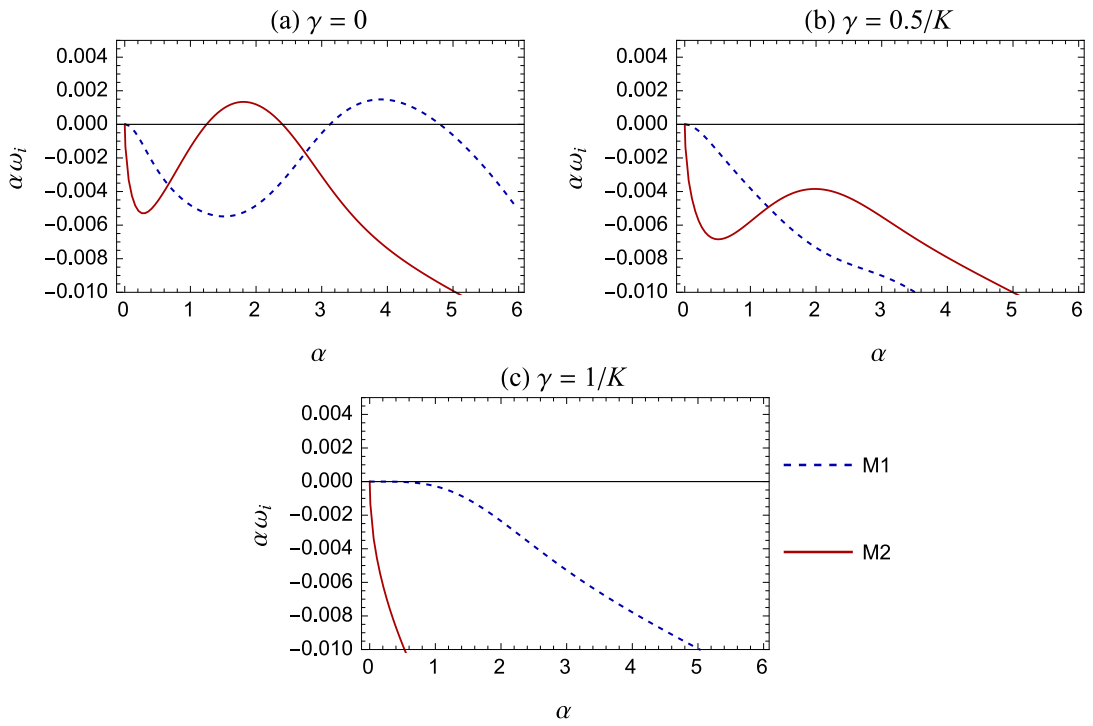

Figure 4.13: Effect of the inter-fluid flux on the short wave instability. Both M1 and M2 short waves are stabilized as the difference of the concentration at the walls from equilibrium is decreased. $\gamma = 1/K$ corresponds to a base state without inter-fluid flux, as the fluids are in equilibrium in this case and have non-varying concentration profiles. Parameter values: $m = 1.5$, $n = 1$, $Ca = 100$, $Ma = 10000$, $D_r = 0.5$, $K = 1.2$, $Pe = 2000$.

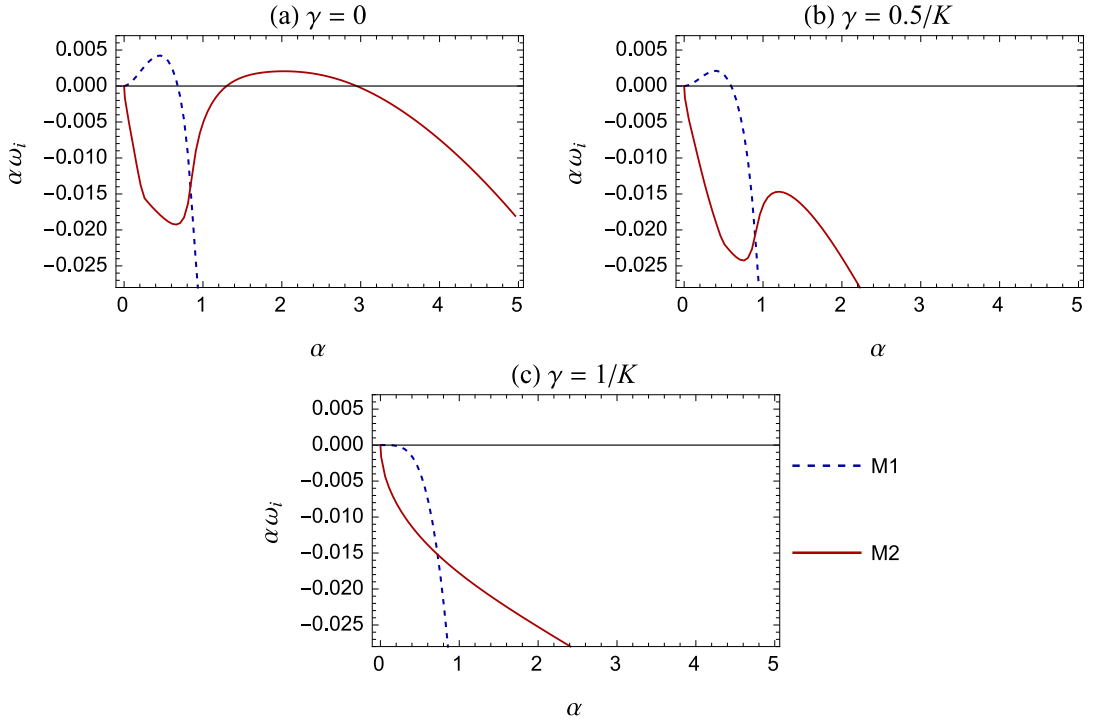

Figure 4.14: Effect of the inter-fluid flux on the long wave instability. The long wave M1 mode, as well as the M2 short wave mode, is stabilized as the difference of the concentration at the walls from equilibrium is decreased. $\gamma = 1/K$ corresponds to a base state without inter-fluid flux, as the fluids are in equilibrium in this case and have non-varying concentration profiles. Parameter values: $m = 0.9$, $n = 1.3$, $Ca = 1$, $Ma = 10000$, $D_r = 0.5$, $K = 1.2$, $Pe = 1000$.

4.12 Influence of finite inertia

Thus far we have focused on the creeping flow regime, wherein we have identified three distinct instability modes - two short waves and one long wave. In this section, we briefly consider the case of small but finite Re. A thorough analysis of the effects of inertia would merit a separate study. Here we discuss only a few specific cases, which illustrate the interplay of the viscosity-induced mode and the solutal Marangoni modes.

We pursue two different lines of inquiry. Firstly, we investigate the influence of inertia on the three Marangoni instability modes. Starting with an unstable creeping flow, the value of Re is increased and its effect on the three modes is observed. Secondly, we investigate the effect of introducing soluble surfactant into a system that is already unstable to the viscosity-induced mode. These two cases are considered separately in the following subsections.

4.12.1 Effect of inertia on the solutal Marangoni instability

In this subsection, the effect of inertia on the three solutal Marangoni modes is investigated for two examples: one for $n^2 < m$ and the other for $n^2 > m$.

The first case of $n^2 < m$ is depicted in Fig. 4.15. Here, creeping flow is unstable to short wave M1-SW and M2-SW modes ($n^2 < m$). In Figs. 4.15a - 4.15f, Re is increased sequentially from 0 to 40. The results for $Re = 1$ (Fig. 4.15b) are similar to the creeping flow case (Fig. 4.15a). However, increasing Re to 5 (Fig. 4.15c) significantly stabilizes both modes. The effect of further increasing Re differs for the two modes. The M2-SW mode becomes unstable again and its growth rate increases with Re. On the other hand, the M1-SW mode undergoes a transition to long waves as Re is increased beyond 10 (Figs. 4.15d - 4.15f). This behaviour is in accordance with the long wave asymptotic prediction (4.22) that inertia destabilizes long waves when $m > 1$ and $n^2 < m$.

Mechanical energy budget (cf. (4.18)) calculations for the local maximum of the M1 and M2 dispersion curves, corresponding to Figs. 4.15a and 4.15f is presented in Tab. 4.3. The dominant work term of the M1 mode changes from MAS_F to MAS_I in accordance with the transition from short waves to long waves. The energy budgets of the most unstable M2 mode for $Re = 0$ and $Re = 40$ are qualitatively the same (MAS_F is the dominant positive term). This confirms that the M2 short wave mode that is unstable at finite Re is qualitatively the same as the M2-SW mode observed in creeping flow.

Fig. 4.16 demonstrates the effect of inertia for a case of $n^2 > m$, wherein the long wave M1 mode and the M2-SW mode are unstable in the creeping flow limit (Fig. 4.16a). As Re is increased, the M2-SW mode is completely stabilized. The long wave M1 insta-

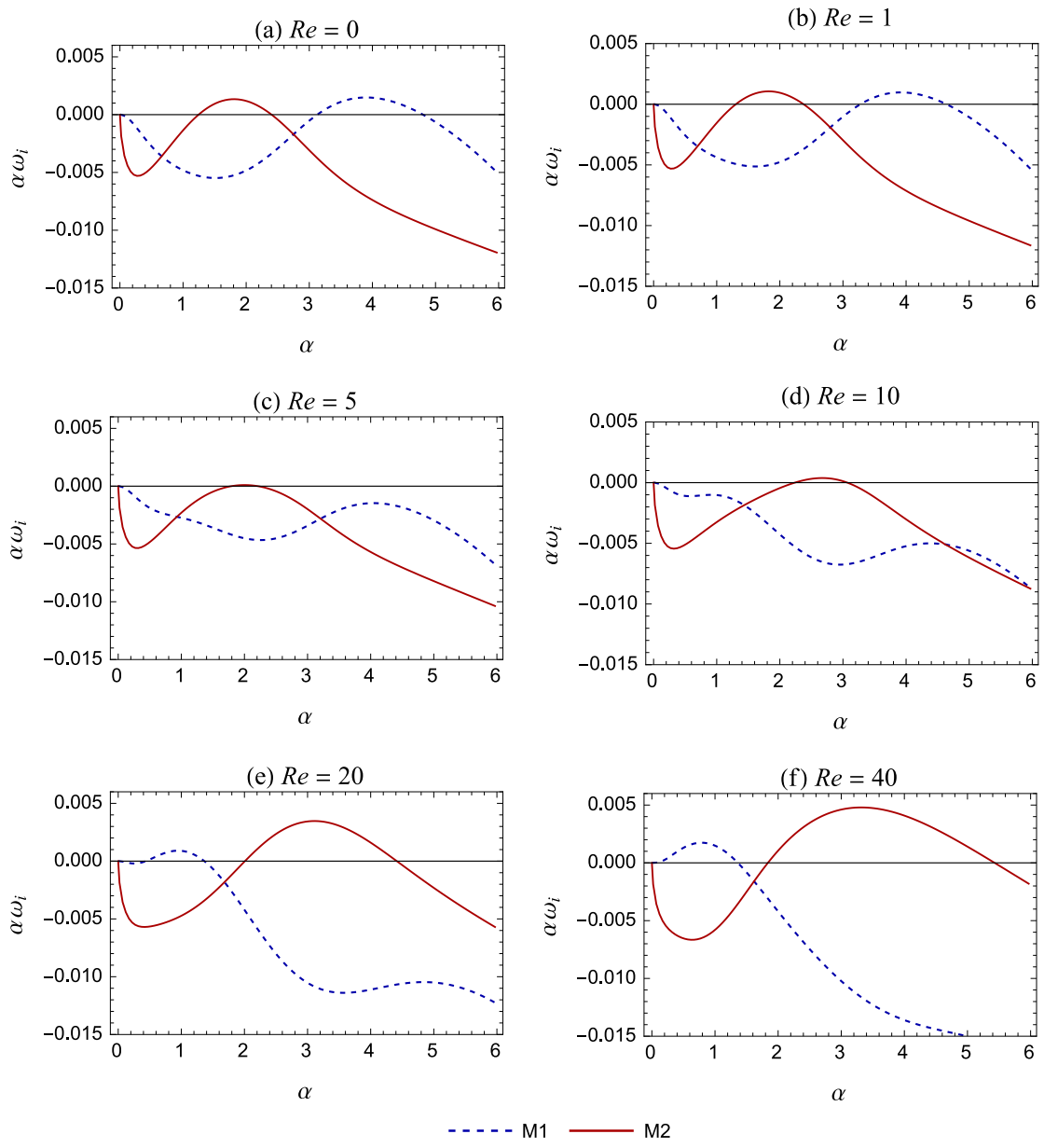

Figure 4.15: Effect of inertia on the solutal Marangoni instability when the M1 mode is short wave. Parameter values: Ma = 10000, m = 1.5, n = 1, Ca = 100, D_r = 0.5, K = 1.2, $\gamma = 0$, Pe = 2000.

Mode	Re	α	$\sum_{j=1}^{2} KE_j$	$\sum_{j=1}^{2} REY_j$	NOR	TAN_μ	MAS_I	MAS_F
M1	0	3.92	0	0	-2.4×10^{-7}	-4.62×10^{-3}	-0.011	1.016
M1	40	0.77	0.002	-0.029	-7.45×10^{-5}	-6.99×10^{-2}	0.730	0.371
M2	0	1.82	0	0	-3.29×10^{-5}	0.115	-0.108	0.994
M2	40	3.32	0.002	-0.024	-2.15×10^{-4}	0.108	0.090	0.828

Table 4.3: Energy budget for M1 and M2 modes corresponding to the local maxima of the dispersion curves in Figs. 4.15a and 4.15f. The values have been normalized by the magnitude of total dissipation so that $(DIS_1 + DIS_2) = -1$. Parameter values are given in the caption of Fig. 4.15.

Mode	Re	α	$\sum_{j=1}^{2} KE_j$	$\sum_{j=1}^{2} REY_j$	NOR	TAN_μ	MAS_I	MAS_F
M1	0	0.47	0	0	-0.014	-0.033	1.676	-0.629
M1	100	0.82	0.009	-0.029	-0.017	-0.037	1.552	-0.459

Table 4.4: Energy budget for long wave M1 modes corresponding to the local maxima of the dispersion curves in Figs. 4.16a and 4.16d. The values have been normalized by the magnitude of total dissipation so that $(DIS_1 + DIS_2) = -1$. Parameter values are given in the caption of Fig. 4.16.

bility, on the other hand, remains unstable. In fact, the growth rate is greater at $Re = 1$ than at creeping flow. This is in accordance with the prediction of the long wave expansion (4.22) for the parameter values of Fig. 4.16 ($n^2 > m$ and $m < 1$, cf. the figure caption). The effect of further increase in Re cannot be predicted by the asymptotic expansion, since it was derived for the case of Re being $O(1)$. Figs. 4.16c - 4.16d show that long wave M1 modes continue to remain unstable, as Re is increased to 100, without significant change in their growth rates. Even at $Re = 100$, these long wave modes are primarily driven by Marangoni stresses associated with interface deformation (MAS_I), as shown by the energy budget calculations presented in Tab. 4.4.

These two examples demonstrate that inertia affects the M1 and M2 Marangoni modes quite differently. Increasing Re can qualitatively modify the M1 branch of eigenvalues and cause a transition between M1 short waves and M1 long waves. This strong influence over the M1 branch is due to the fact that the viscosity-induced mode manifests itself through the M1 branch of eigenvalues. (When $Ma = 0$ and $Re \neq 0$, the unstable viscosity induced mode emerges as long waves on the M1 branch, as shown in Sec. 4.12.2.) On the other hand, increasing Re does not modify the basic qualitative features of the M2-SW mode. The effect on its growth rate, however, can be non-monotonic, causing intermediate stabilization of the system over a narrow range of Re as demonstrated by Fig. 4.15b - 4.15d.

4.12.2 Effect of soluble surfactant on the viscosity-induced instability at finite *Re*

In the absence of soluble surfactant effects ($Ma = 0$), a finite Re flow is unstable to the long wave viscosity-induced instability, provided $m > 1$ ($m < 1$) when $n^2 < m$ ($n^2 > m$) (cf. Sec. 4.6). In this section, we follow the changes in stability characteristics that occur on applying a transverse gradient of soluble surfactant. Two examples are studied in this section, corresponding to $n^2 < m$ (with $m > 1$) and $n^2 > m$ (with $m < 1$). Based on the preceding creeping flow analysis, the M1-SW Marangoni mode is expected to play a more significant role than the M1-LW mode in the first case, while

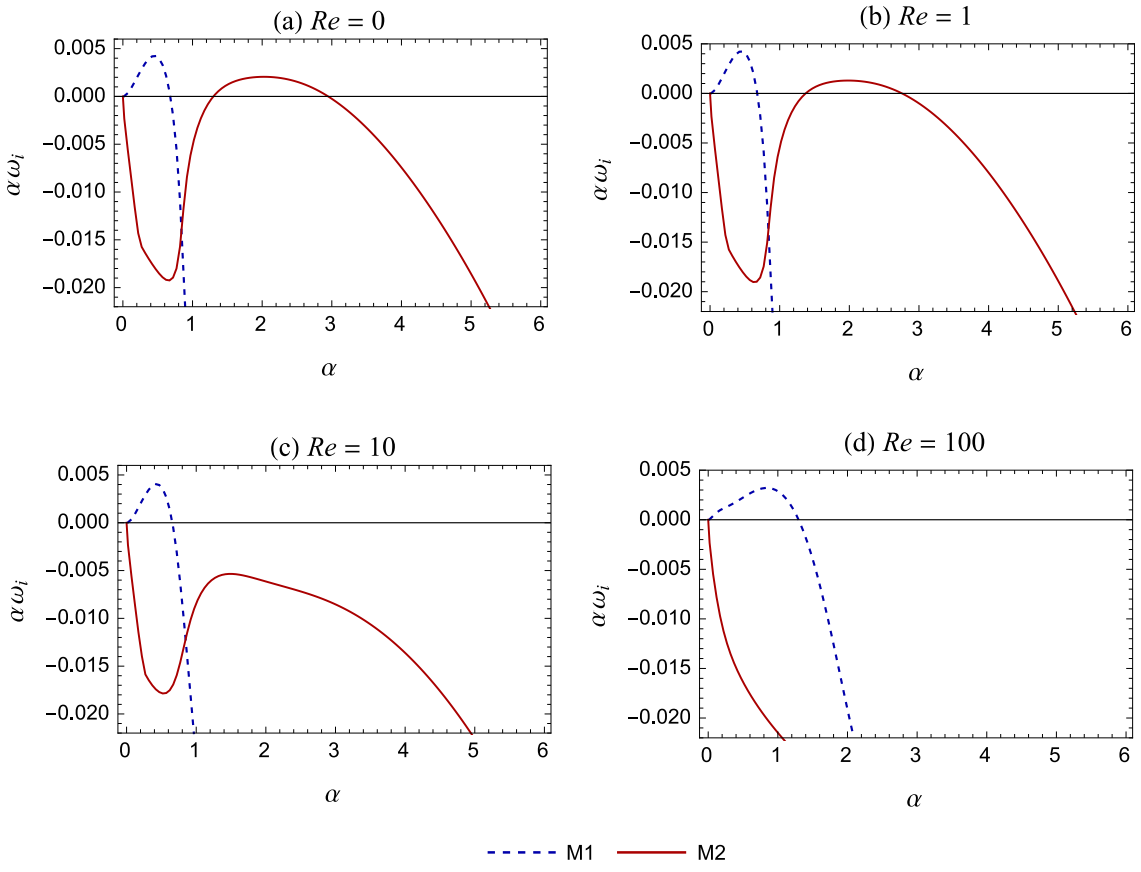

Figure 4.16: Effect of inertia on the solutal Marangoni instability when the M1 mode is long wave. Parameter values: Ma = 10000, m = 0.9, n = 1.3, Ca = 1, D_r = 0.5, K = 1.2, $\gamma = 0$, Pe = 1000.

Mode	Ma	α	$\sum_{j=1}^{2} KE_j$	$\sum_{j=1}^{2} REY_j$	NOR	TAN_μ	MAS_I	MAS_F
M1	0	0.92	1.51×10^{-3}	-7.51×10^{-3}	-1.63×10^{-3}	1.010	0	0
M1	13000	4.67	1.17×10^{-4}	-1.47×10^{-3}	-2.91×10^{-6}	1.19×10^{-3}	-0.182	1.182

Table 4.5: Energy budget showing the transition from the viscosity induced mode to the solutal Marangoni M1-SW mode. Calculations correspond to the fastest growing mode in Figs. 4.17a and 4.17e. The values have been normalized by the magnitude of total dissipation so that $(DIS_1 + DIS_2) = -1$. Parameter values are given in the caption of Fig. 4.17.

the opposite is true of the second case (cf. Sec. 4.8). The M2-SW mode could impact the flow in either case.

Fig. 4.17 corresponds to the case of $n^2 < m$. When $Ma = 0$ (Fig. 4.17a), the long wave viscosity-induced mode is unstable. The identity of this mode is confirmed by energy budget calculations, presented in Tab. 4.5, which show that the dominant work term is TAN_μ (Boomkamp and Miesen, 1996). Since the viscosity-induced mode manifests itself via the M1 branch of eigenvalues, the M1 Marangoni modes (M1-SW in this case) are expected to have a direct impact on it. Indeed, on increasing Ma, the viscosity induced mode is suppressed and undergoes a transition to the short wave M1 Marangoni mode (Fig. 4.17b - 4.17e). This transition is confirmed by the energy budget calculations presented in Tab. 4.5. At $Ma = 13000$, TAN_μ is negligible in comparison with MAS_F, which is the dominant positive term. This is characteristic of the energy budget of the short wave solutal Marangoni mode (Sec. 4.9).

Along with the emergence of the M1-SW mode, the M2-SW mode also becomes unstable as Ma is increased beyond 10000 (Fig. 4.16d - 4.16f). Therefore, as Ma is increased, solutal Marangoni effects dominate and become the primary cause for instability of the flow.

An example in which $n^2 > m$ is considered in Fig. 4.18. As in the previous case (Fig. 4.17), short waves from the M2 branch (M2-SW mode) become unstable on increasing Ma. The growth rates of the long waves increase with Ma, but the M1 dispersion curve does not change qualitatively. To investigate the nature of this long wave instability, the variation of the energy budget with Ma for $\alpha = 1$ is plotted in Fig. 4.19. For small Ma, TAN_μ is dominant, indicating that the instability is due to the viscosity induced mode. As Ma is increased, TAN_μ decreases while the Marangoni stress terms $MAS_I + MAS_F$ increase. The crossover point occurs around $Ma = 2000$. By $Ma = 7000$ (Fig. 4.18b), TAN_μ is negative and solutal Marangoni forces are the dominant cause of instability. The energy budget of the fastest growing long wave modes for $Ma = 0$ and $Ma = 20000$ (Figs. 4.18a and 4.18d respectively) are presented in Tab. 4.6. While TAN_μ is the largest positive term for $Ma = 0$, the energy budget for $Ma = 20000$ is dominated by the MAS_I term, which is characteristic of the long wave

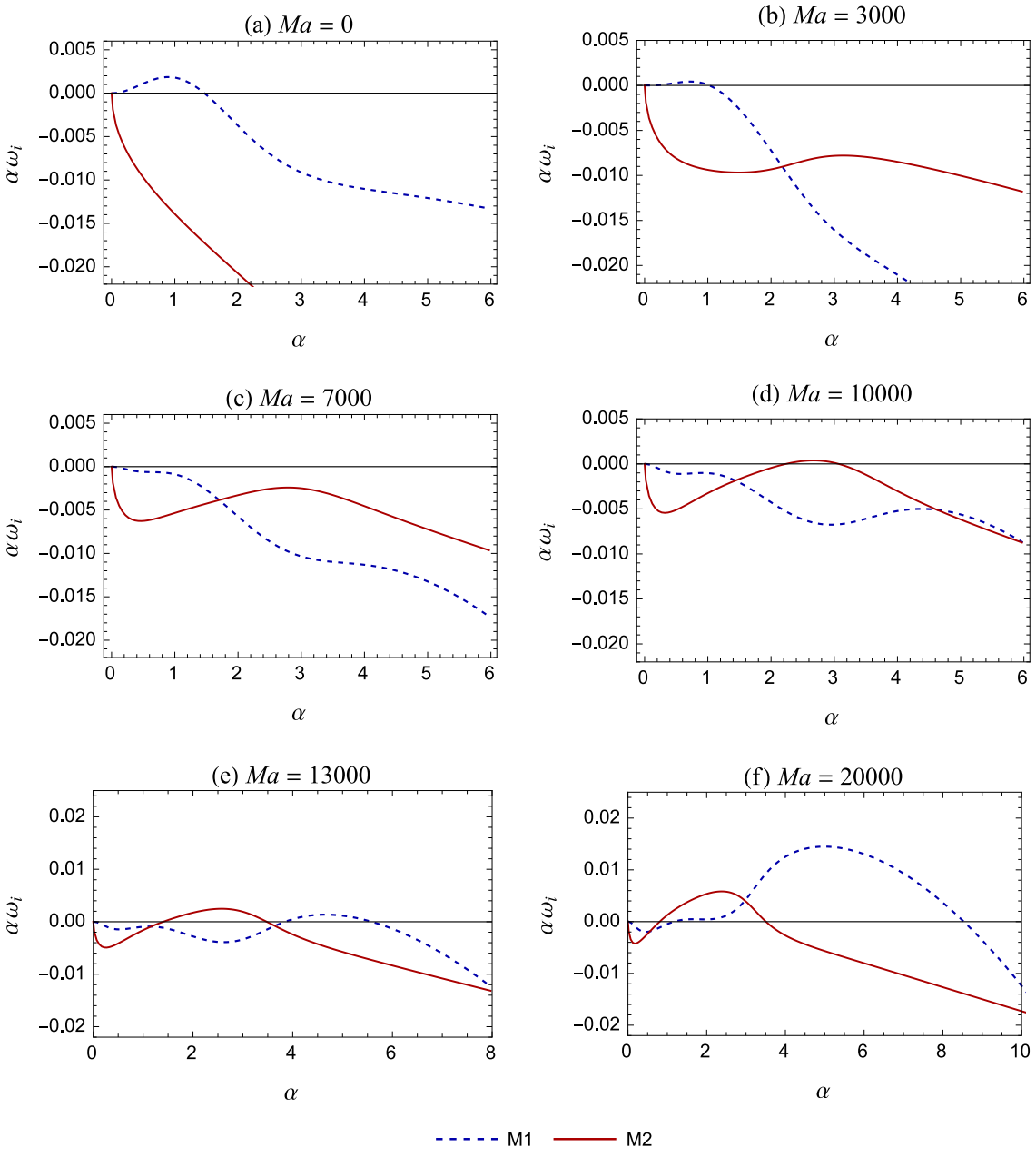

Figure 4.17: Effect of soluble surfactant on the viscosity-induced interfacial instability. The chosen parameter values correspond to the case of $n^2 < m$, for which the short wave M1-SW and M2-SW modes are unstable in the creeping flow limit. Parameter values: Re = 10, m = 1.5, n = 1, Ca = 100, D_r = 0.5, K = 1.2, $\gamma = 0$, Pe = 2000.

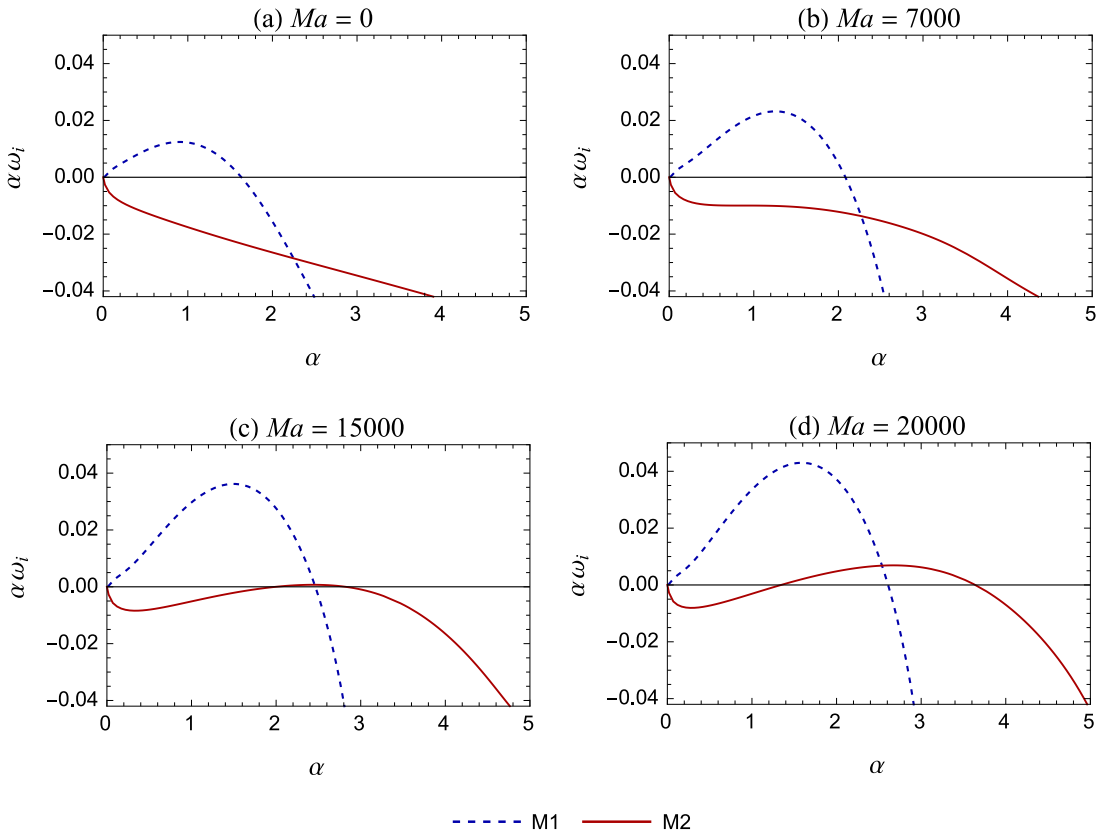

Figure 4.18: Effect of soluble surfactant on the viscosity-induced interfacial instability. The chosen parameter values correspond to the case of $n^2 > m$, for which the long wave M1 and short wave M2-SW instabilities are prevalent in the creeping flow limit. Parameter values: Re = 100, m = 0.5, n = 1.3, Ca = 1, D_r = 0.5, K = 1.2, $\gamma = 0$, Pe = 1000.

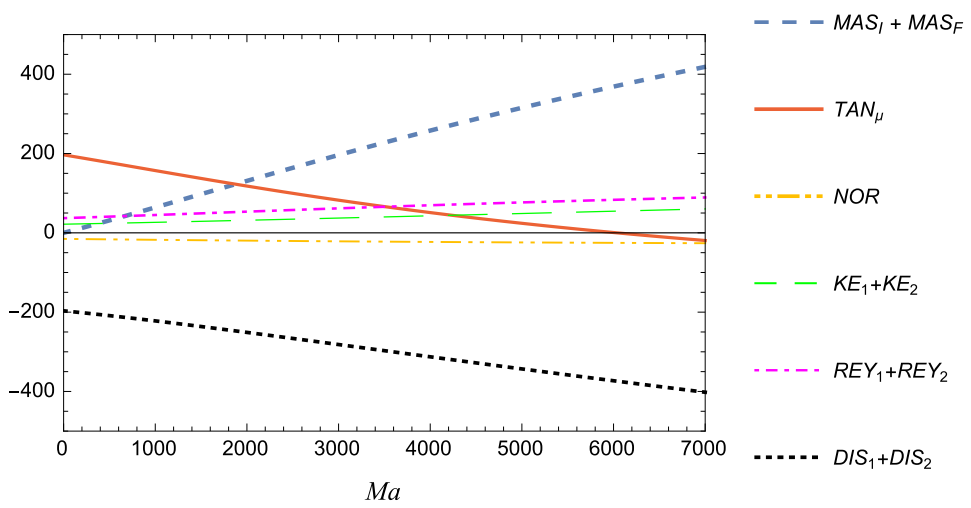

Figure 4.19: Transition from the viscosity-induced instability (driven by TAN_μ) to the long wave solutal Marangoni instability (driven by MAS_I). The variation of terms in the energy budget is depicted as Ma is varied, for the mode corresponding to α = 1 in Fig. 4.18. Parameter values are given in the caption of Fig. 4.18.

Mode	Ma	α	$\sum_{j=1}^{2} KE_j$	$\sum_{j=1}^{2} REY_j$	NOR	TAN_μ	MAS_I	MAS_F
M1	0	0.92	0.119	0.183	-0.069	1.005	0	0
M1	20000	1.57	0.168	0.165	-0.086	-0.281	1.254	0.117

Table 4.6: Energy budget showing the transition from the viscosity induced mode to the long wave solutal Marangoni M1 mode. Calculations correspond to the fastest growing mode in Figs. 4.18a and 4.18d. The values have been normalized by the magnitude of total dissipation so that $(DIS_1 + DIS_2) = -1$. Parameter values are given in the caption of Fig. 4.18.

solutal Marangoni instability M1-LW (Sec. 4.8).

In summary, introducing a gradient of soluble surfactant into an unstable small Re flow causes a transition from the viscosity induced mode to the solutal Marangoni instability (provided Ma is sufficiently large). When the M1-SW Marangoni mode is dominant ($n^2 < m$), this transition may cause the system to become stable in an intermediate range of Ma (cf. Fig. 4.17). This is because the long wave viscosity induced mode is first suppressed before arising again as the short wave M1-SW Marangoni mode. On the other hand, when the long wave M1-LW Marangoni mode is dominant ($n^2 > m$) the flow becomes increasingly unstable to long wave disturbances, on increasing Ma. The viscosity-induced mode eventually transitions to the Marangoni M1-LW mode.

4.13 Comparison with previous work

In this section, we compare our results with the closely related study by Wei (2006), on the thermocapillary instability of Couette flow. We also discuss the implications of

neglecting concentration perturbations caused by interface deformation, as is done in You *et al.* (2014).

Wei (2006) has studied the stability of two-phase layered *Couette* flow between flat plates, which are maintained at different temperatures. The temperature variation across the fluids in the base state is analogous to the variation of solute concentration in the present solutal Marangoni problem. In fact, our entire analysis is valid for thermocapillary instabilities in *Poiseuille* flow, provided we set $K = 1$ (as temperature is continuous at the interface) and restrict Ma to positive values (since interfacial tension decreases with temperature). Also D_r must be identified with the ratio of thermal diffusivities.

Wei (2006) considered the problem in the "thin layer limit", in which one fluid layer is very thin in comparison with the other fluid layer. He obtained a long wave instability mode, which is driven by thermocapillary stresses caused by deformation of the interface in the presence of a base state temperature gradient. This is the thermocapillary analogue of the M1-LW mode (Sec. 4.8). The mode was found to be unstable when the thin layer is heated. If we consider fluid one to be the thin fluid, then we have $n \gg 1$ and consequently $n^2 > m$ for any finite viscosity ratio m. Under these conditions our analysis predicts instability of the long wave M1-LW mode (cf. (4.22)) if the concentration at plate 1 is greater than that at plate 2 ($\gamma < 1$), which is analogous to heating the thin fluid.

Wei (2006) also finds that the growth rate for small wavenumber is linearly proportional to D_r. Our long wavelength asymptotic result (4.22) shows that the growth rate varies as $n^2 D_r/(D_r + n)^2$, which implies linear proportionality with D_r in the thin layer limit of large n. (Note that the wavenumber should be rescaled with the depth of fluid 2 before taking the limit of large n in (4.22).) Furthermore, at small nonzero Re, it was observed that the viscosity induced mode reinforces the long wave thermocapillary mode if the thin layer is more viscous ($m < 1$), and suppresses it if the thin layer is less viscous ($m > 1$). This interaction is entirely analogous to that predicted by (4.22) for the case of a heated thin layer ($n \gg 1$ and $\gamma < 1$). Thus our results for the M1-LW mode are in qualitative agreement with Wei (2006). Further quantitative comparison is not possible since Wei (2006) studied Couette flow while we have analysed Poiseuille flow.

Neither of the short wave instability modes (M1-SW, M2-SW) are identified by the asymptotic analysis of Wei (2006). Their absence in the thin layer limit implies that, for a fixed finite Ma, the short wave modes are stabilized as one fluid layer is made much thinner that the other. Numerical calculations that demonstrate this behavior are presented in Fig. 4.20. Each plot in this figure is a thin layer variation of a case studied in a previous section of this chapter, wherein one or both of the short wave modes are unstable. For example, Fig. 4.20a is plotted for the same parameter values (including Ma) as Fig. 4.5a, except for the thickness ratio n. For $n = 1$ (Fig. 4.5a) both M1-SW and M2-SW are unstable, but when the depth of fluid 2 is significantly decreased

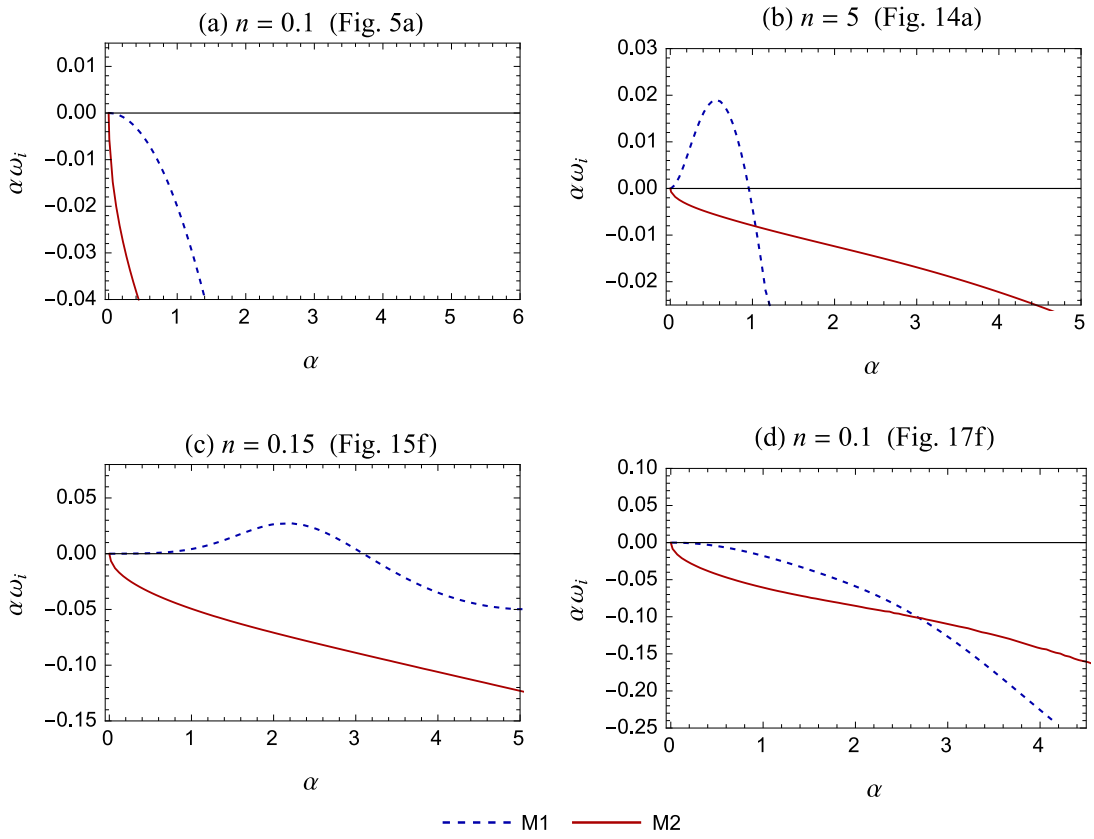

Figure 4.20: Stabilization of short wave modes (M1-SW and M2-SW) when one fluid layer is much thinner than the other. Each plot has the same parameter values as a previous figure in this chapter (mentioned above each plot), with the exception of the thickness ratio n. Moderate values of n are used in the previous figures, wherein one or both of the short wave modes are unstable. In contrast, the new values of n, displayed above each plot, correspond to cases in which either fluid 1 or fluid 2 has a relatively small depth. Making one of the fluid layers thin (while Ma is fixed) clearly has a stabilizing effect on the short wave modes (compare each plot with the figure mentioned above it).

($n = 0.1$, Fig. 4.20a) both short wave modes become stable. Comparing Fig. 4.20b with Fig. 4.14a shows that the M2-SW mode is stabilized on decreasing the thickness of fluid 1. The long wave mode M1-LW, on the other hand becomes more unstable as n is increased, in accordance with the long wave asymptotic prediction (4.22). Fig. 4.20c and Fig. 4.20d show that this behaviour persists when inertial effects are included (nonzero Re). Consequently, the simplified equations of the thin layer limit (Wei, 2006) predict only long wave instability modes. An analysis of the governing equations for moderate thickness ratios, will most likely uncover M1-SW and M2-SW modes in Couette flow as well.

Athough Wei (2006) did not observe the M1-SW and M2-SW modes, he did find a range of Ca in which the long wave instability transitions to an intermediate wavelength mode that has a range of unstable wavenumbers bounded away from zero (cf. Fig. 4 of Wei (2006)). This mode cannot be identified with the M1-SW mode because it was found to stabilize completely on decreasing Ca, which is contrary to the behaviour of the

M1-SW mode (cf. Sec. 4.9). Moreover, since it transitions smoothly to the long wave instability on increasing Ca, it is not the M2-SW mode either. Instead it is most likely the analogue of the intermediate wavelength M1 mode shown in Fig. 4.11d of Sec. 4.10, which arises as a distinct mode in the transition of M1-SW to M1-LW modes.

The physical problem studied by You *et al.* (2014) is identical to that of the present work. However, they do not account for the effect of interface deformation on the concentration perturbations at the interface. As a result, the Marangoni stresses due to interface deformation are absent (the second term multiplying Ma in (4.7)). In this work, we have shown that these Marangoni stresses are the cause of the long wave Marangoni instability. In terms of the energy budget, the MAS_I term that is dominant in the budget of the M1-LW mode is absent. Consequently, the M1-LW mode will not appear in the model analyzed by You *et al.* (2014).

You *et al.* (2014) do, however, report long wave instabilities at very small Re. These are unstable even when $n^2 < m$, in contradiction with our asymptotic result (4.22) for long wave Marangoni modes. These modes do not correspond to the viscosity induced mode either, because You *et al.* (2014) report that they are stabilized as Re is increased beyond unity. Moreover, their calculations for cases of $n = 1$ and $m \neq 1$ show the flow to be stable when $Re > 1$. This is in contradiction with the established results of Yih (1967) and Yiantsios and Higgins (1988), which predict instability to the viscosity induced mode at any non-zero value of Re when $n = 1$ and $m \neq 1$. On the other hand, both our asymptotic and numerical results are consistent with the instability of the viscosity induced mode at finite Re (Yiantsios and Higgins, 1988).

You *et al.* (2014) also report one short wave instability that occurs above a critical value of Ma, at small Re. Accounting for differences in the definition of dimensionless groups, we find that the neutral stability curves presented in You *et al.* (2014) correspond to large Ca of $O(10^3)$ and greater. Since the M2-SW mode dominates over the M1-SW mode at very large Ca (cf. Sec. 4.9), the short wave mode reported by You *et al.* (2014) is probably the M2-SW mode.

In summary, Wei (2006) found the M1-LW mode in *Couette* flow, while You *et al.* (2014) found the M2-SW mode in *Poiseuille* flow. In this work, we have found an additional short wave mode - M1-SW - that becomes unstable in the region where the long wave M1-LW mode is stable. The dominant instability is shown to switch between these three modes as parameters are varied. The M1-SW instability is dominant at smaller values of Ca (cf. Sec. 4.9) and thus is expected to be important in microchannel flows.

4.14 Concluding Remarks

This work has shown that the presence of a soluble surfactant can destabilize layered flow via solutal Marangoni effects, provided a transverse concentration gradient is maintained across the fluids. Three distinct Marangoni instability modes are present, which destabilize the system even in the limit of creeping flow. One of these is a long wave mode (M1-LW), which is destabilized by concentration variations due to deformation of the interface in the presence of a base transverse concentration gradient. The other two modes are short wave instabilities (M1-SW and M2-SW), which are amplified by the coupling between the disturbance flow and the interface concentration perturbations. One of the short wave modes (M1-SW) remains unstable even in the limit of large interfacial tension ($Ca \to 0$), wherein the interface is non-deforming. Thus, the base unidirectional flow may be unstable, leading to higher mass transfer rates, even in experiments that report a flat stationary interface.

When Re is nonzero, the long wave viscosity-induced instability comes into play and interacts with the Marangoni instability. In certain regions of parameter space ($\gamma < 1/K$, $n^2 > m$, $m > 1$), the viscosity-induced mode counteracts the long wave Marangoni mode and has a stabilizing influence. In other cases ($\gamma < 1/K$, $n^2 > m$, $m < 1$), the viscosity-induced mode promotes the instability of long wave disturbances.

A summary of the instabilities that destabilize the system under different conditions is presented in Tab. 4.7. Surfactant laden creeping flow ($Re \ll 1$) is unstable to three different Marangoni instability modes. The long wave M1-LW mode is unstable when $n^2 > m$ (Tab. 4.7, (1)) whereas the short wave M1-SW mode can be unstable when $n^2 < m$ (Tab. 4.7, (2)). The second short wave mode, M2-SW, can be unstable at any value of n (Tab. 4.7, (1-2)). The short wave modes are unstable only if the magnitude of Ma is greater than a critical value, which is different for each mode and depends on the other parameters. The critical Ma is significantly greater when one of the fluid layers is much thinner than the other.

A necessary condition for these Marangoni instabilities is the presence of inter-fluid mass transfer in the base state. Therefore, the Marangoni modes are suppressed when equilibrium concentrations are maintained at the bounding plates ($\gamma = 1/K$) (Tab. 4.7, (3)). The flow stability in this case is the same as that in the absence of surfactant effects ($Ma = 0$). When Re is increased to finite values the flow becomes unstable to the viscosity induced mode (Boomkamp and Miesen, 1996) (Tab. 4.7, (4)). If soluble surfactant effects and inertia are present simultaneously, then both Marangoni and viscosity induced modes are present (Tab. 4.7, (5)). The outcome of mutual interaction between these effects depends on the viscosity and thickness ratio of the fluids. Inertia can stabilize or destabilize the flow, as well as change the nature of the dominant instability from short

Sr. No.	Condition	M1-LW	M1-SW	M2-SW	Viscosity-induced
1	$Re \ll 1, n^2 > m$	✓	✗	✓	✗
2	$Re \ll 1, n^2 < m$	✗	✓	✓	✗
3	$Re \ll 1, \gamma = 1/K$	✗	✗	✗	✗
4	$Re > 1, \gamma = 1/K$	✗	✗	✗	✓
5	$Re > 1$ $(\gamma \neq 1/K)$	✓	✓	✓	✓

Table 4.7: Summary of the instabilities present in the system under different conditions. The three Marangoni modes are the long wave and short wave instabilities from the M1 eigenvalue branch (M1-LW and M1-SW respectively), the short wave instability from the M2 branch. The viscosity-induced mode is the long wave instability first identified by Yih (1967). Re is restricted to small values in this classification. Ma is non-zero and $\gamma < 1/K$ in all cases, unless explicitly stated otherwise. The latter inequality implies that mass transfer occurs from plate 1 to plate 2. Reversing the direction of mass transfer reverses the condition on the transition between long and short waves.

wave to long wave, as shown in Sec. 4.12.

The term $(n^2 - m)$ plays a key role in the stability characteristics of the M1-LW and M1-SW Marangoni modes (Tab. 4.7). It is associated with the transverse gradient of the base state velocity field at the interface ($d\overline{u}_i/dy|_{y=0}$). The gradient is positive if $(n^2 < m)$, negative if $(n^2 > m)$ and zero if $(n^2 = m)$. This term is also prominent in the viscosity-induced mode (cf. Sec. 4.6 and Yiantsios and Higgins (1988)) and in the instability caused by insoluble surfactants (Frenkel and Halpern, 2002; Halpern and Frenkel, 2003; Wei, 2005, 2007). Elucidating the physical mechanisms through which this term influences these different instabilities is an interesting avenue for further work.

An important task for future work is the extension of the present two-dimensional stability analysis to the analysis of three dimensional instability modes, i.e to include disturbances with variations in the direction perpendicular to the flow but parallel to the bounding plates. Wei (2006) has shown that such 3D modes are more unstable than 2D modes for the case of thermocapillary instability in layered Couette flow. It is thus quite possible that the inclusion of 3-D modes will lower the critical Marangoni number of the present Poiseuille layered flow.

In an effort to understand the key effects of solutal Marangoni stresses on the flow's stability, we have used a simplified model for mass transfer of the solute. In this model, adsorption and desorption of the solute to and from the interface is assumed to be instantaneous. This is an idealization. For a solute that adsorbs and desorbs at a finite rate, the distribution of solute at the interface will be affected by surface convection and diffusion in the Gibbs adsorption layer. These processes can have a subtle effect on the dynamics of the system. In the context of solutal Marangoni instability in *stationary* fluid layers, accumulation and transport at the interface can stabilize or destabilize the system, depending on parameter values. The temporal nature of the linear instability modes (oscillatory or

stationary) can also be affected (Kovalchuk and Vollhardt, 2006; Schwarzenberger *et al.*, 2014). In the nonlinear regime, surface transport of solute can lead to complex dynamical states, such as spontaneous oscillations (Tadmouri *et al.*, 2010). It would therefore be interesting to extend the present model to account for these processes, and examine their influence on the stability of flowing fluid layers.

This study indicates that the solutal Marangoni instability can play an important role in applications involving low Re layered flow, such as solvent extraction in microchannels (Assmann *et al.*, 2013). It has revealed the importance of the direction of mass-transfer between the fluids, which controls whether a long wave instability or a short wave instability is observed. This is of practical importance since long wave modes become unstable at any non-zero Ma while short wave instability modes require Ma to be greater than a critical value for instability. In order to accurately predict the instability threshold for these systems, however, the longitudinal variation of the base state concentration field must be accounted for. If this variation is gradual (large Pe), then a weakly nonparallel stability analysis (Huerre and Monkewitz, 1990; Chomaz, 2005) can be carried out, in which the base state is treated as non-varying *locally* at each point along the flow direction. In case the longitudinal concentration variation is rapid (small Pe), then the disturbance cannot be decomposed into wave-like normal modes. Instead *global* eigenmodes (Chomaz, 2005; Theofilis, 2003), with aperiodic variation along both the transverse and longitudinal directions, should be analyzed.

CHAPTER 5

Steady Layered Flow through Curved Microchannels

"(Newton's law) implies that if we study the mass times the acceleration and call the product the force, i.e., if we study the characteristics of force as a program of interest, then we shall find that forces have some simplicity. The law is a good program for analyzing nature; it is a suggestion that the forces will be simple."

– R. Feynman, *Feynman Lectures on Physics, Vol I*

5.1 Introduction

In the previous chapters (Ch. 2 to Ch. 4), we have neglected the bounding walls in the out of plane direction, as they do not modify the essential physics of mass transport in straight channels. However, when the channel is curved, the presence of bounding walls has a profound effect on the flow. The no-slip condition at the walls results in a non-uniform axial velocity profile and a corresponding non-uniform distribution of centrifugal forces. This in turn leads to a three-dimensional flow, with circulations in the cross-sectional plane, which can have a significant magnitude if the channels aspect ratio is close to unity. Keeping in mind, the potential of these circulations to enhance mass transfer, we study the structure of these three-dimensional flows in detail, in this chapter.

Fluid flow in curved channels has been the focus of several investigations owing to both, the subject's intrinsic theoretical value as well as practical relevance (Vashisth *et al.*, 2008; Ku, 1997; Carlo, 2009). This class of flows is illustrative of the situation in which inertial effects, though small, have a significant impact on the nature of a viscous flow. A viscous fluid flowing in a curved channel experiences a transverse centrifugal force. This force is proportional to the square of the axial component of velocity. Consequently it is strongest at the center of the channel and weakens near the walls, where the no-slip condition applies. This spatially varying centrifugal force results in a secondary circulatory motion that is superposed on the primary axial flow. This circulatory flow exists at any non-zero Reynolds number (Re). As a result, the axial velocity profile as well as the net flow through the channel is modified.

The context for this two phase flow analysis is set by the many studies carried out on single phase flows in curved channels. Regular perturbation expansions have proved to be an important tool in the analysis of curved channel flows. The transverse secondary motion is induced even in channels with small values of longitudinal curvature. This makes the problem amenable to an asymptotic analysis in the limit of a narrow channel width i.e. when the radius of curvature of the channel is considerably greater than the characteristic dimension of its cross-section (a gently curved channel). The first such study was carried out by Dean (1927, 1928*b*) for fully developed flow of a single phase fluid in a curved channel of circular cross-section. He demonstrated the helical motion of fluid elements due to the presence of a pair of secondary counter-rotating vortices (Dean vortices). Similar analyses were carried out by (Cuming, 1952) for a rectangular channel and (Topakoglu, 1967) for a circular annulus. These studies were successful at capturing the key features of the flow in curved channels at low Reynolds numbers and for a gentle curvature of the channel. Later studies investigated the developing flow and the effect of finite curvature and high Reynolds numbers. Detailed reviews of these studies are presented by Berger *et al.* (1983) and Vashisth *et al.* (2008). One feature of the flow at high Reynolds number is the bifurcation of the two vortex solution to a four vortex solution (Nandakumar and Masliyah, 1982; Winters, 1987). These studies have been crucial in understanding and exploiting flow in curved geometries, which occur either naturally, e.g. blood flow in arteries (Ku, 1997), or in man-made systems. The latter include heat exchangers, reactors and other process equipment (Vashisth *et al.*, 2008), fluid mixers in micro systems (Carlo, 2009) and stents used in the treatment of vascular disease (Peterson, 2010).

While the effects of longitudinal curvature on single phase flows through curved channels have been studied extensively, the extension of this knowledge to two-phase flows is challenging, and is a topic of ongoing research (Vashisth *et al.*, 2008). The primary challenges associated with the mathematical analysis of two phase flows in curved geometries are associated with the description of the fluid-fluid interface. The configuration of the interface is unknown a priori and must be determined as part of the solution. In addition, accounting for interfacial tension forces acting at the interface introduces nonlinear terms into the mathematical problem. Apart from interfacial phenomena, the coupling of the flow fields in the two fluids results in a richness of hydrodynamic behavior, unseen in the single phase case. Due to these challenges, most work on two-phase curved channel flows have focused on constructing coarse flow regime maps and measuring pressure drop and phase holdups (Ellenberger *et al.*, 1988; Bandaru and Rajendra, 2002; Kirpalani *et al.*, 2008; Donaldson *et al.*, 2011; Sarkar *et al.*, 2012). Among the few studies that have presented a more detailed analysis of the flow field, are the works of Muradoglu and Stone (2007) and Kumar *et al.* (2007) on slug flow, and Ghosh *et al.* (2011), Picardo and Pushpavanam (2013) and Ooms *et al.* (2015) on core-annular flow. Gelfgat *et al.* (2003)

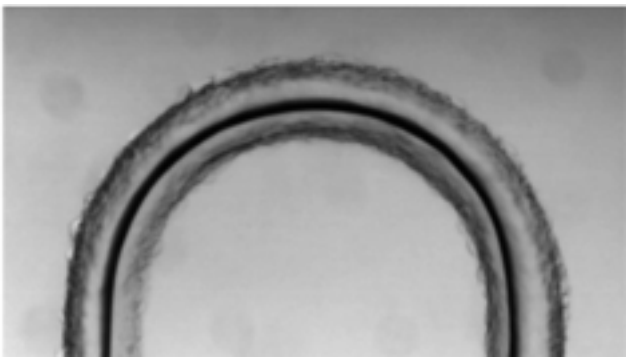

Figure 5.1: Micrograph of laterally layered flow in the curved section of a microchannel. The inner fluid is water and the outer fluid is cyclohexane with a small amount of surfactant (Tween 80, 0.3 vol%). The flow rates are 480 μl min^{-1} and 280 μl min^{-1} respectively. The channel's width and height are 150 μm. The interface is seen as a dark line located near the center of the channel. (Micrograph provided by Mr. Avinash Sahu.)

have simulated vertically layered flow and demonstrated the ability of Dean vortices to enhance inter-fluid mass transfer. However, because they carried out simulations for a limited set of parameters, they observed only one vortex pattern in co-current flow at low Re. They also assumed the interface to be flat, which is not true in general. A detailed study of the flow field in co-flowing vertical fluid layers has been carried out by Garg *et al.* (2015), who by applying the methodology presented in this chapter have identified *nine different vortex patterns*. They have also studied the influence of the circulatory flow on the interface shape and the axial velocity profile, in detail.

The purpose of this chapter is to investigate fully developed steady flow of laterally layered fluids in a curved channel. Laterally layered flows have taken on a new significance in microfluidics, as efficient systems for carrying out inter-fluid mass transfer and chemical reactions. Several workers have successfully applied these flows to liquid-liquid extraction (Assmann *et al.*, 2013; Novak *et al.*, 2012; Znidarsic-Plazl and Plazl, 2007) and phase transfer catalysis (Aljbour *et al.*, 2010). The length scales (l_c) of the microchannels used in these studies range from $O(10)$ to $O(10^2)$ μm, resulting in small values of the Reynolds number $\left(l_c v_c \rho/\mu\right)$. The relative Bond number $\left(\left(\rho_1 - \rho_2\right) g l_c^2/\gamma\right)$ is also very small, implying that capillary forces dominate gravitational effects; this allows the fluids to remain laterally stratified despite differences in density. A typical example, reported by Fries *et al.* (2008), involves the flow of water (W) and toluene (T) through a microchannel of width 300 μm and height 150 μm. Stable layered flow was obtained for flow rates ranging from 100-150 μl min^{-1}. At 150 μl min^{-1}, the Reynolds numbers are Re_W = 69 and Re_T = 180 (where Re_i is defined on the basis of the pressure drop, as in Sec. II). The relative Bond number is 7×10^{-4} and the Capillary number $\left(Ca = v_c \mu/\gamma\right)$ is approximately 2×10^{-3}. In Fig. 5.1, a micrograph of steady layered flow in the curved section of a microchannel is presented. The inner fluid is water and the outer fluid is cyclohexane with a small amount of surfactant (Tween 80, 0.3 vol%). The stable interface is seen as a thick dark line near the center of the channel.

We focus on three important aspects of the flow – secondary circulations and vortex patterns, the shape of the deformed interface and the modified axial velocity profile. To gain insight into the physical mechanisms governing these flow features, we study the problem in the asymptotic limit of small curvature ratios (ε: ratio of the channel's half width to its radius of curvature) and low Reynolds numbers (Re). This asymptotic limit is particularly relevant to curved microchannels. We also assume a $90\,\mathrm{deg}$ contact angle between the inter-fluid interface and the top or bottom wall. In general, the contact angle will depend on the relative wettability of the wall by the two fluids, as well as the flow field near the three-phase contact line (Davis, 2000). However, as our aim is to understand the effects of centrifugal forces on the bulk flow, we consider the mathematically simplest case of a *fixed* $90\,\mathrm{deg}$ contact angle. This condition implies that the interface would be flat in a straight channel, which enables us to obtain an analytical solution by applying of the method of domain perturbations. Moreover, any deformation of the interface due to centrifugal forces will be revealed most clearly in this case. The analytical solution enables an efficient exploration of parameter space, facilitating a detailed study of the influence of fluid properties and operating conditions on the flow field. Apart from its importance for microchannel applications, this parametric study also sheds light on the physics of the flow. The range of validity (in Re and ε) of the perturbation solution is assessed by comparison with three-dimensional numerical simulations, for specific sets of parameter values.

The contents of this chapter are organized as follows. The mathematical formulation of the problem is presented in Sec. 5.2. In Sec. 5.3, the method of domain perturbations is applied to obtain an asymptotic solution. The transverse circulatory flow is analyzed in Sec. 5.4. In Sec. 5.4.1 the five basic vortex patterns are presented. The parameter space is organized on the basis of these flow patterns in Sec. 5.4.2, while the influence of each parameter is explained in Sec. 5.4.3. The strength of the circulatory flow is studied in Sec. 5.4.4, and in Sec. 5.4.5 we determine the optimum aspect ratios of the channel for which the circulation strength is maximized ,in either fluid. In Sec. 5.5 the deformation of the interface is investigated. The influence of each parameter on the deformation is also studied. In Sec. 5.6, redistribution of the axial velocity is analyzed, in terms of *inertial* and *geometric* effects. The resultant change in flow rates of the two fluids is also examined. In Sec. 5.7, we compare the asymptotic solution with numerical simulations to assess its accuracy. We conclude in Sec. 5.8, with a summary of the key results and a discussion of their significance. We also suggest some topics for future work.

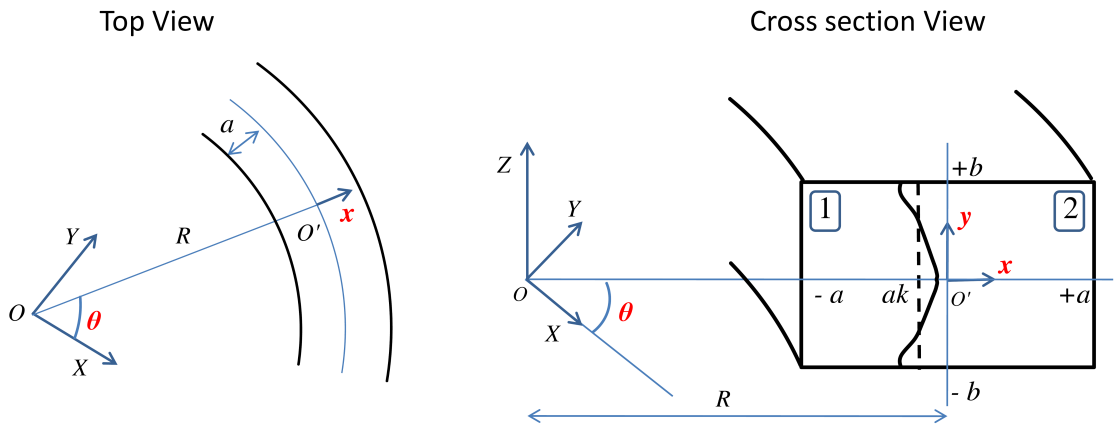

Figure 5.2: Schematic of layered flow in a curved channel. (X, Y, Z) is the Cartesian coordinate system and (x, y, θ) is the curvilinear orthogonal coordinate system used in this study. In the cross-section view of the channel, the dashed line represents the undeformed interface, as it would be in a straight channel, while the solid curve represents the interface in the curved channel.

5.2 Governing equations

A schematic of the flow system under consideration is shown in Fig. 5.2. Here, O is the origin of the Cartesian coordinate axes (X, Y, Z). O' marks the center of the lateral cross-section of the channel. The line OO' lies in the X-Y plane, at an angle of θ with the X axis. With O' as the origin, two new orthogonal axes, x and y, are defined with y parallel to the Z Cartesian axis. (x, y, θ) form a curvilinear, orthogonal coordinate system. This coordinate system was used by Cuming (1952) to study single phase flow in curved rectangular channels.

The channel is of width $2a$ and of height $2b$. The radius of curvature of the channel (the length of the segment OO') is R. The interface between the two laterally layered fluid is expected to deform, under the action of centrifugal forces. The position of the interface is represented by the function F according to the equation $x = aF(y/b)$. The fluid on the inner part of the channel $(-a \leq x \leq aF(y/b))$ is denoted as fluid 1 and that on the outer part $(aF(y/b) \leq x \leq +a)$ as fluid 2. The fraction of the channel volume occupied by fluid 1 (called the volume fraction, α) is a specified input to the problem, which $F(y/b)$ must satisfy. In addition, we assume that the contact angle of the interface with the wall is $90\,\mathrm{deg}$. In Fig. 5.2b (cross-section view), the vertical dashed line at (ak) represents the flat interface that would be present if the channel were straight. The flat interface position (k) is directly determined by the volume fraction (holdup) of fluid 1 (α) as $k = 2\alpha - 1$.

Along with the volume fraction of fluid 1 (α), the pressure drop applied along the channel must be specified. In the case of steady fully developed flow, the azimuthal derivative of pressure along the channel $\frac{\partial Pi_i}{\partial \theta}$ is a constant (independent of position and

time), and is identical in both fluids ($i = 1, 2$). Let this value be $-GR$. Specifying G fixes the pressure drop that drives the flow. This parameter is used to scale the pressure and velocity variables as follows:

$$x = a\bar{x}; \quad y = a\bar{y}; \quad P_i = Ga\bar{P}_i; \quad (w_i, u_i, v_i) = \frac{Ga^2}{\mu_i}(\bar{w}_i, \bar{u}_i, \bar{v}_i) \tag{5.1}$$
$$\text{where} \quad G = \left(-\frac{1}{R}\frac{\partial P_i}{\partial \theta}\right)$$

Here the velocity components in the (x, y, θ) directions are denoted as (u, v, w). The over-bar denotes dimensionless variables. This scaling gives rise to seven dimensionless parameters. A Reynolds number for each fluid (Re_i), the interface location if the channel was straight (k), the aspect ratio of the channel (λ), the ratio of fluid viscosities $(\mu_{12} = \mu_1/\mu_2)$, the Capillary number (Ca) and the curvature ratio (ε).

$$\mathrm{Re}_i = \frac{\rho_i G a^3}{\mu_i^2}; \quad \lambda = \frac{a}{b}; \quad Ca = \frac{Ga^2}{\gamma}; \quad \varepsilon = \frac{a}{R} \tag{5.2}$$

In this work the influence of gravity is neglected. This approximation is appropriate for pressure driven flow through small channels in which $\frac{|(\rho_1 - \rho_2)|ga^2}{\gamma} << 1$.

The non-dimensional continuity and Navier-Stokes equations in the (x, y, θ) curvilinear coordinate system (cf. Fig. 5.2) are presented below, for the case of fully developed flow of an incompressible fluid (Cuming, 1952). In the following, the over-bar on dimensionless variables is dropped for convenience.

$$\frac{\partial u_i}{\partial x} + \lambda\frac{\partial v_i}{\partial y} + \varepsilon\frac{(u_i)}{(1 + x\varepsilon)} = 0 \tag{5.3a}$$

$$\mathrm{Re}_i\left[u_i\frac{\partial u_i}{\partial x} + \lambda v_i\frac{\partial u_i}{\partial y} - \varepsilon\frac{{w_i}^2}{(1 + x\varepsilon)}\right] = -\frac{\partial P_i}{\partial x} + \lambda^2\frac{\partial^2 u_i}{\partial y^2} - \lambda\frac{\partial^2 v_i}{\partial y \partial x} \tag{5.3b}$$

$$\mathrm{Re}_i\left[u_i\frac{\partial v_i}{\partial x} + \lambda v_i\frac{\partial v_i}{\partial y}\right] = -\lambda\frac{\partial P_i}{\partial y} + \frac{\partial^2 v_i}{\partial x^2} - \lambda\frac{\partial^2 u_i}{\partial y \partial x} + \frac{\varepsilon}{(1 + x\varepsilon)}\left(\frac{\partial v_i}{\partial x} - \lambda\frac{\partial u_i}{\partial y}\right) \tag{5.3c}$$

$$\mathrm{Re}_i\left[u_i\frac{\partial w_i}{\partial x} + \lambda v_i\frac{\partial w_i}{\partial y} + \varepsilon\frac{w_i u_i}{(1 + x\varepsilon)}\right] = \frac{1}{(1 + x\varepsilon)} + \frac{\partial^2 w_i}{\partial x^2} + \lambda^2\frac{\partial^2 w_i}{\partial y^2} + \frac{\varepsilon}{(1 + x\varepsilon)}\frac{\partial w_i}{\partial x} - \frac{\varepsilon^2 w_i}{(1 + x\varepsilon)^2} \tag{5.3d}$$

This particular form of the momentum equations are obtained by substituting $\nabla^2\mathbf{v} = -\nabla \times \nabla \times \mathbf{v} + \nabla(\nabla \cdot \mathbf{v})$, and applying the continuity equation for incompressible flow, $\nabla \cdot \mathbf{v} = 0$. The gradient, divergence and curl operators in the (x, y, θ) coordinate system may be obtained by following the general procedure described in Aris (1989). Equations (5.3) are applicable to each fluid $(i = 1, 2)$ in its respective domain $(-1 \leq x \leq F(y)$ for

$i = 1$ and $F(y) \leq x \leq +1$ for $i = 2$ (cf. Fig. 5.2).

Equations (5.3a) to (5.3d) are subject to a total of 28 boundary conditions. At the walls, the no-slip condition is applicable, leading to the following 18 boundary conditions:

$$\{u_1; v_1; w_1\} = 0 \qquad \text{at} \quad x = -1; \quad -1 \leq y \leq +1 \tag{5.4a}$$

$$\{u_1; v_1; w_1\} = 0 \qquad \text{at} \quad y = +1; \quad -1 \leq x \leq F(+1) \tag{5.4b}$$

$$\{u_1; v_1; w_1\} = 0 \qquad \text{at} \quad y = -1; \quad -1 \leq x \leq F(-1) \tag{5.4c}$$

$$\{u_2; v_2; w_2\} = 0 \qquad \text{at} \quad x = +1; \quad -1 \leq y \leq +1 \tag{5.4d}$$

$$\{u_2; v_2; w_2\} = 0 \qquad \text{at} \quad y = +1; \quad F(+1) \leq x \leq +1 \tag{5.4e}$$

$$\{u_2; v_2; w_2\} = 0 \qquad \text{at} \quad y = -1; \quad F(-1) \leq x \leq +1 \tag{5.4f}$$

At the interface, $x = F(y)$, continuity of the velocity field yields 3 more conditions:

$$\{u_1; v_1; w_1\} = \mu_{12} \{u_2; v_2; w_2\} \quad \text{at} \quad x = F(y); \quad -1 \leq y \leq +1 \tag{5.5}$$

The viscosity ratio arises in (5.5) because the velocity scales for the two fluids are different – each scale contains the respective fluid's viscosity. Another 3 boundary conditions result from the balance of normal and tangential stresses at the interface (cf. Ch. 2 of Leal (2007)). First we define the outward unit normal ($\boldsymbol{n}$) to the interface (directed into fluid 2). If the interface location is represented implicitly by $H(x, y) = x - F(y) = 0$, then $\boldsymbol{n} = \nabla H / |\nabla H|$, which yields

$$\boldsymbol{n} = \left(\hat{\mathbf{e}}_x - \lambda \frac{dF}{dy} \hat{\mathbf{e}}_y \right) \left(1 + \left(\lambda \frac{dF}{dy} \right)^2 \right)^{-1/2} \tag{5.6}$$

Here, $\hat{\mathbf{e}}_x$ and $\hat{\mathbf{e}}_y$ are the unit vectors in the x and y directions respectively. The normal stress balance, in terms of the deviatoric stress tensor ($\mathbf{T}_i$) and the capillary number (Ca), reads

$$P_1 - P_2 + \left[(\boldsymbol{n} \cdot \boldsymbol{n} \cdot \mathbf{T}_2) - (\boldsymbol{n} \cdot \boldsymbol{n} \cdot \mathbf{T}_1) \right] = \frac{1}{Ca} (\nabla \cdot \boldsymbol{n}) \quad \text{at} \quad x = F(y) \tag{5.7}$$

The tangential stress balance comprises of two scalar equations and is given below in vectorial form.

$$\boldsymbol{n} \cdot \mathbf{T}_2 - (\boldsymbol{n} \cdot \boldsymbol{n} \cdot \mathbf{T}_2) \boldsymbol{n} = \boldsymbol{n} \cdot \mathbf{T}_1 - (\boldsymbol{n} \cdot \boldsymbol{n} \cdot \mathbf{T}_1) \boldsymbol{n} \quad \text{at} \quad x = F(y) \tag{5.8}$$

The components of ($\mathbf{T}$), for the case of fully developed flow, are given below:

$$\mathbf{T}_{xx} = 2\frac{\partial u}{\partial x}; \quad \mathbf{T}_{yy} = 2\lambda\frac{\partial v}{\partial y}; \quad \mathbf{T}_{\theta\theta} = 2\frac{u\varepsilon}{1+\varepsilon x} \tag{5.9}$$
$$\mathbf{T}_{xy} = \frac{\partial v}{\partial x} + \lambda\frac{\partial u}{\partial y}; \quad \mathbf{T}_{x\theta} = \frac{\partial w}{\partial x} - \frac{w\varepsilon}{1+\varepsilon x}; \quad \mathbf{T}_{y\theta} = \lambda\frac{\partial w}{\partial y}$$

The expressions in (5.2) are valid for each fluid and the index i has been excluded for convenience.

The kinematic condition, which expresses the fact that fluid cannot cross the interface, must also be satisfied. This yields

$$u_1 - \lambda\frac{dF}{dy}v_1 = 0 \quad \text{at} \quad x = F(y) \tag{5.10}$$

Three additional conditions on $F(y)$ are necessary to determine the location of the interface. The first two fix the contact angle of the interface at the walls as $90\,\mathrm{deg}$, which allows the interface to be vertical and flat in a straight channel.

$$\frac{dF}{dy} = 0 \quad \text{at} \quad y = \pm 1 \tag{5.11}$$

The final condition is the input specification of the volume fraction of fluid 1 (α):

$$\frac{\int_{-1}^{+1} dy \int_{-1}^{F(y)} dx\,(1+\varepsilon x)}{\int_{-1}^{+1} dy \int_{-1}^{+1} dx\,(1+\varepsilon x)} = \frac{1}{4}\int_{-1}^{+1} dy \int_{-1}^{F(y)} dx\,(1+\varepsilon x) = \alpha \tag{5.12}$$

Specifying the value of α is equivalent to specifying the position of the interface in a straight channel (k); the relationship between the two quantities is $\alpha = (k+1)/2$. Note that the pressure drop has been inherently specified by its use in the velocity scales.

Equations (5.3) to (5.12) describe fully developed layered flow in a curved rectangular channel. Their solution requires the pressure drop and volume fraction (holdup) to be specified as inputs. On setting $\varepsilon = 0$, these equations describe layered flow in a straight channel and admit an analytical series solution. For the case of a curved channel ($\varepsilon \neq 0$), the governing equations are nonlinear and coupled and demand a numerical solution. However, an asymptotic solution can be derived by considering the problem in the limit of small curvature ratios ($\varepsilon \ll 1$). This is carried out in Sec. 5.3.

5.3 Solution by the method of domain perturbations

In this section, the method of domain perturbations (Johns and Narayanan, 2002; Joseph, 1975; Leal, 2007; Van Dyke, 1975) is applied to obtain an asymptotic solution as a power series expansion in ε. The procedure results in a sequence of linear problems, which can be solved analytically. It further eases the calculations by decoupling the solution of the velocity and pressure fields from the determination of the interface location. We first outline the general procedure and then carry out the calculation to $O(\varepsilon^1)$.

5.3.1 Outline of the method of domain perturbations

Consider the problem defined by (5.3) to (5.12) as one among a family of problems parameterized by the curvature ratio ε. Now, consider the special case of $\varepsilon = 0$, which corresponds to layered flow in a straight channel. This is referred to as the base problem. The corresponding base solution has only an axial component of velocity $(u_i = v_i = 0)$. With a contact angle of $90\,\mathrm{deg}$ at the top and bottom walls $(y = \pm 1)$, the interface in the base problem will be flat and located at $x = k$. For values of ε slightly greater than zero (perturbed problem), one would expect, physically, a solution only slightly different from the base solution at $\varepsilon = 0$. Formally, the solution and its derivatives with respect to ε have a continuous dependence on ε (solution is analytic in ε). This is the primary prerequisite of the method of domain perturbations, by which the flow in a gently curved channel is approximated as a *regular* perturbation of the flow in a straight channel.

An asymptotic power series expansion in ε is proposed as the solution of the perturbed problem. For u_i, the expansion reads as

$$u_i\left(x, y; \varepsilon\right) = u_{i,0}\left(x, y\right) + u_{i,1}\left(x, y\right)\varepsilon + u_{i,2}\left(x, y\right)\varepsilon^2 + O\left(\varepsilon^3\right) \tag{5.13a}$$

Similar expansions are assumed for v_i, w_i and P_i. Here, the first subscript denotes the fluid and the second subscript denotes the order of the term in the expansion. The function that determines the interface location $x = F(y, \varepsilon)$ is also expanded as a power series in ε:

$$F\left(y, \varepsilon\right) = k + f_1\left(y\right)\varepsilon + f_2\left(y\right)\varepsilon^2 + O\left(\varepsilon^3\right) a \tag{5.13b}$$

The perturbation solution must satisfy the input specification of the volume fraction of fluid 1 at all orders. The solution at $O(\varepsilon^0)$ corresponds to unidirectional layered flow in a straight channel $(\varepsilon = 0)$. The terms at $O(\varepsilon^1)$ capture the most important effects of the curvature of the channel on the flow field and the interface position. The higher order terms account for increasingly smaller effects of the curved channel on the flow, such as

the influence of Coriolis forces.

The perturbation solution is obtained by successively solving a series of problems for the unknown functions in the expansions (5.13a) and (5.13b). These problems are obtained by substituting the expansions into the governing equations (cf. (5.3) to (5.12)) and equating the coefficients of various powers of ε (cf. Ch. 4 of Leal (2007)). The procedure is straightforward except when considering the boundary conditions at the interface (5.5) to (5.12). Since the interface deforms as ε is varied, the terms in the boundary condition have an implicit dependence on ε. This dependence is made explicit by expanding the functions in a Taylor series about ε = 0 (Van Dyke, 1975; Leal, 2007). As an example, consider the continuity condition on the axial component of velocity at the interface (cf. (5.5)):

$$w_1\left(x = F\left(y,\varepsilon\right), y\right) = \left(\mu_{12}\right) w_2\left(x = F\left(y,\varepsilon\right), y\right) \qquad -1 \leq y \leq +1 \tag{5.14a}$$

On expanding in a Taylor series about $\varepsilon = 0$, one obtains

$$\begin{aligned} w_1\left(x = k, y\right) + \varepsilon \left.\frac{\partial w_1}{\partial x}\right|_{x=k} \left.\frac{\partial F\left(y,\varepsilon\right)}{\partial \varepsilon}\right|_{\varepsilon=0} \\ = \left(\frac{\mu_1}{\mu_2}\right)\left[w_2\left(x = k, y\right) + \varepsilon \left.\frac{\partial w_2}{\partial x}\right|_{x=k} \left.\frac{\partial F\left(y,\varepsilon\right)}{\partial \varepsilon}\right|_{\varepsilon=0}\right] + O\left(\varepsilon^2\right) \end{aligned} \tag{5.14b}$$

Substituting from (5.13a) and (5.13b) and grouping terms of different orders of ε yields

$$\begin{aligned} w_{1,0}\left(x = k, y\right) + \varepsilon\left(w_{1,1}\left(x = k, y\right) + f_1 \left.\frac{\partial w_{1,0}}{\partial x}\right|_{x=k}\right) \\ = \mu_{12}\left[w_{2,0}\left(x = k, y\right) + \varepsilon\left(w_{2,1}\left(x = k, y\right) + f_1 \left.\frac{\partial w_{2,0}}{\partial x}\right|_{x=k}\right)\right] + O\left(\varepsilon^2\right) \end{aligned} \tag{5.14c}$$

Equating terms at various orders of ε leads to a sequence of boundary conditions, all of which are applied at the flat interface of the base problem, $x = k$. A similar procedure is applied to the other interface boundary conditions. Note that the functions $f_i(y)$, which determine the position of the interface (cf. (5.13b)), enter the perturbation problem via the boundary conditions at the interface. In the following subsections, the calculation is carried out to $O(\varepsilon^1)$.

Before proceeding with the calculations, a few comments on the interpretation of the expansions in (5.13a) and (5.13b) are in order. The formulation of the method of domain perturbations adopted here is the so-called Eulerian formulation. It has the benefit of ease of application and conceptual simplicity. However, the following technical difficulty may arise when evaluating the expansions in (5.13a) and (5.13b). The terms in the expansions (RHS of (5.13a) and (5.13b)) are obtained by solving the perturbations

equations on the base domain with undeformed boundaries; i.e. a flat interface. However, the solution approximated by the asymptotic expansion (LHS of (5.13a)) is valid on a domain with deformed boundaries, i.e. a deflected interface. Thus when evaluating the solution at points close to the deflected interface, one must evaluate the terms in the expansions at points that are not part of the base domain over which these functions were determined. This apparent difficulty may be overcome by analytic continuation of the functions beyond the base domain to include the new points enclosed by the deformed boundaries. Such a rationalization of the Eulerian formulation is granted credence by the work of Joseph (1975). He presents an alternative Lagrangian formulation of the method of domain perturbations that avoids the above difficulty, by defining an explicit mapping between the perturbed domain and the base domain. The final solution is shown to be independent of the specific mapping chosen. Finally, using analytic continuation, the Lagrangian and Eulerian formulations are shown to be equivalent. An elegant exposition of the Lagrangian formulation is presented by Johns and Narayanan (2002), along with several examples and applications to the analysis of interfacial instabilities. Van Dyke (1975), in his classic text on perturbation methods, adopts the Eulerian formulation, as we have done here.

5.3.2 Base solution at $O(\varepsilon^0)$

The equations at $O(\varepsilon^0)$ for the base case of layered flow in a straight rectangular channel are given below:

$$u_{i,0} = v_{i,0} = 0 \tag{5.15a}$$

$$\frac{\partial^2 w_{i,0}}{\partial x^2} + \lambda^2 \frac{\partial^2 w_{i,0}}{\partial y^2} = -1 \tag{5.15b}$$

(5.15b) is subject to the following boundary conditions.

At the channel walls:

$$w_{1,0} = 0 \qquad \text{at} \quad y = \pm 1; \quad -1 \leq x \leq k \tag{5.16a}$$

$$w_{2,0} = 0 \qquad \text{at} \quad y = \pm 1; \quad k \leq x \leq +1 \tag{5.16b}$$

$$w_{1,0} = 0 \qquad \text{at} \quad x = -1; \quad -1 \leq y \leq +1 \tag{5.16c}$$

$$w_{2,0} = 0 \qquad \text{at} \quad x = +1; \quad -1 \leq y \leq +1 \tag{5.16d}$$

The interface is flat and located at $x = k$. The continuity of the velocity field and the tangential stress balance yield the following conditions at the interface ($x = k;\ -1 \leq$

$y \leq +1$):

$$w_{1,0} = (\mu_{12})\, w_{2,0} \tag{5.16e}$$

$$\frac{\partial w_{1,0}}{\partial x} = \frac{\partial w_{2,0}}{\partial x} \tag{5.16f}$$

The kinematic condition is trivially satisfied and the normal stress balance implies that the pressure is continuous across the flat interface. The general solution to (5.15b) is obtained by the method of eigenfunction expansions (Cornish, 1928) and is given by

$$w_{i,0} = \sum_{n=0}^{\infty} \left[\frac{16(-1)^n}{\lambda^2 \left\{ (2n+1)\,\pi \right\}^3} \left\{ A_{in} \cosh\left((2n+1)\,\frac{\pi}{2} \lambda x \right) + B_{in} \sinh\left((2n+1)\,\frac{\pi}{2} \lambda x \right) + 1 \right\} \cos\left((2n+1)\,\frac{\pi}{2} y \right) \right] \tag{5.17}$$

Each term of this series satisfies (5.16a) and (5.16b) by construction. The four constants, A_{1n}, A_{2n}, B_{1n} and B_{2n} are obtained analytically, for arbitrary n, by solving the system of 4 algebraic equations, which results from substituting (5.17) into the boundary conditions (5.16c) to (5.16f). This series solution converges rapidly. The maximum relative difference between the solutions with 5 terms and 11 terms is less than 0.3 %.

5.3.3 Transverse circulatory flow at $O(\varepsilon^1)$

The effects of the curvature of the channel on the flow are first encountered at $O(\varepsilon^1)$. Here we find that the equations for $u_{i,1}$, $v_{i,1}$ and $P_{i,1}$ are independent of $w_{i,1}$. These are solved first to determine the transverse flow field and the interface shape. The axial velocity $w_{i,1}$ and the flow rates are obtained in a subsequent subsection.

The equations governing the transverse flow and the interface deformation at $O(\varepsilon^1)$ are given below. In the x-direction momentum equation (5.18b), the base axial flow $(w_{i,0})$ appears as an inhomogeneous term. This term accounts for the centrifugal force that drives the secondary transverse flow.

$$\frac{\partial u_{i,1}}{\partial x} + \lambda \frac{\partial v_{i,1}}{\partial y} = 0 \tag{5.18a}$$

$$-Re_i (w_{i,0})^2 = -\frac{\partial P_{i,1}}{\partial x} + \lambda^2 \frac{\partial^2 u_{i,1}}{\partial y^2} - \lambda \frac{\partial^2 v_{i,1}}{\partial y \partial x} \tag{5.18b}$$

$$0 = -\lambda \frac{\partial P_{i,1}}{\partial y} + \frac{\partial^2 v_{i,1}}{\partial x^2} - \lambda \frac{\partial^2 u_{i,1}}{\partial y \partial x} \tag{5.18c}$$

The boundary conditions at the wall are

$$\left\{u_{1,1}; v_{1,1}\right\} = 0 \qquad \text{at} \quad x = -1; \quad -1 \le y \le +1 \tag{5.19a}$$

$$\left\{u_{2,1}; v_{2,1}\right\} = 0 \qquad \text{at} \quad x = +1; \quad -1 \le y \le +1 \tag{5.19b}$$

$$\left\{u_{1,1}; v_{1,1}\right\} = 0 \qquad \text{at} \quad y = \pm 1; \quad -1 \le x \le k \tag{5.19c}$$

$$\left\{u_{2,1}; v_{2,1}\right\} = 0 \qquad \text{at} \quad y = \pm 1; \quad k \le x \le +1 \tag{5.19d}$$

The boundary conditions at the interface, at $O(\varepsilon^1)$, applied at $x = k$ $(-1 \le y \le 1)$ are

$$\left\{u_{1,1}; v_{1,1}\right\} = \mu_{12} \left\{u_{2,1}; v_{2,1}\right\} \tag{5.19e}$$

$$u_{1,1} = 0 \tag{5.19f}$$

$$\lambda \frac{\partial u_{1,1}}{\partial y} + \frac{\partial v_{1,1}}{\partial x} = \lambda \frac{\partial u_{2,1}}{\partial y} + \frac{\partial v_{2,1}}{\partial x} \tag{5.19g}$$

(5.19a) to (5.19g) are the 16 boundary conditions required by the partial differential equations (5.18a) to (5.18c). These conditions do not involve $f_1(y)$. Thus the solutions of $u_{i,1}$ and $v_{i,1}$ are independent of $f_1(y)$. Since there is no transverse flow in the base solution at $O(\varepsilon^0)$, the deformation of the interface does not affect the transverse flow at $O(\varepsilon^1)$; it will contribute only at $O(\varepsilon^2)$. In this subsection we solve equations (5.18a) to (5.19g) for $u_{i,1}$ and $v_{i,1}$. The shape of the interface is determined in the next subsection by applying the normal stress balance at $O(\varepsilon^1)$.

Because the flow is fully developed, we can use the stream function formulation. Here $u_{i,1}$ and $v_{i,1}$ are written in terms $\psi_{i,1}(x, y)$, which is defined so that (5.18a) is satisfied:

$$u_{i,1} = \lambda \frac{\partial \psi_{i,1}}{\partial y} \quad and \quad v_{i,1} = -\frac{\partial \psi_{i,1}}{\partial x} \tag{5.20}$$

(5.20) is substituted into the momentum equations (5.18b) and (5.18c), which are then cross differentiated and subtracted to eliminate pressure. This results in two fourth order biharmonic equations for $\psi_{i,1}$.

$$\nabla^4 \psi_{i,1} = \frac{\partial^4 \psi_{i,1}}{\partial x^4} + 2\lambda^2 \frac{\partial^4 \psi_{i,1}}{\partial x^2 \partial y^2} + \lambda^4 \frac{\partial^4 \psi_{i,1}}{\partial y^4} = -Re_i \lambda \frac{\partial}{\partial y}\left({w_{i,0}}^2\right) \tag{5.21}$$

$$\text{where} \quad \nabla^2 = \left(\frac{\partial^2}{\partial x^2} + \lambda^2 \frac{\partial^2}{\partial y^2}\right)$$

These two equations are coupled via their boundary conditions, which are obtained by substituting (5.20) into (5.19a) to (5.19g). Taking a reference value for the streamfunction

as $\psi_{1,1}(-1,-1)=0$, the boundary conditions simplify to

$$\psi_{1,1}=0; \quad \frac{\partial \psi_{1,1}}{\partial x}=0 \qquad \text{at} \quad x=-1; \quad -1\le y\le +1 \tag{5.22a}$$

$$\psi_{2,1}=0; \quad \frac{\partial \psi_{2,1}}{\partial x}=0 \qquad \text{at} \quad x=+1; \quad -1\le y\le +1 \tag{5.22b}$$

$$\psi_{1,1}=0; \quad \frac{\partial \psi_{1,1}}{\partial y}=0 \qquad \text{at} \quad y=\pm 1; \quad -1\le x\le k \tag{5.22c}$$

$$\psi_{2,1}=0; \quad \frac{\partial \psi_{2,1}}{\partial y}=0 \qquad \text{at} \quad y=\pm 1; \quad k\le x\le +1 \tag{5.22d}$$

At $x=k$, for $-1\le y\le 1$, we have

$$\psi_{1,1}=\psi_{2,1}=0 \tag{5.22e}$$

$$\frac{\partial \psi_{1,1}}{\partial x}=(\mu_{12})\,\frac{\partial \psi_{2,1}}{\partial x} \tag{5.22f}$$

$$\lambda^2\frac{\partial^2\psi_{1,1}}{\partial y^2}-\frac{\partial^2\psi_{1,1}}{\partial x^2}=\lambda^2\frac{\partial^2\psi_{2,1}}{\partial y^2}-\frac{\partial^2\psi_{2,1}}{\partial x^2} \tag{5.22g}$$

To solve (5.21) to (5.22g), we adopt the method of superposition. This method was used by Meleshko (1996, 1998) to solve single phase Stokes flow in a cavity with moving walls. Here, we extend the method to solve the two phase problem defined by (5.21) to (5.22g). The solution consists of a sum of two infinite series of complete orthogonal eigenfunctions in the x and y directions. The procedure is described in Appendix B.1.

$$\begin{aligned}&\psi_{1,1}(x,y)=\\ &\sum_{n=1}^{\infty}\left[\ \phi_{ny,1}(y)\ \left\{\begin{array}{l} C_{1n}\cosh\left(\omega_{ny,1}\,x\right)+C_{2n}\sinh\left(\omega_{ny,1}\,x\right)+C_{3n}x\cosh\left(\omega_{ny,1}\,x\right)\\ +C_{4n}x\sinh\left(\omega_{ny,1}\,x\right)+s_{1,n}(x)\end{array}\right\}\ \right]\\ &\quad+\sum_{m=1}^{\infty}\left[\ \phi_{mx,1}(x)\ \left\{C_{5m}\sinh\left(\lambda^{-1}\omega_{mx,1}\,y\right)+C_{6m}y\cosh\left(\lambda^{-1}\omega_{mx,1}\,y\right)\right\}\ \right]\end{aligned} \tag{5.23a}$$

$$\begin{aligned}&\psi_{2,1}(x,y)=\\ &\sum_{n=1}^{\infty}\left[\ \phi_{ny,2}(y)\ \left\{\begin{array}{l} C_{7n}\cosh\left(\omega_{ny,2}\,x\right)+C_{8n}\sinh\left(\omega_{ny,2}\,x\right)+C_{9n}x\cosh\left(\omega_{ny,2}\,x\right)\\ +C_{10n}x\sinh\left(\omega_{ny,2}\,x\right)+s_{2,n}(x)\end{array}\right\}\ \right]\\ &\quad+\sum_{m=1}^{\infty}\left[\ \phi_{mx,2}(x)\ \left\{C_{11m}\sinh\left(\lambda^{-1}\omega_{mx,2}\,y\right)+C_{12m}y\cosh\left(\lambda^{-1}\omega_{mx,2}\,y\right)\right\}\ \right]\end{aligned} \tag{5.23b}$$

Here, the functions $s_{i,n}(x)$ are particular solutions of inhomogeneous ordinary differential equations (B.5a), in which the inhomogeneity arises from the base axial flow $w_{i,0}$ (cf. Appendix B.1). A similar solution was obtained by (Cuming, 1952) for single phase flow in a curved rectangular channel.

The constants C_{1n} to C_{12m} must be evaluated by applying the boundary conditions (5.22a) to (5.22g). The solution is approximated by truncating each series to N terms. The set of 12 N equations for the unknown constants are coupled in a nontrivial manner and must be solved simultaneously (cf. Appendix B.1). As N is increased, the values of all the constants are refined and the two series converge to the solution (Meleshko, 1996, 1998). In this problem, the convergence is rapid and 4-5 terms of each series in (5.23a) and (5.23b) are found to be sufficient. An example calculation is presented in Appendix B.2. The convergence is particularly fast within the domain of the fluids, since the magnitude of the hyperbolic terms in the series decrease exponentially as one moves away from the boundaries.

5.3.4 Interface deformation at $O(\varepsilon^1)$

The transverse flow in each fluid exerts viscous stresses at the interface. The normal component of this stress along with the pressure difference across the interface must be balanced by capillary forces that arise when the interface has a mean curvature. The balance of these normal stresses (cf. (5.7)) at $O(\varepsilon^1)$ yields

$$P_{1,1} - P_{2,1} + 2\left(\frac{\partial u_{2,1}}{\partial y} - \frac{\partial u_{1,1}}{\partial y}\right) = \frac{1}{Ca}\left(-\lambda^2 \frac{d^2 f_1}{dy^2} + 1\right) \quad \text{at } x = k \tag{5.24}$$

This equation has two curvature terms contributing to capillary forces. The first term, involving the second derivative of $f_1(y)$, represents the deformation of the cross-sectional shape of the interface, away from a flat line. The constant unity term is the longitudinal curvature, which is due to the curved nature of the channel itself i.e. even when the interface appears flat over the cross-section of the channel (i.e. when $f_1(y) = 0$), it still has a mean curvature because the channel itself is curved.

In order to use (5.24) to determine $f_1(y)$, we must calculate the pressure distribution in both fluids. This is obtained by integrating the momentum equations (5.18b) and (5.18c). In terms of the stream function, we obtain

$$P_1(x,y) = -\frac{1}{\lambda}\int \frac{\partial^3 \psi_{1,1}}{\partial x^3} dy - \lambda \frac{\partial^2 \psi_{1,1}}{\partial x \partial y} + D_1 \tag{5.25a}$$

$$P_2(x,y) = -\frac{1}{\lambda}\int \frac{\partial^3 \psi_{2,1}}{\partial x^3} dy - \lambda \frac{\partial^2 \psi_{2,1}}{\partial x \partial y} + D_2 \tag{5.25b}$$

D_1 and D_2 are arbitrary constants of integration. We are at liberty to set $D_1 = 0$, as this merely sets a convenient reference value for the pressure field. However, the second constant D_2 remains unknown at this stage and must be determined along with the interface shape. Substituting (5.25a) and (5.25b) into (5.24) yields the following equation for

$f_1(y)$:

$$\frac{d^2 f_1}{dy^2} = \frac{Ca}{\lambda^2}\left(\frac{1}{\lambda}\int \frac{\partial^3 \psi_{1,1}}{\partial x^3} dy + 3\lambda \frac{\partial^2 \psi_{1,1}}{\partial x \partial y} - \frac{1}{\lambda}\int \frac{\partial^3 \psi_{2,1}}{\partial x^3} dy - 3\lambda \frac{\partial^2 \psi_{2,1}}{\partial x \partial y}\right) + \frac{CaD_2}{\lambda^2} + \frac{1}{\lambda^2} \tag{5.26}$$

The right hand side of (5.26) is evaluated at $x = k$. This is a second order ordinary differential equation (ODE) for $f_1(y)$, which contains an arbitrary constant D_2. Direct integration yields a general solution with three arbitrary constants. Thus, to uniquely determine $f_1(y)$, one must apply the three conditions (5.11) – (5.12). The first two require the contact angle to be $90\,\mathrm{deg}$:

$$\frac{df_1}{dy} = 0 \quad \text{at } y = \pm 1 \tag{5.27a}$$

(5.12) specifies the volume fraction of fluid 1 (α). At $O(\varepsilon^1)$, we have

$$\alpha = \frac{k+1}{2} = \frac{1}{4}\int_{-1}^{+1} dy \int_{-1}^{k+\varepsilon f_1(y)} dx\,(1 + \varepsilon x) \tag{5.27b}$$

Expanding (5.27b) as a power series in ε, using Leibniz rule, and retaining terms to $O(\varepsilon^1)$, we obtain the third condition on $f_1(y)$:

$$\int_{-1}^{+1} f_1(y)\, dy = 1 - k^2 \tag{5.27c}$$

On integrating (5.26) and using the conditions (5.27a) and (5.27c), we obtain the solution for $f_1(y)$. (The resulting expression is lengthy and is not reproduced here.) This completes the solution of the circulatory flow field and the interface shape to $O(\varepsilon^1)$.

5.3.5 Axial velocity and flow rate modification at $O(\varepsilon^1)$

In this section, we calculate the change to the axial velocity at $O(\varepsilon^1)$. Then, accounting for the deflection of the interface, we calculate the flow rates of the two fluids through the curved channel. The governing equation for $w_{i,1}$, obtained from (5.3d), is given below:

$$\frac{\partial^2 w_{i,1}}{\partial x^2} + \lambda^2 \frac{\partial^2 w_{i,1}}{\partial y^2} = Re_i \left[u_{i,1}\frac{\partial w_{i,0}}{\partial x} + \lambda v_{i,1}\frac{\partial w_{i,0}}{\partial y}\right] - \frac{\partial w_{i,0}}{\partial x} + x \tag{5.28}$$

No-slip boundary conditions, applied at the walls, are

$$w_{1,1} = 0 \qquad \text{at} \quad y = \pm 1; \quad -1 \leq x \leq k \tag{5.29a}$$

$$w_{2,1} = 0 \qquad \text{at} \quad y = \pm 1; \quad k \leq x \leq +1 \tag{5.29b}$$

$$w_{1,1} = 0 \qquad \text{at} \quad x = -1; \quad -1 \leq y \leq +1 \tag{5.29c}$$

$$w_{2,1} = 0 \qquad \text{at} \quad x = +1; \quad -1 \leq y \leq +1 \tag{5.29d}$$

The boundary conditions applied at the interface ($x = k$; $-1 \leq y \leq 1$) are

$$w_{1,1} + f_1(y)\frac{\partial w_{1,0}}{\partial x} = \mu_{12}\left(w_{2,1} + f_1(y)\frac{\partial w_{2,0}}{\partial x}\right) \tag{5.29e}$$

$$\frac{\partial w_{1,1}}{\partial x} + f_1(y)\frac{\partial^2 w_{1,0}}{\partial x^2} - w_{1,0} - \lambda^2 \frac{df_1}{dy}\frac{\partial w_{1,0}}{\partial y} = \frac{\partial w_{2,1}}{\partial x} + f_1(y)\frac{\partial^2 w_{2,0}}{\partial x^2} - w_{2,0} - \lambda^2 \frac{df_1}{dy}\frac{\partial w_{2,0}}{\partial y} \tag{5.29f}$$

The solution of (5.28) to (5.29f) is obtained as a series of eigenfunctions, in a manner similar to the solution of $w_{i,0}$. Since $w_{i,1}$ is an even function of y (because the inhomogeneous terms of (5.28) are even functions of y), the solution takes the following form:

$$w_{i,1} = \sum_{n=0}^{\infty}\left[g_{i,n}(x)\cos\left((2n+1)\frac{\pi}{2}y\right)\right] \tag{5.30}$$

where $g_{i,n}(x)$ satisfies the ordinary differential equations that are obtained after taking the inner product of (5.28) with the eigenfunctions $\cos\left((2n+1)\frac{\pi}{2}y\right)$. For each value of n, we obtain the following equation:

$$\frac{d^2 g_{i,n}}{dx^2} - \lambda^2\left((2n+1)\frac{\pi}{2}\right)^2 g_{i,n} = \int_{-1}^{1}\left[Re_i\left(u_{i,1}\frac{\partial w_{i,0}}{\partial x} + \lambda v_{i,1}\frac{\partial w_{i,0}}{\partial y}\right) - \frac{\partial w_{i,0}}{\partial x} + x\right]\cos\left((2n+1)\frac{\pi}{2}y\right)dy \tag{5.31}$$

The boundary conditions for these equations are obtained by taking the inner products of (5.29c) to (5.29f) with $\cos\left((2n+1)\frac{\pi}{2}y\right)$.

The lengthy inhomogeneous term on the right hand side (RHS) of (5.31) does not allow for a simple closed form particular solution. However, analytical solutions may be readily obtained (using a symbolic package, e.g. Mathematica) if the inhomogeneity consists of polynomials in x. To take advantage of this, we decompose the RHS of (5.31) into a series of Chebyshev polynomials. Seven Chebyshev polynomials are sufficient to represent this function accurately. With the inhomogeneity in this polynomial form, (5.31) is solved to obtain $g_{i,n}(x)$. The convergence of the series in (5.30) is illustrated in Appendix B.2. Four terms were found to be sufficient.

Next, we calculate the flow rates of the two fluids. Focusing on the inner fluid, we begin with the formula for the flow rate:

$$Q_1 = \int_{-1}^{1} \int_{-1}^{F(y)} w_1 dxdy \tag{5.32a}$$

In terms of the perturbations series to $O(\varepsilon^1)$, this formula yields

$$Q_1 = \int_{-1}^{1} \int_{-1}^{k+\varepsilon f_1} \left(w_{1,0} + \varepsilon w_{1,1}\right) dxdy \tag{5.32b}$$

Expanding the integral as a series in ε, using Leibniz rule, and neglecting terms of order higher than ε^1, we obtain

$$\begin{aligned} Q_1 = Q_{1,0} + \varepsilon \left(Q_{1,1} + Q_{1,f}\right) = \\ \int_{-1}^{1} \int_{-1}^{k} \left(w_{1,0}\right) dxdy + \varepsilon \left[\int_{-1}^{1} \int_{-1}^{k} \left(w_{1,1}\right) dxdy + \int_{-1}^{1} \left(f_1 w_{1,0}\left(x = k\right)\right) dy \right] \end{aligned} \tag{5.33a}$$

This expression for the flow rate is composed of three parts: (i) the flow rate through a straight channel at $O(\varepsilon^0)$: $Q_{1,0}$ (ii) the change in the flow rate because of the modification of the axial velocity: $Q_{1,1}$ (iii) the change in the flow rate due to the deformation of the interface: $Q_{1,f}$. The deformed interface causes the fluids to occupy different regions of the cross section, compared with their positions in a straight channel. The formula for Q_2 is derived analogously to that for Q_1:.

$$\begin{aligned} Q_2 = Q_{2,0} + \varepsilon \left(Q_{2,1} - Q_{2,f}\right) = \\ \int_{-1}^{1} \int_{k}^{1} \left(w_{2,0}\right) dxdy + \varepsilon \left[\int_{-1}^{1} \int_{k}^{1} \left(w_{2,1}\right) dxdy - \int_{-1}^{1} \left(f_1 w_{2,0}\left(x = k\right)\right) dy \right] \end{aligned} \tag{5.33b}$$

Comparing (5.33a) and (5.33b), we see that the deformation of the interface has opposite effects on the flow rates of the two fluids. If it increases the flow rate of the inner fluid, it decreases that of the outer fluid.

Using (5.33a) and (5.33b), we can calculate the flow rates of both fluids at the specified pressure drop and holdup. These formulas are essential for performing the reverse calculation iteratively, i.e. determining the pressure drop and holdup, when the flow rates are specified.

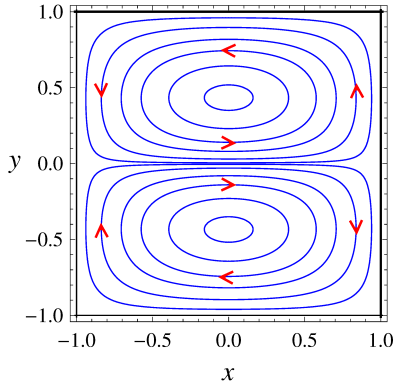

Figure 5.3: Secondary transverse flow (Dean vortices) in a rectangular channel (Dean, 1927; Cuming, 1952). This figure depicts the helical streamlines projected onto the cross-sectional plane. The Reynolds number is 10 and the aspect ratio is unity. The arrows indicate the direction of secondary flow.

5.4 Analysis of the circulatory flow

5.4.1 Basic circulatory flow patterns: principal, sandwich and reversed vortices

Before examining the two-phase flow field, it is instructive to consider the analogous single phase problem. At a low Reynolds number and a small curvature ratio, the fully developed flow field consists of two counter-rotating secondary vortices (Cuming, 1952). Fig. 5.3 is a plot of the streamlines for single phase flow, at $O(\varepsilon^1)$, projected onto the cross-sectional (x-y) plane. These projected streamlines are contours of the stream function at $O(\varepsilon^1)$. The fluid elements execute a helical motion as they move along the curved channel. These vortices are commonly known as Dean vortices, as they were first studied by Dean (1927) in flow through a curved channel of circular cross-section. This secondary circulatory flow exists for any non-zero Reynolds number, and is caused by a non-uniform distribution of centrifugal forces in the vertical (y) direction. The axial velocity is maximum at the centerline ($y = 0$) and decays to zero at the vertical bounding walls ($y = \pm 1$), where no-slip applies. Because the centrifugal force varies as the square of the axial velocity, the fluid at the channel's center is pushed outward (towards positive x) more strongly than the fluid near the vertical bounding walls. This inequality of forces causes fluid to flow outward along the centerline and recirculate along the vertical walls, resulting in a pair of counter-rotating vortices (Fig. 5.3).

In two-phase layered flow, similar vortex motions are present within each fluid. These circulatory flows are coupled to each other, since the tangential velocities and shear stresses of the two viscous fluids must be equal at the interface. This coupling results in five different flow patterns, which are discussed in this subsection.

Centrifugal forces act on the two fluids simultaneously, causing them to circulate.

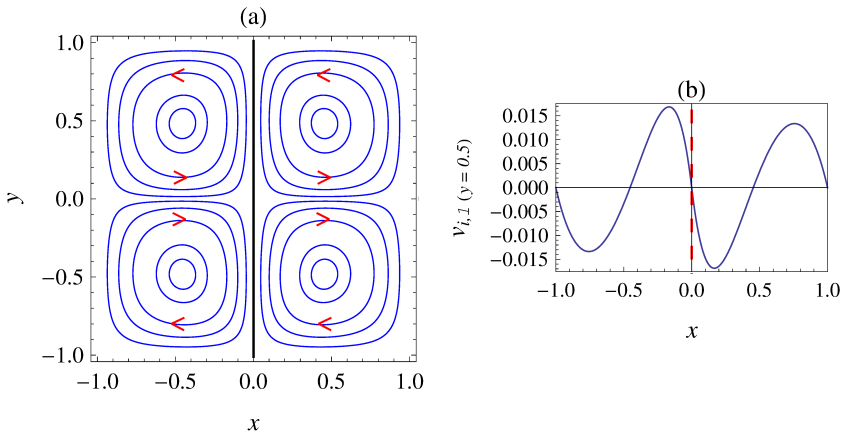

Figure 5.4: (a) Secondary vortices of the *principal-principal* (p-p) circulatory flow. The arrows indicate the direction of flow. (b) Plot of $vi, 1$ across the cross-section at $y = 0.5$. Parameter values: $k = 0$, $Re_1 = 50$, $Re_2 = 50$, $\mu_{12} = 1$, $\lambda = 1$. The inner wall of the channel is at $x = -1$ and the outer wall is at $x = +1$ (cf. Fig. 5.3). The contours of $\psi_{i,1}$ plotted in (a) are selected to reveal the structure of the circulatory flow. The relative magnitude of the cross-flow in each fluid may be inferred from (b).

As fluid cannot cross the interface, one would expect to find a separate pair of counter-rotating Dean vortices in each fluid. An example of this flow pattern is shown in Fig. 5.4a, which depicts the secondary vortices at $O(\varepsilon^1)$, by plotting contours of the stream function $\psi_{i,1}$. In this case, both fluids circulate in the same manner as they would in single phase flow; the vortex motion is dictated solely by the centrifugal force. We call these vortices principal vortices and name this flow pattern the *principal-principal* (p-p) flow.

A distinguishing feature of principal-principal (p-p) flow is that the vertical motion $(v_{i,1})$ of the fluids is in opposite directions on either side of the interface. Such a flow would violate continuity of the velocity field, unless $v_{i,1}$ is identically zero at the interface. Fig. 5.4b shows that this is indeed the case. This figure depicts the y-component of velocity $v_{i,1}$ across the cross-section, at $y = 0.5$. In this figure, we see that $v_{i,1}$ is zero at five locations. Three of these zeros correspond to the inner wall, the outer wall and the interface. The two zeros of $v_{i,1}$ within each fluid correspond closely to the centers of the principal vortices. Note that the derivative of $v_{i,1}$ is positive at the two principal vortex zeros.

The principal-principal flow pattern is a very special case, in which the circulatory flow in the two fluids is perfectly balanced. This delicate balance occurs for a limited set of parameter values. (In the example depicted in Fig. 5.4, the Reynolds numbers, viscosities and volume fractions of the fluids are equal.) In a more general case, there will be an imbalance between the two circulatory flows, with one dominating the other. In such cases, the two fluids will not flow in opposite vertical directions near the interface. Instead, one of the fluids will dictate the flow near the interface and drag the other fluid along with it.

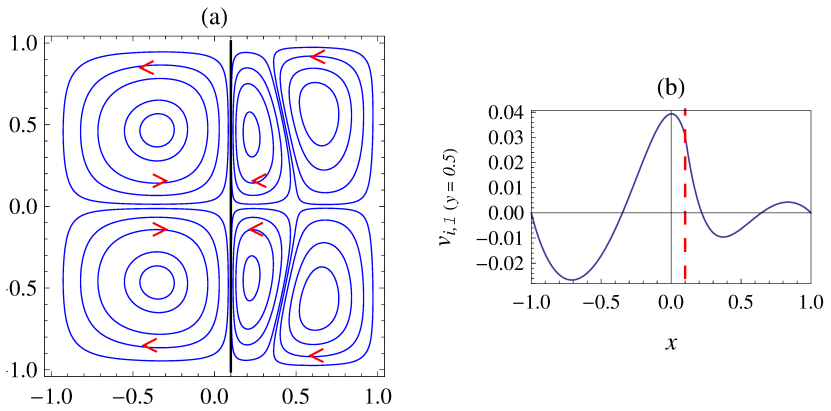

Figure 5.5: (a) Secondary vortices of the *principal-sandwich* circulatory flow. (b) plot of $v_{i,1}$ across the cross-section at $y = 0.5$. Parameter values: $k = 0.1$, $Re_1 = 50$, $Re_2 = 35$, $\mu_{12} = 2$, $\lambda = 1$.

In Fig. 5.5, an example in which the inner fluid (fluid 1) dominates the flow near the interface is depicted. Here, the inner fluid forces the outer fluid (fluid 2) to flow along with it, causing a local reversal of the circulatory flow within the outer fluid, near the interface. The result is that the inner fluid contains a principal vortex while the outer fluid has two vortices (Fig. 5.5a). A principal vortex is located away from the interface, while adjacent to the interface there is a vortex that circulates in a direction contrary to the influence of the centrifugal force (opposite to the principal vortex in the outer fluid). This vortex is called a sandwich vortex and is a result of the influence of the inner fluid on the outer one. This flow pattern is termed *principal-sandwich* (p-sw) flow.

The plot of $v_{i,1}$ at $y = 0.5$ (Fig. 5.5b) confirms that the velocity is not zero at the interface. Instead, there are now three zeros of $v_{i,1}(y = 0.5)$ within the fluid domains, rather than the two that were present in principal-principal flow. The two zeros at which the derivative of $v_{i,1}$ is positive corresponds to the principal vortices. The intermediate zero within fluid 2, at which the derivative is negative, represents the sandwich vortex.

Next, in Fig. 5.6, we illustrate a case that is the opposite of Fig. 5.5. This is *sandwich-principal* (sw-p) circulatory flow, in which the outer fluid dominates near the interface and causes a sandwich vortex to form within the inner fluid.

As the influence of one fluid on the other increases, the size of the sandwich vortex in the dominated fluid increases, relative to its principal vortex. Eventually the principal vortex disappears, and the flow in the dominated fluid is completely reversed. The sandwich vortex now occupies the entire dominated fluid, and is called a reversed vortex. An example, in which the outer fluid is reversed, is presented in Fig. 5.7. This flow pattern is called *principal-reversed* (p-r) flow. The opposite case of *reversed-principal* (r-p) flow is depicted in Fig. 5.8. Here, the inner fluid is reversed. In both these cases, the plot of $v_{i,1}$ at $y = 0.5$ shows one zero within the domain of each fluid. The derivative is positive

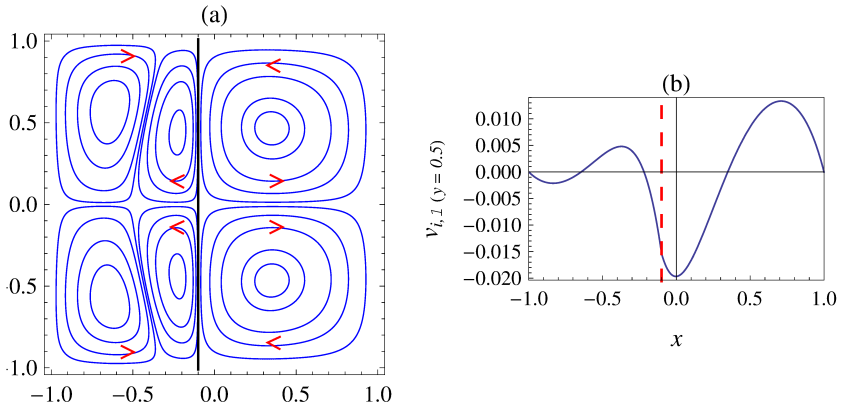

Figure 5.6: (a) Secondary vortices of the *sandwich-principal* circulatory flow. (b) plot of $v_{i,1}$ across the cross-section at $y = 0.5$. Parameter values: $k = -0.1$, $Re_1 = 35$, $Re_2 = 50$, $\mu_{12} = 1/2$, $\lambda = 1$.

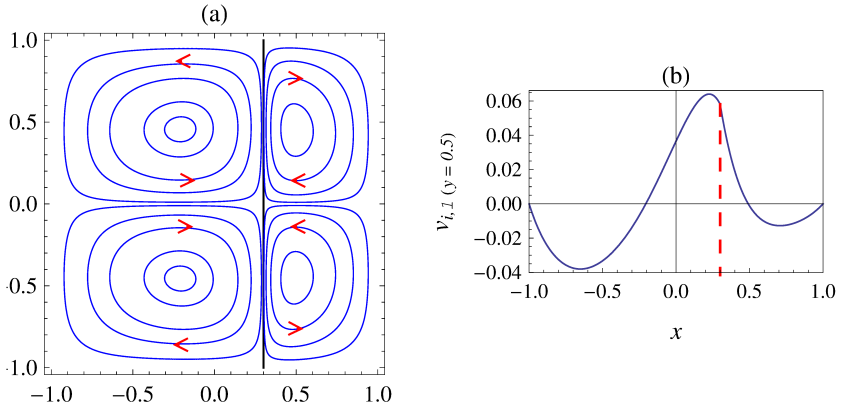

Figure 5.7: (a) Secondary vortices of the *principal-reversed* circulatory flow. (b) plot of $v_{i,1}$ across the cross-section at $y = 0.5$. Parameter values: $k = 0.3$, $Re_1 = 50$, $Re_2 = 20$, $\mu_{12} = 3$, $\lambda = 1$.

at the zero corresponding to the principal vortex and negative at the zero corresponding to the reversed vortex.

In this subsection, we have identified five different circulatory flow patterns: (i) principal-principal (p-p), (ii) principal-sandwich (p-sw), (iii) sandwich-principal (sw-p), (iv) principal-reversed (p-r) and (v) reversed-principal (r-p). Each flow pattern occurs over a different range of parameter values. Varying the parameters affects the competition between the two fluids, and changes the flow pattern. The role of each parameter is explained in the next subsection.

The circulatory flow field studied in this section does not include any effects of the deformed interface. This effect occurs at the higher order of ε^2; consequently the flow at $O(\varepsilon^1)$ is plotted on the base domain with an undeformed interface. At low capillary numbers, the deformation of the interface is very small (cf. Sec. 5.5), and its effect on the flow can be ignored to a good approximation.

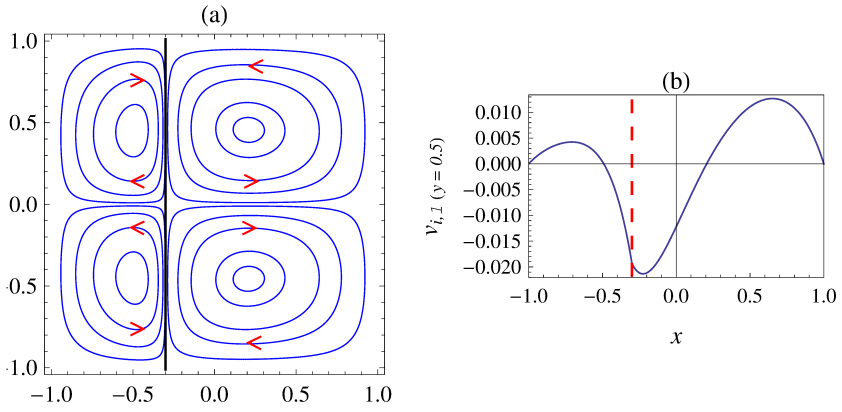

Figure 5.8: (a) Secondary vortices of the *reversed-principal* circulatory flow. (b) plot of $v_{i,1}$ across the cross-section at $y = 0.5$. Parameter values: $k = -0.3$, $Re_1 = 20$, $Re_2 = 50$, $\mu_{12} = 1/3$, $\lambda = 1$.

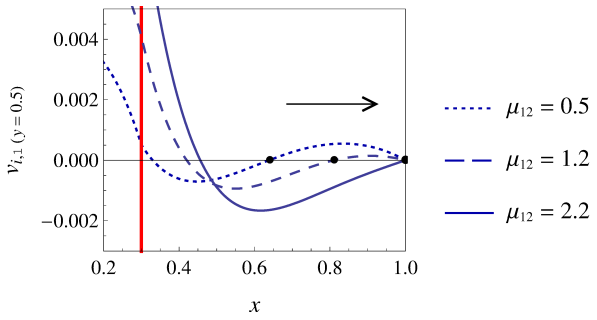

Figure 5.9: Transition from principal-sandwich to principal-reversed flow as the viscosity ratio is increased. The solid circle marks the location of the principal vortex in the outer fluid. As the viscosity ratio is increased, the principal vortex zero shifts towards the wall, eventually coinciding with the zero at $x = 1$. The parameter values are $k = 0.30$, $Re_1 = 10$, $Re_2 = 10$, $\lambda = 1$.

5.4.2 Construction of flow regime maps

In this section, we take advantage of the unique feature of each flow pattern to construct flow regime maps. The construction of these maps is greatly simplified because of the analytical solution obtained for the velocity field. These maps serve as a guiding tool for identifying the parameter values at which experiments or simulations should be carried out to obtain a desired flow pattern.

The information of the key features of each circulatory flow pattern, discussed in Sec. 5.4.1, is contained in the plot of $v_{i,1}(x, y = 0.5)$ (cf. Figs. 5.4b to 5.8b). The zeros of $v_{i,1}(x, y = 0.5)$ located within the two fluid domains ($-1 < x < k$ and $k < x < 1$ for fluids 1 and 2 respectively) correspond to different vortices. The nature of each vortex can be identified by the sign of the derivative of $v_{i,1}(x, y = 0.5)$ at the corresponding zero. At the transition between different flow regimes, the location of the zeros, and the corresponding derivatives, must satisfy special conditions. Using these conditions, we can find the boundaries of each flow regime in the parameter space.

The simplest condition corresponds to the principal-principal (p-p) flow. In this case, $v_{i,1}(x, y = 0.5)$ must be zero at the interface, $x = k$. Thus, the condition for (p-p) is

$$v_{1,1}\left(x = k, y = 0.5\right) = 0 \tag{5.34a}$$

Next, we identify the condition for the transition from a sandwich to a reversed vortex. As the sandwich vortex becomes larger, the principal vortex in the dominated fluid shrinks and move closer to the wall. Thus, the zero corresponding to the principal vortex moves towards the wall, where another zero of $v_{i,1}$ is located, due to the no-slip condition. This motion of the principal vortex zero is shown in Fig. 5.9, for the transition from principal-sandwich (p-sw) to principal-reversed (p-r) flow, as the viscosity ratio is increased. At the transition point, the zero of the principal vortex in fluid 2 merges with the zero at the wall, resulting in an extremum of $v_{2,1}(y = 0.5)$ at the wall. Thus, at the boundary between p-sw and p-r flow, the following condition must be satisfied:

$$\frac{d}{dx} v_{2,1}\left(x, y = 0.5\right) = 0 \quad \text{at } x = 1 \tag{5.34b}$$

A similar condition marks the boundary between sw-p and r-p flow:

$$\frac{d}{dx} v_{1,1}\left(x, y = 0.5\right) = 0 \quad \text{at } x = -1 \tag{5.34c}$$

Substituting the analytical solution for $v_{i,1}$, derived in Sec. 5.3.3, into the critical conditions (5.34a) to (5.34c) yields three relations among the five parameters – λ, Re_1, Re_2, μ_{12} and k (or the holdup, α). On fixing the values of any three parameters, one obtains a set of three curves in the plane of the remaining two free parameters. These curves divide the parameter plane into five flow regimes, yielding a flow regime map. Flow regimes maps on the $Re_1 - \mu_{12}$ plane are presented in Fig. 5.10 for the case of a square channel ($\lambda = 1$) and three different interface locations (different holdup values). The value of Re_2 is fixed at 10. Two sets of boundary curves are shown here. The dotted curves are approximate boundaries, computed by using only the first term of the analytical solution for $v_{i,1}$ – i.e we take $m = 1$ and $n = 1$ in (5.23a) and (5.23b) and use expression (B.6) for $s_{i,1}(x)$ (cf. Appendix B.1). These approximate dotted curves are relatively easy to calculate and can be obtained analytically (using symbolic computing software, e.g Mathematica). The other set of bold curves in Fig. 5.10 are the accurate boundaries, computed by using the converged solution for $v_{i,1}$ in (5.34a) to (5.34c) (at least five terms are used for $v_{i,1}$, i.e. $m = 5$ and $n = 5$). In this case, (5.34a) to (5.34c) are solved numerically by an iterative scheme, which uses the approximate dotted boundaries as initial guesses.

By analyzing the flow regimes maps in Fig. 5.10, we can understand the role of each parameter on the inter-fluid competition. This is the subject of the next subsection.

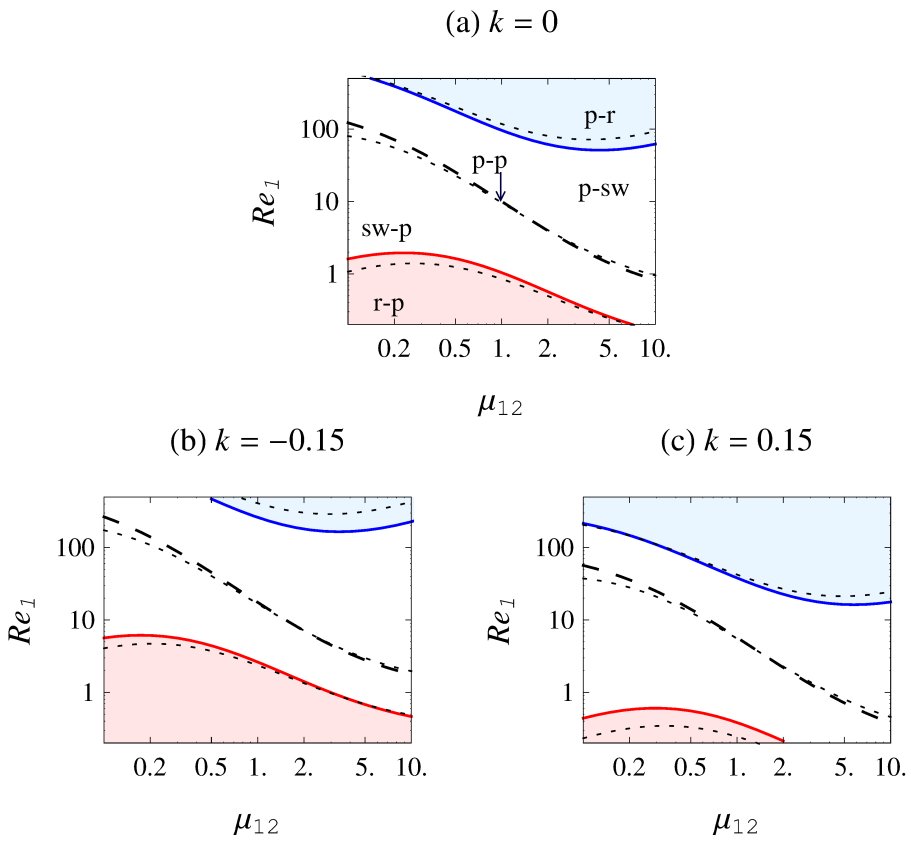

Figure 5.10: Flow regime maps that organize of the parameter space into five flow regimes: (1) principal-principal (p-p) (2) principal-sandwich (p-sw) (3) sandwich-principal (sw-p) (4) principal-reversed (p-r) (5) reversed-principal (r-p). Maps are presented for three values of the interface location (a) $k = 0$ (b) $k = -0.15$ (c) $k = +0.15$. In all cases $Re_2 = 10$, $\lambda = 1$. The dotted curves are approximate boundaries, computed analytically with an approximate one term solution for $v_{i,1}$. The bold curves are the accurate boundaries, computed numerically using the five term converged solution for $v_{i,1}$.

5.4.3 Influence of Reynolds numbers, viscosity ratio and holdup on inter-fluid competition

Along the p-p curve, in the flow regime maps (Fig. 5.10), the circulatory flows in the two fluids are precisely balanced. In the other four flow regimes, one of the fluids dominates the other. Fluid 1 dominates the flow in the p-sw and p-r regimes, while fluid 2 dominates in the sw-p and r-p regimes. Focusing on the line $\mu_{12} = 1$, in the case of $k = 0$ (Fig. 5.10a), we see that p-p flow occurs when $Re_1 = Re_2 = 10$. Increasing Re_1 results in fluid 1 dominating the flow (p-sw regime), while decreasing Re_1 leads to fluid 2 dominating (sw-p regime). The Reynolds number represents the relative strength of the inertial forces (including centrifugal force), compared to viscous forces. Thus a fluid tends to dominate the flow as its Reynolds number is increased relative to the other fluid.

Again, consider the principal-principal flow at $\mu_{12} = 1$, $k = 0$ and $Re_1 = Re_2 = 10$, but now vary μ_{12} while keeping Re_1 constant. We find that fluid 1 dominates (p-sw) if it has the higher viscosity, while fluid 2 dominates otherwise (sw-p). This effect of viscosity is caused by its role in the balance of tangential stresses. However, the viscosity ratio has a *subtle second effect* on the circulatory flow pattern, because of its influence over the axial velocity profile. The less viscous fluid flows with a greater average axial velocity, which results in stronger centrifugal forces within the less viscous fluid. At a relatively large viscosity contrast, this second effect comes to the fore and promotes the circulatory flow within the less viscous fluid. This is responsible for the minimum (maximum) in the boundary between the p-sw and p-r (sw-p and r-p) regimes. Increasing μ_{12} across the minima in Fig. 5.10a (e.g. while $Re_1 = 95$), causes a transition from p-sw to p-r and then back to p-sw. The first transition is due to the effect of μ_{12} via the interface boundary conditions, while the second transition occurs as a result of the effect of μ_{12} on the axial velocity profile. For moderate values of the viscosity ratio, the former effect is more significant, and the more viscous fluid dominates the flow.

The effect of the holdup (α, or k since $\alpha = (k+1)/2$), can be deduced by comparing the three maps in Fig. 5.10. Increasing the holdup of the inner fluid ($\alpha > 1/2, k > 0$), increases the region in which it dominates (compare Fig. 5.10b and Fig. 5.10c). This is because the effective Reynolds numbers, based on the actual width occupied by each fluid, are given by $(1 + k)^3 Re_1$ and $(1 - k)^3 Re_2$, for fluids 1 and 2 respectively (c.f. (5.2)). Similarly, the region in which the outer fluid dominates increases as the holdup of the outer fluid is increased (k is decreased).

In summary, *the fluid that dominates the flow will have one or more of these attributes: (a) a higher Reynolds number (b) a greater viscosity (c) occupy a larger portion of the channel.* The fluid that satisfies more of these criteria, or any one of them to a greater extent, will contain only a principal vortex, while the other fluid will have a

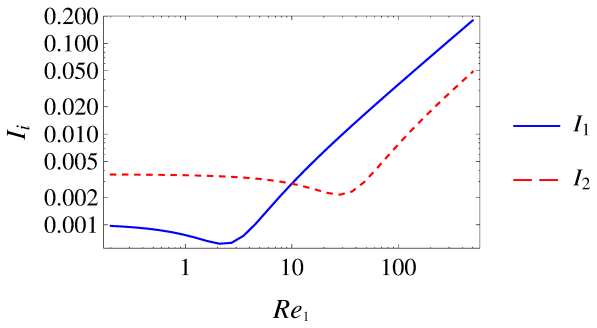

Figure 5.11: Circulatory flow intensities of both fluids as a function of Re_1. Parameter values: $k = 0$, $Re_2 = 10$, $\mu_{12} = 1$, $\lambda = 1$. As Re_1 is increased, the flow pattern changes according to the flow regime map in Fig. 5.10a.

sandwich or reversed vortex.

5.4.4 Intensity (strength) of the circulatory flow

In this section, we compare the strength of the transverse circulatory flow in the two fluids, for different flow regimes. To quantify the strength of the circulatory flow, we define a circulatory flow intensity for each fluid (I_i):

$$I_1 = \left[\int_{-1}^{+1} \int_{-1}^{k} \left(u_{1,1}^2 + v_{1,1}^2 \right) dxdy \right]^{1/2} \quad \text{and} \quad I_2 = \left[\int_{-1}^{+1} \int_{k}^{+1} \left(u_{2,1}^2 + v_{2,1}^2 \right) dxdy \right]^{1/2} \tag{5.35}$$

Consider the case of $k = 0$, $\mu_{12} = 1$, $Re_2 = 10$, $\lambda = 1$. On varying Re_1 from 0.5 to 200, we encounter all five flow regimes, as shown in Fig. 5.10a. The variation in the circulation intensities of the two fluids, as Re_1 is increased, is plotted in Fig. 5.11. We observe that the two fluids have equal intensities for the case of principal-principal flow, i.e. when $Re_1 = 10$. This is consistent with the fluids being in balance. For $Re_1 > 10$, the flow pattern changes to principal-sandwich flow, and then to principal-reversed flow at even higher Re_1 (cf. Fig. 5.10a). Fig. 5.11 shows that the circulation intensity is stronger in fluid 1 for these flow regimes, which confirms that fluid 1 dominates the flow. Similarly, we see that fluid 2 circulates more strongly in the sandwich-principal and reversed-principal regimes, corresponding to $Re_1 < 10$. These results show that *the fluid with only a principal vortex does indeed dominate the other fluid, which has a sandwich or reversed vortex.*

The non-monotonic variation of I_i (cf. Fig. 5.11) is due to the sandwich vortices. Consider the variation of I_1. At high Re_1, fluid 1 contains only a principal vortex, the strength of which depends on Re_1. Thus, decreasing Re_1 also decreases I_1. However, once Re_1 becomes less than 10, a sandwich vortex is formed within fluid 1. The strength

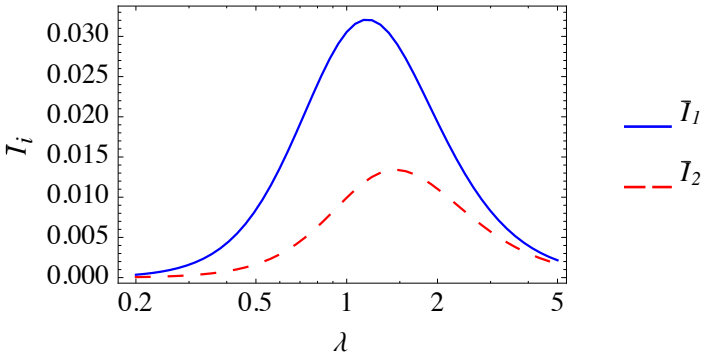

Figure 5.12: Circulatory flow intensity as a function of the aspect ratio of the channel. Parameter values: $k = 0$, $Re_1 = 50$, $Re_2 = 50$, and $\mu_{12} = 2$.

of this sandwich vortex depends on Re_2, which is constant in this case. Decreasing Re_1 further makes the principal vortex smaller and weaker, while the sandwich vortex, whose strength is independent of Re_1 grows. Once the sandwich vortex becomes sufficiently large, it causes the value of I_1 to rise again. This accounts for the minimum in the curve. A similar explanation applies to the profile of I_2.

5.4.5 Effect of the aspect ratio on the strength of circulations

In the previous sections, we have studied the circulatory flow in a square channel $(\lambda = 1)$. The flow patterns described will be observed for other aspect ratios as well (not too far from unity), and the procedure outlined in Sec. 5.4.2 can be followed to construct flow regime maps. In this section, we focus on the effect of the aspect ratio on the *intensity* of circulations. This study will help improve designs for curved channels meant to enhance mixing and mass transfer by exploiting Dean vortex flow.

In order to have a fair basis for comparing channels of different aspect ratios, the cross sectional area of the channel is kept constant at a value of $4a^2$. Then a channel of aspect ratio λ must have a width of $2a\sqrt{\lambda}$ and a height of $2a/\sqrt{\lambda}$. If instead one kept the width of the channel constant, then the cross sectional area for flow $(4ab = 4a^2/\lambda)$ will decrease as the aspect ratio is increased. Since the applied pressure drop is the same in all channels, the larger aspect ratio channels (with smaller area of cross section) will have a much smaller axial flow; this in turn will result in a small intensity of circulation. To eliminate this bias, we keep the cross-sectional area constant and change both the width and height to obtain channels of different aspect ratios.

Another subtlety, related to the Reynolds numbers and characteristic velocity scales, arises while comparing channels of different aspect ratios. Since the width of each channel is different, the corresponding Reynolds numbers and velocity scales will differ; these will be equal to $\lambda^{3/2}Re_i$, and $\lambda V_{c,i}$ respectively, where Re_i and $V_{c,i}$ are the Reynolds num-

bers and velocity scales for a square channel. While comparing the values of the intensity factors, we take $V_{c,i}$ as the common scale. Thus the intensity factor for flow in a curved channel, of aspect ratio λ and cross sectional area $4a^2$, that is driven by a pressure drop of $-GR$ is:

$$\bar{I}_1 = \lambda^{3/2}\left[\int_{-1}^{+1}\int_{-1}^{k}\left(u_{1,1}^2+v_{1,1}^2\right)dxdy\right]^{1/2} \quad \text{and} \quad \bar{I}_2 = \lambda^{3/2}\left[\int_{-1}^{+1}\int_{k}^{+1}\left(u_{2,1}^2+v_{2,1}^2\right)dxdy\right]^{1/2} \tag{5.36}$$

In these formula, Re_i is replaced by $\lambda^{3/2}Re_i$ while calculating $u_{i,1}$ and $v_{i,1}$, to account for the changing dimensions of the channel as the aspect ratio is varied.

In Fig. 5.12, the intensity of circulation is plotted as a function of the aspect ratio for the case of $k = 0$, $Re_1 = 50$, $Re_2 = 50$, and $\mu_{12} = 2$. In this case, fluid 1 dominates the flow and its circulatory flow intensity is higher than that in fluid 2. Fig. 5.12 clearly shows that the intensity of the transverse flow is strongly influenced by the choice of the aspect ratio of the channel. Interestingly, there is a distinct peak in the circulatory flow intensity profiles of each fluid. Moreover, the aspect ratio at which the circulation intensity is maximum is different for each fluid. We denote these aspect ratios as $\lambda_{max,i}$. In Fig. 5.12, the circulation intensity in fluid 1 and fluid 2 peaks at $\lambda_{max,1} = 1.17$ and $\lambda_{max,2} = 1.52$, respectively.

Channels designed to enhance transport by using curved sections will perform best at high circulation intensities. Therefore, these channels should be designed with aspect ratios close to either $\lambda_{max,1}$ or $\lambda_{max,2}$. Most microfluidic extraction studies reported in the literature have been carried out in wide channels with aspect ratios about 2 and greater. In Fig. 5.12, it can be seen that the circulation intensity in fluid 1 for $\lambda = 2$ is significantly lower than the value at $\lambda_{max,1} = 1.17$. Thus, curved channels that are intended to enhance transport should be designed with an aspect ratio closer to $\lambda_{max,i}$. In Tab. 5.1, we present values of $\lambda_{max,1}$ and $\lambda_{max,2}$ for a range of parameter values. It is found that $\lambda_{max,i}$ depends on the ratio of Reynolds numbers rather than their individual magnitudes. In addition it is a function of the interface location (k) and the viscosity ratio (μ_{12}).

5.5 Deformation of the Interface

The interface between the fluids deforms in response to normal stresses associated with centrifugal forces and the circulatory flow. This deformation is counteracted by capillary forces. We investigate the shape of the interface, and its dependence on physical parameters, in this section.

$\lambda_{max,1}$ / $\lambda_{max,2}$					
k = -0.3					
μ_{12} \ Re_1 / Re_2	1/10	1/5	1	5	10
1/10	0.75 / 0.81	0.75 / 0.81	0.73 / 0.81	2.13 / 0.81	2.10 / 0.80
1/5	0.77 / 0.84	0.77 / 0.84	0.75 / 0.83	1.96 / 0.83	1.90 / 0.83
1	0.85 / 0.96	0.83 / 0.96	0.76 / 0.97	1.44 / 1.00	1.39 / 1.07
5	0.89 / 1.14	0.84 / 1.14	1.37 / 1.16	1.28 / 1.22	1.27 / 1.23
10	0.89 / 1.19	0.87 / 1.20	1.33 / 1.21	1.27 / 1.25	1.26 / 1.27
k = 0					
μ_{12} \ Re_1 / Re_2	1/10	1/5	1	5	10
1/10	0.94 / 1.09	0.93 / 1.09	1.77 / 1.09	1.71 / 1.10	1.70 / 1.12
1/5	0.95 / 1.11	0.93 / 1.11	1.68 / 1.11	1.60 / 1.15	1.59 / 1.24
1	0.98 / 1.24	1.18 / 1.25	1.32 / 1.32	1.25 / 1.18	1.24 / 0.98
5	1.24 / 1.58	1.15 / 1.60	1.11 / 1.68	1.11 / 0.93	1.11 / 0.95
10	1.12 / 1.70	1.10 / 1.71	1.09 / 1.77	1.09 / 0.93	1.09 / 0.94
k = 0.3					
μ_{12} \ Re_1 / Re_2	1/10	1/5	1	5	10
1/10	1.27 / 1.26	1.25 / 1.27	1.21 / 1.33	1.20 / 0.87	1.19 / 0.89
1/5	1.23 / 1.27	1.22 / 1.28	1.16 / 1.37	1.14 / 0.84	1.14 / 0.89
1	1.07 / 1.39	1.00 / 1.43	0.97 / 0.76	0.96 / 0.83	0.96 / 0.85
5	0.83 / 1.90	0.83 / 1.97	0.83 / 0.75	0.84 / 0.77	0.84 / 0.77
10	0.80 / 2.07	0.81 / 2.18	0.81 / 0.73	0.81 / 0.75	0.81 / 0.75

Table 5.1: The aspect ratios at which the circulatory flow intensity ($\bar{I}_i$) is maximum in fluid 1 ($\lambda_{max,1}$) and fluid 2 ($\lambda_{max,2}$).

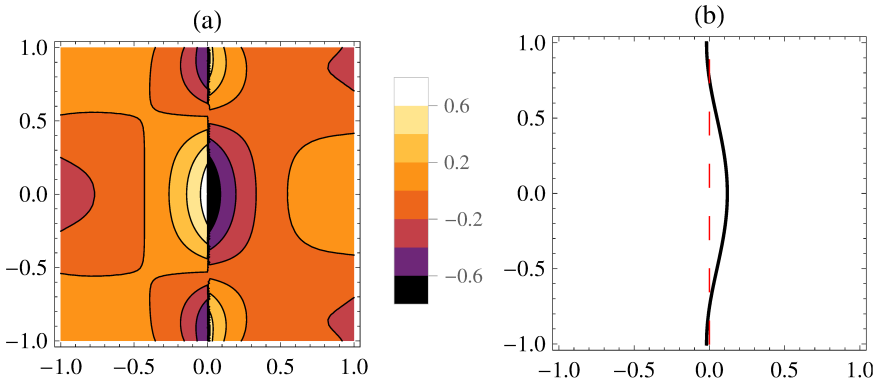

Figure 5.13: Pressure distribution and interface deflection corresponding to the principal-principal vortex flow depicted in Figs. 5.4. (a) Pressure distribution at $O(\varepsilon^1)$ across the cross section of the channel (b) the deflected interface at $O(\varepsilon^1)$. The curvature ratio is taken as $\varepsilon = 0.1$ and the capillary number as $Ca = 5$. The other parameters: $k = 0$, $Re_1 = 50$, $Re_2 = 50$, $\mu_{12} = 1$, $\lambda = 1$.

5.5.1 Generic features of the deflected interface

The pressure distribution across the cross-section of the channel and the deformation of the interface were calculated simultaneously using the normal stress balance at $O(\varepsilon^1)$, in Sec. 5.3.4. In Fig. 5.13, the pressure distribution and the interface configuration, at $O(\varepsilon^1)$, are depicted for the simple case of identical fluid properties. The corresponding principal-principal circulatory flow was illustrated in Fig. 5.4. As in the case of the circulatory flow at $O(\varepsilon^1)$, the pressure distribution at $O(\varepsilon^1)$ is depicted on the base domain (with a flat interface); the deflection of the interface will impact the pressure field only at $O(\varepsilon^2)$.

Fig. 5.13a clearly shows a pressure jump across the interface. At the centerline $(y = 0)$, the pressure is higher on the inner side of the interface, which causes it to bulge outward. Near the top and bottom walls, the pressure is slightly higher on the outer side, causing the interface to shift marginally towards the inner wall. The new interface shape, at $O(\varepsilon^1)$, is plotted in Fig. 5.13b. The deformed interface has a mean curvature in the cross-sectional plane. The capillary forces associated with this curvature counter-act the pressure jump and viscous normal stresses exerted by the flow, thus maintaining the balance of normal stresses to $O(\varepsilon^1)$ at the interface.

Fig. 5.14 displays the deformed interface for four other cases, whose circulatory flow is plotted in Fig. 5.5 to Fig. 5.8. These correspond to the other four flow regimes. In these calculations the curvature ratio is taken as $\varepsilon = 0.1$ and the Capillary number as $Ca = 5$.

From Fig. 5.13b and Fig. 5.14, we identify the following generic features of the interface, which are independent of the parameter values. (i) The interface is deflected towards the outer half of the channel. (ii) The deflected interface is symmetric about the horizontal centerline $(y = 0)$. This is consistent with the symmetry of the axial velocity and the circulatory flow. (iii) The deformation is maximum at the horizontal centerline

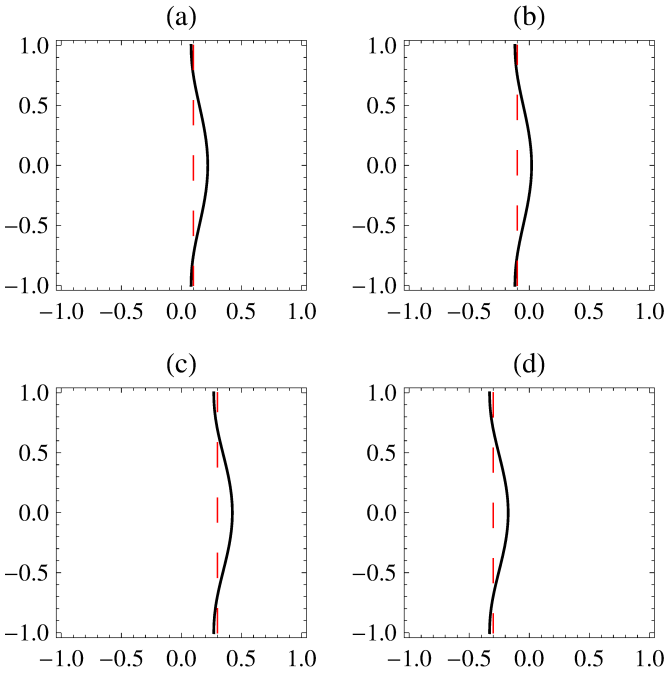

Figure 5.14: The deflected interface corresponding to the flow patterns shown in Fig. 5.5 to Fig. 5.8. (a) principal-sandwich: $k = 0.1$, $Re_1 = 50$, $Re_2 = 35$, $\mu_{12} = 2$ (b) sandwich-principal: $k = -0.1$, $Re_1 = 35$, $Re_2 = 50$, $\mu_{12} = 1/2$ (c) principal-reversed: $k = 0.3$, $Re_1 = 50$, $Re_2 = 20$, $\mu_{12} = 3$ (d) reversed-principal: $k = -0.3$, $Re_1 = 20$, $Re_2 = 50$, $\mu_{12} = 1/3$. In all cases, $\varepsilon = 0.1$, $Ca = 5$ and $\lambda = 1$.

$(y = 0)$. Since the axial velocity is maximum at $y = 0$, the centrifugal force acts most strongly here.

As per the input specification (5.12), the holdup (volume fraction) of each fluid in the curved channel should be the same as that in the straight channel. Fig. 5.13b and Fig. 5.14 seem to contradict this condition, since the inner fluid is shown to occupy a larger portion of the cross section when the channel is curved. This apparent contradiction is resolved when we realize that the volume per unit area of cross section is lower in the inner half of the curved channel (the volume corresponding to an element of cross-section $\Delta x \Delta y$ located at x is $(R + x)\Delta\theta\Delta x\Delta y$ and $x < 0$ on the inner half). Thus, the holdup specification is indeed satisfied by the interface shapes in Fig. 5.13b and Fig. 5.14.

5.5.2 Effect of parameters on the deformation of the interface

While the basic features of the deflected interface, discussed in Sec. 5.5.1, are parameter independent, the extent of deformation depends on the parameters. According to the perturbation expansion (5.13b), the magnitude of interface deformation increases linearly with the curvature ratio, at $O(\varepsilon^1)$. In this section, we study the effect of other parameters. To measure the extent of deformation, we calculate the magnitude of the difference between the positions of the interface at the center of the channel and at the top wall, i.e.

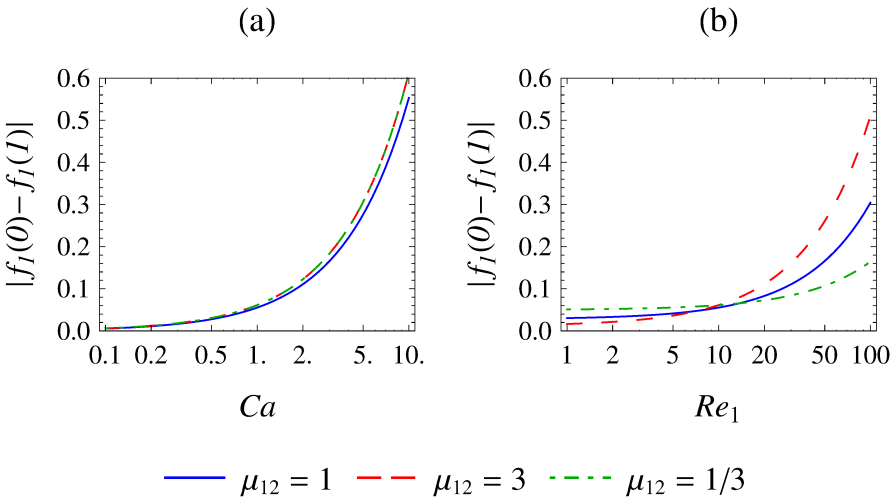

Figure 5.15: Variation of the extent of interface deformation as a function of the parameters. (a) Variation with the Capillary number (Ca), for $Re_1 = 10$. (b) Variation with the Reynolds number of the inner fluid Re_1, for $Ca = 1$. Three viscosity ratios are considered in each case. Other parameter values are: $k = 0$, $Re_2 = 10$, $\lambda = 1$.

$\left|f_1(0) - f_1(1)\right|$. This quantity may be viewed as the magnitude of a three point central difference approximation to $\frac{d^2 f_1}{dy^2}$; it is indicative of the curvature of the interface in $x - y$ plane. Clearly, $\left|f_1(0) - f_1(1)\right|$ is zero for a flat interface.

The Capillary number (Ca) accounts for the interfacial tension acting on the interface; it is the ratio of the viscous forces to capillary forces and is defined as $Ca = \mu_1 v_c/\gamma = Ga^2/\gamma$. When Ca is small, interfacial forces are relatively strong and the interface is deformed to a smaller extent. This is shown in Fig. 5.15a, in which the variation of $\left|f_1(0) - f_1(1)\right|$ with Ca is plotted for three different viscosity ratios. In microchannels, (a) ranges from $O(10^{-4})$ to $O(10^{-5})$ meters and Ca can be very small. As an example, layered flow of water and toluene, at equal flow rates of 200 μL/min, in a channel of width 300 μm and height 150 μm has $Ca \approx 10^{-2}$ (Fries *et al.*, 2008). Thus, Fig. 5.15 implies that the interface remains relatively undeformed in layered micro flows.

Next, we consider the effect of the Reynolds number. In Fig. 5.15b, $\left|f_1(0) - f_1(1)\right|$ is plotted as a function of Re_1, while Re_2 and Ca are kept constant at 10 and unity respectively. The extent of deformation increases as the Reynolds number increases. This is to be expected since higher Reynolds numbers imply stronger centrifugal forces and a stronger circulatory flow.

We can gain some insight into the effect of the vortex pattern on the interface deformation, by studying the curves for different viscosity ratios in Fig. 5.15. In Fig. 5.15a, we see that the interface deforms the least when $\mu_{12} = 1$. This corresponds to principal-principal flow. The interface deformation is larger by equal amounts in the other two cases: $\mu_{12} = 3$ and $\mu_{12} = 1/3$, which correspond to principal-sandwich and sandwich-principal flow respectively. Thus, the presence of a sandwich vortex, in either fluid,

increases the deformation of the interface. This also explains the results in Fig. 5.15b. Here, when $Re_1 > Re_2$, the interface deforms the most for $\mu_{12} = 3$. This is because the sandwich vortex in fluid 2 is largest in this case. Similarly, when $Re_1 < Re_2$, the deformation is most for $\mu_{12} = 1/3$, for which the sandwich vortex in fluid 1 is large.

5.6 Axial velocity and flow rates in a curved channel

5.6.1 Redistribution of axial velocity: geometric and inertial effects

The axial velocity profile (w_i) in a curved channel differs from that in a straight one. This redistribution of the axial velocity is most clearly visible in the shifted location of the maximum of w_i. The redistribution is caused by two different factors, called the geometric and inertial effects (Picardo and Pushpavanam, 2013).

The geometric effect arises due to the difference in axial path lengths on the inner and outer halves of the channel. On the inner side, the axial path from θ_1 to θ_2 is $(R - ax)(\theta_2 - \theta_1)$, while on the outer side it is $(R + ax)(\theta_2 - \theta_1)$. As the path length is shorter on the inner side, the pressure gradient is larger ($\frac{dP}{d\theta}$ is constant for fully developed flow). This causes the axial velocity to be higher on the inner half of the curved channel. This effect is contained in the first term on the RHS of (5.3d), and is captured by the domain perturbation equations at $O(\varepsilon^1)$ as the last term on the RHS of (5.28). In addition, the viscous diffusion of momentum from the centerline to the walls of the channel also causes the velocity to be higher on the inner side, where the volume per unit $\Delta\theta$ is lower (captured by the second last term on the RHS of (5.28)).

The inertial effect refers to the redistribution of axial velocity by the circulations in the curved channel. The circulatory flow transports axial momentum, across the cross-section, along its streamlines (cf. the terms multipled by Re_i on the RHS of (5.28)). In single phase flow, this effect shifts the maximum axial velocity towards the outer half of the channel, since the Dean vortices flow from the inside towards the outside of the channel, along the horizontal centerline $(y = 0)$ (Cuming, 1952). In two-phase layered flow, the circulatory flow will redistribute the axial velocity within each fluid separately, as there is no flow across the interface.

The geometric and inertial effects act simultaneously, attempting to modify the axial velocity profile in significantly different ways. Their relative importance is decided by the values of the Reynolds numbers and curvature ratio. The inertial effect becomes more pronounced as the Reynolds numbers are increased, since the strength of the circulatory flow increases. The geometric effect, on the other hand depends only on the curvature ratio. Thus at low Re, the geometric effect dictates the redistribution of axial velocity,

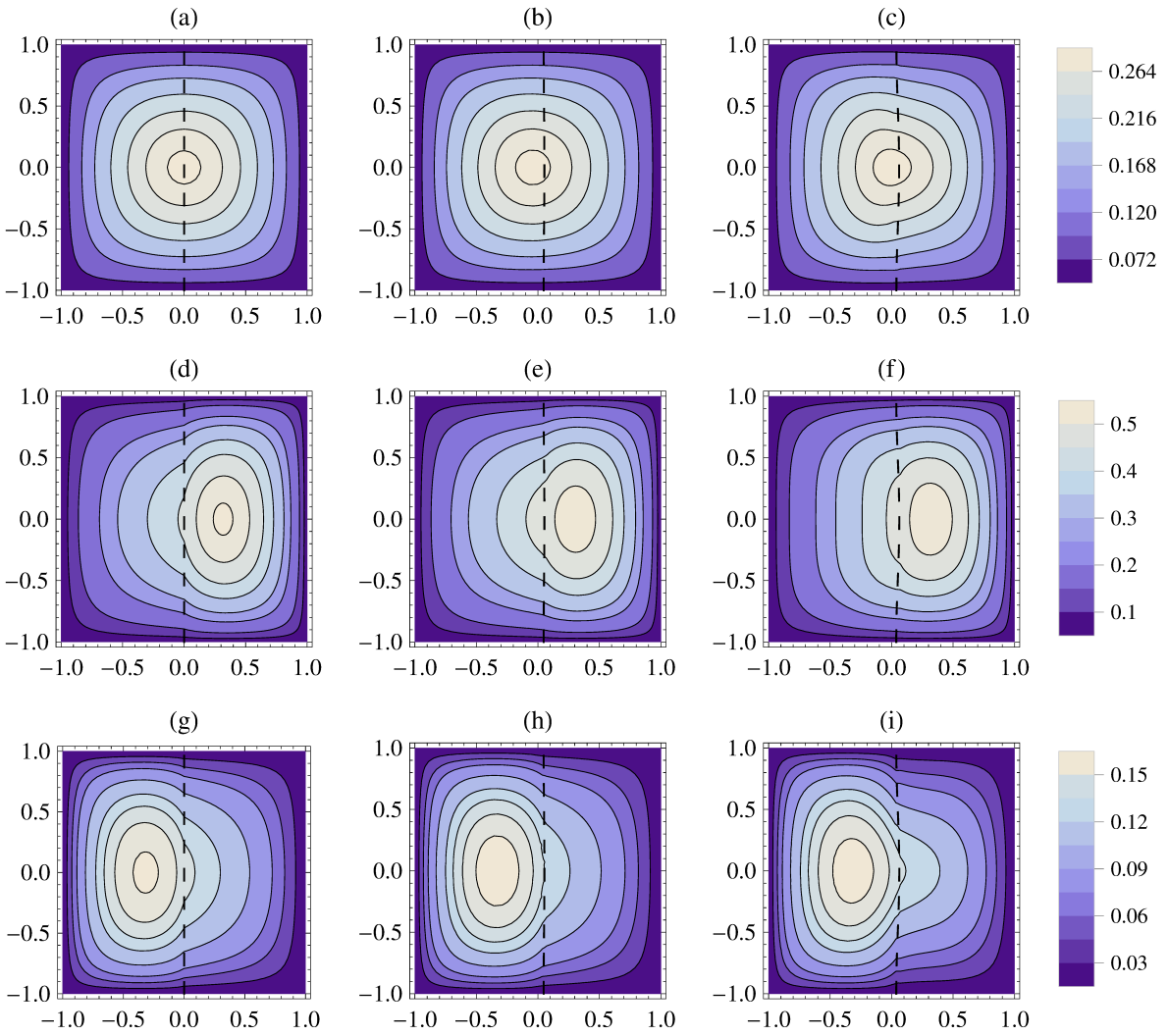

Figure 5.16: Contour plots of the axial velocity in a curved channel at $O(\varepsilon^1)$, $w_{i,0} + \varepsilon w_{i,1}$. The figures in each row are plotted for a different viscosity ratio: The first row (Figs. (a), (b), (c)) has $\mu_{12} = 1$, while the second and third rows correspond to $\mu_{12} = 3$ and $\mu_{12} = 1/3$, respectively. The first column (Figs. (a), (d), (g)) depicts the axial velocity contours for flow in straight channels, while the other two columns show the modified contours for flow in a curved channel of $\varepsilon = 0.1$. The second column (Figs. (b), (e), (h)) corresponds to $Re_1 = Re_2 = 50$, while the third column (Figs. (c), (f), (i)) corresponds to $Re_1 = Re_2 = 200$. Other parameter values: $k = 0$, $\lambda = 1$, $Ca = 0.2$, $\varepsilon = 0.1$.

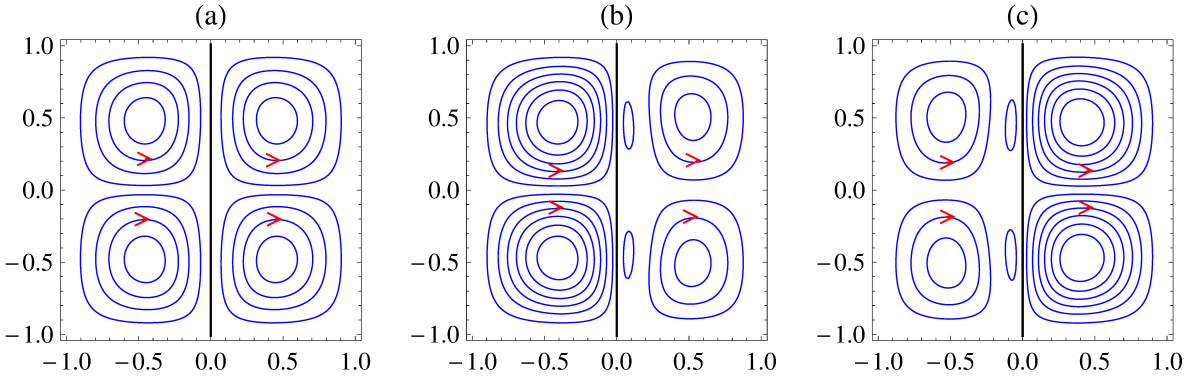

Figure 5.17: Secondary circulations for the three cases studied in Fig. 5.16. (a) $\mu_{12} = 1$ (b) $\mu_{12} = 3$ and (c) $\mu_{12} = 1/3$. The circulation streamlines at $O(\varepsilon^1)$ are the same for both $Re_1 = Re_2 = 50$ and 200, although the magnitude of the cross flow is higher in the latter case. In these plots, the contours of the stream function are plotted at equal intervals; the spacing between the contour lines is indicative of the strength of circulation – less spacing implies a stronger circulatory flow. Other parameter values: $k = 0$, $\lambda = 1$.

while at higher Re, the inertial effect becomes more important.

Keeping these two effects in mind, we now examine the axial velocity profile in a curved channel for different parameter values. In Fig. 5.16, contours of the axial velocity at $O(\varepsilon^1)$ $(w_{i,0} + \varepsilon w_{i,1})$ are plotted for nine different cases. Each row of plots corresponds to a different viscosity ratio (μ_{12} = 1, 3, $1/3$ respectively). The first column depicts the contours for a straight channel $(\varepsilon = 0)$, while the other two columns show contours for a curved channel with a curvature ratio of $(\varepsilon = 0.1)$. The plots in the second (third) column correspond to a case of relatively low (high) Reynolds numbers: $Re_1 = Re_2 = 50$ (200). The streamlines of the circulatory flow corresponding to Figs. 5.16b and 5.16c are presented in Fig. 5.17a. The circulatory flow corresponding to Figs. 5.16e and 5.16f is depicted in Fig. 5.17b, and that of Figs. 5.16h and 5.16i is depicted in Fig. 5.17c.

In the case of $Re_1 = Re_2 = 50$ (Figs. 5.16b, 5.16e, 5.16h), the geometric effect is dominant. Hence, the axial velocity increases on the inner side of the curved channel. This is apparent on comparing Fig. 5.16b, Fig. 5.16e and Fig. 5.16h, for the curved channel, with Fig. 5.16a, Fig. 5.16d and Fig. 5.16g, for the straight channel, respectively. The contours are clearly shifted towards the inner wall of the curved channel. However, the shape of the contours remain unchanged, since the inertial effect is insignificant at these low Reynolds numbers.

Next, we consider the case of higher Reynolds numbers, $Re_1 = Re_2 = 200$. The axial velocity contours are plotted in the third column of Fig. 5.16 (subplots (c),(f),(i)). The streamlines of the circulatory flow corresponding to these three cases are presented in Fig. 5.17a, Fig. 5.17b and Fig. 5.17c, respectively. Due to the higher value of Re, the inertial effect is dominant and the axial velocity profile is modified by the circula-

μ_{12}	Re_1=Re_2	$Q_{1,0}$	$Q_{2,0}$	$Q_{1,0}$+$Q_{2,0}$	$Q_{1,1}$	$Q_{2,1}$	$Q_{1,f}$=-$Q_{2,f}$	Q_1	Q_2	Q_1+Q_2
1	50	0.281	0.281	0.562	0.079	-0.079	0.206	0.310	0.253	0.562
1	200	0.281	0.281	0.562	0.030	-0.029	0.215	0.306	0.257	0.562
3	50	0.365	0.593	0.958	0.146	-0.293	0.309	0.410	0.533	0.943
3	200	0.365	0.593	0.958	0.051	-0.180	0.325	0.402	0.543	0.945
1/3	50	0.198	0.122	0.319	0.098	-0.049	0.103	0.218	0.106	0.324
1/3	200	0.198	0.122	0.319	0.060	-0.017	0.108	0.215	0.109	0.324

Table 5.2: The flow rate in a curved channel at $O(\varepsilon^1)$ for parameter values corresponding to the cases illustrated in 5.16. (Q_i): flow rates in a curved channel; $(Q_{i,0})$: flow rates in a straight channel; $(\varepsilon Q_{i,1})$: the change due to the axial velocity redistribution; $(\varepsilon Q_{f,i})$: the change due to the interface deformation. Other parameter values are: $k = 0$, $\lambda = 1$, $Ca = 0.2$, $\varepsilon = 0.1$.

tory flow. Comparing the modified axial velocity contours in Fig. 5.16c, Fig. 5.16f and Fig. 5.16i with the corresponding contours in the straight channel, Fig. 5.16a, Fig. 5.16d and Fig. 5.16g respectively, we see that the contours are distorted by transport of axial momentum along the streamlines of the circulatory flow. In Fig. 5.16f, the contours are more distorted within the inner fluid, since the circulatory flow is stronger in the inner fluid (cf. Fig. 5.17b). Similarly, the axial velocity contours are more distorted within the outer fluid in Fig. 5.16i, as the outer fluid has a stronger circulatory flow in this case (cf. Fig. 5.17c).

5.6.2 Change in the flow rates of the fluids

Due to a redistribution of axial velocity, the flow rates of the fluids in a curved channel will differ from their values in a straight channel. The flow rates are also modified by the deformation of the interface, which changes the region of the cross section occupied by each fluid. (As is the case throughout this chapter, the pressure drop and holdup in the curved channel is kept the same as that in the straight channel.) In Sec. 5.3.5, we derived formulas (5.33a) and(5.33b) for the flow rates in a curved channel (Q_i), in terms of the flow rates in a straight channel $(Q_{i,0})$, the change due to axial velocity redistribution $(\varepsilon Q_{i,1})$ and the change due to interface deformation $(\varepsilon Q_{f,i})$. These quantities are computed for the six curved channel flows studied in Fig. 5.16 (subplots (b), (c), (e), (f), (h), (i)). The results are presented in Tab. 5.2. Here, the velocity in both fluids is scaled with the same scale (Ga^2/μ_1) to enable a fair comparison.

The results in Tab. 2 show that the effect of the interface deformation on the flow rates $Q_{i,f}$ is considerably more than that due to the axial velocity redistribution $Q_{i,1}$. However, $Q_{i,f}$ will decrease as the capillary number (Ca) becomes smaller, since the interface will become flatter and less deformed (cf. Sec. 5.5.2). We also note that $Q_{1,f}$ is always positive while $Q_{2,f}$ is always negative. This implies that the interface deformation increases the flow rate of the inner fluid, while decreasing that of the outer fluid. The

interface deflects outward along the horizontal centerline ($y = 0$), allowing more of the inner fluid to occupy the central portion of the channel. Since the axial velocity is higher near the center of the channel, the flow rate of the inner fluid is increased. Tab. 2 also shows that $Q_{1,1}$ is always positive, while $Q_{2,1}$ is always negative. This is caused by the geometric effect, which increases the axial velocity on the inner half of the channel.

In addition to the effects of interfacial deformation and axial velocity redistribution, the flow rates will be reduced by another factor at $O(\varepsilon^2)$. This reduction is due to the energy cost of driving the circulatory flow. This $O(\varepsilon^2)$ effect has been observed for single phase flow, wherein the flow rates remain unchanged at $O(\varepsilon^1)$. This is in contrast to the present case of laterally layered flow, wherein the flow rate changes are more significant and occur at $O(\varepsilon^1)$.

5.7 Three dimensional numerical simulations

In this section, we carry out numerical simulations of the nonlinear governing equations (5.3a)-(5.12), for finite Reynolds numbers and curvature ratios. By comparing these results with the perturbation solution, we identify the range of Reynolds numbers and curvature ratios for which the first order perturbation solution is accurate. Simulations are carried out, assuming a flat interface. This was shown in Sec. 5.5.2 to be a good approximation when the Capillary number is small (as is the case in microchannel flows).

We have developed a numerical code to solve the nonlinear equations for fully developed, three-dimensional, two-phase flow in a curved channel. The solution is obtained by iteratively solving a sequence of nonlinear, 2-D two-phase flows. The numerical scheme begins with an initial guess for the velocity field. Treating the axial velocity as a known quantity, the continuity equation (5.3a) and the momentum equations in the x and y directions (5.3b)-(5.3c) are solved to determine the 2-D circulatory flow (u_i and v_i). Next, the axial velocity (w_i) is updated, by substituting the calculated values of u_i and v_i into the axial momentum equation (5.3d), and solving for w_i. The updated w_i is in turn used to correct the circulatory flow. This procedure is repeated until the velocity fields converge. The 2-D flow problem at each iteration is solved using the vorticity-stream function formulation, with a finite difference based discretization. A 210 x 160 (x-y) grid is required for a grid independent solution, at the Reynolds numbers investigated here (up to 600). For quicker convergence, we used the perturbation solution as the initial guess for simulations at low values of Re and ε, which in turn provided initial guesses for computations at higher values of Re and ε.

Using the flow regime maps presented in Sec. 5.4.2, we carry out simulations for different parameter values and obtain all five circulatory flow patterns. As an example,

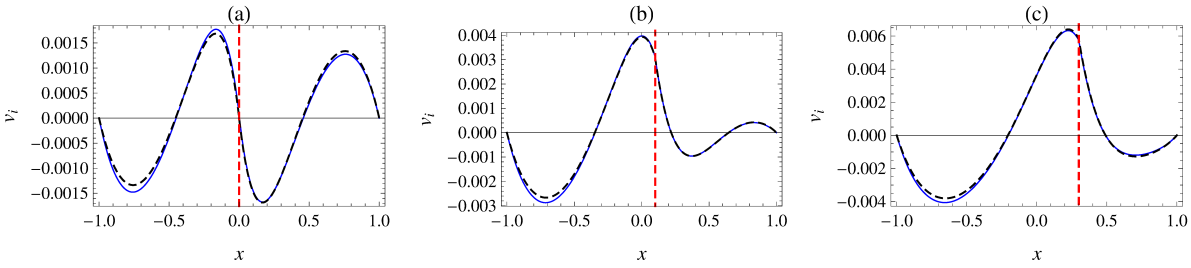

Figure 5.18: Comparison of the perturbation solution (dashed line) with numerical simulations (solid line) for different flow regimes: plots of the cross flow component v_i along the x-direction at $y = 0.5$. (a) p-p: $Re_1 = 50$, $Re_2 = 50$, $k = 0$, $\mu_{12} = 1$ (b) p-sw: $Re_1 = 50$, $Re_2 = 35$, $k = 0.1$, $\mu_{12} = 2$ (c) p-r: $Re_1 = 50$, $Re_2 = 20$, $k = 0.3$, $\mu_{12} = 3$. Other parameter values are $\lambda = 1$, $\varepsilon = 0.1$.

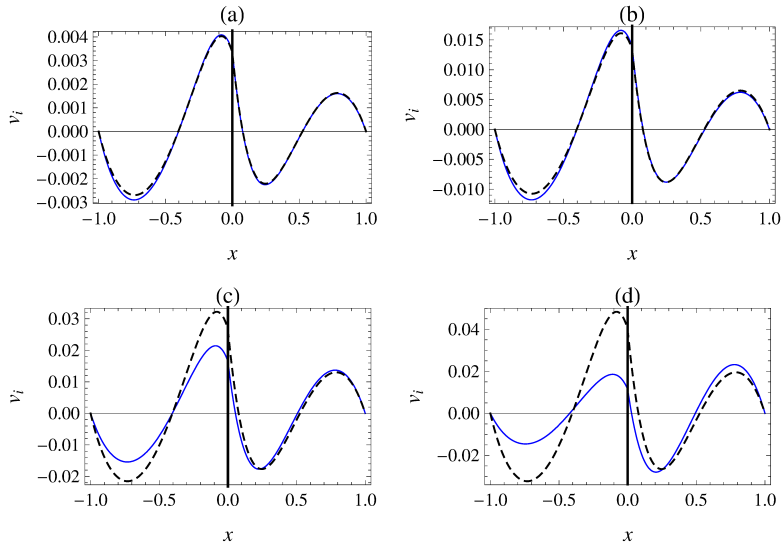

Figure 5.19: Comparison of the perturbation solution (dashed line) with numerical simulations (solid line): plots of the cross flow component v_i along the x-direction at $y = 0.5$. (a) Re_1 = Re_2 = 50, (b) Re_1 = Re_2 = 200, (c) Re_1 = Re_2 = 400, (d) Re_1 = Re_2 = 600. Other parameter values are $k = 0$, $\mu_{12} = 3$, $\lambda = 1$, $\varepsilon = 0.1$.

numerical results for principal-principal, principal-sandwich and principal-reversed flow patterns are presented in Fig. 5.18, along with the predictions of the perturbation solution. For ease of comparison, line plots of v_i, at $y = 0.5$, are presented in Fig. 5.18; the corresponding secondary flow streamlines were presented in Fig. 5.4, Fig. 5.5 and Fig. 5.7, in Sec. 5.4.1. We find a close match between the numerical and asymptotic results in all these cases.

Next, we focus on the particular case of $k = 0$, $\mu_{12} = 3$, $\lambda = 1$, $\varepsilon = 0.1$ (principal-sandwich flow) and study the effect of increasing the Reynolds number of both fluids. The numerical results, computed for Re_1 and Re_2 ranging from 50 to 600, are compared with the perturbation solution in Fig. 5.19, Fig. 5.20 and Fig. 5.21. Line plots of v_i, at $y = 0.5$, are compared in Fig. 5.19, and line plots of w_i, at $y = 0.5$, are compared in Fig. 5.20. We find that the perturbation solution predicts the cross flow quite accurately up to Reynolds

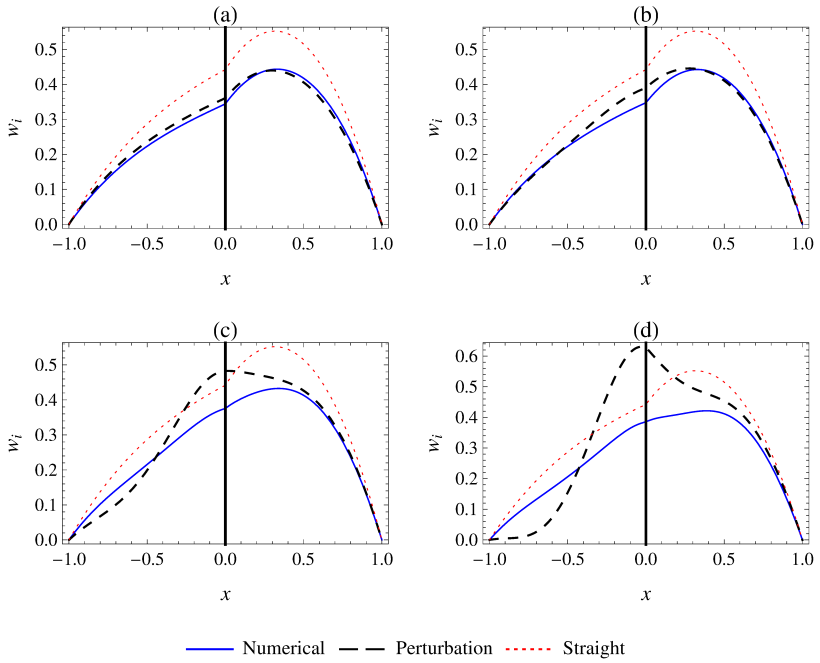

Figure 5.20: Comparison of the perturbation solution (dashed line) with numerical simulations (solid line): plots of the the axial velocity w_i along the x-direction at $y = 0.5$. (a) Re_1 = Re_2 = 50, (b) Re_1 = Re_2 = 200, (c) Re_1 = Re_2 = 400, (d) Re_1 = Re_2 = 600. Other parameter values are $k = 0$, $\mu_{12} = 3$, $\lambda = 1$, $\varepsilon = 0.1$.

numbers of 200 (Fig. 5.19b). On the other hand, the prediction of the axial velocity shows some deviation from the numerical results at this Reynolds number (Fig. 5.20b). By $Re_i = 400$, the perturbation solution shows qualitative as well as quantitative departures from the numerical results (Fig. 5.19c and Fig. 5.20c).

The streamlines of the circulatory flow, in each case, are presented in Fig. 5.21. The streamlines predicted by the perturbation solution (Fig. 5.21a are independent of Re and ε; only the magnitude of the cross-flow increases with these parameters. In reality, the increasing strength of inertial forces causes qualitative changes in the circulation pattern, which are captured by the numerical results. Comparing the cases of Re_i = 50 (Fig. 5.21b) with those of Re_i = 400 and 600 (Figs. 5.21d - 5.21e), we find that the sandwich vortices shrink in size, as Re_i is increased; also, the vortices in the inner fluid develop sharper edges. These changes, however, only become significant beyond Re_i = 200. Up to Re_i = 200, the perturbation solution predicts the circulatory flow well (cf. Figs. 5.21a - 5.21c).

The numerical simulations and the perturbation solution show deviations for relatively high values of the curvature ratio, as well. An example is depicted in Fig. 5.22, for $\varepsilon = 0.3$ and $Re_1 = Re_2 = 50$. It is important to note that the perturbation calculation is more accurate for the same curvature ratio, if the Reynolds numbers are smaller.

The results presented in this section, along with additional simulations run for dif-

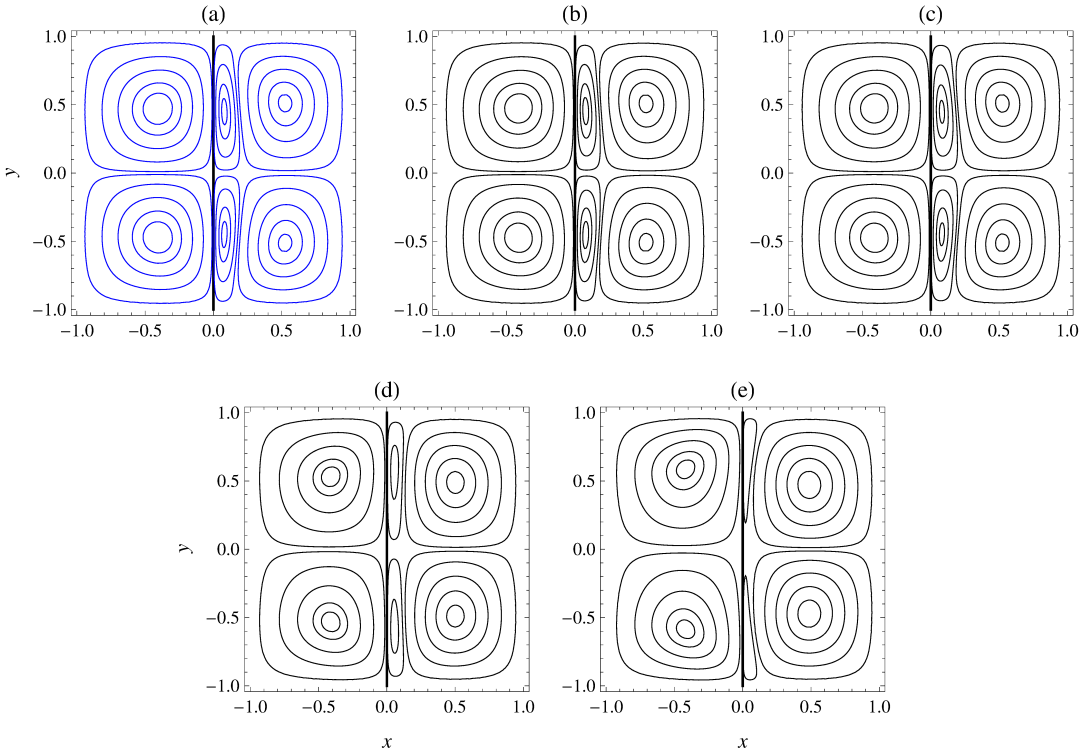

Figure 5.21: Secondary flow streamlines, predicted by the perturbation solution and numerical simulations for cases of increasing Reynolds numbers. The plot in (a) is the $O(\varepsilon^1)$ perturbation solution – the streamlines are the same for all Re. The other plots are numerical simulation results for (a) Re_1 = Re_2 = 50, (b) Re_1 = Re_2 = 200, (c) Re_1 = Re_2 = 400, (d) Re_1 = Re_2 = 600. Other parameter values are $k = 0$, $\mu_{12} = 3$, $\lambda = 1$, $\varepsilon = 0.1$.

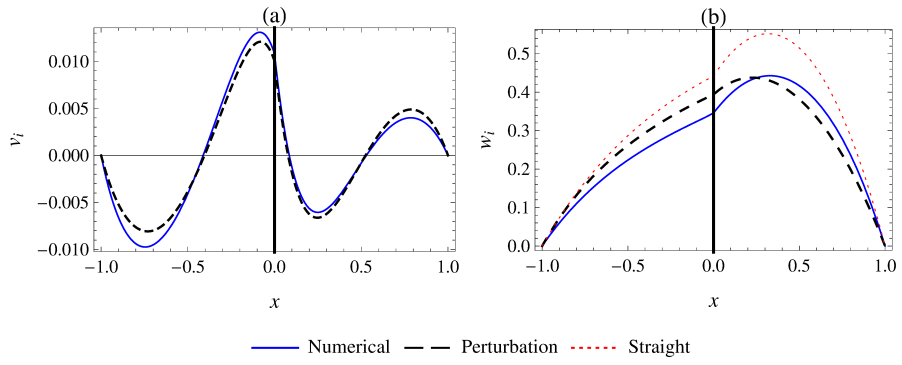

Figure 5.22: Comparison of the perturbation solution (dashed line) with numerical simulations (solid line) for a relatively high value of $\varepsilon = 0.3$. (a) plot of the cross flow component v_i along the x-direction at $y = 0.5$. (b) plot of the axial velocity w_i along the x-direction at $y = 0.5$. Other parameter values: $Re_1 = Re_2 = 50$, $k = 0$, $\mu_{12} = 3$, $\lambda = 1$.

ferent parameter values, have demonstrated that the perturbation solution predicts the circulatory flow accurately, up to Reynolds number of 100-200 and curvature ratios of about 0.2. The axial velocity predictions, however, are quantitatively accurate only up to Re_i of 50 and ε of 0.1; qualitatively, the perturbation solution matches the numerical results for Re_i of 100-200 and ε of 0.2. These limits on Re_i and ε are sufficiently high for the perturbation solution to be applied to layered flows in microchannels (Fries *et al.*, 2008; Znidarsic-Plazl and Plazl, 2007).

5.8 Concluding remarks

In this chapter, we have analyzed the laterally layered, fully developed flow, of two immiscible fluids in a curved channel. We obtained a perturbation solution for the case of a small curvature ratio (i.e. the channel's width is much smaller than its radius of curvature) by the method of domain perturbations. This solution is valid at low Reynolds numbers and when interfacial forces dominate gravitational effects – a regime commonly encountered in microfluidics. It is important to note that the condition of small curvature ratio ($\varepsilon = a/R$) does not necessarily imply a gently curved channel. Instead, if the width of the channel (a) is sufficiently small, one will have a small curvature ratio despite a finite radius of curvature.

A circulatory flow was shown to exist within each fluid, driven by centrifugal forces. The fluids were found to be in competition, since the natural effect of centrifugal forces is to drive the fluids in opposite directions, on either side of the interface. Depending on the parameter values, one of the fluids dominates over the other, leading to *five different vortex patterns*. We presented a computationally efficient method to construct *flow regime maps*, using conditions for the transition between flow regimes. These maps allowed us to understand the role of each parameter on the flow pattern.

Apart from inducing transverse circulations, the centrifugal force was shown to deform the interface between the fluids. The interface bulges outward along the horizontal centerline, to an extent that increases with the Reynolds numbers and Capillary number. The axial velocity profile was found to differ from that in a straight channel; the nature of this velocity redistribution depends on the relative importance of the *geometric* and *inertial* effects.

Targeted numerical simulations confirmed the accuracy of the perturbation solution for small, but finite, values of the Reynolds numbers (up to 200) and curvature ratios (up to 0.2). Thus the perturbation solution and the results given in this chapter, along with the inferences drawn from them, may be applied with confidence to layered microflows. These flows are encountered in solvent extraction (Assmann *et al.*, 2013) and

phase transfer catalysis (Aljbour *et al.*, 2010). Carrying out these applications in curved channels will enhance intra-fluid mixing and increase the device efficiency. The existence of optimum aspect ratios, which maximize the strength of the cross-flow in each fluid, is particularly significant for these applications. Most microchannels used in applications have wide cross-sections, with aspect ratios greater than 2. In contrast, the *optimum aspect ratios were found to be closer to unity* for many parameter values. Thus, it will be beneficial to design microchannels with cross-sections closer to a square.

Throughout this chapter, we have specified the pressure drop and holdup (volume fraction) as inputs to the calculation. In practice, however, the flow rates are easier to specify. The calculations for specified flow rates must proceed iteratively, beginning with guess values for the holdup and pressure drop. The formulas for the flow rates in (5.33a) and (5.33b) will enable these calculations.

The stability of two-phase layered flow in curved channels is currently an open problem; no studies on this topic have been reported in the literature. Based on the stability of layered flow between flat plates, we anticipate that the interface will be susceptible to the viscosity-induced instability and the centrifugally driven Rayleigh-Taylor instability, even at low Reynolds numbers (Boomkamp and Miesen, 1996; Yiantsios and Higgins, 1988; Barmak *et al.*, 2016). However, these interfacial modes are stabilized by surface tension, which may explain the observation of stable layered flows under a range of conditions in microchannels (Fries *et al.*, 2008; Kuban *et al.*, 2002; Novak *et al.*, 2012). The flow can also become unstable due to increasing centrifugal forces. However, this is possible only at relatively high Reynolds numbers, provided the channel is not very tall. (The centrifugal instability in tall channels is analyzed in Ch. 6.) In single phase flow through rectangular channels, the critical Reynolds number at which the two vortex flow looses stability (bifurcating to a four vortex flow) is about 1277 (recalculated according to the definition in this chapter), for a curvature ratio of 0.2 (Thangam and Hur, 2006). Therefore, on the basis of existing literature and available experimental evidence (cf. Fig. 5.1), we expect the solutions presented here to be stable at low values of the Reynolds number, the curvature ratio and the Capillary number. These conditions are the same as those encountered in micrchannels and for which the asymptotic solution is valid. A linear stability analysis of the steady flow field presented here will be a significant step towards understanding the stability of layered flow in rectangular curved channels.

The theoretical analysis presented here opens up new areas for future work on layered flows in curved channels. On the theoretical front, the stability of the flow presents an intriguing problem. Also, the effect of different flow patterns on inter-fluid mass transfer must be studied in order to maximize the transport enhancement afforded by the circulatory flow. For example, it may be beneficial to have a strong principal vortex flow in the fluid with lower solute diffusivity. Extending the solutions presented here to the

case of arbitrary interface contact angles will make for an interesting computational fluid dynamics study. When the contact angle is not $90\,\mathrm{deg}$, then the interface will be curved even in a straight channel, and one will have to proceed numerically. However, only a few targeted simulations may be sufficient to understand the flow field, if the results in this chapter are used to anticipate the types of vortex patterns and their locations in parameter space. Experimental visualization of the circulatory flow and interface deformation in the cross-sectional plane of a curved channel poses a significant challenge, and calls for novel experimental techniques. Clearly, simple steady layered flow becomes quite interesting once the channel is curved.

CHAPTER 6

Centrifugal Instability of Layered Flows

"...mathematical analysis of physical problems frequently leads to physical ideas that become evident only after the formal analysis has been carried through... (this) can best be expressed by another of von Karman's favorite aphorisms: Mathematics is sometimes more intelligent than the people who use it!"

– J. Miles, *An Applied Mathematician's Apology*

6.1 Introduction

The circulatory flows described in Ch. 5 become weak in tall channels, wherein the influence of the bounding walls on the axial velocity profile decreases. On the other hand, the base flow in tall channels is susceptible to a centrifugal instability, which may give rise to strong vortex flows, similar to the well known Taylor-Couette vortices (Drazin and Reid, 2004; Dean, 1928*b*). In this chapter, we study the onset of this instability in layered two-phase Poiseuille flow. For simplicity, the limit of an infinitely tall curved channel is considered. In this case, the base flow is unidirectional and fully developed in the azimuthal direction (axisymmetric), with a cylindrical interface separating the fluids. We carry out a linear stability analysis to determine the critical Reynolds number as a function of physical parameters and operating conditions. We also analyze features of the secondary flow arising at the onset of instability.

Dean (1928*a*) was the first to show that a (single phase) fluid flowing in a curved channel with infinitely tall walls can be destabilized by centrifugal forces. The no-slip condition at the outer wall causes angular momentum to decrease in the outward direction. This is an inherently unstable configuration. At a sufficiently high Reynolds number and curvature ratio (ratio of the channel's width to the radius of curvature of the inner wall), viscous forces are overcome and the base flow gives way to an array of axisymmetric vortices (Drazin and Reid, 2004; Sparrow, 1964). This *centrifugal instability* is analogous to that which arises in Taylor-Couette flow, in which fluid is driven by rotation of cylindrical walls (Drazin and Reid, 2004).

Almost all prior work on the two-phase centrifugal instability has been carried out in the context of two-phase Taylor-Couette flow (Renardy and Joseph, 1985; Baier and Graham, 1998). Recent work by Graham and coworkers (Baier and Graham, 1998, 2000; Baier *et al.*, 2000; Peng and Zhu, 2010) has been motivated by applications in liquid-liquid extraction. An important example is the separation of biological products from a carrier stream by contact with a solvent. Dispersing one fluid in another can damage biological molecules; hence mass transfer across layered fluids with a single interface is preferable. Onset of secondary circulations, due to the centrifugal instability, enhances mass transfer in these systems, while maintaining layered flow. The two-phase pressure driven Dean flow considered here is a potential candidate for these applications.

A base state in which the fluids are laterally layered may be realized when centrifugal forces are strong enough to overcome gravitational forces and to prevent capillary breakup of the interface due to interfacial tension forces. In two-phase Taylor-Couette flow, this is achieved by rotating the cylinders sufficiently rapidly. In the present two-phase Dean problem, the strength of centrifugal forces depends on the velocity of the pressure driven flow, which scales linearly with the pressure drop applied across the curved channel: $v_c = \frac{Gd^2}{\mu}$ where G is the pressure drop per unit length, d is the channel width and μ is the mean viscosity of the fluids. Thus, centrifugal forces will dominate gravity when $\frac{v_c^2}{gR} \gg 1$ or $\frac{G^2 d^4}{\mu^2 gR} \gg 1$, where R is the radius of the inner wall. Baier and Graham (1998) found that capillary breakup of the cylindrical interface in Taylor-Couette flow is prevented when $\frac{(\rho_1-\rho_2)(\Omega R_i)^2 R_i}{\gamma} \gg 1$, where Ω is the angular velocity of the cylinders, R_i is the location of the interface and ρ_1, ρ_2 are the densities of the inner and outer fluids respectively. Analogously, we expect a layered base state in two-phase Dean flow if $\frac{(\rho_1-\rho_2)G^2 d^4 R_i}{\mu_1^2 \gamma} \gg 1$.

Previous work on two-phase Dean flow has been carried out by Gelfgat *et al.* (2001). However, we find that their results significantly over-predict the critical Reynolds number. An incomplete set of recombined Chebyshev functions were used as a basis in their Galerkin spectral method. Hence, the most dangerous modes were not described accurately. In this work we adopt their basic Galerkin spectral technique, but construct a complete set of recombined Chebyshev functions, which are used as a basis for the two-fluid domain. The results of this method are cross-checked with a standard shooting technique.

While our focus in this work is on the centrifugal instability, the base flow is susceptible to other instabilities as well. These include *interfacial* and *non-interfacial* instabilities. In interfacial instabilities, deformation of the interface plays a key role and drives the secondary flow. The *Rayleigh-Taylor* instability (Chandrasekhar, 1961) (due to centrifugal acceleration rather than gravitational), the *capillary (Rayleigh-Plateau)* instability (Johns and Narayanan, 2002) and the long wave and short wave *viscosity-induced*

instabilities are interfacial modes. The viscosity-induced modes originate from the difference in viscosities of the two fluids. The perturbations grow as a result of a transfer of energy from the base flow to the disturbance flow, via the action of viscous tangential stresses (Boomkamp and Miesen, 1996; Govindarajan and Sahu, 2014). The category of non-interfacial modes includes the centrifugal instability and the *shear* instability. While the centrifugal instability is exclusively associated with curved channels, the shear instability occurs in straight channels as well (Yiantsios and Higgins, 1988; Boomkamp and Miesen, 1996) and is of the Tollmien-Schlichting type (Drazin and Reid, 2004). This instability occurs at a much higher value of the Reynolds number, compared to the other instability modes. In this classification, gravitational acceleration is neglected in comparison to centrifugal acceleration – an assumption that is maintained throughout this work.

To accurately interpret the results of a general linear stability analysis, in which all instabilities are significant, one must be able to distinguish these different instability modes. This requires a knowledge of their characteristic features, which can be obtained by studying simpler problems involving only a few modes. The literature contains detailed information on all these modes, except the two-phase centrifugal instability. Our aim, in this work, is to analyze the centrifugal mode in detail, under conditions when it dominates and is the primary source of instability.

Hence, we focus on the limit of small Capillary numbers (Ca) (relatively strong surface tension forces). In this case, the viscosity-induced and Rayleigh-Taylor modes are suppressed by surface tension. The shear mode is unimportant since, in a curved channel, the centrifugal instability becomes unstable at much lower Reynolds numbers. (Gibson and Cook (1974) have shown for single-phase flow that the curvature ratio must be smaller than 2.179×10^{-5} for the shear mode to be important at the onset of instability.) The capillary instability is also excluded if the curved walls of the channel have a radii of curvature larger than their height divided by 2π (Johns and Narayanan, 2002). We shall assume this to be the case, with the understanding that the width of the channel is still sufficiently small compared to its height to allow its approximation by infinite cylinders. Thus, in the limit of small Ca, the centrifugal instability dominates the system.

This chapter is organized as follows. The governing dynamic equations are presented in Sec. 6.2 and linearized about the base state in Sec. 6.3. We then simplify the linear equations in the limit of small Capillary numbers (Sec. 6.4). The resulting eigenvalue problem is solved in Sec. 6.5. We begin our analysis in Sec. 6.6 with a discussion of the mechanism of instability, along with Rayleigh's stability criterion. In Sec. 6.7, some important definitions of critical parameters are given. The different types of instability modes (from stationary toroidal vortices to rotating spirals) are presented and classified in Sec. 6.8. We discuss the effect of the curvature ratio in Sec. 6.10 before analyzing

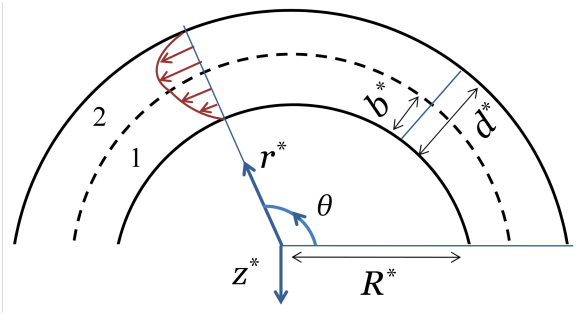

Figure 6.1: Schematic of the flow system consisting of laterally stratified two-phase Poiseuille flow in an infinitely tall curved channel. A cylindrical coordinate system (r, z, θ) is adopted. The positive z axis is perpendicular to the plane of the paper and extends outward.

the effect of other parameters in Sec. 6.11. Here, we pay close attention to transitions (mode switching) that occur between different types of instability modes as parameters are varied. In Sec. 6.12, we investigate the impact of interchanging the location of the two fluids on the system's stability. We conclude in Sec. 6.13, by summarizing the key results and discussing their significance.

6.2 Governing dynamic equations

A schematic of the flow system is depicted in Fig. 6.1, along with the cylindrical coordinate system (r, z, θ) adopted in the analysis. The z axis is perpendicular to the plane of the paper and extends to infinity.

The two fluids are radially stratified and the flow is driven by a pressure gradient imposed along the azimuthal direction. The base steady state (whose stability is to be determined) has a unidirectional, azimuthal flow. The velocity varies radially across the gap between the two cylinders. The inner and outer fluids are labeled 1 and 2 respectively. R^* is the radius of the inner cylinder, d^* is the gap width and b^* is the width occupied by the inner fluid. The ratio of the gap width (d^*) to the radius of the inner cylinder (R^*) is the curvature ratio (a). $a = 0$ represents the case of parallel flat plates. The superscript $(*)$ denotes dimensional quantities.

The governing dynamic equations (6.1) consist of the Continuity equation and the Navier-Stokes equations, in cylindrical coordinates.

$$\boldsymbol{\nabla}^* \cdot \boldsymbol{v}_i^* = 0 \tag{6.1a}$$

$$\rho^* \left(\frac{\partial \boldsymbol{v}_i^*}{\partial t^*} + \boldsymbol{v}_i^* \cdot \boldsymbol{\nabla}^* \boldsymbol{v}_i^* \right) = -\boldsymbol{\nabla}^* \left(-G^* R^* \theta + p_i^* \right) + \mu^* \nabla^{*2} \boldsymbol{v}_i^* \tag{6.1b}$$

Here, bold face symbols denote vectorial quantities. The subscript (i) takes the values 1 and 2 to denote the inner and outer fluids respectively. $(-G^* R^*)$ is the constant azimuthal

derivative of pressure, which drives the unidirectional flow in the base state. All additional pressure variations are contained in p_i^*. In the base state, p_i^* is independent of z^* and because the base flow is azimuthal and fully developed. It is however an increasing function of r^*, since the outward centrifugal force is balanced by the pressure distribution in the base state. These equations are subject to the following boundary conditions in the radial direction. The no-slip condition at both lateral walls gives

$$\boldsymbol{v}_1^* = 0 \qquad \text{at } \; r^* = R^* \tag{6.2a}$$

$$\boldsymbol{v}_2^* = 0 \qquad \text{at } \; r^* = R^* + d^* \tag{6.2b}$$

Let the position of the interface be given by $H^*(z^*, \theta^*)$, with $H^* = b^*$ in the base state. Then continuity of the velocity field at the interface implies

$$\boldsymbol{v}_1^* = \boldsymbol{v}_2^* \qquad \text{at } \; r^* = H^* \tag{6.3}$$

The normal and tangential stress balances at the interface $(r^* = H^*)$ read as (cf. Ch. 2 of Leal (2007))

$$p_1^* - p_2^* + \left[(\boldsymbol{n}\cdot\boldsymbol{n}\cdot\mathbf{D}_2^*) - (\boldsymbol{n}\cdot\boldsymbol{n}\cdot\mathbf{D}_1^*)\right] = \gamma^*\left(\nabla\cdot\boldsymbol{n}\right) \tag{6.4}$$

$$\boldsymbol{n}\cdot\mathbf{D}_2^* - (\boldsymbol{n}\cdot\boldsymbol{n}\cdot\mathbf{D}_2^*)\,\boldsymbol{n} = \boldsymbol{n}\cdot\mathbf{D}_1^* - (\boldsymbol{n}\cdot\boldsymbol{n}\cdot\mathbf{D}_1^*)\,\boldsymbol{n} \tag{6.5}$$

Here, $\mathbf{D}_i^*$ is the deviatoric stress tensor and γ^* is the surface tension. $\boldsymbol{n}$ is the unit normal to the interface, directed into fluid 2. Denoting the unit vectors in the three coordinate directions as $\boldsymbol{e}_x$, $\boldsymbol{e}_\theta$ and $\boldsymbol{e}_z$, we have

$$\boldsymbol{n} = \left(\boldsymbol{e}_r - \frac{\partial H^*}{\partial z^*}\boldsymbol{e}_z - \frac{1}{R^*}\frac{\partial H^*}{\partial \theta}\boldsymbol{e}_\theta\right)\left(1 + \left(\frac{\partial H^*}{\partial z^*}\right)^2 + \left(\frac{1}{R^*}\frac{\partial H^*}{\partial t}\right)^2\right)^{-1/2} \tag{6.6}$$

Finally, the kinematic condition must be satisfied at the interface.

$$\boldsymbol{v}_1 \cdot \left(\boldsymbol{e}_r - \frac{\partial H^*}{\partial z^*}\boldsymbol{e}_z - \frac{1}{R^*}\frac{\partial H^*}{\partial \theta}\boldsymbol{e}_\theta\right) = \frac{\partial H^*}{\partial t} \tag{6.7}$$

Boundary effects in the z and θ directions are neglected in this stability analysis. The impact of this assumption on the form of perturbations is discussed in Sec. 6.3.

The pressure scale (G^*d^*) and the gap width (d^*) are used to non-dimensionalize these equations. Since the base flow is stable when viscous forces dominate, we adopt a viscous scale for the velocity. Specifically, the velocity is scaled by $G^*{d^*}^2/12\mu_1^*$, which is the average velocity of fluid 1 when it flows in a unidirectional, fully developed manner between flat plates with a gap width of d^*. The dimensionless parameters that describe the system are the Reynolds number, Capillary number, curvature ratio, position of the

interface and ratios of viscosities and densities of the two fluids.

$$Re = \frac{G^* {d^*}^3 \rho_1}{12\mu_1^2}, \quad Ca = \frac{G^* {d^*}^2}{12\gamma}, \quad a = \frac{d^*}{R^*}, \quad b = \frac{b^*}{d^*}, \quad \mu_{12} = \frac{\mu_1}{\mu_2}, \quad \rho_{12} = \frac{\rho_1}{\rho_2} \tag{6.8}$$

To simplify the governing equations while retaining the essential physics, we make the narrow gap approximation or the gentle curvature approximation, which assumes that $d^* \ll R^*$ or $a \ll 1$. Effectively, this approximation eliminates the effect of curvature on the base flow but retains it in the linearized evolution equations; it is often used in the analysis of curved channel flows (Dean, 1928*a*; Reid, 1958). A detailed discussion of this assumption is presented in Appendix C.

For convenience, the radial coordinate r^* is transformed to x, defined as $x = (r^* - R^*)/d^*$. The inner and outer walls of the curved channel correspond to $x = 0$ and $x = 1$ respectively. The non-dimensional equations, after transforming r^* to x and making the narrow gap approximation, reduce to the following

$$\frac{\partial u_i}{\partial x} + a\frac{\partial v_i}{\partial t} + \frac{\partial w_i}{\partial z} = 0 \tag{6.9a}$$

$$\frac{Re\rho_{1i}}{\mu_{1i}}\left[\frac{\partial u_i}{\partial t} + u_i\frac{\partial u_i}{\partial x} + av_i\frac{\partial u_i}{\partial \theta} + w_i\frac{\partial u_i}{\partial z} - a{v_i}^2\right] = -12\mu_{1i}\frac{\partial p_i}{\partial x} + \frac{\partial^2 u_i}{\partial x^2} + a^2\frac{\partial^2 u_i}{\partial \theta^2} + \frac{\partial^2 u_i}{\partial z^2} \tag{6.9b}$$

$$\frac{Re\rho_{1i}}{\mu_{1i}}\left[\frac{\partial w_i}{\partial t} + u_i\frac{\partial w_i}{\partial x} + av_i\frac{\partial w_i}{\partial \theta} + w_i\frac{\partial w_i}{\partial z}\right] = -12\mu_{1i}\frac{\partial p_i}{\partial z} + \frac{\partial^2 w_i}{\partial x^2} + a^2\frac{\partial^2 w_i}{\partial \theta^2} + \frac{\partial^2 w_i}{\partial z^2} \tag{6.9c}$$

$$\frac{Re\rho_{1i}}{\mu_{1i}}\left[\frac{\partial v_i}{\partial t} + u_i\frac{\partial v_i}{\partial x} + av_i\frac{\partial v_i}{\partial \theta} + w_i\frac{\partial v_i}{\partial z} + au_iv_i\right] = 12\mu_{1i} - 12a\mu_{1i}\frac{\partial p_i}{\partial \theta} + \frac{\partial^2 v_i}{\partial x^2} + a^2\frac{\partial^2 v_i}{\partial \theta^2} + \frac{\partial^2 v_i}{\partial z^2} \tag{6.9d}$$

Here (u, w, v) are the non-dimensional velocities in the (x, z, θ) directions respectively. Note that in spite of assuming a to be small, we have retained terms involving (aRe). This is because the flow becomes unstable as Re is increased, and its value can be sufficiently large for terms involving (aRe) to contribute. We have also retained terms of the form $a\frac{\partial}{\partial\theta}$ and $a^2\frac{\partial^2}{\partial\theta^2}$, in order to account for short wavelength azimuthal disturbances.

6.3 Linearization

The base steady state consists of unidirectional fully developed (axisymmetric) flow in the azimuthal direction, i.e. $\bar{\boldsymbol{v}}_i = V_i(x)\,\boldsymbol{e}_\theta$, where the azimuthal base velocity field is

given by:

$$V_1 = \frac{6x\left[b^2\left(1-\mu_{12}\right)+\mu_{12}\right]}{\left[b\left(1-\mu_{12}\right)+\mu_{12}\right]} - 6x^2 \tag{6.10a}$$

$$V_2 = \mu_{12}V_1 + \frac{6\mu_{12}b\left(1-b\right)\left(1-\mu_{12}\right)}{\left[b\left(1-\mu_{12}\right)+\mu_{12}\right]} \tag{6.10b}$$

Note that the base flow profile is a function of the interface position and the viscosity ratio alone and not of the Reynolds number or the density ratio. The pressure distribution in the base state is given by $-\frac{\theta}{a} + P_i\left(x\right)$ where $p_i = P_i\left(x\right)$ and may be determined from the momentum balance in the radial direction

$$\frac{dP_i}{dx} = \frac{Re_i}{\rho_{1i}}\left(\frac{aV_i^2}{12}\right) \tag{6.11}$$

The governing equations (6.9) are linearized about the base state (6.10) by considering infinitesimally small perturbations to the base velocity and pressure fields:

$$u_i = \epsilon\,\hat{u}_i\left(x\right)\exp\left[i(kz+m\theta)+\omega t\right] \tag{6.12a}$$

$$w_i = \epsilon\,\hat{w}_i\left(x\right)\exp\left[i(kz+m\theta)+\omega t\right] \tag{6.12b}$$

$$v_i = V_i(x) + \epsilon\,\hat{v}_i\left(x\right)\exp\left[i(kz+m\theta)+\omega t\right] \tag{6.12c}$$

$$p_i = -\frac{\theta}{a}P_i(x) + \epsilon\,\hat{p}_i\left(x\right)\exp\left[i(kz+m\theta)+\omega t\right] \tag{6.12d}$$

$$H = b + \epsilon\,h\left(x\right)\exp\left[i(kz+m\theta)+\omega t\right] \tag{6.12e}$$

Here ϵ is the infinitesimal magnitude of the perturbations ($\epsilon \ll 1$), which have typical normal mode forms. k and m are wave numbers in the z direction and the azimuthal direction respectively. Since we focus on a temporal stability analysis, these wave numbers are restricted to real values while ω can be complex. Since the cylindrical walls extend to infinity in the z direction, the axial wavenumber is real, i.e. $k \in \mathbb{R}$.

In the azimuthal direction, boundary conditions must be imposed at the inlet and outlet of the curved channel. We have assumed periodic boundary conditions on the perturbations to facilitate a stability analysis using normal modes of the form $\exp\left[i(kz+m\theta)+\omega t\right]$. The permissible values of the azimuthal wavenumber m depend on the length of the curved channel. If the arc length of the inner wall is $\theta_L R^*$, then the azimuthal wavenumber m assumes a discrete set of real values given by $2\pi n/\theta_L$ with $n = 1, 2, 3...$ In order to study the maximum number of azimuthal modes, we consider the limiting case of $\theta_L = 2\pi$, which corresponds to $m = n = 1, 2, 3...$ In a practical curved channel θ_L will be less than 2π, and some modes will be disallowed; e.g. if $L = \pi$ then $m = 2n = 2, 4...$ and only even numbered modes are permitted.

The real part of ω (Re[ω]) is the growth rate; it describes the temporal growth/decay of the disturbance. The imaginary part of ω (Im[ω]) determines the temporal nature of the mode. If Im[ω] $= 0$, then the normal mode represents a stationary spatial wave, else it is a travelling wave that propagates in the direction $k\boldsymbol{e}_r + m\boldsymbol{e}_\theta$ with a phase speed of -Im[ω] $(k^2 + m^2)^{-1/2}$.

On substituting (6.12) into (6.9) and linearizing (retaining terms of $O(\epsilon^1)$), we obtain the following equations for the radial dependence of the perturbations

$$\frac{d\hat{u}_i}{dx} + iam\hat{v}_i + ik\hat{w}_i = 0 \tag{6.13a}$$

$$\frac{Re\mu_{1i}}{\rho_{1i}}\left[\omega\hat{u}_i + iamV_i\hat{u} - 2aV_i\hat{v}_i\right] = -12\mu_{1i}\frac{d\hat{p}_i}{dx} + \frac{d^2\hat{u}_i}{dx^2} - \left(a^2m^2 + k^2\right)\hat{u}_i \tag{6.13b}$$

$$\frac{Re\mu_{1i}}{\rho_{1i}}\left[\omega\hat{w}_i + iamV_i\hat{w}_i\right] = -12mu_{1i}\left(ik\hat{p}_i\right) + \frac{d^2\hat{w}_i}{dx^2} - \left(a^2m^2 + k^2\right)\hat{w}_i \tag{6.13c}$$

$$\frac{Re\mu_{1i}}{\rho_{1i}}\left[\omega\hat{v}_i + \frac{\partial V_i}{\partial x}\hat{u}_i + iamV_i\hat{v}_i + aV_i\hat{u}_i\right] = -12\mu_{1i}\left(iam\hat{p}_i\right) + \frac{d^2\hat{v}_i}{dx^2} - \left(a^2m^2 + k^2\right)\hat{v}_i \tag{6.13d}$$

The boundary conditions for these equations are derived from (6.2) to (6.7), by linearizing and making the gentle curvature approximation. At the walls, we have

$$\hat{u}_1 = \hat{v}_1 = \hat{w}_1 = 0 \qquad \text{at} \quad x = 0 \tag{6.14a}$$

$$\hat{u}_2 = \hat{v}_2 = \hat{w}_2 = 0 \qquad \text{at} \quad x = 1 \tag{6.14b}$$

The interface boundary conditions, linearized by the method of domain perturbations (Johns and Narayanan, 2002; Leal, 2007), are applied at $x = b$.

$$\hat{u}_1 = \hat{u}_2 \tag{6.14c}$$

$$\hat{w}_1 = \hat{w}_2 \tag{6.14d}$$

$$\hat{v}_1 + h\frac{dV_1}{dx} = \hat{v}_2 + h\frac{dV_2}{dx} \tag{6.14e}$$

$$\hat{u}_1 - imaV_1h = \omega h \tag{6.14f}$$

$$\mu_{12}\left(ik\hat{u}_1 + \frac{d\hat{w}_1}{dx}\right) = \left(ik\hat{u}_2 + \frac{d\hat{w}_2}{dx}\right) \tag{6.14g}$$

$$\mu_{12}\left(\frac{d\hat{v}_1}{dx} + ima\hat{u}_1\right) = \frac{d\hat{v}_2}{dx} + ima\hat{u}_2 \tag{6.14h}$$

$$12\left(\hat{p}_1 - \hat{p}_2\right) + 2\left(\frac{1}{M\mu_{12}}\frac{d\hat{u}_2}{dx} - \frac{d\hat{u}_1}{dx}\right) = \frac{1}{Ca}\left(-a^2 + k^2 + a^2m^2\right)h \tag{6.14i}$$

Equations (6.13) to (6.14) constitute an eigenvalue problem in which (ω) is the complex eigenvalue. On solving this eigenvalue problem for a specified disturbance mode (defined by the wave numbers k and m) and fixed parameter values, a spectrum of complex

eigenvalues is obtained. The entire spectrum must be in the left half of the complex plane ($\mathrm{Re}[\omega] \leq 0$) for the system to be stable to the disturbance. The onset of instability occurs when the real part of one or more eigenvalues first becomes zero. The modes corresponding to these critical eigenvalues are called critical modes; they determine the nature of the secondary flow close to the onset of instability (Cross and Greenside, 2009).

6.4 Limit of small Capillary number

In this work, we consider the limit of small capillary numbers ($Ca \ll 1$), for which interfacial deformation does not impact the onset of instability or the secondary flow significantly. To derive simplified equations for this limit, we expand the eigenfunctions $\hat{u}_i$, $\hat{v}_i$, $\hat{w}_i$, $\hat{p}_i$, h as power series in Ca, as follows

$$\{\hat{u}_i,\, \hat{v}_i,\, \hat{w}_i,\, \hat{p}_i\} = \{\hat{u}_{i,0},\, \hat{v}_{i,0},\, \hat{w}_{i,0},\, \hat{p}_{i,0}\} + Ca\,\{\hat{u}_{i,0},\, \hat{v}_{i,0},\, \hat{w}_{i,0},\, \hat{p}_{i,0}\} + O(Ca^2) \tag{6.15a}$$

$$h = h_0 + Ca\, h_1 + O(Ca^2) \tag{6.15b}$$

Substituting these expansions into (6.13)-(6.14), and equating coefficients of like powers of Ca, we obtain a sequence of linear equations for every order of the expansion. The domain equations remain unchanged, as they do not contain Ca. The boundary conditions however are simplified. At $O(Ca^0)$, the normal stress condition (6.14i) reduces to:

$$\left(-a^2 + k^2 + a^2 m^2\right) h_0 = 0 \tag{6.16}$$

This equation implies that the interface is undeformed at $O(Ca^0)$, i.e. $h_0 = 0$, unless the prefactor $(-a^2 + k^2 + a^2 m^2)$ is zero. The latter case occur only when the disturbance is axisymmetric ($m = 0$) and if $k = a$. This condition on k corresponds to the cut off axial wavenumber for the capillary instability (Johns and Narayanan, 2002); a curved interface is unstable to capillary breakup when $k < a$, or the axial wavelength $(2\pi d^*/k)$ is greater than the circumference of the circular interface ($\approx 2\pi R^*$). The coefficients in the series expansion of h (6.15b) can be determined only if $k \neq a$. This is guaranteed if the height of the cylindrical walls (L) is less than the circumference of the inner cylinder ($2\pi R^*$), i.e. if $k > a$. This condition effectively stabilizes the system to the capillary instability (Johns and Narayanan, 2002) and ensures that interfacial deformations are negligibly small as Ca approaches zero. Note that even with this restriction on the height of the walls (L), we may approximate them as semi-infinite cylinders provided $d^* \ll L < R^*$. Under these conditions, the prefactor $(-a^2 + k^2 + a^2 m^2)$ is nonzero and positive and (6.16) yields $h_0 = 0$.

Thus for small capillary numbers, the stability threshold of the system and the crit-

ical eigenmodes can be approximated by analyzing the problem with a non-deforming interface. The simplified boundary conditions at the interface, at $O(Ca^0)$, are

$$\hat{u}_{1,0} = \hat{u}_{2,0} = 0 \tag{6.17a}$$

$$\hat{w}_{1,0} = \hat{u}_{2,0} \tag{6.17b}$$

$$\hat{v}_{1,0} = \hat{u}_{2,0} \tag{6.17c}$$

$$\mu_{12}\left(ik\hat{u}_{1,0} + \frac{d\hat{w}_{1,0}}{dx}\right) = \left(ik\hat{u}_{2,0} + \frac{d\hat{w}_{2,0}}{dx}\right) \tag{6.17d}$$

$$\mu_{12}\left(\frac{d\hat{v}_{1,0}}{dx} + ima\hat{u}_{1,0}\right) = \frac{d\hat{v}_{2,0}}{dx} + ima\hat{u}_{2,0} \tag{6.17e}$$

At the walls, we have

$$\hat{u}_{1,0} = \hat{v}_{1,0} = \hat{w}_{1,0} = 0 \tag{6.17f}$$

$$\hat{u}_{2,0} = \hat{v}_{2,0} = \hat{w}_{2,0} = 0 \tag{6.17g}$$

These boundary conditions, along with the linearized domain equations (6.13) at $O(Ca^0)$, specify the eigenvalue problem for $\hat{u}_{i,0}, \hat{v}_{i,0}, \hat{w}_{i,0}, \hat{p}_{i,0}$.

In this work, we do not proceed to calculate the corrections to the eigenfunction and growth rate at higher orders in Ca. However, the first approximation to the small deformations of the interface can be calculated, without extra effort, from the normal stress condition (6.14i) at $O(Ca)$.

$$h_1 = \frac{1}{(-a^2 + k^2 + a^2m^2)}\left[12\left(\hat{p}_{1,0} - \hat{p}_{2,0}\right) + 2\left(\frac{1}{mu_{12}}\frac{d\hat{u}_{2,0}}{dx} - \frac{d\hat{u}_{1,0}}{dx}\right)\right] \qquad \text{at} \quad x = b \tag{6.18}$$

Since, $\hat{u}_{i,0}$ and $\hat{p}_{i,0}$ are known from the solution of the zeroth order problem, (6.18) provides an explicit formula for evaluating h_1, the deformation of the interface at $O(Ca)$.

6.5 Solution of the eigenvalue problem

In this section, we solve the eigenvalue problem to $O(Ca^0)$ by applying two numerical schemes - a novel two-phase RCGS method and a standard shooting method. Firstly, (6.13) are simplified by eliminating $\hat{p}_{i,0}$ using (6.13a) and $\hat{w}_{i,0}$ using (6.13c). These manipulations result in a fourth order equation for $\hat{u}_{i,0}$ and a second order equation for

$\hat{v}_{i,0}$:

$$\omega\left[\frac{Re_i\mu_{1i}}{\rho_{1i}}\frac{\left(a^2m^2+k^2\right)}{k^2}\hat{u}_{i,0}-\frac{Re_i\mu_{1i}}{\rho_{1i}}\frac{1}{k^2}\frac{d^2\hat{u}_{i,0}}{dx^2}\right]=-\frac{1}{k^2}\frac{d^4\hat{u}_{i,0}}{dx^4}$$
$$+\left[2\frac{\left(a^2m^2+k^2\right)}{k^2}+\frac{Re_i\mu_{1i}}{\rho_{1i}}\frac{am}{k^2}V_ii\right]\frac{d^2\hat{u}_{i,0}}{dx^2}-\left[\frac{Re_i\mu_{1i}}{\rho_{1i}}\frac{a^2m}{k^2}V_ii\right]\frac{d\hat{u}_{i,0}}{dx}$$
$$-\left[\frac{\left(a^2m^2+k^2\right)^2}{k^2}+\frac{Re_i\mu_{1i}}{\rho_{1i}}\frac{am\left(a^2m^2+k^2\right)}{k^2}V_ii+\frac{Re_i\mu_{1i}}{\rho_{1i}}\frac{am}{k^2}\left(\frac{d^2V_i}{dx^2}+a\frac{dV_i}{dx}\right)i\right]\hat{u}_{i,0}$$
$$+\left[\frac{Re_i\mu_{1i}}{\rho_{1i}}\frac{2aV_i\left(a^2m^2+k^2\right)}{k^2}\right]\hat{v}_{i,0} \tag{6.19a}$$

$$\omega\left[-\frac{Re_i\mu_{1i}}{\rho_{1i}}\left(\frac{am}{k^2}i\right)\frac{d\hat{u}_{i,0}}{dx}+\frac{Re_i\mu_{1i}}{\rho_{1i}}\left(1+\frac{a^2m^2}{k^2}\right)\hat{v}_{i,0}\right]=-\left[\frac{am}{k^2}i\right]\frac{d^3\hat{u}_{i,0}}{dx^3}$$
$$+\left[\frac{am}{k^2}\left(a^2m^2+k^2\right)i-\frac{Re_i\mu_{1i}}{\rho_{1i}}\frac{a^2m^2}{k^2}V_i\right]\frac{d\hat{u}_{i,0}}{dx}-\left[\frac{Re_i\mu_{1i}}{\rho_{1i}}\left(\frac{dV_i}{dx}+aV_i\right)\right]\hat{u}_{i,0}$$
$$+\left[1+\frac{a^2m^2}{k^2}\right]\frac{d^2\hat{v}_{i,0}}{dx^2}-\left[\frac{\left(a^2m^2+k^2\right)^2}{k^2}+\frac{Re_i\mu_{1i}}{\rho_{1i}}amV_i\frac{\left(a^2m^2+k^2\right)}{k^2}i\right]\hat{v}_{i,0} \tag{6.19b}$$

The boundary conditions for (6.19) are obtained from (6.17). For $\hat{u}_{i,0}$, the following conditions are obtained:

$$\hat{u}_{1,0}=\frac{d\hat{u}_{1,0}}{dx}=0 \qquad \text{at} \quad x=0 \tag{6.20a}$$
$$\hat{u}_{2,0}=\frac{d\hat{u}_{2,0}}{dx}=0 \qquad \text{at} \quad x=1 \tag{6.20b}$$
$$\hat{u}_{1,0}=\hat{u}_{2,0}=0 \qquad \text{at} \quad x=b \tag{6.20c}$$
$$\frac{d\hat{u}_{1,0}}{dx}=\frac{d\hat{u}_{2,0}}{dx} \qquad \text{at} \quad x=b \tag{6.20d}$$
$$\mu_{12}\frac{d^2\hat{u}_{1,0}}{dx^2}=\frac{d^2\hat{u}_{2,0}}{dx^2} \qquad \text{at} \quad x=b \tag{6.20e}$$

The conditions on $\hat{v}_{i,0}$ follow:

$$\hat{v}_{1,0}=0 \qquad \text{at} \;\; x=0 \tag{6.21a}$$
$$\hat{v}_{2,0}=0 \qquad \text{at} \;\; x=1 \tag{6.21b}$$
$$\hat{v}_{1,0}=\hat{v}_{2,0} \qquad \text{at} \;\; x=b \tag{6.21c}$$
$$\mu_{12}\frac{d\hat{v}_{1,0}}{dx}=\frac{d\hat{v}_{2,0}}{dx} \qquad \text{at} \;\; x=b \tag{6.21d}$$

Here, the conditions on the first derivative of $\hat{u}_{i,0}$ are derived from the boundary conditions on $\hat{w}_{i,0}$. This eigenvalue problem (6.19)-(6.21) is solved numerically, as described in subsections 6.5.1 and 6.5.2.

6.5.1 Two-phase Recombined Chebyshev Galerkin Spectral (RCGS) method

In this method a set of basis functions, which analytically satisfy all the boundary conditions of the eigenvalue problem, is constructed from combinations of Chebyshev functions. Using this "recombined" basis set, the Galerkin procedure is applied to obtain a matrix eigenvalue problem, which is readily solved by QZ decomposition. While this conceptual framework has been in place for several years, it is only with the recent and rapid increase of computer memory that it has become a viable numerical strategy. This has coincided with the development of symbolic computing packages, such as Mathematica, which may be used to construct the basis set easily and implement the entire procedure efficiently. The revival of this method is largely due to Gelfgat and coworkers, who have successfully applied it to single-phase problems (Gelfgat and Tanasawa, 1994; Gelfgat *et al.*, 1999; Gelfgat, 2001).

The two-phase RCGS method is explained in detail in Appendix D. Here, we outline the procedure in brief. The functions $\hat{u}_{1,0}$ and $\hat{u}_{2,0}$, defined on $[0, b]$ and $[b, 1]$ respectively, are combined into a single vector function $\hat{\mathbf{u}}_\mathbf{0} = (\hat{u}_{1,0}, \hat{u}_{2,0})^\mathsf{T}$ defined over the entire domain $[0, 1]$. Similarly, we define $\hat{\mathbf{v}}_\mathbf{0} = (\hat{v}_{1,0}, \hat{v}_{2,0})^\mathsf{T}$. Here the superscript T denotes the transpose operation. $\hat{\mathbf{u}}_\mathbf{0}$ and $\hat{\mathbf{v}}_\mathbf{0}$ belong to the direct sum Hilbert space $\mathcal{L}_2[0, b] \oplus \mathcal{L}_2[b, 1]$. These vectors are expanded in terms of basis sets $\left\{\boldsymbol{\phi}_{\mathbf{u},n}\right\}_{n=0}^{\infty}$ and $\left\{\boldsymbol{\phi}_{\mathbf{v},n}\right\}_{n=0}^{\infty}$ respectively.

$$\hat{\mathbf{u}}_\mathbf{0} = \sum_{n=0}^{N} c_n \boldsymbol{\phi}_{\mathbf{u},n} \quad \text{and} \quad \hat{\mathbf{v}}_\mathbf{0} = \sum_{n=0}^{N} d_n \boldsymbol{\phi}_{\mathbf{v},n} \tag{6.22}$$

Each $\boldsymbol{\phi}_{\mathbf{u},n}$ satisfies the boundary conditions on $\hat{u}_{1,0}$ and $\hat{u}_{2,0}$ (6.20), while each $\boldsymbol{\phi}_{\mathbf{u},n}$ satisfies the boundary conditions on $\hat{u}_{1,0}$ and $\hat{u}_{2,0}$ (6.21). The construction of these basis functions are described in Appendix D.2.

The Galerkin procedure is then applied to discretize (6.19). The inner products are evaluated using Gaussian quadrature (cf. Appendix D.1). This results in a generalized matrix eigenvalue problem:

$$\mathbf{A}\mathbf{x} = \omega \mathbf{B}\mathbf{x} \tag{6.23}$$

$\mathbf{x}$ is the vector of $2(N + 1)$ unknown coefficients: $\{c_n\}_{n=0}^{N} \cup \{d_n\}_{n=0}^{N}$. $\mathbf{A}$ and $\mathbf{B}$ are square, non-singular matrices of dimension $2(N + 1) \times 2(N + 1)$. Non-singularity of $\mathbf{B}$ is a particular advantage of the two-phase RCGS method over traditional collocation or Tau spectral methods.

The matrix eigenvalue problem (6.23) is solved by QZ-decomposition (zgeev routine of LAPACK) to yield a set of eigenvalues that approximate the point spectrum of the differential eigenvalue problem (6.19)-(6.21). For some parameter values, a single positive spurious eigenvalue is obtained from the computation. It is typically two orders of magnitude greater than the true eigenvalues and thus can be easily identified and eliminated.

Results of the RCGS method are crosschecked with those obtained using a shooting method with orthonormalization. The shooting technique is described in subsection 6.5.2. The two methods are in good agreement, as demonstrated by the example presented in Appendix D.3. Numerical results demonstrating the convergence characteristics of the two-phase RCGS method are also presented in Appendix D.3. Twenty four basis functions are found to provide sufficient accuracy for all the cases considered in this work.

6.5.2 Shooting method with orthonormalization

We also use a shooting method with orthonormalization to solve (6.19)-(6.21). This method is based on a technique described by Conte (1966). A similar approach has been used successfully to solve the single phase Orr-Sommerfeld equations (Schmid and Henningson, 2001; Drazin and Reid, 2004) and to study the stability of two-phase layered plane Poiseuille flow (Hooper, 1989). This method is fundamentally different from the spectral method discussed in Sec. 6.5.1. It is an iterative local method that, rather than approximating the entire spectrum, allows the determination of a single eigenvalue starting from an initial guess. Alternatively, the marginal Reynolds number, which marks the stability boundary, can be directly identified by setting the growth rate to zero ($\mathrm{Re}[\omega] = 0$) and treating the Reynolds number as an eigenvalue. The smallest value of the Reynolds number obtained from the shooting method is the marginal Reynolds number.

6.6 Rayleigh's criterion implies instability prone outer layer

The centrifugal instability is caused by an unstable stratification of angular momentum in any one (or both) of the fluids. If the angular momentum of the base flow, $xV_i(x)$, decreases radially outward, then centrifugal forces have a tendency to induce circulations and destabilize the flow (Drazin and Reid, 2004). This situation is analogous to the case of a density stratified fluid at rest in a gravitational field. If the density decreases in the direction of the gravitational force, then the stationary state is unstable.

For the case of single-phase inviscid flow in a curved channel, Rayleigh's criterion

gives a formal stability condition (Drazin and Reid, 2004). It is valid for axisymmetric disturbances. This single phase result may be directly extended to the case of layered inviscid fluids, if the regime of small Ca is considered, wherein interfacial deformation is negligible. Here, Rayleigh's criterion may be applied separately to each fluid, since the linear stability equations for the two fluids are independent and individually identical to the single-phase equations. The criterion is based on the value of the Rayleigh discriminant $\Phi_i(x)$ in each fluid, which is given by

$$\Phi_i(x) = \frac{1}{x^3}\frac{d}{dx}\left(xV_i\left(x\right)\right)^2 \tag{6.24}$$

If $\Phi_i(x) < 0$ within the domain of either fluid, then the inviscid base flow is unstable. In the case of viscous fluids the flow is stabilized by viscous dampening at low Reynolds number. However, when the Reynolds number exceeds a critical value, the centrifugal instability will set in.

In Fig. 6.2, the base velocity profiles (6.10) and the corresponding values of the Rayleigh discriminant are plotted for different viscosity ratios. $\Phi_i(x)$ varies considerably across the channel and is discontinuous at the interface when the fluids have different viscosities. (This is induced by the balance of tangential stresses, cf. (6.5).) Fig. 6.2 shows that $\Phi_i(x)$ is generally positive near the inner wall and negative near the outer wall. This is because the velocity is zero at both walls (no-slip condition); as we move from the inner to the outer wall, the velocity first increases, attains a maximum, and then decreases again. $\Phi_i(x)$ can also be negative in the inner fluid, if the maximum is located within the inner fluid. This occurs when $\mu_{12} < 1$ (e.g. $\mu_{12} = 1/5$ in Fig. 6.2) or $b < 1/2$. In all cases, as $\Phi_i(x) < 0$ in some part of the flow, the centrifugal instability will destabilize the base state when the Reynolds number exceeds a critical value.

The regions where $\Phi_i(x) < 0$ are said to be locally unstable while the regions of positive $\Phi_i(x)$ are termed locally stable. In single-phase flow, it has been shown that the magnitude of the secondary flow at the onset of instability is greater within the locally unstable regions (Reid, 1958; Drazin and Reid, 2004). Extending this to two-phase flows, one can expect a stronger secondary flow within the fluid layer with a more negative value of $\Phi_i(x)$. This has been confirmed for two-phase Taylor-Couette flow by Baier and Graham (1998). Based on Fig. 6.2, we expect *a stronger secondary flow within the outer fluid* for a majority of parameter values. Physically, this implies that *the outer fluid has a more unstable stratification of angular momentum*, even if the fluids have similar properties.

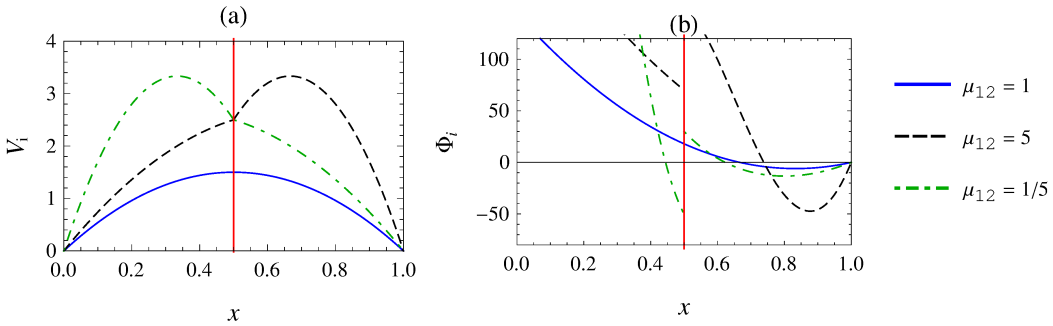

Figure 6.2: Plots of the base velocity profile for different viscosity ratios and the corresponding profiles of the Rayleigh discriminant $\Phi_i(x)$. In the plot for $\mu_{12} = 1/5$, the velocity has been rescaled with μ_2 to facilitate a clear comparison with the plot for $\mu_{12} = 5$.

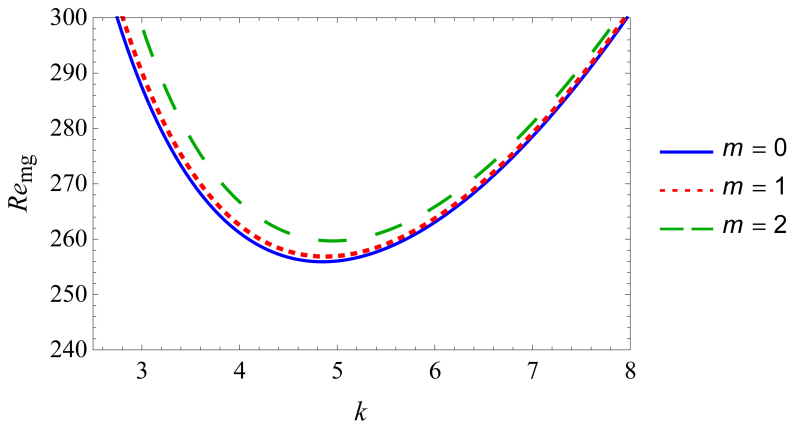

Figure 6.3: Marginal Reynolds number (Re_{mg}) for various disturbance modes. The minimum of each curve corresponds to the least marginal Reynolds number ($Re_{c,m}$) at each value of m. These are $Re_{c,m} = 255.92$, $k_{c,m} = 4.85$ ($m = 0$); $Re_{c,m} = 256.87$, $k_{c,m} = 4.88$ ($m = 1$); $Re_{c,m} = 259.69$, $k_{c,m} = 4.95$ ($m = 2$). The critical mode in this case is $m_c = 0$, $k_c = 4.85$, $Re_c = 255.92$, which is axisymmetric. Parameter values: $\mu_{12} = 0.5$, $\rho_{12} = 0.5$, $b = 0.5$, $a = 0.1$.

6.7 Definition of marginal and critical *Re*

We now define some key stability parameters that are used in the presentation of results. For a specified disturbance mode (fixed values of k and m) and fixed values of physical parameters, the Reynolds number at which the maximum of Re[ω] (growth rate) is zero is defined as the marginal Reynolds number (Re_{mg}). The system is unstable to the specified disturbance for all Reynolds numbers greater than Re_{mg}. Clearly, the marginal Reynolds number is a function of the disturbance (k and m).

In Fig. 6.3, the marginal Reynolds number is plotted for different disturbance modes, for the case of $\mu_{12} = 0.5, \rho_{12} = 0.5, b = 0.5, a = 0.1$. These are the neutral stability curves. For a given azimuthal wave number (m), the smallest value of Re_{mg} across all k is called the least marginal Reynolds number and denoted by $Re_{c,m}$. The corresponding axial wave number is $k_{c,m}$.

In Fig. 6.3, the smallest value of $Re_{c,m}$ corresponds to the axisymmetric mode, $m = 0$ (details are given in the figure caption). This is called the critical Reynolds number Re_c and the corresponding disturbance mode is the critical instability mode (k_c, m_c). In Fig. 6.3 we have $m_c = 0, k_c = 4.85, Re_c = 255.92$. Centrifugal instability first occurs when Re exceeds Re_c.

Neutral stability curves of qualitative structure similar to those in Fig. 6.3 occur for a variety of physical problems. Well known examples are the Rayleigh-Benard instability and Turing patterns (Cross and Greenside, 2009). These instabilities, classified as Type-I by Cross and Hohenberg (1993), exhibit similar linear stability characteristics and weakly nonlinear behavior.

6.8 Classification of instability modes

Just above the critical point, when the Reynolds number slightly exceeds Re_c, only modes in a close neighborhood of k_c, m_c will be unstable (cf. Fig. 6.3). After an initial period of exponential growth, the ensuing three dimensional flow will saturate via nonlinear mechanisms to a new flow state. The spatiotemporal variation of the new flow will correspond closely to the critical mode (assuming a supercritical bifurcation), provided Re is sufficiently close to Re_c (Cross and Greenside, 2009). Thus, a significant change in the nature of the critical mode signifies a new type of secondary flow pattern.

The critical instability mode and the corresponding secondary flow state can be of two types, depending on the value of Im[ω] at the critical point (when Re[ω] = 0). If Im[ω] = 0, then the instability is stationary and the new emergent state is a steady state. On the other hand if Im[ω] is non-zero, the instability is oscillatory. Such a mode can take the form of either a travelling or standing wave. Standing waves are ruled out in this problem due to the absence of reflection symmetry in the azimuthal direction (because of the base flow). Hence, when Im[ω] is nonzero, the critical mode is a travelling wave.

This temporal nature of the instability is closely connected to the azimuthal dependence of the critical mode. The linearized equations (6.19)-(6.21) reveal that an axisymmetric critical mode is stationary while a non-axisymmetric mode is a travelling wave. If the mode is axisymmetric $(m_c = 0)$ then the simplified eigenvalue problem is real and we find that Im[ω] = 0 for the critical mode. On the other hand if m_c is non-zero, then the eigenvalue problem (6.19)-(6.21) is complex and Im[ω] is non-zero.

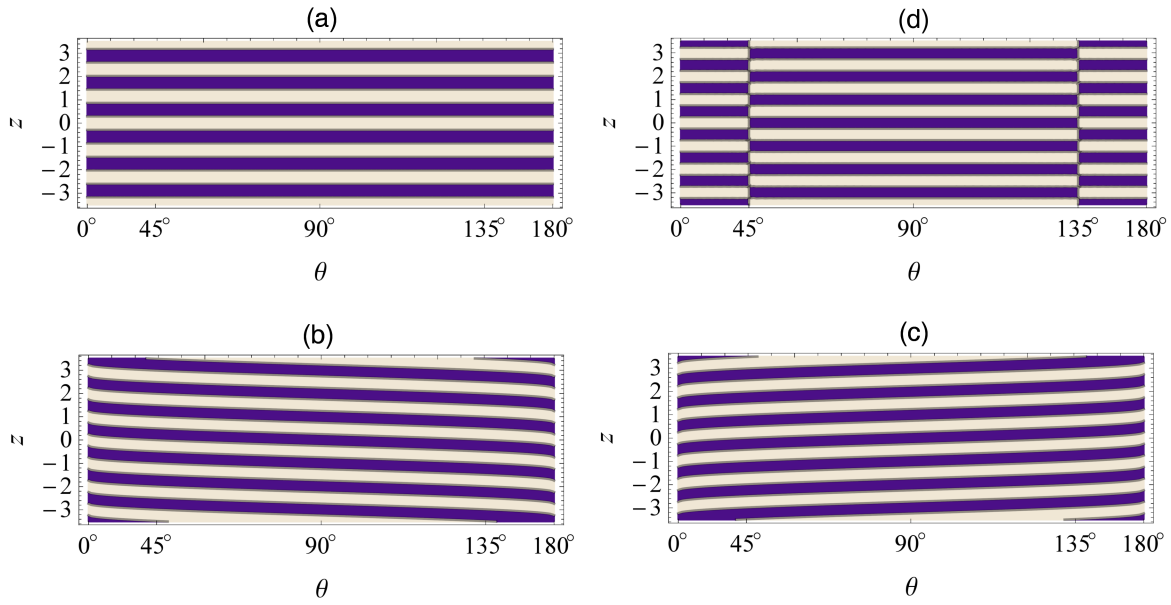

Figure 6.4: Visualization of vortex array patterns (external structure) corresponding to critical modes at different parameter values. (a) axisymmetric toroidal vortices (b) left handed rotating spirals (c) right handed rotating spirals (d) ribbon vortex state- superposition of (b) and (c). The dark and light regions correspond to different vortex regions across which the fluid does not mix. Each figure represents the external structure of a critical mode as seen through the outer cylindrical wall. Hence linear positions along the x axis correspond to $R^* \cos(\theta)/a^*$. A visualization window with a small axial length is selected for better clarity, and the axes in the figures are drawn to scale for a more realistic visualization. Parameter values: (a) $Re_c = 36.049, k_c = 5.43, m_c = 0, Im[\omega_c] = 0, \mu_{12} = 1.9, \rho_{12} = 0.5, b = 0.5$ (b) $Re_c = 391.378, k_c = 6.32, m_c = 2, Im[\omega_c] = -0.227, \mu_{12} = 0.66, \rho_{12} = 0.3, b = 0.76$ (c) $Re_c = 391.378, k_c = -6.32, m_c = 2, Im[\omega_c] = -0.227, \mu_{12} = 0.66, \rho_{12} = 0.3, b = 0.76$. In all cases, $a = 0.1$.

6.8.1 Stationary axisymmetric vortices and rotating spirals

We discuss the temporal nature of the modes along with their azimuthal dependence, as these are interconnected. In Fig. 6.4, we plot the variation along the (z-θ) surface of two modes with distinct spatio-temporal behavior. These plots depict the vortex arrays as seen through the surface of the outer cylindrical wall. Each plot corresponds to a critical mode computed for specific parameter values, which are given in the caption of Fig. 6.4.

Fig. 6.4a corresponds to an axisymmetric and stationary critical mode that manifests as toroidal vortices. These vortices are two-phase analogues of single phase Dean vortex arrays (Reid, 1958). Similar axisymmetric vortices have been observed experimentally in two-phase Taylor-Couette flow (cf. Fig. 11 in Baier and Graham (1998)).

Fig. 6.4b and Fig. 6.4c depict two non-axisymmetric travelling modes. These modes have identical mathematical descriptions, except for the sign of k_c. Both modes become critical simultaneously, as the eigenvalue problem (6.19)-(6.21) is invariant to the sign of k_c. They have the structure of spirals that start at the inlet of the channel and terminate at the outlet. They appear to rotate and propagate through the cylinder. The case in

Fig. 6.4b corresponds to $k_c > 0$. This is a left-handed spiral, which propagates axially upward. The other mode, in Fig. 6.4c, has $k_c < 0$ and is a right handed spiral that propagates axially downward. In fact these two modes are reflections of each other about the (r-θ) plane. We expect the spiral flow pattern that emerges when a non-axisymmetric mode is critical to be distorted at the inlet and outlet of the channel due to boundary effects. However, away from these boundaries, the non-axisymmetric critical modes are expected to manifest clearly as rotating spiral vortices.

The simultaneous criticality of both types of spiral modes is a natural outcome of symmetry-breaking (Crawford and Knobloch, 1991; Stewart and Golubitsky, 1992). The base flow possesses reflection symmetry in the z direction. While the axisymmetric stationary modes retain this symmetry, the spiral travelling waves break it. When reflection symmetry is broken at the onset of instability, the set of possible emerging flow states should be related to each other via the same reflection transformation, i.e. reflection of any one spiral state about the r-θ plane should yield another equally possible spiral flow state. Depending on the initial perturbation, either mode can dominate and lead to a left or right-handed rotating spiral flow.

These degenerate spiral modes can also superpose with equal amplitudes and give rise to a new state, which only propagates azimuthally. This combined mode is depicted in Fig. 6.4d and is called a ribbon state (Golubitsky and Langford, 1988). The ribbon flow is a standing wave with respect to the axial direction. For Type-I instabilities (which includes the centrifugal instability), it is known that if both travelling waves and standing waves are critical (according to the linear theory) then only one of the two can be stable (Cross and Hohenberg, 1993; Cross and Greenside, 2009). Stability is parameter dependent and may be determined from the associated amplitude equations. Hence for parameter values that support rotating spirals, the ribbon state will not be observed and vice-versa. Both patterns have been observed experimentally in Taylor-Couette flow (Tagg *et al.*, 1989). It should be noted that in the single-phase Dean problem, the axisymmetric mode is always critical and hence only axisymmetric stationary vortices like those in Fig. 6.4a have been reported. On the other hand, the two-phase problem involves many more parameters that affect the inter-fluid interaction and give rise to spirals or ribbon flow states.

6.8.2 Internal circulatory flow structure

Having described the external vortex pattern of the critical modes (z, θ variation), we now turn to their internal flow structure (x or radial variation). We find three distinct types, based on the relative strength of the circulatory flow within the two fluids: (i) the inner fluid circulates faster, (ii) the outer fluid circulates faster, (iii) both fluids have comparable

cross flow velocities. This *difference of the secondary flow within the two fluids originates from the stratification of angular momentum in the base flow*. The profile of the Rayleigh discriminant (cf. Sec. 6.6) is indicative of this dissimilarity between the fluids.

The first two cases of the internal vortex structures are illustrated for axisymmetric modes in Fig. 6.5. Here the eigenfunctions have been normalized such that the coefficient of $\boldsymbol{\phi}_{\mathbf{u},1}$ is unity. The magnitude of the circulatory flow in the two fluids may be compared using the line plot of the z-component of velocity, along the centerline of the vortices in the upper half of the axial periodic cell, i.e. $z = \pi/(4k_c)$. Fig. 6.5a is an example of a mode with stronger circulatory flow in the outer fluid. Such modes are called outer modes. Fig. 6.5b exemplifies the opposite scenario; it is called an inner mode. Based on k_c, we observe that the vortices are generally larger (k_c is smaller) in the outer mode (compare the scales of the z axes in Fig. 6.5a and Fig. 6.5b). A similar disparity in the magnitude of circulatory flow within the two fluids has been observed in critical modes of two-phase Taylor-Couette flow (Baier and Graham, 1998).

The third case, wherein the secondary flow is of comparable magnitude in both fluids, is called a uniform mode. An example is presented in Fig. 6.6. This particular critical two-phase mode is also present in single phase Dean flow, as an experimentally unobservable mode. Single phase flow bifurcates to Dean vortices at $Re_c = 121.35$ ($a = 0.1$). On increasing the Reynolds number beyond critical, we find that a second eigenvalue crosses the imaginary axis at $Re = 593.92$. The corresponding eigenfunction is the second most unstable single phase mode. This mode has exactly the same structure as the uniform two phase mode shown in Fig. 6.6.

6.8.3 Six categories of instability modes

Altogether we have identified six different types of critical modes based on their temporal nature and vortex pattern, in sections 6.8.1 and 6.8.2. We assign the letter S for stationary axisymmetric modes and the letter T for travelling spiral modes. The radial vortex structure of these modes can correspond to either outer, inner or uniform modes, which we denote by the letters O, I and U respectively. Thus we have six different classes of critical modes, labelled as O-S, O-T, I-S, I-T, U-S, U-T. The nature of the critical mode can change from one type to another as the parameters are varied. Examples of such transitions are presented in Sec. 6.11, along with a discussion of physical causes for mode switching.

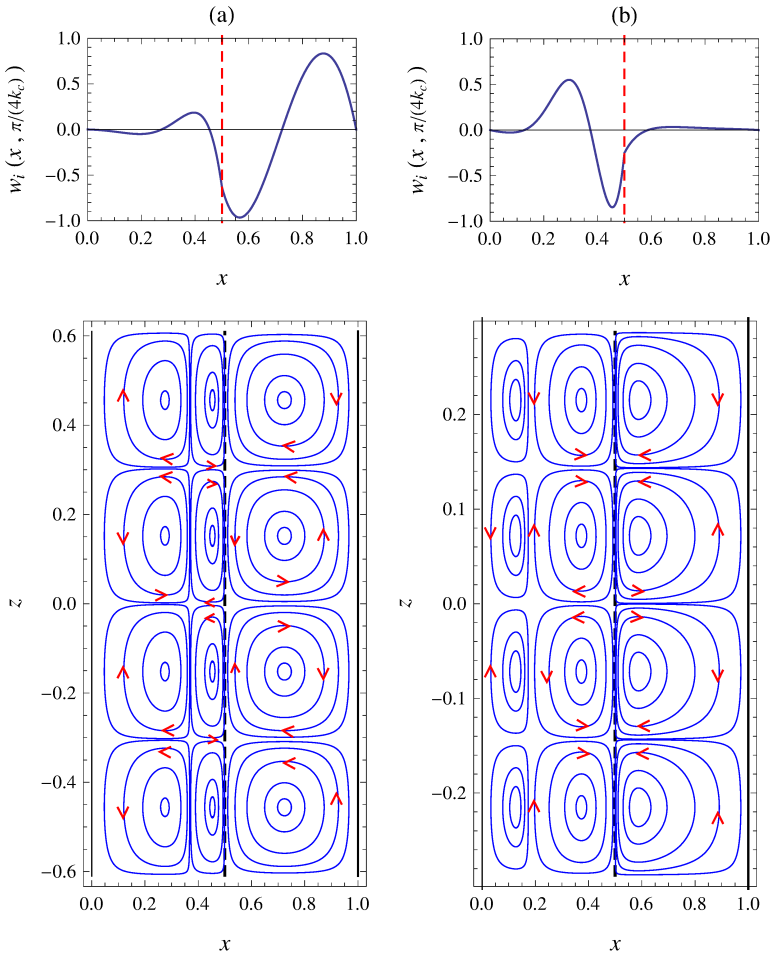

Figure 6.5: Internal circulatory flow structure of the critical modes at the onset of instability (a) axisymmetric outer mode (O-S), with stronger circulations in the outer fluid (b) axisymmetric inner mode (I-S), with stronger circulations in the inner fluid. The vortices depicted in the figure are projections of the streamlines of the flow onto a cross section of the cylindrical channel. A single axial periodic cell is visualized, i.e. $z \in [-\pi/(k_c), -\pi/(k_c)]$. The critical parameters are (a) $Re_c = 992.83, k_c = 5.167, m_c = 0, \mu_{12} = 0.525, \rho 12 = 2, b = 0.5, a = 0.1$ (b) $Re_c = 2353.736, k_c = 10.954, m_c = 0, \mu_{12} = 0.2, \rho_{12} = 2, b = 0.5, a = 0.1$.

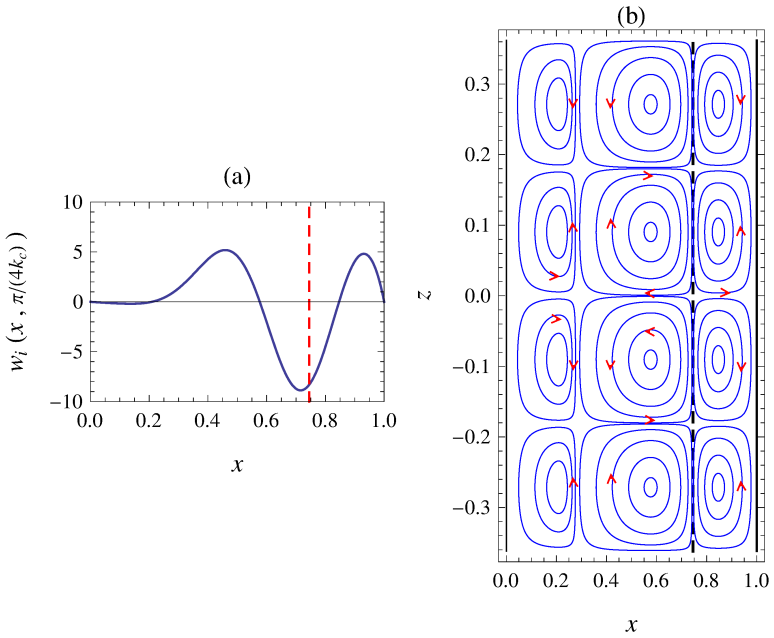

Figure 6.6: Internal circulatory flow structure at the onset of instability of a critical uniform mode. Parameter values: $Re_c = 611.385, k_c = 8.18, \mu_{12} = 1, \rho_{12} = 1, b = 0.74, a = 0.1$. This vortex patern happens to be identical to that of the second most unstable single-phase mode, which is critial at $Re_c = 593.92, k_c = 8.683$ (for the most unstable single-phase mode $Re_c = 121.35, k_c = 4.087$).

6.9 Small interface deformations

The results presented in Fig. 6.5 and Fig. 6.6 are the $O(Ca^0)$ approximations to the secondary flows. At this order of approximation, interfacial deformations are entirely absent. However, we can calculate the interfacial deformation at $O(Ca^1)$, from the pressure and velocity fields at $O(Ca^0)$, using the normal stress balance (cf. (6.18) in Sec. 6.4). The result of this calculation for the case of Fig. 6.5a is presented in Fig. 6.7. Here, the pressure perturbations at the interface have been normalized by the value of $\hat{p}_{1,0}$ at $x = b, z = 0$. The interface deflection has also been normalized by its magnitude at $z = 0$.

In most cases, we find that pressure forces dominate viscous normal stresses, at the interface (cf. (6.18)), and are an order of magnitude greater. In Fig. 6.7, the perturbed pressure at $z = 0$ is positive within the inner fluid (Fig. 6.7a) and negative in the outer fluid (Fig. 6.7b). Thus the interface is pushed outwards at $z = 0$, as shown in Fig. 6.7c.

6.10 Dependence of stability on the channel's curvature

The centrifugal instability sets in when destabilizing centrifugal forces overcome viscous forces. The relative strength of centrifugal forces is directly related to the magnitude of the Reynolds number (Re) and the curvature ratio (a). Hence, in a channel with a smaller

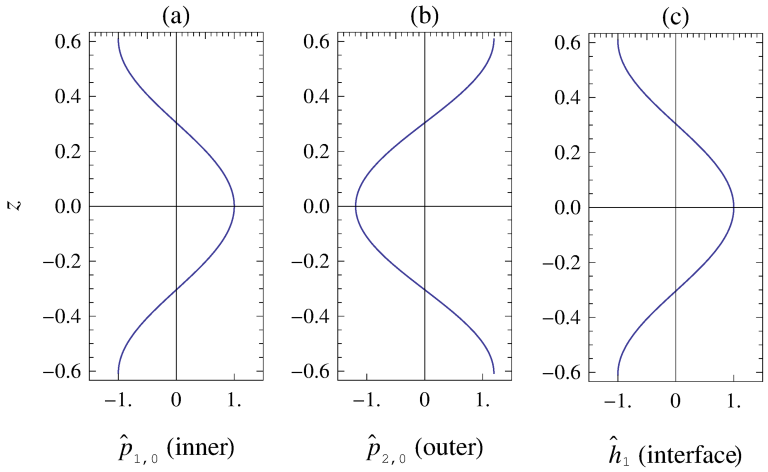

Figure 6.7: Pressure perturbations at the interface, in the inner fluid (a) and outer fluid (b), and the resulting interface deflection (c) at $O(Ca^1)$. These results are for the same case as Fig. 6.5a. Parameter values: $Re_c = 992.83, k_c = 5.167, m_c = 0, \mu_{12} = 0.525, \rho_{12} = 2, b = 0.5, a = 0.1$

curvature ratio (less curved), the critical Reynolds number is larger. This relationship is depicted in Fig. 6.8 (solid line).

In the limit of small curvature ratios, the critical Reynolds number is nearly proportional to $a^{-1/2}$. This relationship is exact if the simplified equations used by Dean are adopted (Dean, 1928*a*) (cf. Appendix C). Under this simplification, a critical Dean number (De_c) that is independent of a can be defined, $De_c = Re_c\sqrt{a}$. In our results, De_c actually varies slowly with a, because we have retained all terms of $O(aRe)$ and $O(ma)$ in the equations. In Fig. 6.8, we have plotted estimates of the critical Reynolds number (red markers) obtained by assuming De_c to be independent of a. Here, De_c is first calculated at $a = 0.01$ (the value is 150.302) and then used to estimate the critical Reynolds number at other values of a, as $De_c a^{-1/2}$. The approximation works well for small values of a, but becomes increasingly inaccurate as a is increased above 0.1.

In the remainder of this work, we only present results for $a = 0.1$. The critical Reynolds number at other small curvature ratios can be estimated by calculating the critical Dean number.

Next, the effect of a on the critical instability mode is discussed. Variation of the curvature ratio within the range 0.01 to 0.3 does not affect the nature of the critical mode, i.e. if the critical mode is axisymmetric and stationary $(m_c = 0)$ for one value of a, then it remains so for all other values as well. Similarly, while the value of m_c for non-axisymmetric does change with a, it remains bounded away from zero. The influence of a on k_c is small; for all the cases studied in Fig. 6.8 we have $k_c = 5.02 \pm 0.007$.

To understand the effect of increasing curvature ratio on the shape of the spiral modes, the influence of a on the azimuthal wavenumber of non-axisymmetric modes is investigated. Results for the critical mode at different curvature ratios is presented in Table 6.1

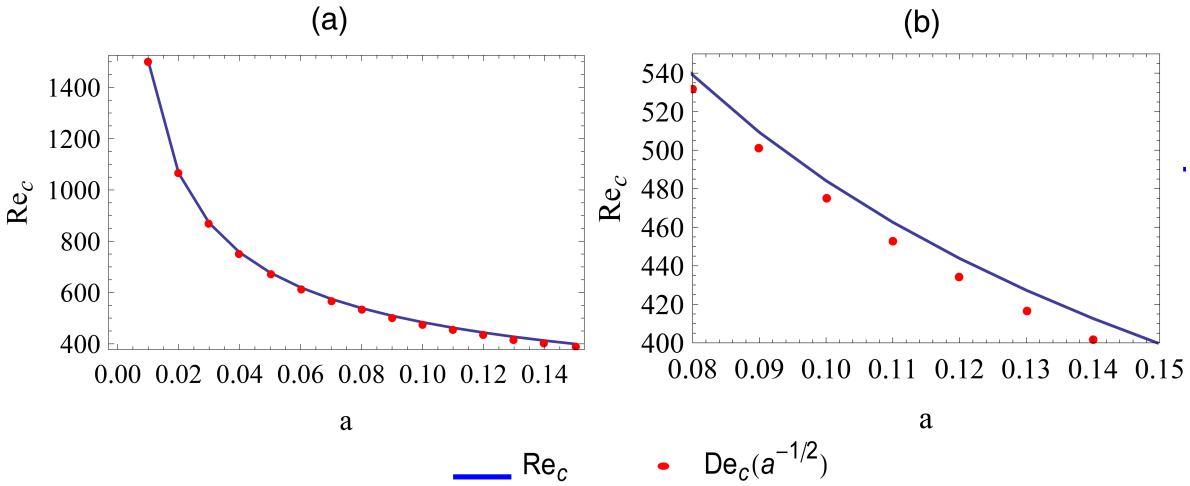

Figure 6.8: Variation of the critical Reynolds number (Re_c) with the curvature ratio (a) for $\mu_{12} = 0.525, \rho_{12} = 1, b = 0.5$. Smaller values of a correspond to more gently curved channels. Plot (b) is an enlarged version of plot (a). The solid line represents the computed values of Re_c and the circular markers represent approximate values obtained by assuming that the critical Dean number (De_c) is independent of a and has a value of 150.302 (evaluated for the case of $a = 0.01$). The instability mode is axisymmetric ($m_c = 0$) and k_c is very nearly independent of a with a value of 5.02 ± 0.007.

a	m_c	k_c	Re_c
0.1	1.970	9.107	561.211
0.05	2.568	9.039	787.772
0.01	5.207	8.971	1750.670

Table 6.1: Effect of the curvature ratio of the channel (a) on the critical mode (m_c and k_c) and the critical Reynolds number (Re_c). Smaller values of a correspond to more gently curved channels. Parameter values: $\mu_{12} = 1, \rho_{12} = 1, b = 0.72$

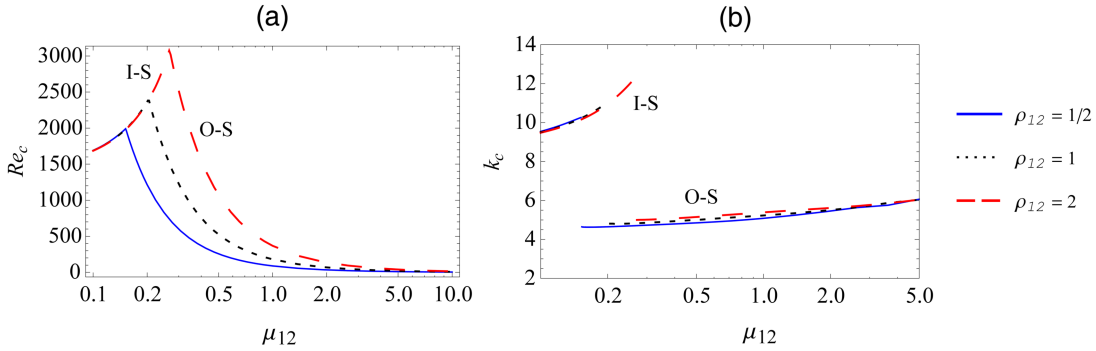

Figure 6.9: Mode switching with variation in viscosity ratio considering different density ratios. The critical mode switches from I-S to O-S as the viscosity ratio is increased, i.e. the stronger vortex moves from the inner to the outer fluid. The critical Reynolds number is plotted in (a) while the critical axial wave number is plotted in (b). The critical azimuthal wave number is $m_c = 0$ (axisymmetric). Parameter values: $b = 0.5, a = 0.1$

for the case of a non-axisymmetric critical mode $(\mu_{12} = 1, \rho_{12} = 1, b = 0.72)$. The dimensional critical azimuthal *wavelength* equals $2\pi R^*/m_c$, which in non-dimensional terms is $2\pi/(am_c)$. In Tab. 6.1 we observe that (am_c) decreases as a decreases, implying that the azimuthal wavelength of the critical mode increases as the channel becomes straighter, i.e. the spirals will have smaller pitch angles in channels that are less curved.

6.11 Mode switching across parameter space

Six different types of instability modes were identified in Sec. 6.8. The critical mode can switch from one type to another as parameters are varied. Such transitions signify a qualitative change (bifurcation) in the secondary flow states. For example at an O-S to I-S transition, the dominant vortex shifts from the outer to the inner fluid, whereas stationary axisymmetric vortices give way to rotating spirals at an O-S to O-T transition. These transitions are codimension-two bifurcations (since two parameters must be specified: the Reynolds number and another parameter such as the viscosity ratio).

In this section, we track the variation of the critical instability mode across parameter space, which includes the density ratio, the viscosity ratio and the volume fraction (interface location). The goal is to locate various codimension-two bifurcations and to identify physical causes for these transitions.

6.11.1 Variation of viscosity and density ratios

First, we analyze the effect of the viscosity ratio. In Fig. 6.9, the critical Reynolds number (Re_c) and the axial wave number (k_c) are plotted as a function of the viscosity ratio for different density ratios. For each density ratio, the profiles of Re_c and k_c consist of two

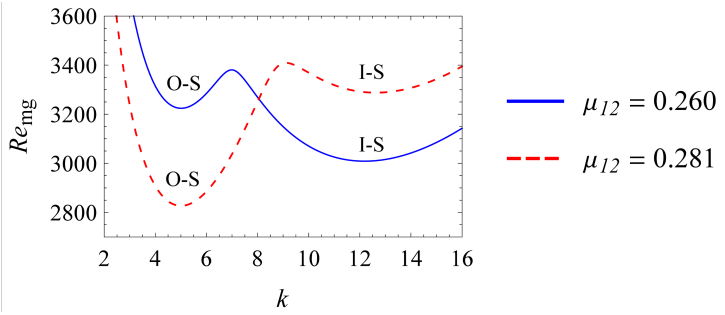

Figure 6.10: Plot of the marginal Reynolds number as a function of the axial wave number, in the neighbourhood of the transition in Fig. 6.9 ($m_c = 0$). Parameter values: $m = 0, \rho_{12} = 1, b = 0.5, a = 0.1$

distinct smooth curves that correspond to two different modes, each of which is critical for different ranges of the viscosity ratio. A transition occurs between these modes at the point marked by discontinuity in the case of k_c and non-differentiability in the profile of Re_c.

While both these modes are axisymmetric ($m_c = 0$), they have different internal velocity fields. Examining the corresponding eigenfunctions (as in Fig. 6.5), we find that the critical mode at small μ_{12} is an I-S mode, i.e. the cross flow is much stronger in the inner fluid. At small μ_{12} the Rayleigh discriminant (cf. Sec. 6.6) is more negative within the inner fluid, implying stronger destabilizing centrifugal forces therein. In addition, viscous effects are weaker within the inner fluid. Both these factors promote cross flow within the inner fluid. However as μ_{12} is increased, the variation of the Rayleigh discriminant and viscous forces eventually reverse to support stronger circulatory flows within the outer fluid (O-S mode). Hence increasing μ_{12} stabilizes the I-S mode while simultaneously destabilizing the O-S mode. This leads to a transition between the two modes.

This transition between modes is more easily visualized in Fig. 6.10. Here the marginal Reynolds number is plotted as a function of the axial wave number for two viscosity ratios on either side of the transition in Fig. 6.9 (dotted curve). Both profiles have two local minima. The one at larger k_c is the I-S mode (smaller vortices, cf. Sec. 6.8) and is the global minimum at the lower value of $\mu_{12} = 0.26$. As the viscosity ratio increases, this local minimum rises (I-S mode becomes more stable) while the minimum at small k_c (O-S mode) falls to smaller values of Re_c. Eventually the global minima switches from one mode to the other (as seen for $\mu_{12} = 0.281$ in Fig. 6.10), marking the transition of the critical mode.

On comparing the results for different density ratios in Fig. 6.9, we find that increasing the density ratio shifts the transition between I-S and O-S modes to higher viscosity ratios. In other words, increasing the relative density of the inner fluid causes the I-S mode to remain critical over a larger range of viscosity ratios, thereby promoting the for-

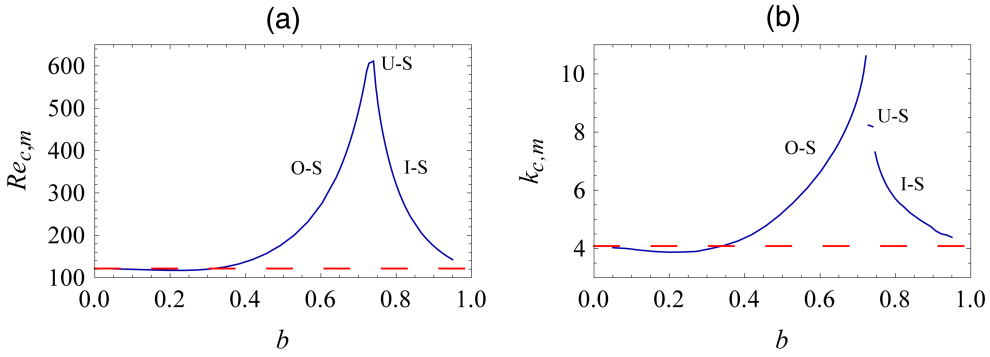

Figure 6.11: Mode switching with variation in the interface position, considering only axisymmetric modes. The most unstable axisymmetric mode switches from O-S to U-S to I-S as the interface nears the outer wall. (a) Plot of the least marginal Reynolds number, (b) Plot of the least marginal axial wave number for the case of $m = 0$. The dashed (red) line is the value for single-phase flow. Parameter values: $\mu_{12} = 1, \rho_{12} = 1, a = 0.1$

mation of stronger vortices within the inner fluid. These results indicate that the cross flow at the onset of instability has a tendency to be stronger in the fluid with higher density. This is consistent with the fact that the magnitude of the centrifugal force experienced by a fluid is proportional to its density.

6.11.2 Variation of volume fraction

Next we investigate the effect of changes in the relative fluid volumes (variation of the interface location, b) on the critical mode. In this case, the critical mode can switch between stationary and travelling modes. For clarity, we first focus on stationary axisymmetric modes alone and study the transition between O-S, U-S and I-S modes. Towards this end, we plot the least marginal Reynolds numbers for $m = 0$ as a function of the volume fraction in Fig. 6.11. Here the most unstable axisymmetric mode switches from O-S to U-S to I-S as the volume fraction occupied by the inner fluid is increased (b is increased). It follows that the cross flow tends to be stronger, at the onset of instability, within the fluid that occupies a larger fraction of the channel. The other fluid occupying a smaller volume fraction is confined in a narrower region and hence the circulatory flow within it is suppressed.

As the most unstable axisymmetric mode switches from O-S to I-S in Fig. 6.11, it undergoes an intermediate transition to the U-S mode. The U-S mode has a cross flow of comparable intensity in both fluids (cf. Fig. 6.6) and represents a compromise between the opposing natures of the O-S and I-S modes. The dashed horizontal lines in Fig. 6.11 mark the stability results for the single-phase case. As expected, the single-phase results are obtained when the volume fraction of either fluid approaches unity.

The calculations in Fig. 6.11 are extended to unequal fluid properties in Fig. 6.12. These plots indicate that larger outer fluid densities cause the O-S mode to be critical

over a larger range of volume fractions. A smaller value of the outer fluid's viscosity has the same effect. In summary, *the outer mode is more unstable* (the cross flow at the onset of instability is stronger in the outer fluid) *when the outer fluid has a lower viscosity, higher density and a larger volume fraction.*

6.11.3 Transition to rotating spirals

So far we have discussed transitions between axisymmetric modes. While axisymmetric modes are critical for all the cases in Fig. 6.9, they are not critical for all values of b in Fig. 6.11. The transition to non-axisymmetric rotating spirals ($m_c \neq 0$) is depicted in Fig. 6.13, which plots the least marginal Reynolds number for $m = 0, 2, 3$, as b is varied. Travelling spiral modes become important in the range of b values corresponding to the transition between the different axisymmetric modes (O-S to I-S via U-S). In this range of volume fractions, the system is relatively stable to axisymmetric disturbances and the non-axisymmetric rotating spirals become critical instead. Fig. 6.13 focuses on this region of interest and depicts the transition of the critical mode from O-S to O-T to U-S to I-T and finally to I-S as b is increased. The four transition points are marked by the intersection of the curves in Fig. 6.13. In this figure we show results for travelling modes corresponding to relatively small values of m as these are the most unstable. Modes with larger azimuthal wave numbers are stabilized by diffusive effects of viscous momentum transfer and have higher marginal Reynolds numbers.

It should be noted that the switch from an axisymmetric to a non-axisymmetric mode occurs when the minimum of a non-axisymmetric ($m \neq 0$) neutral curve falls below that of the $m = 0$ neutral curve, and vice versa. Here, the location of the critical Reynolds number shifts from one neutral curve to another. In contrast, the switch between different axisymmetric modes (e.g. O-S to I-S) occurs along the same neutral curve (corresponding to $m = 0$). The transition occurs when the global minimum of the axisymmetric neutral curve shifts location from one local minimum to another, as demonstrated in Fig. 6.10.

Another illustration of critical mode switching is given in Fig. 6.14, where the variation of the density ratio causes a switch from O-S at low ρ_{12} to O-T, I-T and I-S as ρ_{12} is increased. This figure is depicted in two parts for the sake of clarity. Again travelling spiral modes are critical in the region where the axisymmetric modes switch from O-S to I-S. For density ratios from 0.6 to 1, the mode with m_c = 3 is critical. The corresponding critical frequency Im[ω], which is related to the speed of the rotating spiral by (-Im[ω] $(k_c^2 + m_c^2)^{-1/2}$), is plotted in Fig. 6.15. The azimuthal motion of the spiral waves is in the direction of the base flow (because Im[ω] < 0).

In Fig. 6.13 we find that the U-S mode is critical over a very small range of interface positions, while in Fig. 6.14 it is never critical. This is typical of the U-S axisymmetric

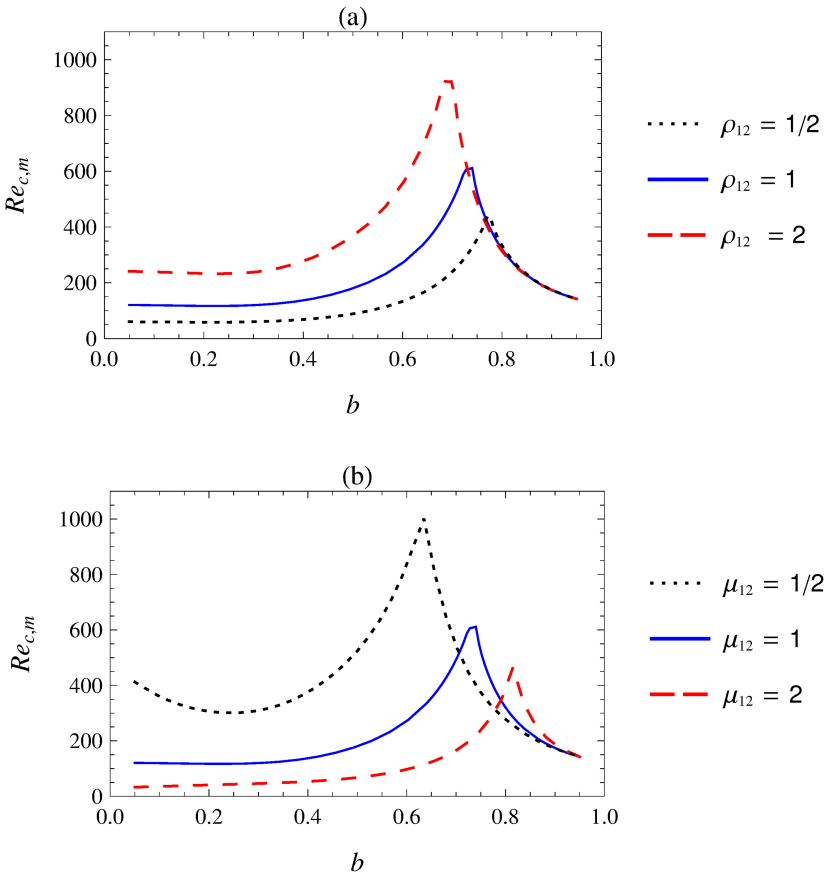

Figure 6.12: Effect of density ratio (a) and viscosity ratio (b) on mode switching with variation in the interface position, considering only axisymmetric modes ($m = 0$). Parameter values: (a) $\mu_{12} = 1, a = 0.1$ (b) $\rho_{12} = 1, a = 0.1$

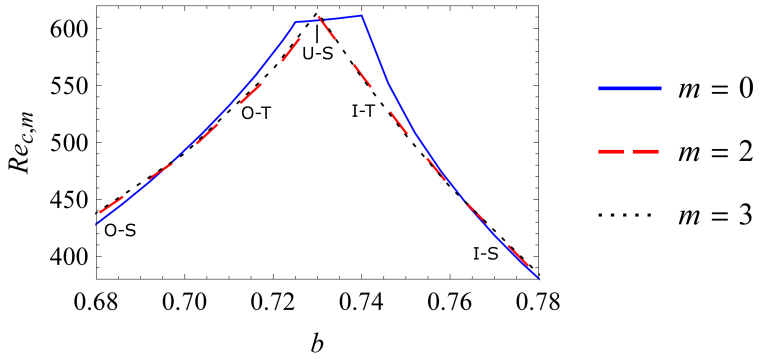

Figure 6.13: Mode switching between axisymmetric and non-axisymmetric modes. Plot of the least marginal Reynolds number as a function of the interface position. Parameter values: $\mu_{12} = 1, \rho_{12} = 1, a = 0.1$

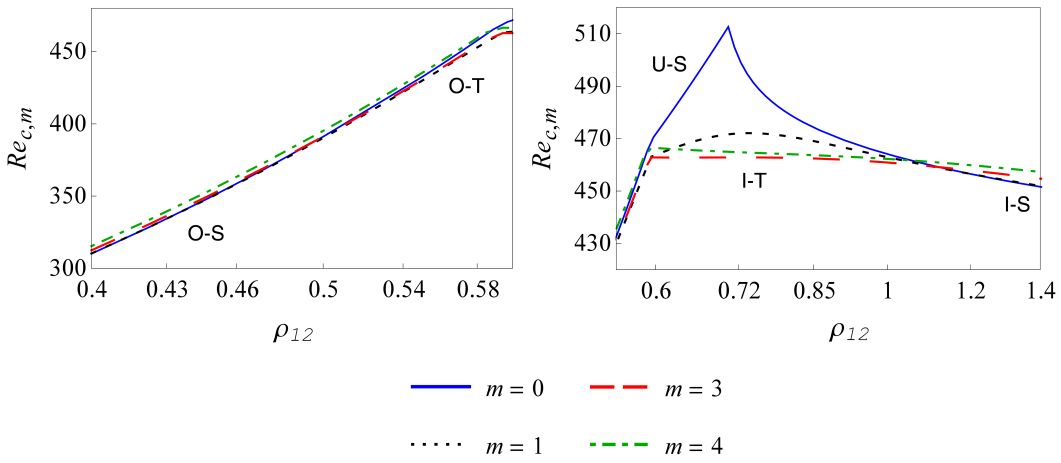

Figure 6.14: Mode switching with variation in density ratio (ρ_{12}). Plot of the least marginal Reynolds number as a function of the density ratio. The figure is split into two parts for better clarity. Parameter values: $\mu_{12} = 1, b = 0.76, a = 0.1$

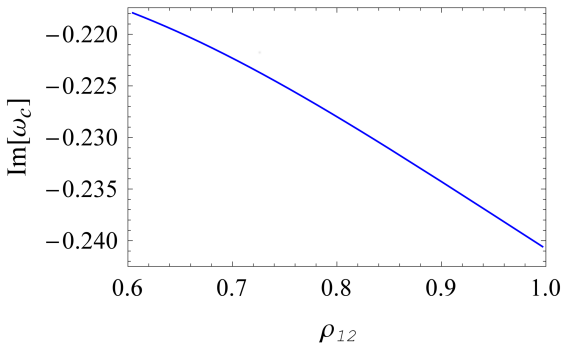

Figure 6.15: Critical frequency Im[ω] corresponding to the critical mode $m_c = 3$ in Fig. 6.14. The speed of the rotating spiral is given in terms of the critical frequency as $-\text{Im}[\omega]\ (k_c^2 + m_c^2)^{-1/2}$.

mode and in an experiment one is much more likely to observe either O-S/I-S axisymmetric vortices or non-axisymmetric rotating spirals.

A common feature, underlying all the results in this section, is that *the outer fluid is more susceptible to the centrifugal instability*. This is particularly evident in Fig. 6.9 and Fig. 6.11. In Fig. 6.9, the mode transition does not occur at a viscosity ratio of unity, despite both fluids having equal densities and occupying equal volumes of the channel ($\rho_{12} = 1$ and $b = 0.5$). Instead, the transition occurs at a low viscosity ratio. Moreover, when the viscosities are equal, the O-S mode is critical and the outer fluid dominates the secondary flow. Similarly, in Fig. 6.11, the transition from O-S to I-S occurs only when the inner fluid occupies significantly more than half the channel. Clearly, *the outer mode, with stronger circulations in the outer fluid, is preferred by the system*. This bias occurs because the stratification of angular momentum is more unstable in the outer fluid, as reflected by the more negative values of the Rayleigh discriminant in the outer fluid (cf. Sec. 6.6). This feature of the two-phase centrifugal instability leads us to investigate the influence of the arrangement of fluids on stability. This is the subject of Sec. 6.12.

6.12 Effect of fluid arrangement on stability

Based on the results in Sec. 6.6 and Sec. 6.11, we expect the arrangement of fluids to have a significant influence on stability. As an example, consider two fluids of nearly equal densities and volume fractions, but with viscosities in the ratio 1:6. If the less viscous fluid is taken as the outer fluid, then $\mu_{12} = 6$, else $\mu_{12} = 1/6$. The Rayleigh discriminant profile for these two cases is very different, as shown in Fig. 6.2. Fig. 6.9 shows that if the less viscous fluid is placed on the outer side ($\mu_{12} = 6$), then the O-S mode will be critical, else the I-S mode will be critical.

Apart from the nature of the critical mode, the critical pressure drop G_c^* will also depend on the arrangement of fluids. G_c^* is the minimum magnitude of the pressure gradient required for the flow to become unstable. We can determine the more unstable fluid arrangement by identifying the arrangement that requires a smaller critical pressure drop.

If the two configurations are labelled A and B, then in the framework of our mathematical model, we obtain two stability problems with parameter sets $(\rho_{12})_A$, $(\mu_{12})_A$, $(b)_A$ and $(\rho_{12})_B$, $(\mu_{12})_B$, $(b)_B$ respectively. Since configurations A and B are related by interchanging the locations of the fluids, the following relations hold between the two sets of parameters:

$$(\rho_{12})_B = 1/(\rho_{12})_A\,; \quad (\mu_{12})_B = 1/(\mu_{12})_A\,; \quad (b)_B = 1 - (b)_A \tag{6.25}$$

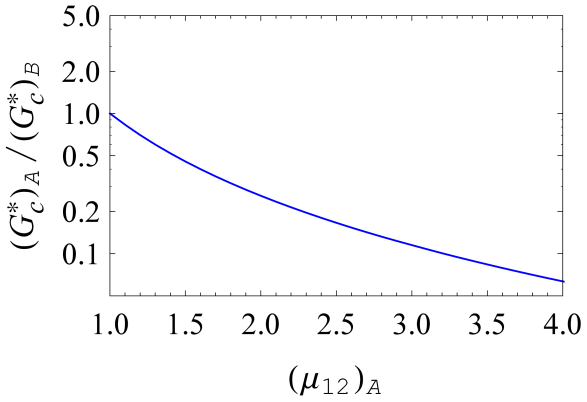

Figure 6.16: Effect of fluid arrangement on stability when the fluids have different viscosities. The ratio of critical pressure drops of configurations A and B is plotted as a function of the viscosity ratio. A: more viscous fluid on the inner side of the channel. B: more viscous fluid on the outer side. Placing the less viscous fluid on the outer side is destabilizing. Parameter values: $\rho_{12} = 1, b = 0.5, a = 0.1$

The corresponding critical Reynolds number are $(Re_c)_A$ and $(Re_c)_B$, from which the ratio of critical pressure drops may be obtained using (6.8):

$$\frac{(G_c^*)_A}{(G_c^*)_B} = \frac{(Re_c)_A}{(Re_c)_B} \frac{(\mu_{12})_A}{(\rho_{12})_A} \tag{6.26}$$

From (6.26) we see that the ratio of critical Reynolds numbers cannot be used to compare the two configurations. This is because the value of the Reynolds number depends on the density and viscosity scales. If the fluids have different physical properties ($\rho_{12} \neq 1, \mu_{12} \neq 1$), then the ratio of critical Reynolds numbers will not be unity when configurations A and B are equally unstable, with $(G_c^*)_A = (G_c^*)_B$. Thus, we must compare the critical pressure drops in order to reliably identify the more unstable fluid arrangement.

Now, we study a few specific fluid pairs with the aim of developing general rules for identifying the more unstable configuration. Firstly, consider the case of the interface located at $b = 0.5$, with fluids of equal densities but unequal viscosities. Let A (B) be the configuration with the more viscous fluid on the inner (outer) side of the channel. In Fig. 6.16, the ratio of critical pressure drops is plotted as a function of the viscosity ratio (as defined for configuration A). Here $(G_c^*)_A$ is always less than $(G_c^*)_B$, i.e. the configuration with the less viscous fluid on the outer side is more unstable. The difference in the stability of the two configurations increases with the difference in the viscosities of the two fluids. A similar result was obtained by Renardy and Joseph (1985) for two-phase Taylor-Couette flow.

Next we consider two fluids of equal viscosity but unequal densities, with the interface at $b = 0.5$. A (B) is the configuration in which the denser fluid is on the inner (outer) side of the channel. The ratio of critical pressure drops is plotted for various den-

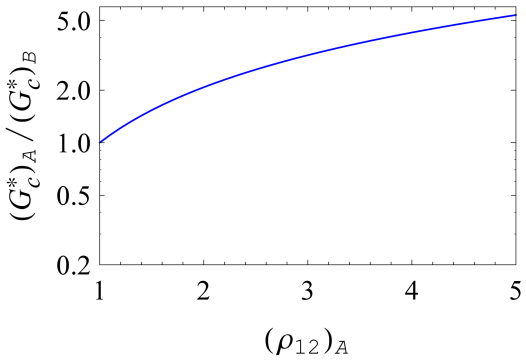

Figure 6.17: Effect of fluid arrangement on stability when the fluids have different densities. The ratio of critical pressure drops of configurations A and B is plotted as a function of the density ratio. A: more dense fluid on the inner side of the channel. B: more dense fluid on the outer side. Placing the denser fluid on the outer side stabilizes the centrifugal mode. Parameter values: $\mu_{12} = 1, b = 0.5, a = 0.1$

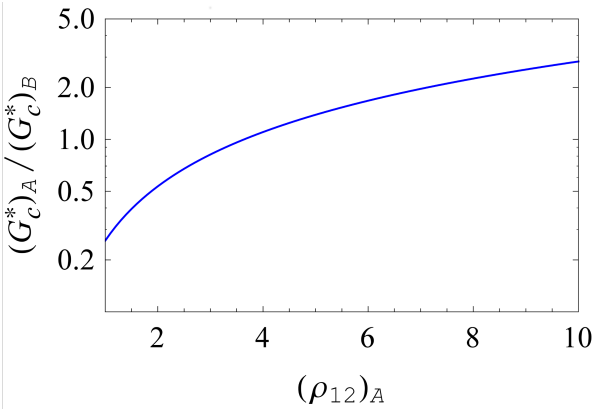

Figure 6.18: Effect of fluid arrangement on stability when the fluids have different densities and viscosities. The ratio of critical pressure drops of configurations A and B is plotted as a function of the density ratio. The viscosity ratio is fixed at 2:1, i.e the denser fluid has twice the viscosity of the less dense fluid. A: more dense, more viscous fluid on the inner side of the channel. B: more dense, more viscous fluid on the outer side. Parameter values: $(\mu_{12})_A = 2, b = 0.5, a = 0.1$

sity ratios (as defined in A) in Fig. 6.17. In this case, $(G_c^*)_A$ is always greater than $(G_c^*)_B$ indicating that the configuration with the denser fluid on the outer side is more unstable. Interestingly, while this arrangement destabilizes the centrifugal instability, it stabilizes interfacial instabilities, i.e. both the (centrifugal) Rayleigh-Taylor and viscosity-induced modes (Boomkamp and Miesen, 1996).

From Fig. 6.16 and Fig. 6.17 we see that the viscosity and density of the outer fluid have opposing effects on stability. Ideally, the outer fluid should be more dense, as well as less viscous, to promote instability. This need not be the case in practice; Fig. 6.18 depicts results for a situation in which the fluid with a greater density has twice the viscosity of the less dense fluid. A is the configuration in which the more dense, more viscous fluid is located on the inner side of the channel. On the basis of Fig. 6.17 and Fig. 6.16, the density difference is expected to stabilize A while the viscosity difference destabilizes A. The ratio of critical pressure drops, plotted in Fig. 6.18, shows that the viscous effect dominates when the density difference between the two fluids is small while the density effect becomes prominent at larger density ratios. These two effects balance out at a density ratio of approximately 3.7:1 when $(G_c^*)_A = (G_c^*)_B$ (A and B are equally unstable). Considering that the viscosity ratio is only 2:1, it seems that *viscosity differences have a greater impact on the centrifugal instability than equivalent density differences.* This is not unexpected, given the dual effect of the viscosity ratio on the relative stability of the fluids. Apart from modulating the extent of viscous dissipation in the two fluids, the viscosity ratio also impacts the base velocity profile and thereby the stratification of angular momentum. In Sec. 6.6, it was shown that the less viscous fluid tends to have a more unstable stratification. In contrast, the density ratio has no influence over the base velocity profile; it only effects the competition between centrifugal forces and viscous dissipation.

Finally we consider two fluids with equal physical properties but occupying unequal volume fractions of the channel. In this case, the ratio of critical pressure drops equals the ratio of critical Reynolds numbers, because $\rho_{12} = \mu_{12} = 1$ in (6.26). The critical Reynolds number was plotted as a function of the volume fraction in Fig. 6.11a. From this figure, we see that the critical Reynolds number is lower when $b < 0.5$. Thus the critical pressure drop is lower when the volume fraction of the inner fluid is smaller. Hence, *the flow will be more unstable when the fluid that occupies a larger fraction of the channel is located on the outer side.*

The cases studied in this section lead to the following general principle: *the two-phase flow is rendered more unstable, to the centrifugal instability, when the fluid that is less viscous, more dense and has a larger volume fraction is chosen as the outer fluid.* Interestingly, these criteria also ensure that the critical mode will be an outer mode (O-S or O-T) with a stronger cross flow within the outer fluid (cf. Sec. 6.11). It is quite possible

that the pair of fluids will have properties with opposing effects on the system's stability (cf. Fig. 6.18). For example, the denser fluid could have a larger viscosity and occupy a smaller volume fraction of the channel. In such cases the more unstable configuration is not obvious, but can be determined by applying the methodology described in this section.

6.13 Concluding remarks

We have studied the centrifugal instability of two-phase layered Poiseuille flow in a curved channel. This problem is a two-phase analogue of the classic Dean problem (Drazin and Reid, 2004) wherein pressure driven flow is susceptible to an instability due to unstable stratification of angular momentum. In the general two-phase problem, the flow can also become unstable to interfacial modes in addition to the centrifugal mode. These include the viscosity-induced instability, (centrifugal) Rayleigh-Taylor and capillary breakup. In this work, we have analyzed the regime of small capillary numbers, wherein interfacial deformations are suppressed by surface tension. (The capillary instability is excluded because of the relatively large radius of curvature of the channel.) Under these circumstances the centrifugal mode dominates, allowing us to study its features in detail. The results presented here for the two-phase centrifugal instability, when taken in conjunction with previous work on interfacial modes (Govindarajan and Sahu, 2014; Johns and Narayanan, 2002), provide a foundation for a general stability analysis of layered flow in curved channels.

Studies across parameter space revealed six types of critical centrifugal modes - three axisymmetric (I-S, U-S, O-S) and three non-axisymmetric (I-T, U-T, O-T). The axisymmetric modes are critical over most of the parameter space. They correspond to a stationary (S) secondary flow consisting of axisymmetric toroidal vortices within each fluid. The non-axisymmetric modes correspond to travelling (T) waves of rotating spiral vortices. The circulatory flow can be stronger within one of the fluids or of comparable intensity in both, leading to a further classification into inner modes (I), outer modes (O) and uniform modes (U). A stronger circulatory flow tends to arise in the fluid with either a lower viscosity, a higher density or a larger volume fraction.

This rich variety of instability modes is a characteristic of the two-phase system that is not seen in the single-phase case. This is due to the influence of the viscosities and interface position on the stratification of angular momentum in the base state, as quantified by the Rayleigh discriminant (Sec. 6.6). In addition, all physical parameters influence the interplay between inertial and viscous forces, which governs the growth of the instability.

It is important to note that even for small super-critical Reynolds numbers, a range

of both axisymmetric modes and travelling waves can become unstable. This is because the marginal Reynolds numbers of these modes are closely spaced, as shown in Fig. 6.3. This is especially true for parameters close to mode switching points (codimension-two bifurcations). The interaction between different modes can result in a variety of flow patterns. A similar situation exists in single-phase Taylor-Couette flow near the transition from Taylor vortex flow (axisymmetric mode) to spiral flow (non-axisymmetric travelling wave) (Andereck *et al.*, 1986; Langford *et al.*, 1988). Interaction between modes results in flow patterns such as ribbons, wavy vortices, twisted vortices and modulated periodic flows (Golubitsky and Stewart, 1986; Golubitsky and Langford, 1988; Itoh, 1996). These flows have been observed experimentally (Andereck *et al.*, 1986) in single-phase Taylor-Couette flow and explained by group theoretic methods (equivariant bifurcation theory) (Crawford and Knobloch, 1991; Golubitsky and Stewart, 1986; Golubitsky and Langford, 1988). In the two-phase flow studied here, an even richer variety of patterns may be expected due to inter-fluid interaction across the interface.

The stability of the flow was found to depend on the arrangement of the fluids. We demonstrated that the critical Reynolds number cannot be used to compare different fluid arrangements. Instead, we compared the minimum pressure drop required for the onset of instability and found a general rule: the flow is more unstable when the fluid with a higher density, lower viscosity and larger fractional flow area is taken as the outer fluid. (These are the same conditions that promote stronger circulations in the outer fluid.)

In finite but tall curved channels, the base flow is nearly uni-directional with only a weak circulatory component. However, the results of this chapter show that, even in these tall channels, strong circulatory flows can be generated by exploiting the centrifugal instability of layered flow. Hence, these tall curved channels could make excellent mass transfer devices, by combining a large interfacial area with good intra-fluid mixing. Such a device, based on two-phase Taylor-Couette flow, has been studied recently by Baier *et al.* (2000). Our results support the viability of a similar system based on pressure driven flow. These devices require the fluids to remain layered. In view of this, the dependence of the centrifugal instability on the fluid configuration is quite favorable. Placing the denser fluid on the outer side of the channel not only stabilizes the interface to the Rayleigh-Taylor instability (stable light over heavy configuration), but also promotes vortex formation by inducing the centrifugal instability at lower pressure drops.

The two-phase eigenvalue problem, associated with the linear stability analysis, has been solved by a two-phase Recombined Chebyshev Galerkin Spectral method (RCGS), which utilizes a novel basis of recombined Chebyshev functions. This recombined basis satisfies the boundary conditions analytically. Thus boundary conditions do not have to be included separately in the matrix eigenvalue problem, as is conventionally done in standard Tau and collocation spectral methods (Boyd, 2001). In these traditional tech-

niques, the rows corresponding to boundary conditions often cause the QZ algorithm to generate spurious, unbounded eigenvalues. This difficulty is circumvented by the present RCGS method. Another advantage of this method is the smaller size of the matrix for the same number of spectral modes. This method is a two-phase extension of the technique used by Gelfgat and coworkers (Gelfgat and Tanasawa, 1994; Gelfgat *et al.*, 1999; Gelfgat, 2001) and can be applied to other two-phase problems that have boundaries located along co-ordinate surfaces. The information provided in Appendix D will aid in such applications.

EPILOGUE

"I do not remember making any forecasts of broad areas of study which have proved fruitful, but I have gone along paths which are attractive to me personally. All my work, like that of most of us, has been concerned with particular problems....it seems to me that it is by attention to specific problems rather than by generalized reasoning that advances are made in our subject."

– G. I. Taylor

A theoretical analysis of layered two-phase micro-flows has been presented in this thesis. We have addressed two aspects of these flows, which are particularly important in mass transfer based applications – diffusion of a solute between fluids, and the influence of centrifugal forces in curved bends. Simplified mathematical models have been used, along with analytical and asymptotic methods where possible, in order to gain fundamental insight into the physics of these flows. The key results are summarized in the paragraphs that follow, with an emphasis on their implication for mass transfer in microchannels. Connections between the phenomena and patterns studied in different chapters are also highlighted. A more detailed summary, as well as specific suggestions for future research projects, may be found in the concluding section of each chapter.

In the course of our investigations, we have identified several promising strategies for enhancing mass transfer in layered flows, while maintaining the integrity of the inter-fluid interface. The first approach involves tuning the operating parameters, so as to obtain optimal performance in co-current layered flow through straight channels. Using the Two Equation Averaged (TEA) model we have identified the range of fluid volume fractions (set by the flow rates) that maximizes either the extent of extraction at equilibrium, or the rate of extraction. These two goals have been shown to be mutually exclusive, and the maximum extraction at equilibrium is achieved for flow rates that correspond to the slowest approach to equilibrium.

A second strategy involves operating in counter-current flow. However, this strategy has been shown to result in significant improvement only for a limited range of operating parameters. Outside this range, the performance gain is not worth the extra effort required to establish and operate counter current flow in microchannels. This analysis has revealed a general principle underlying the relative performance of co-current and counter-current

systems: 'maximum gain at mediocre performance'. It will be interesting to see if this principle applies to other separation processes as well.

A third method for improving mass transfer is to introduce curved channels, in which circulatory flows are developed due to centrifugal forces. The type of vortex pattern and the strength of circulations can be controlled by adjusting the fluid's volume fractions. This will be useful in applications, where stronger circulations (associated with a principal vortex) may be desired in the fluid with lower solute diffusivity.

Finally, mass transfer can be enhanced by taking advantage of instabilities that occur due to solutal-Marangoni effects or the influence of centrifugal forces. In either case, it is important to adjust the system parameters so that only instabilities that leave the interface undisturbed are permitted. For example, in case of solutal-Maranogni flows, one must attempt to induce the M1-SW mode, while suppressing other Marangoni modes, as well as the viscosity-induced interfacial mode. The appropriate parameter ranges have been identified, along with the physical mechanisms that drive the various instabilities.

Using any one, or a combination of these strategies, mass transfer in layered flows may be improved significantly. However, a detailed quantification of transport enhancement due to solutal Marangoni and centrifugal effects remains to be carried out. This calls for appropriate experiments and numerical simulations, all of which are interesting avenues for future work.

Aside from their potential for improving mass transfer, layered flows in curved channels make for an interesting study due to the rich variety of circulatory flow patterns that arise. This is true of the secondary vortices in rectangular channels, as well as the instability induced vortex arrays in infinitely tall channels. In rectangular channels, different vortex patterns arise from an inherent competition between the circulatory flows in the two fluids. These flows interact across the inter-fluid interface via viscous shear stresses. In case of the centrifugal instability in tall channels, the distribution of the base axial velocity plays a crucial role in deciding the relative strength of the vortex flows in the two fluids. The outer fluid is inherently more unstable and has a tendency to generate stronger vortex flows at the onset of instability. Thus, the arrangement of fluids has a significant influence on the circulatory flow, unlike in the rectangular channel where the positioning of the fluids is irrelevant (in the small curvature limit).

The viscosity contrast between the two fluids has been shown to be a key parameter governing the transition between different flow patterns/instability modes. This is true in both curved channel flow problems (Ch. 5 and Ch. 6), as well as in the solutal Marangoni problem (Ch. 4). The viscosity contrast influences these problems via three distinct routes:

1. The viscosity ratio modulates the extent of viscous dissipation in the two fluids.

Disturbances experience less dampening within the fluid with lower viscosity. This effect of viscosity is captured by the Reynolds number of the fluid.

2. The viscosity ratio modifies the base flow profile and thereby has a significant effect on both the threshold of instability and the nature of the instability mode. This effect is seen quite prominently in the centrifugal instability, wherein the viscosity contrast controls the position of the maximum of the base flow profile, which marks the transition between regions with stable and unstable angular momentum stratification (cf. Sec 6.6 and Sec. 6.11.1). This influence of the viscosity ratio is also seen in the vortex patterns in rectangular curved channels in Ch. 5. For equal volume fractions, the maximum of axial velocity tends to lie in the less viscous fluid, which consequently experiences greater centrifugal forces (cf. Sec. 5.4.3). However, the greater effect of the viscosity ratio in this problem is via its role in the tangential stress balance. This brings us to the third effect of the viscosity ratio.

3. The viscosity ratio governs the coupling between the secondary flows in two fluids via the mutual exertion of viscous shear stresses. This effect is most clearly seen in Ch. 5, wherein the more viscous fluid is shown to reverse the circulatory flow within the less viscous fluid (Re being the same in both) and generate sandwich and reversed vortices (cf. Sec 5.4).

These intricate and intertwined effects of the viscosity ratio are key aspects of the physics of these layered flows, and are responsible for many of the interesting flow features identified in this thesis. In a recent review, Govindarajan and Sahu (2014) examine the complex role of viscosity stratification and its non-intutive consequences in a variety of situations, involving both immiscible and miscible fluid layers.

Ch. 4 is the first comprehensive study of solutal Marangoni instability in layered Poiseuille flow. Here, we have found two short wave modes that have not been reported or characterized previously (the long wave mode is analogous to that studied by Wei (2006) in thermocapillary Couette flow). This work opens up many avenues for exploration. A weakly nonlinear analysis can be carried out to determine whether these modes bifurcate supercritically or subcritically. Full numerical simulations can then be used to understand their nonlinear evolution and their influence on the layered flow state. Existing long-wave asymptotic methods, such as the weighted residual integral boundary layer (WRIBL) method (Dietze and Ruyer-Quil, 2013; Kalliadasis *et al.*, 2012), can be applied to study the nonlinear dynamics of the long-wave solutal Marangoni instability, at a reduced computational cost. This will be important for microchannel applications, because the long wave mode becomes unstable at much lower Re than the short wave modes. The spatio-temporal nature of these modes (absolute or convective) must also be studied (Huerre, 2000; Huerre and Rossi, 1998; Chomaz, 2005), in order to understand

their influence on flow in practical systems, in which the channel will be of finite length and the base state concentration may vary along the flow direction.

A novel averaging technique, based on the Lyapunov-Schmidt reduction, has been presented in Ch. 2, in the context of diffusion between fluid layers. Here, we have shown that averaging over each fluid separately leads to a superior reduced model, when compared to averaging across both layers together. Separate fluid averaging enables us to describe mass transfer between the fluids before they equilibrate. Therefore, we can capture the evolution of the average concentrations within the two fluids, right from the inlet where they first come into contact. This is not possible when the fluids are averaged simultaneously, because this implicitly restricts the reduced model to situations in which the fluids have undergone an initial equilibration; only deviations from this equilibrium can be described (e.g. due to a slow reaction, as in Ch. 2).

A challenging future task is to attempt to apply this new averaging method to the Navier-Stokes equations, and thereby develop an averaged model capable of describing coupled mass transfer and fluid dynamic phenomena in layered flows. Such a model would be very useful in analyzing the dynamics of the solutal-Marangoni instability encountered in Ch. 4. The Lyapunov-Schmidt averaging of the Navier-Stokes is likely to closely parallel the center-manifold reduction methodology developed by Roberts (2015) for single phase thin films flows. However, care should be taken to capture inter-phase viscous transfer of momentum by interfacial shear stresses, just as inter-phase diffusion was captured in Ch. 2. An alternative route to an averaged model is via the weighted residual integral boundary layer (WRIBL) method, which has already been used successfully to describe the dynamics of layered two-phase flows in the absence of a solute (Dietze and Ruyer-Quil, 2013, 2015). In fact, it would be very interesting to compare the Lyapunov-Schimdt based model of Ch. 2) with one derived via the WRIBL method. Comparing them for the relatively simple case of diffusion in steady layered flow should shed light on both techniques, and help in deciding which technique is more suitable for describing simultaneous mass and momentum transport in layered flow.

APPENDIX A

Analytical Solution of the Co-current Extraction Model

> *"...(transformations) can be rendered self-adjoint by negotiating the parent Hilbert space of the system vector and its inner product. ...this exercise is in quest of a hidden symmetry, the unfolding of which produces a picturesquely prismatic partitioning of the Hilbert space in which the skeletal structure of the unknown vector is revealed. For this view to emerge, however, it is crucial that the vector be traced to its most natural habitat, one that not only relies on mathematical symmetry but, as we shall see, resonates with nature."*
>
> – Ramkrishna and Aris , *The Beauty of Self-Adjoint Symmetry (1999)*

The construction of the solution to the co-current model (3.9) and (3.10) is described in this appendix.

(3.9) may be represented concisely in linear operator form as:

$$-\frac{dc}{dx} = \mathbf{L}c \tag{A.1}$$

Here $\mathbf{L}$ is a Sturm-Liouville operator defined on the Hilbert Space $\mathcal{L}_2[0,1]$ as follows:

$$\mathbf{L}c = -\frac{1}{v_r(y)}\frac{d}{dy}\left[\frac{1}{Pe}\frac{dc}{dy}\right] \qquad 0 \le y \le 1 \tag{A.2}$$

where c is piecewise continuous, and Pe is piecewise constant:

$$c = \left\{ \begin{array}{c} c_1(x,y) \\ c_2(x,y) \end{array} \right\}, \quad Pe = \left\{ \begin{array}{c} Pe_1 \\ Pe_2 \end{array} \right\} \qquad \text{for} \quad y = \left\{ \begin{array}{c} 0 \le y \le h_r \\ h_r < y \le 1 \end{array} \right\} \tag{A.3}$$

Following the treatment of (Ramkrishna and Amundson, 1974) we define an inner product that renders the operator $\mathbf{L}$ self-adjoint.

$$\langle f, g \rangle = \int_0^{h_r} f_1(y) g_1(y) dy + \left(\frac{K}{\beta}\frac{Pe_2}{Pe_1}\right) \int_{h_r}^{1} f_2(y) g_2(y) dy \tag{A.4}$$

The factor $\left(\frac{K}{\beta}\frac{Pe_2}{Pe_1}\right)$ is equivalent to $K(v_2/v_1)$, which can viewed as a ratio of the relative capacities of fluid 1 and fluid 2 to hold solute within the channel. Mathematically, this

factor ensures that $\mathbf{L}$ is self-adjoint, i.e. it satisfies $\langle \mathbf{L}f, g\rangle = \langle f, \mathbf{L}g\rangle$. This property considerably simplifies the construction of a solution as an eigenfunction expansion, as outlined below. This problem may be added to the numerous examples that demonstrate a basic principle of applied mathematics, which is that mathematically symmetric and thereby 'beautiful' formulations often turn out to be most useful in practice (Ramkrishna and Aris, 1999; Poincare, 1914).

A self-adjoint operator possess a discrete spectrum of eigenvalues, and the corresponding eigenfunctions form an orthonormal basis in $\mathcal{L}_2[0,1]$ (Ramkrishna and Amundson, 1985). Thus we can represent the solution as

$$c(x,y) = \sum_n \big\langle c(x,y), \varphi_n(y)\big\rangle\, \varphi_n(y) \tag{A.5}$$

where $\varphi_n(y)$ is the nth orthonormal eigenfunction. The eigenvalue problem is given by $\mathbf{L}\varphi_n = \lambda_n^2\varphi_n$, where λ_n^2 are the non-negative eigenvalues. The eigenfunctions are piecewise continuous with a single point of discontinuity at the interface. Solving this eigenvalue problem, we obtain

$$\begin{aligned}\varphi_n &= \left\{ \begin{array}{ll} \varphi_{1,n} & 0 \le y \le h_r \\ \varphi_{2,n} & h_r < y \le 1 \end{array} \right\} \\ &= \left\{ \begin{array}{c} A\sin\left(\lambda_n\sqrt{Pe_1}y\right) + B\cos\left(\lambda_n\sqrt{Pe_1}y\right) \\ C\sin\left(\lambda_n\sqrt{Pe_2}\,(1-y)\right) + D\cos\left(\lambda_n\sqrt{Pe_2}\,(1-y)\right) \end{array} \right\}\end{aligned} \tag{A.6}$$

Here λ_n is the positive root of λ_n^2 . The no-flux boundary conditions in (3.10a) require that $A = C = 0$. The boundary conditions at the interface (3.10b) and (3.10c) give rise to a set of two homogeneous linear algebraic equations. For non-trivial solutions, the determinant of this system of equations must vanish. This condition yields the characteristic equation that determines the eigenvalues:

$$\begin{aligned}\sqrt{Pe_2}\cos\left(\lambda_n\sqrt{Pe_1}h_r\right)\sin\left(\lambda_n\sqrt{Pe_2}\,(1-h_r)\right) + \\ K\beta\sqrt{Pe_1}\sin\left(\lambda_n\sqrt{Pe_1}h_r\right)\cos\left(\lambda_n\sqrt{Pe_2}\,(1-h_r)\right) = 0\end{aligned} \tag{A.7}$$

This equation is transcendental in λ_n and must be solved numerically. Care should be taken to ensure that all eigenvalues are obtained. Further, they must be paired correctly with the corresponding eigenfunctions in the series solution. The eigenfunctions are given by

$$\varphi_{1,n}(y) = b_n\cos\left(\lambda_n\sqrt{Pe_1}y\right) \tag{A.8a}$$

$$\varphi_{2,n}(y) = d_n\cos\left(\lambda_n\sqrt{Pe_2}\,(1-y)\right) \tag{A.8b}$$

where b_n and d_n are calculated to ensure orthonormality of the eigenfunctions under the inner product defined in (A.4):

$$b_n = \left[\frac{2\lambda_n\sqrt{Pe_1}h_r + \sin\left(2\lambda_n\sqrt{Pe_1}h_r\right)}{4\lambda_n\sqrt{Pe_1}} + \left\{ K\beta^2 \frac{Pe_1}{Pe_2} \frac{\sin^2\left(\lambda_n\sqrt{Pe_1}h_r\right)}{\sin^2\left(\lambda_n\sqrt{Pe_2}\,(1-h_r)\right)} \right.\right.$$
$$\left.\left. \times \frac{2\,(1-h_r)\,\lambda_n\sqrt{Pe_2} + \sin\left(2\lambda_n\sqrt{Pe_2}\,(1-h_r)\right)}{4\lambda_n\sqrt{Pe_2}} \right\} \right]^{-1/2} \tag{A.9a}$$

$$d_n = -b_n\beta \frac{\sqrt{Pe_1}}{\sqrt{Pe_2}} \frac{\sin\left(\lambda_n\sqrt{Pe_1}h_r\right)}{\sin\left(\lambda_n\sqrt{Pe_2}\,(1-h_r)\right)} \tag{A.9b}$$

The eigenvalue problem (A.7) admits a zero eigenvalue for $n = 0$. The corresponding eigenfunction is

$$\varphi_{1,0} = \left[h_r + \left(Pe_2/Pe_1\right) \frac{(1-h_r)}{\beta K} \right]^{-1/2} \tag{A.10a}$$

$$\varphi_{2,0} = \frac{1}{K}\varphi_{1,0} \tag{A.10b}$$

The coefficients of the eigenfunctions in (A.5) are obtained by taking the inner product of (A.1) with $\varphi_n(y)$ and using the property of self-adjointness:

$$-\frac{d\left\langle c, \varphi_n(y)\right\rangle}{dx} = \left\langle \mathbf{L}c, \varphi_n(y)\right\rangle = \left\langle c, \mathbf{L}\varphi_n(y)\right\rangle = \lambda_n^2 \left\langle c, \varphi_n(y)\right\rangle \tag{A.11}$$

On solving this ordinary differential equation and substituting the result in (A.5) we obtain the infinite series solution as:

$$c(x,y) = \sum_n \left\langle c\,(0,y)\,, \varphi_n(y)\right\rangle e^{-\lambda_n^2 x}\varphi_n(y) \tag{A.12}$$

Substituting the eigenfunctions from (A.8) - (A.10) in (A.12), we obtain the solution given in (3.11).

APPENDIX B

Analytical Solutions and Convergence Tests for Chapter 5

In this appendix, we develop a series solution to the biharmonic equations, governing the two-phase circulatory flow in curved channels (Sec. 5.3.3), and verify its convergence. We also demonstrate the convergence of the series solution for the axial velocity modification $w_{i,1}$ (Sec. 5.3.5).

B.1 Solution of biharmonic equations in two-phase flow

Here, we construct the solution of the biharmonic problem (5.21) to (5.22g), governing the two-phase circulatory flow in curved channels, using the method of superposition (Meleshko, 1996, 1998). The method involves constructing a separable solution as a sum of two infinite series; one series satisfies (5.21) and the other satisfies the homogeneous version of this equation. These series consist of complete orthogonal eigenfunctions, in the x and y directions, corresponding to the second order operators present in (5.21). We first determine these eigenfunctions and then construct the general solution to (5.21).

(5.21) contains two second order self-adjoint differential operators in the definition of ∇^2 – one in x and the other in y. These operators along with the homogeneous Dirichlet boundary conditions in (5.22a) to (5.22e) define two eigenvalue problems in each fluid:

$$-\lambda^2 \frac{d^2\phi_{ny,i}}{dy^2} = \omega^2_{y,i}\phi_{ny,i}\,; \quad \phi_{ny,i}\,(-1) = \phi_{ny,i}\,(+1) = 0 \quad \text{where } i = 1,2 \tag{B.1a}$$

$$-\frac{d^2\phi_{nx,1}}{dx^2} = \omega^2_{x,1}\phi_{nx,1}\,; \quad \phi_{nx,1}\,(-1) = \phi_{nx,1}\,(k) = 0 \tag{B.1b}$$

$$-\frac{d^2\phi_{nx,2}}{dx^2} = \omega^2_{x,2}\phi_{nx,2}\,; \quad \phi_{nx,2}\,(k) = \phi_{nx,2}\,(+1) = 0 \tag{B.1c}$$

Here, n takes values 1,2,3, etc., and $i = 1, 2$, denoting fluid 1 and fluid 2 respectively.

The eigenfunctions defined by (B.1) form complete orthogonal basis sets in their respective Hilbert spaces (Ramkrishna and Amundson, 1985). Solving the eigenvalue problem in the y direction, one obtains

$$\phi_{ny,i}\,(y) = \sin\left(\frac{n\pi}{2}\,(1-y)\right); \quad \omega_{ny,i} = \left(\frac{n\pi\lambda}{2}\right)^2 \tag{B.2}$$

These functions are odd for $n = 0, 2, 4...$ and even otherwise. The inhomogeneous forcing term in (5.21) is an odd function in y and the boundary conditions in y are symmetric.

Therefore $\psi_{i,1}$ must also be an odd function in y. Thus only the eigenfunctions which are odd, corresponding to $n = 0, 2, 4...$ need be considered. These may be rewritten in the more convenient form given below:

$$\phi_{ny,1}(y) = \sin(n\pi y); \quad \omega^2_{ny,1} = (n\pi\lambda)^2 \quad \text{for} \quad -1 \le x \le k \tag{B.3a}$$

$$\phi_{ny,2}(y) = \sin(n\pi y); \quad \omega^2_{ny,2} = (n\pi\lambda)^2 \quad \text{for} \quad k \le x \le 1 \tag{B.3b}$$

where, n = 1,2,3, etc.

In the x direction, the eigenfunctions have different forms in each fluid:

$$\phi_{mx,1}(x) = \sqrt{\frac{2}{1+k}} \sin\left(m\pi \frac{(x-k)}{(1+k)}\right); \quad \omega^2_{mx,1} = \left(\frac{m\pi}{1+k}\right)^2 \quad \text{for} \quad -1 \le x \le k \tag{B.3c}$$

$$\phi_{mx,2}(x) = \sqrt{\frac{2}{1-k}} \sin\left(m\pi \frac{(x-k)}{(1-k)}\right); \quad \omega^2_{mx,2} = \left(\frac{m\pi}{1-k}\right)^2 \quad \text{for} \quad k \le x \le 1 \tag{B.3d}$$

These eigenfunctions have been normalized so as to form orthonormal basis sets. We now seek a general solution to (5.21), as a sum of two series of these eigenfunctions:

$$\psi_{i,1}(x,y) = \sum_{n=1}^{\infty} a_{n,i}(x)\,\phi_{ny,i}(y) + \sum_{m=1}^{\infty} b_{m,i}(y)\,\phi_{mx,i}(x) \tag{B.4a}$$

where

$$a_{n,i}(x) = \int_{-1}^{+1} \psi_{i,1}(x,y)\,\phi_{ny,i}(y)\,dy; \qquad (i = 1, 2) \tag{B.4b}$$

$$b_{m,1}(y) = \int_{-1}^{k} \psi_{1,1}(x,y)\,\phi_{mx,1}(x)\,dx; \quad b_{m,2}(y) = \int_{k}^{+1} \psi_{2,1}(x,y)\,\phi_{mx,2}(x)\,dx \tag{B.4c}$$

The first series of $\phi_{ny,i}$ is required to satisfy (5.21), while the second series of $\phi_{mx,i}$ is required to satisfy the homogeneous version of (5.21). The coefficients $a_{n,i}$ and $b_{m,i}$ of these eigenfunctions are evaluated by multiplying (5.21) (and its homogeneous version) throughout by the respective eigenfunction and integrating over the corresponding domain. Then, using the property of self-adjointness of the operators and the definition of the eigenfunctions, one obtains a fourth order ordinary differential equation for each of the coefficients:

$$\left(\frac{d^4}{dx^4} - 2\omega^2_{ny,i}\frac{d^2}{dx^2} + \omega^4_{ny,i}\right) a_{n,i}(x) = \int_{-1}^{+1} -Re_i\lambda \frac{\partial}{\partial y}\left({w_{i,0}}^2\right)\phi_{ny,i}(y)\,dy \tag{B.5a}$$

$$\left(\lambda^4 \frac{d^4}{dy^4} - 2\lambda^2 \omega_{mx,i}^2 \frac{d^2}{dy^2} + \omega_{mx,i}^4\right) b_{m,i}(y) = 0 \tag{B.5b}$$

Solving these equations for the coefficients, $a_{n,i}$ and $b_{m,i}$, and substituting into (B.4a) yields the general solution for the stream functions (5.23a) - (5.23b) given in Sec. 5.3.3. In these expressions, the functions $s_{i,n}(x)$ are the particular solutions of (B.5a). Their form becomes increasingly complex and lengthy as more terms of the series for $w_{i,0}$ are used (cf. (5.17)). For the simplest case, in which only the first term of (5.17) is used for $w_{i,0}$, the calculations are more tractable, and only $s_{1,1}(x)$ and $s_{2,1}(x)$ are non-zero. These functions are given below:

$$s_{i,1}(x) = \frac{128 Re_i}{\pi^9 \lambda^7} \left[\begin{array}{l} 1 + \frac{1}{2}\left(A_{i0}^2 - B_{i0}^2\right) + \frac{32}{9} A_{i0} \cosh\left(\frac{1}{2}\pi\lambda x\right) + \frac{32}{9} B_{i0} \sinh\left(\frac{1}{2}\pi\lambda x\right) + \\ \\ \frac{1}{16}\left(A_{i0}^2 + B_{i0}^2\right)(\pi\lambda)^2 x^2 \cosh(\pi\lambda x) + \frac{1}{8} A_{i0} B_{i0} (\pi\lambda)^2 x^2 \sinh(\pi\lambda x) \end{array} \right] \tag{B.6}$$

When more terms of $w_{i,0}$ are considered, the calculations may be carried out using a symbolic computing software (eg. Mathematica) to obtain $s_{i,n}(x)$. A converged solution for $\psi_{i,1}$ is obtained when the first four terms of (5.17) are taken for $w_{i,0}$. An illustration of this convergence is shown in the following subsection (B.2).

The constants C_{1n} to C_{12m} in (5.23a) - (5.23b) are evaluated by applying the boundary conditions (5.22a) to (5.22g). In the y direction the boundary condition is applied at $y = +1$ only. Since the solution is odd in y, satisfying the boundary condition at $y = +1$ ensures that it is satisfied at $y = -1$ as well. Thus, there are a total of 12 boundary conditions to be applied.

Since the eigenfunctions satisfy the 6 Dirichlet boundary conditions, one of the two series in the solution goes to zero when these are applied. Requiring the other series to satisfy the boundary condition, results directly in equations for the unknown constants. However, when applying the remaining 6 non-Dirichlet boundary conditions, all the terms from both series survive. For example, on applying the Neumann condition for $\psi_{1,1}$ at $y = +1$, one obtains

$$\begin{aligned} &\sum_{n=1}^{\infty} \left[n\ \pi \cos(n\pi) \quad \left\{ \begin{array}{l} C_{1n} \cosh\left(\omega_{ny,1} x\right) + C_{2n} \sinh\left(\omega_{ny,1} x\right) + \\ C_{3n} x \cosh\left(\omega_{ny,1} x\right) + C_{4n} x \sinh\left(\omega_{ny,1} x\right) + s_1(x) \end{array} \right\} \right] \\ &+ \sum_{m=1}^{\infty} \left[\phi_{mx,1}(x) \quad \left\{ \begin{array}{l} C_{5m}\left(\omega_{mx,1}\lambda^{-1}\right) \cosh\left(\omega_{mx,1}\lambda^{-1}\right) \\ + C_{6m}\left(\cosh\left(\omega_{mx,1}\lambda^{-1}\right) + \left(\omega_{mx,1}\lambda^{-1}\right) \sinh\left(\omega_{mx,1}\lambda^{-1}\right)\right) \end{array} \right\} \right] = 0 \end{aligned} \tag{B.7}$$

This equation contains different functional forms in x and thus cannot be used in the present form to compute the unknown coefficients. In order to obtain equations for the

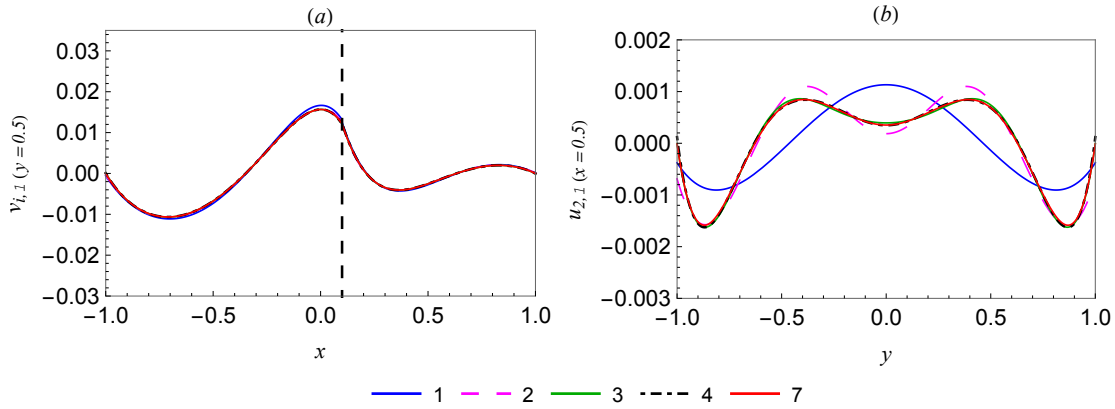

Figure B.1: Convergence of the series solution for the secondary circulatory flow. The number of terms used in (5.23a) - (5.23b) (value of n and m) is sequentially increased and the solutions obtained are compared. (a) The y-component of velocity $(v_{i,1})$, at $y = 0.5$, is plotted along the channel width (x). (b) The x-component of velocity in fluid 2 $(u_{2,1})$, at $x = 0.5$, is plotted along the channel height (y). The number of terms are indicated in the legend. Parameter values: $k = 0.1$, $Re_1 = 20$, $Re_2 = 15$, $\mu_{12} = 2$, $\lambda = 1$.

unknown coefficients, each of the functions in x must be projected onto the complete orthogonal eigenfunctions $\phi_{mx,1}(x)$. For example the function multiplying C_{1n} in (5.23a) may be expanded as

$$C_{1n}\cosh\left(\omega_{ny,1}x\right) = C_{1n}\sum_{m=1,2}^{N}\left(\int_{-1}^{k}\cosh\left(\omega_{ny,1}x\right)\phi_{mx,1}(x)dx\right)\phi_{mx,1}(x) \qquad \text{(B.8)}$$

Then, by requiring the coefficient of $\phi_{mx,1}(x)$ to be zero at every m, one obtains equations for the constants C_{1n} to C_{6m}. A similar procedure must be applied for the other 5 non-Dirichlet boundary conditions.

The solution is approximated by truncating each series to N terms. The set of $12N$ equations for the unknown constants are coupled and must be solved simultaneously. As N is increased, the values of all the constants are refined and the series converges to the solution (Meleshko, 1996, 1998). Four to five terms are found to be sufficient for this two-phase problem. In the following subsection, we compare the solution as N is increased, for a specific example, to demonstrate the convergence of the series.

B.2 Convergence of series solutions

In this subsection, we present results which demonstrate the convergence of the series solutions for the secondary streamfunction $\psi_{i,1}$ and the axial velocity modification $w_{i,1}$.

First, we illustrate the convergence of the infinite series solution for the circulatory flow (5.23a) - (5.23b). In Fig. B.1, line plots of $v_{i,1}$ and $u_{i,1}$, calculated using an increasing

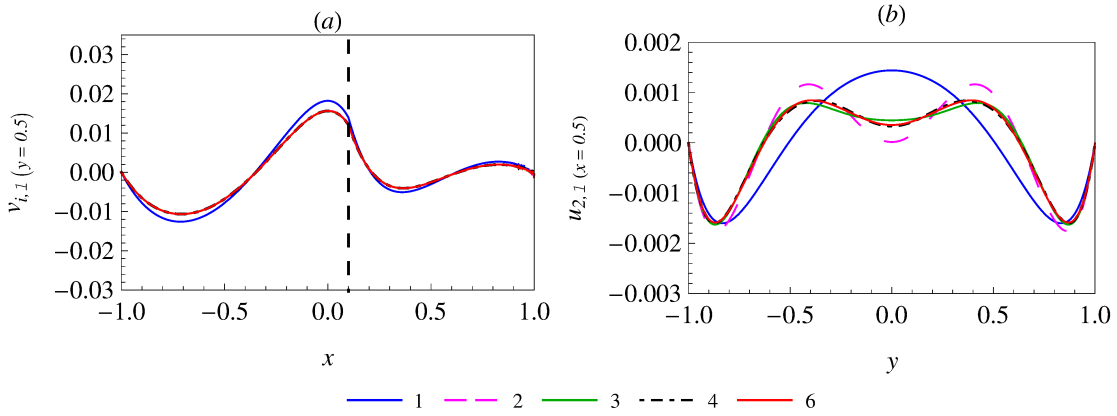

Figure B.2: Convergence of the circulatory flow field, as an increasing number of terms are taken in the series for the base axial velocity $(w_{i,0})$. (a) The y-component of velocity $(v_{i,1})$, at $y = 0.5$, is plotted along the channel width (x). (b) The x-component of velocity in fluid 2 $(u_{2,1})$, at $x = 0.5$, is plotted along the channel height (y). The number of terms are indicated in the legend. Parameter values: $k = 0.1$, $Re_1 = 20$, $Re_2 = 15$, $\mu_{12} = 2$, $\lambda = 1$.

number of terms, are compared (i.e. the maximum value of n and m in (5.23a) - (5.23b) are increased successively from 1 to 7). We see that the solution converges rapidly. In this case, four terms of each series are sufficient $(n = m = 4)$. This is found to be true for all the cases studied in this work.

Before calculating the stream function and the circulatory flow, the base axial velocity $w_{i,0}$ must be determined using the infinite series given in (5.17). The accuracy of the solution for the circulatory flow increases as more terms are used to compute $w_{i,0}$. However, if many terms are used for $w_{i,0}$, then the expressions for $\psi_{i,1}$ become lengthy and further analysis becomes difficult, even with symbolic computing software. Thus, it is important to know the minimum number of terms that must be considered in calculation of $w_{i,0}$, in order to obtain a converged solution for $\psi_{i,1}$. This is investigated in Fig. B.2, which presents line plots of $v_{i,1}$ (Fig. B.2a) and $u_{2,1}$ (Fig. B.2b), calculated using an increasing number of terms in the series for $w_{i,0}$ (i.e. the maximum value of n in (5.17) is increased from 1 to 6). These results show that the convergence is quite rapid. In all cases considered in this work, four terms of the $w_{i,0}$ series (5.17) are found to be sufficient for a converged circulatory flow field.

Next, we show an example of the convergence of the series solution for the axial velocity modification at $O(\varepsilon^1)$ (cf. (5.30) - (5.31)). Fig. B.3 presents line plots of $w_{i,1}$, which are computed using an increasing number of terms in (5.30) (i.e. the maximum value of n in (5.30) is increased from 1 to 5). In Fig. B.3a, in which $\mu_{12} = 1$, four terms are necessary, whereas in Fig. B.3b, in which $\mu_{12} = 3$, only two terms are required.

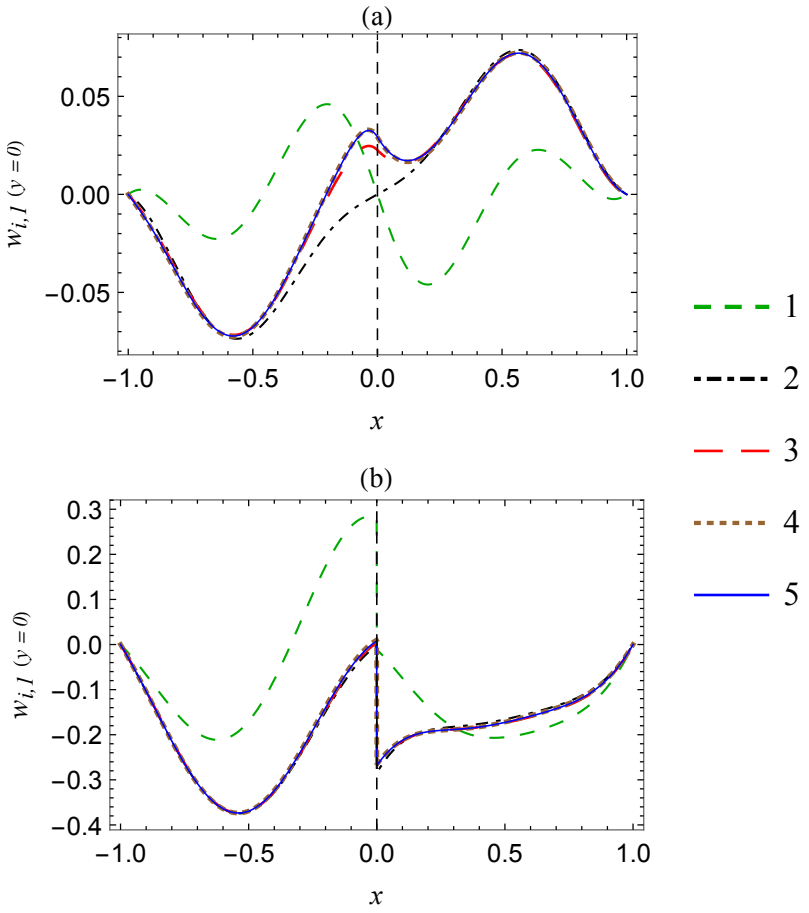

Figure B.3: Convergence of the series solution for the axial velocity modification at $O(\varepsilon^1)$, $w_{i,1}$, as more terms of the series are considered (cf. (5.30) - (5.31)). In these plots, $w_{i,1}$ at the horizontal centerline $(y = 0)$ is plotted along the width of the channel. The parameter values are: (a) $k = 0$, $Re_1 = 200$, $Re_2 = 200$, $\mu_{12} = 1$, $\lambda = 1$, $Ca = 0.2$; (b) $k = 0$, $Re_1 = 200$, $Re_2 = 200$, $\mu_{12} = 3$, $\lambda = 1$, $Ca = 0.2$. The number of terms are indicated in the legend.

APPENDIX C

The Gently Curved Approximation and the Centrifugal Instability

In Chapter 6, a simplified set of equations were used to analyze the centrifugal instability of two-phase layered flow (two-phase Dean instability). These equations are appropriate when the channel width (annular gap between the concentric cylinders) is much smaller than the radius of curvature of the channel. This narrow gap approximation (or gently curved approximation) is discussed in more detail in this appendix.

The governing equations, before making the narrow gap approximation, are given below. Here (u, w, v) are the non-dimensional velocities in the (x, z, θ) directions respectively $(x = (r^* - R^*)/d^*)$.

$$\frac{\partial u_i}{\partial x} + \frac{a u_i}{(1+ax)} + \frac{a}{(1+ax)}\frac{\partial v_i}{\partial \theta} + \frac{\partial w_i}{\partial z} = 0 \tag{C.1}$$

$$\frac{Re_i \mu_{1i}}{\rho_{1i}}\left[\frac{\partial u_i}{\partial t} + u_i\frac{\partial u_i}{\partial x} + \frac{a v_i}{(1+ax)}\frac{\partial u_i}{\partial \theta} + w_i\frac{\partial u_i}{\partial z} - \frac{a {v_i}^2}{(1+ax)}\right] = -12\mu_{1i1i}\frac{\partial p_i}{\partial x} + \frac{\partial^2 u_i}{\partial x^2} + \frac{a}{(1+ax)}\frac{\partial u_i}{\partial x} - \frac{a^2 u_i}{(1+ax)^2} + \frac{a^2}{(1+ax)^2}\frac{\partial^2 u_i}{\partial \theta^2} + \frac{\partial^2 u_i}{\partial z^2} - \frac{2a^2}{(1+ax)^2}\frac{\partial v_i}{\partial \theta} \tag{C.2}$$

$$\frac{Re_i \mu_{1i}}{\rho_{1i}}\left[\frac{\partial w_i}{\partial t} + u_i\frac{\partial w_i}{\partial x} + \frac{a v_i}{(1+ax)}\frac{\partial w_i}{\partial \theta} + w_i\frac{\partial w_i}{\partial z}\right] = -12\mu_{1i}\frac{\partial p_i}{\partial z} + \frac{\partial^2 w_i}{\partial x^2} + \frac{a}{(1+ax)}\frac{\partial w_i}{\partial x} + \frac{a^2}{(1+ax)^2}\frac{\partial^2 w_i}{\partial \theta^2} + \frac{\partial^2 w_i}{\partial z^2} \tag{C.3}$$

$$\frac{Re_i \mu_{1i}}{\rho_{1i}}\left[\frac{\partial v_i}{\partial t} + u_i\frac{\partial v_i}{\partial x} + \frac{a v_i}{(1+ax)}\frac{\partial v_i}{\partial \theta} + w_i\frac{\partial v_i}{\partial z} + \frac{a u_i v_i}{(1+ax)}\right] = \frac{12\mu_{1i}}{(1+ax)} - \frac{12a\mu_{1i}}{(1+ax)}\frac{\partial p_i}{\partial \theta} + \frac{\partial^2 v_i}{\partial x^2} + \frac{a}{(1+ax)}\frac{\partial v_i}{\partial x} - \frac{a^2 v_i}{(1+ax)^2} + \frac{a^2}{(1+ax)^2}\frac{\partial^2 v_i}{\partial \theta^2} + \frac{\partial^2 v_i}{\partial z^2} + \frac{2a^2}{(1+ax)^2}\frac{\partial u_i}{\partial \theta} \tag{C.4}$$

In the limit of a narrow gap or gently curved channel, the curvature ratio $a \ll 1$. Then terms of $O(a)$ in (C.1) - (C.4) may be dropped in comparison with terms of $O(1)$. Effectively, this eliminates the effect of curvature on the base flow and retains it only in the linearized stability equations. Dean (1928*a*) and Reid (1958), in their stability analyses of single-phase flow, only retained $(-aRev_i^2)$ and dropped all other terms multipled by

a. On the other extreme, Sparrow (1964) used the full set of equations without neglecting any terms. His results indicate that using the simplified equations of Dean (1928*a*) and Reid (1958) results in significant errors for curvature ratios greater than 0.1. For example, the results of Reid (1958) under-predict the critical Reynolds number by 7.4 % and 23.3 % for $a = 0.1$ and $a = 0.3$ respectively (Sparrow, 1964).

In this work, we aim for an intermediate level of simplification. All terms mutliplied by a and Re are retained, since we are interested in studying the onset of instability at which the critical Reynolds number may be large enough for these terms to become significant. In addition, we retain terms involving products of a and derivatives of θ, each raised to the same power. This enables a more accurate description of short wavelength azimuthal disturbances, which will have large values of the azimuthal derivative. Apart from the aforementioned exceptions, all other terms multiplied by a are dropped.

The effect of retaining the terms multiplied by Re may be assessed by comparing the results of our simplified equations (6.9) with those of Reid (1958) and Sparrow (1964) for the single-phase linear stability problem. We obtain a critical Reynolds number of $Re_c = 121.352$ at $a = 0.1$. For this case Reid (1958) reports a value of 114.86 while Sparrow's complete equations (Sparrow, 1964) predict 124.05. Since we retain all terms mutliplied by (aRe), our value of the critical Reynolds number is in between those reported by Reid (1958) and (Sparrow, 1964). The terms involving derivatives of θ do not play a significant role in the single-phase problem because the critical disturbance is axisymmetric. However, these terms will be important in the two-phase problem, wherein non-axisymmetric critical modes dominate for some parameter ranges.

Apart from simplifying calculations, Dean's approximation (Dean, 1928*a*) also enables one to combine the dependence of stability on the Reynolds number and curvature ratio into a single dimensionless number-the Dean number (De) defined as $Re\sqrt{a}$. This representation is not possible when some of the terms involving a are retained. Rather, the stability threshold must be described in terms of the critical Reynolds number (Re_c) calculated at specific values of the curvature ratio (a). However, the Dean number can be used to approximate the variation of Re_c with a, for small values of a, as shown in Sec. 6.10 of Ch. 6.

APPENDIX D

Two-phase Recombined Chebyshev Galerkin Spectral Method

D.1 Description of the method

In this appendix, we describe the two-phase RCGS method that was used to numerically solve the eigenvalue problem associated with the linear stability of layered flow in curved channels (Chapter 6). The construction of the recombined Chebyshev basis functions is duscussed, as well as the numerical implementation of Galerkin projections via Gaussian quadrature.

The basis functions are defined across both fluid domains by adopting the framework of direct sum spaces (Ramkrishna and Amundson, 1985). The functions $\hat{u}_{1,0}$ and $\hat{u}_{2,0}$, defined on $[0, b]$ and $[b, 1]$ respectively, are combined into a single vector function $\hat{\mathbf{u}}_\mathbf{0} = (\hat{u}_{1,0}, \hat{u}_{2,0})^\mathsf{T}$ defined over the entire domain $[0, 1]$. Similarly, we define $\hat{\mathbf{v}}_\mathbf{0} = (\hat{v}_{1,0}, \hat{v}_{2,0})^\mathsf{T}$. Here the superscript T denotes the transpose operation. While $\hat{u}_{1,0}$, $\hat{v}_{1,0}$ belong to the Hilbert space $\mathcal{L}_2[0, b]$ and $\hat{u}_{2,0}$, $\hat{v}_{2,0}$ belong to the Hilbert space $\mathcal{L}_2[b, 1]$, the composite functions $\hat{\mathbf{u}}_\mathbf{0}$ and $\hat{\mathbf{v}}_\mathbf{0}$ belong to the direct sum space $\mathcal{L}_2[0, b] \oplus \mathcal{L}_2[b, 1]$. This is a Hilbert space containing all elements $\mathbf{f} = (f_1, f_2)^T$ where $f_1 \in \mathcal{L}_2[0, b]$ and $f_2 \in \mathcal{L}_2[b, 1]$. Linear combinations in direct sum space are defined as follows:

$$\alpha\mathbf{f} + \beta\mathbf{g} = \left(\alpha f_1(x) + \beta g_1(x), \alpha f_2(x) + \beta g_2(x)\right)^\mathrm{T} \tag{D.1}$$

where

$$\mathbf{f}, \mathbf{g} \in \mathcal{L}_2[0, b] \oplus \mathcal{L}_2[b, 1]; \quad f_1, g_1 \in \mathcal{L}_2[0, b]; \quad f_2, g_2 \in \mathcal{L}_2[b, 1]$$
$$\mathbf{f} = (f_1, f_2)^\mathrm{T}; \quad \mathbf{g} = (g_1, g_2)^\mathrm{T}; \quad \alpha, \beta \in \mathfrak{R}$$

It follows from (D.1) that if vectors $\mathbf{f}$ and $\mathbf{g}$ both satisfy a set of homogeneous boundary conditions (applied at x = 0, 1 and b), then their linear combination must also satisfy the same boundary conditions. Thus, the set of all functions in $\mathcal{L}_2[0, b] \oplus \mathcal{L}_2[b, 1]$, which satisfy the boundary conditions (6.20) form a linear subspace $\mathcal{S}_u \in \mathcal{L}_2[0, b] \oplus \mathcal{L}_2[b, 1]$. Similarly, the set of functions satisfying boundary conditions (6.21) define another subspace $\mathcal{S}_v \in \mathcal{L}_2[0, b] \oplus \mathcal{L}_2[b, 1]$.

The unknown vector functions $\hat{\mathbf{u}}_\mathbf{0}$ and $\hat{\mathbf{v}}_\mathbf{0}$ defined by the eigenvalue problem (6.19) - (6.21) belong to the subspaces $\mathcal{S}_u$ and $\mathcal{S}_v$ respectively. The two-phase RCGS method

determines these functions by expanding them in terms of basis sets that also belong to the same subspaces. Let $\left\{\boldsymbol{\phi}_{\mathbf{u},n}\right\}_{n=0}^{\infty}$ and $\left\{\boldsymbol{\phi}_{\mathbf{v},n}\right\}_{n=0}^{\infty}$ be basis sets of $\mathcal{L}_2[0,b] \oplus \mathcal{L}_2[b,1]$, belonging to $\mathcal{S}_u$ and $\mathcal{S}_v$ respectively. Then $\hat{\mathbf{u}}_\mathbf{0}$ and $\hat{\mathbf{v}}_\mathbf{0}$ may be expanded as follows:

$$\hat{\mathbf{u}}_\mathbf{0} = \sum_{n=0}^{N} c_n \boldsymbol{\phi}_{\mathbf{u},n} \quad \text{and} \quad \hat{\mathbf{v}}_\mathbf{0} = \sum_{n=0}^{N} d_n \boldsymbol{\phi}_{\mathbf{v},n} \tag{D.2}$$

Here, linear combinations of $\boldsymbol{\phi}_{\mathbf{u},n}$ and $\boldsymbol{\phi}_{\mathbf{v},n}$ are defined according to (D.1).

The basis functions are composed of combinations of Chebyshev polynomials:

$$\boldsymbol{\phi}_{\mathbf{u},n} = \begin{cases} \boldsymbol{\phi}^{(1)}_{\mathbf{u},n}(x) = \sum_{j=0}^{4} \alpha^{(1)}_{j,n} T_{p(n)+j}\left[2\left(\frac{x}{b}\right) - 1\right] & 0 \le x < b \\ \boldsymbol{\phi}^{(2)}_{\mathbf{u},n}(x) = \sum_{j=0}^{4} \alpha^{(2)}_{j,n} T_{q(n)+j}\left[2\left(\frac{x-b}{1-b}\right) - 1\right] & b \le x \le 1 \end{cases} \tag{D.3}$$

$$\boldsymbol{\phi}_{\mathbf{v},n} = \begin{cases} \boldsymbol{\phi}^{(1)}_{\mathbf{v},n}(x) = \sum_{j=0}^{2} \beta^{(1)}_{j,n} T_{p(n)+j}\left[2\left(\frac{x}{b}\right) - 1\right] & 0 \le x < b \\ \boldsymbol{\phi}^{(2)}_{\mathbf{v},n}(x) = \sum_{j=0}^{2} \beta^{(2)}_{j,n} T_{q(n)+j}\left[2\left(\frac{x-b}{1-b}\right) - 1\right] & b \le x \le 1 \end{cases} \tag{D.4}$$

Here, $T_r[y]$ are Chebyshev polynomials of order r defined as $\cos(\arccos(y))$ with $y \in [-1,1]$. Each $\boldsymbol{\phi}^{(i)}_{\mathbf{u},n}(x)$ $(i = 1,2)$ consists of 5 Chebyshev polynomials, belonging to the respective fluid domain. On the other hand, each $\boldsymbol{\phi}^{(i)}_{\mathbf{v},n}(x)$ is composed of only three Chebyshev polynomials. This difference is because the number of boundary conditions on $\hat{\mathbf{u}}_\mathbf{0}$ and $\hat{\mathbf{v}}_\mathbf{0}$ are different. p and q are non-negative integers whose values depend on n. They specify the orders of the Chebyshev polynomials that must be combined to form the n^{th} basis function, $\boldsymbol{\phi}^{(i)}_{\mathbf{u},n}(x)$ or $\boldsymbol{\phi}^{(i)}_{\mathbf{v},n}(x)$.

$$p = \begin{cases} 0 \le n < 4 & \begin{cases} 0 & \text{if } n : \text{even} \\ 1 & \text{if } n : \text{odd} \end{cases} \\ n \ge 4 & \begin{cases} n/2 & \text{if } n : \text{even} \\ ((n-1)/2) - 1 & \text{if } n : \text{odd} \end{cases} \end{cases} \tag{D.5}$$

$$q = \begin{cases} 0 \le n < 4 & \begin{cases} 0 & \text{if } n < 2 \\ 1 & \text{if } n \ge 2 \end{cases} \\ n \ge 4 & \begin{cases} n/2 & \text{if } n : \text{even} \\ (n-1)/2 & \text{if } n : \text{odd} \end{cases} \end{cases} \tag{D.6}$$

The rationale behind these formula and the structure of the basis functions is outlined in subsection D.2.

The coefficients $\alpha^{(i)}_{j,n}$ and $\beta^{(i)}_{j,n}$ must satisfy the conditions that $\boldsymbol{\phi}_{\mathbf{u},n} \in \mathcal{S}_u$ and $\boldsymbol{\phi}_{\mathbf{v},n} \in \mathcal{S}_v$. This requires $\boldsymbol{\phi}_{\mathbf{u},n}$ to satisfy (6.20a) - (6.20e), which results in 8 equations for 10 unknown coefficients $\alpha^{(i)}_{j,n}$, at every n. Setting $\alpha^{(1)}_{0,n}$ and $\alpha^{(2)}_{0,n}$ to unity, these equations

are solved to determine the remaining eight coefficients. Using a symbolic computing package, analytical expressions are obtained for $\alpha_{j,n}^{(i)}$ in terms of j and n. In a similar manner, $\beta_{j,n}^{(i)}$ are determined from (6.21a) - (6.21d), after setting $\beta_{0,n}^{(1)}$ and $\beta_{0,n}^{(2)}$ to unity.

These recombined Chebyshev basis sets are now used in a standard Galerkin procedure to convert equations (6.19a) and (6.19b) into a matrix eigenvalue problem (Boyd, 2001). The expansions in (D.2) are substituted into (6.19a) and (6.19b), which are then projected onto the basis functions $\boldsymbol{\phi}_{\mathbf{u},n}$ and $\boldsymbol{\phi}_{\mathbf{v},n}$ to yield a set of 2(N+1) homogeneous equations in 2(N+1) unknowns, $\{c\}_{n=0}^{N}$ and $\{d\}_{n=0}^{N}$. The inner product in $\mathcal{L}_2[0,b] \oplus \mathcal{L}_2[b,1]$ is defined as follows

$$\langle \mathbf{f} \cdot \mathbf{g} \rangle = \int_0^b \frac{1}{\sqrt{1-\left(2\frac{x}{b}-1\right)^2}} f_1(x)\, g_1(x)\, dx + \int_b^1 \frac{1}{\sqrt{1-\left(2\frac{x-b}{1-b}-1\right)^2}} f_2(x)\, g_2(x)\, dx \tag{D.7}$$

where

$$\mathbf{f}, \mathbf{g} \in \mathcal{L}_2[0,b] \oplus \mathcal{L}_2[b,1]; \quad f_1, g_1 \in \mathcal{L}_2[0,b]; \quad f_2, g_2 \in \mathcal{L}_2[b,1]$$
$$\mathbf{f} = (f_1, f_2)^{\mathrm{T}}; \quad \mathbf{g} = (g_1, g_2)^{\mathrm{T}}$$

This inner product has been defined with weight functions that facilitate the application of Gaussian quadrature. This substantially reduces the time required for computing inner products. The standard quadrature formula must be suitably modified to account for the mapping of the domains $[0,b]$ and $[b,1]$ to $[-1,1]$. The modified formula are given below

$$\int_0^b \frac{1}{\sqrt{1-\left(2\frac{x}{b}-1\right)^2}} h_1(x)\, dx = \sum_{i=0}^{M} w_{1,i} h_1\left(\bar{x}_{1,i}\right) \tag{D.8}$$

where

$$\bar{x}_{1,i} = \left[\cos\left(\frac{i\pi}{M}\right)+1\right]\left(\frac{b}{2}\right) \quad \text{and} \quad w_{1,i} = \begin{cases} \pi b/(4M) & i = 0, M \\ \pi b/(2M) & i = 1,2,...M-1 \end{cases}$$

$$\int_b^1 \frac{1}{\sqrt{1-\left(2\frac{x-b}{1-b}-1\right)^2}} h_2(x)\, dx = \sum_{i=0}^{M} w_{2,i} h_2\left(\bar{x}_{2,i}\right) \tag{D.9}$$

where

$$\bar{x}_{2,i} = \left[\cos\left(\frac{i\pi}{M}\right)+1\right]\left(\frac{1-b}{2}\right)+b \quad \text{and} \quad w_{2,i} = \begin{cases} \pi(1-b)/(4M) & i = 0, M \\ \pi(1-b)/(2M) & i = 1,2,...M-1 \end{cases}$$

Here, M is the number of Gauss-Lobatto grid points ($\bar{x}_{1,i}$ and $\bar{x}_{2,i}$) used to evaluate the integral in each fluid domain. This grid yields exact results for polynomials of order $2M-1$.

D.2 Construction of the basis functions

In this discussion, we focus on $\boldsymbol{\phi}_{\mathbf{u},n}$ as the construction of $\boldsymbol{\phi}_{\mathbf{v},n}$ is entirely analogous. The set $\left\{T_r[2(x/b)-1]\right\}_{r=0}^{\infty}$ forms a basis in $\mathcal{L}_2[0,b]$, while $\left\{T_r[2(x-b)/(1-b)-1]\right\}_{r=0}^{\infty}$ forms a basis in $\mathcal{L}_2[b,1]$ (Ramkrishna and Amundson, 1985). (Note that the arguments of these Chebyshev polynomials map $[0,b]$ and $[b,1]$ onto $[-1,1]$.) A sequence of polynomials is selected from each Chebyshev family and combined to ensure that $\boldsymbol{\phi}_{\mathbf{u},n} \in \mathcal{S}_u$, i.e. the combined function belongs to $\mathcal{L}_2[0,b] \oplus \mathcal{L}_2[b,1]$ and satisfies the eight boundary conditions on $\hat{u}_{1,0}$ and $\hat{u}_{2,0}$ (6.20). Since these boundary conditions are homogeneous, the total number of Chebyshev functions used must be more than eight to ensure a non-trivial combination. In (D.3), a sequence of five polynomials is taken in each fluid domain, giving a total of ten. The coefficients in the combination are determined by applying equations (6.20), after setting the values of two coefficients to unity.

The selection of the values of p and q in (D.3) is based on the structure of direct sum spaces. The first step is to realize that when $\boldsymbol{\phi}_{\mathbf{u},n}$ is considered on each fluid sub-domain separately, then it forms basis sets in $\mathcal{L}_2[0,b]$ and $\mathcal{L}_2[b,1]$ respectively. This fact leads naturally to the construction of an elementary basis set in the direct sum space. While this elementary basis does not belong to $\mathcal{S}_u$, it does indicate the size of the subset of p and q values that would form the desired basis.

First consider the part of $\boldsymbol{\phi}_{\mathbf{u},n}$ defined on $[0,b]$ in (D.3), i.e. $\boldsymbol{\phi}_{\mathbf{u},n}^{(1)}(x)$. This function belongs to $\mathcal{L}_2[0,b]$. For $p=r$, $\boldsymbol{\phi}_{\mathbf{u},n}^{(1)}\big|_{p=r}$ includes one Chebyshev polynomial of higher order than the polynomials included when $p=r-1$ in $\boldsymbol{\phi}_{\mathbf{u},n}^{(1)}\big|_{p=r-1}$. Hence, $\boldsymbol{\phi}_{\mathbf{u},n}^{(1)}\big|_{p=r}$ and $\boldsymbol{\phi}_{\mathbf{u},n}^{(1)}\big|_{p=r-1}$ are linearly independent. The same argument when applied to arbitrary r $(r>0)$ leads to the conclusion that the entire set $\left\{\boldsymbol{\phi}_{\mathbf{u},n}^{(1)}\right\}_{p=0}^{\infty}$ is linearly independent. In fact, as this set contains all the Chebyshev polynomials $\left\{T_r[2(x/b)-1]\right\}_{r=0}^{\infty}$, it must form a basis in $\mathcal{L}_2[0,b]$.

Similarly, the set $\left\{\boldsymbol{\phi}_{\mathbf{u},n}^{(2)}\right\}_{q=0}^{\infty}$ forms a basis in $\mathcal{L}_2[b,1]$. From these two sets, one can obtain, in a straightforward manner, a natural basis set for the direct sum space $\mathcal{L}_2[0,b] \oplus \mathcal{L}_2[b,1]$. This is done by combining every function in $\left\{\boldsymbol{\phi}_{\mathbf{u},n}^{(1)}\right\}_{p=0}^{\infty}$ with the zero vector from $\mathcal{L}_2[b,1]$ to obtain independent functions in $\mathcal{L}_2[0,b] \oplus \mathcal{L}_2[b,1]$. Similarly, functions in $\left\{\boldsymbol{\phi}_{\mathbf{u},n}^{(2)}\right\}_{q=0}^{\infty}$ are combined with the zero vector from $\mathcal{L}_2[0,b]$. The union of these two sets, $\left\{(\boldsymbol{\phi}_{\mathbf{u},n}^{(1)},0)\right\}_{p=0}^{\infty} \cup \left\{(\boldsymbol{\phi}_{\mathbf{u},n}^{(2)},0)\right\}_{q=0}^{\infty}$, forms a basis in the direct sum space $\mathcal{L}_2[0,b] \oplus \mathcal{L}_2[b,1]$ (Ramkrishna and Amundson, 1985).

The natural basis $\left\{(\boldsymbol{\phi}_{\mathbf{u},n}^{(1)},0)\right\}_{p=0}^{\infty} \cup \left\{(\boldsymbol{\phi}_{\mathbf{u},n}^{(2)},0)\right\}_{q=0}^{\infty}$ does not belong to $\mathcal{S}_u$. However, it does lead to the following key insight. If the first N_0 functions from $\left\{\boldsymbol{\phi}_{\mathbf{u},n}^{(1)}\right\}_{p=0}^{\infty}$ and $\left\{\boldsymbol{\phi}_{\mathbf{u},n}^{(2)}\right\}_{q=0}^{\infty}$ are used in a numerical calculation, then the truncated natural basis set in

N_0	(p, q)					
	(0 , 0)	**(0 , 1)**	(0 , 2)	(0 , 3)	(0 , 4)	(0 , 5)
2	**(1 , 0)**	**(1 , 1)**	**(1 , 2)**	(1 , 3)	(1 , 4)	(1 , 5)
3	(2 , 0)	(2 , 1)	**(2 , 2)**	**(2 , 3)**	(2 , 4)	(2 , 5)
4	(3 , 0)	(3 , 1)	(3 , 2)	**(3 , 3)**	**(3 , 4)**	(3 , 5)
5	(4 , 0)	(4 , 1)	(4 , 2)	(4 , 3)	**(4 , 4)**	**(4 , 5)**
6	(5 , 0)	(5 , 1)	(5 , 2)	(5 , 3)	(5 , 4)	**(5 , 5)**

Figure D.1: Selection of appropriate pairs of p and q to form a basis in subspace $\mathcal{S}_u$ of $\mathcal{L}_2[0,b] \oplus \mathcal{L}_2[b,1]$. Truncated basis sets for$N_0 = 2, 3..6$ are illustrated ($p \leq N_0$, $q \leq N_0$).

the direct sum space will contain $2N_0$ functions: $\left\{(\boldsymbol{\phi}^{(1)}_{\mathbf{u},n}, 0)\right\}_{p=0}^{N_0-1} \cup \left\{(\boldsymbol{\phi}^{(2)}_{\mathbf{u},n}, 0)\right\}_{q=0}^{N_0-1}$. Thus, $2N_0$ linearly independent functions of the form $\boldsymbol{\phi}_{\mathbf{u},n}$, with p and q restricted to values between 0 and $N_0 - 1$, are required to form a truncated basis that belongs to $\mathcal{S}_u$. Considering all possible combinations of p and q in (D.3) results in N_0^2 different functions. Since in general $N_0^2 > 2N_0$, this total set is linearly dependent. To form a truncated basis we must choose a subset of $2N_0$ pairs of p and q from N_0^2 possibilities, such that the subset of functions is linearly independent. The procedure for selecting these pairs is discussed next.

The selection of pairs of p and q values is illustrated in Fig. D.1, for $N_0 = 2, 3..6$. For $N_0 = 2$, $N_0^2 = 2N_0$, and all four possible functions are required. However for $N_0 = 3$, only two additional functions must be included in the basis from a total of 5 new possibilities. The diagonal term $(2, 2)$ is selected, as it is obvious independent of the previous four functions. Another independent function is taken from just above the diagonal element $(1, 2)$. This completes the truncated basis in $\mathcal{S}_u$ for $N_0 = 3$. This procedure is repeated for all other $N_0 > 2$, i.e. inclusion of the diagonal element and the one just above it (an obvious alternative is to select elements just below the diagonal instead, i.e. $(2, 1)$, $(3, 2)$, etc.). The selected functions are highlighted in Fig. D.1. This scheme is presented as a formula for p and q in (D.1). On generalizing the selection scheme to arbitrarily high N_0 we obtain a basis set for $\mathcal{L}_2[0,b] \oplus \mathcal{L}_2[b,1]$, which belongs to $\mathcal{S}_u$. A basis set belonging to $\mathcal{S}_v$ is constructed in a similar manner. It is composed of the Chebyshev groups $\boldsymbol{\phi}^{(1)}_{\mathbf{v},n}(x)$ and $\boldsymbol{\phi}^{(2)}_{\mathbf{v},n}(x)$, as defined by (D.4). Here, $\boldsymbol{\phi}_{\mathbf{v},n}$ must satisfy the 4 boundary conditions given in (6.21). Hence, sequences of three polynomials are used in each fluid domain.

D.3 Convergence and validation

The convergence characteristics of the two-phase RCGS method are illustrated in Tab. D.1 for two sets of parameter values. The table presents values of the smallest marginal

m \ N	4	8	12	16	20	24	28
			$\mu_{12} = 1;\ \rho_{12} = 1$				
0	175.338	181.166	180.235	180.217	180.216	180.216	180.216
3	180.320	185.668	184.937	184.881	184.884	184.884	184.884
6	197.849	198.434	198.975	198.709	198.736	198.735	198.735
9	249.294	219.165	223.641	222.651	222.767	222.761	222.761
			$\mu_{12} = 5;\ \rho_{12} = 3$				
0	58.940	58.530	58.795	58.727	58.733	58.732	58.732
3	59.865	59.178	59.641	59.528	59.540	59.540	59.540
6	62.588	61.136	62.262	62.000	62.035	62.032	62.032
9	66.883	64.430	66.939	66.389	66.463	66.459	66.459

Table D.1: Convergence characteristics of the two-phase RCGS method. Each entry is the least marginal Reynolds number across all k ($Re_{c,m}$), at a specified value of m (rows), calculated using N basis functions (columns) in the expansions of $\hat{\mathbf{u}}_\mathbf{0}$ and $\hat{\mathbf{v}}_\mathbf{0}$ (6.22).

Reynolds number across all k for specified values of m (cf. Sec. 6.7). The calculations are repeated successively with an increasing number of basis functions. The results in Tab. D.1 are representative of computations at other parameter values as well. In all cases, the calculation with 16 basis functions predicts a value that is within 0.2% of the converged least marginal Reynolds number. The convergence is slower for non-axisymmetric modes ($m \neq 0$) and more basis functions are required to describe disturbances with short azimuthal wavelengths (large m). However, as we shall see, the most dangerous disturbances are either axisymmetric or of relatively long wavelength (small m) for which 24 basis functions are sufficient. For analyzing axisymmetric modes, even fewer basis functions are required.

The two-phase RCGS method was cross-checked by repeating several of the calculations with the shooting-orthonormalization technique. A representative comparison of the two methods is shown in Fig. D.2. In this figure, the marginal Reynolds number is plotted as a function of k for $m = 0$. In this case, the most dangerous disturbance is in fact axisymmetric and corresponds to the minima of the curve in Fig. D.2. The agreement between the results of the two methods is very good. Since the shooting-orthonormalization method is well established, this comparison serves as a verification of the two-phase RCGS method.

The previous work of Gelfgat *et al.* (2001) on the two-phase centrifugal instability used an incomplete set of functions as a basis set. In fact, only the diagonal entries in Fig. D.1 were selected ($p = q = n$). Therefore, the most dangerous disturbances could not be accounted for accurately, we find that their results overpredict the critical Reynolds number. For example, with $\mu_{12} = 0.91$, $\rho_{12} = 0.9$, $b = 0.5$ and $a = 0.1$, the incomplete basis predicts a critical Reynolds number of 821.211. This value has been obtained from

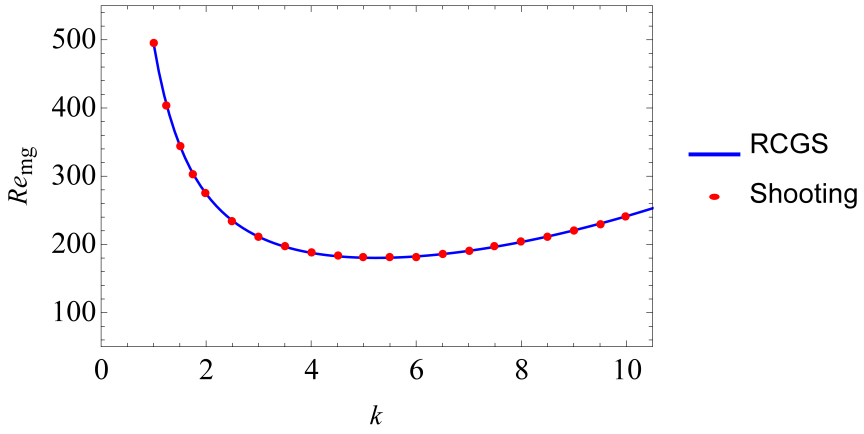

Figure D.2: Comparison of the two-phase RCGS and shooting-orthonormalization methods. The marginal Reynolds number (Re_{mg}, defined in Sec. Sec. 6.7) is plotted as a function of the axial wave number (k) for a fixed azimuthal wave number of $m = 0$. Parameter values: $\mu_{12} = 0.5$, $\rho_{12} = 0.5$, $b = 0.5$, $a = 0.1$. In this case, the critical Reynolds number corresponds to the axisymmetric mode ($m = 0$).

Gelfgat *et al.* (2001) after accounting for differences in the definition of the Reynolds number. The corresponding result using the two-phase RCGS method and the shooting-orthonormalization technique is 188.131. This rather large discrepancy persists for all parameter values.

APPENDIX E

Mathematical Expressions

E.1 Expressions for Chapter 2

The constants in the expressions of the velocity field (2.1) are given below:

$$\begin{aligned}
A_1 &= \frac{6(h+\mu_{12}\,(1-h))}{h\left(h^2(\mu_{12}-1)-\mu_{12}\,(3-2h)\right)} \\
B_1 &= \frac{6\left(h^2(\mu_{12}-1)-\mu_{12}\right)}{h\left(h^2(\mu_{12}-1)-\mu_{12}\,(3-2h)\right)} \\
C_1 &= 0 \\
A_2 &= \frac{6(h+\mu_{12}\,(1-h))}{(1-h)\left(-h^2(\mu_{12}-1)+\mu_{12}\,(2h-1)-4h\right)} \\
B_2 &= \frac{6\left(h^2(\mu_{12}-1)-\mu_{12}\right)}{(1-h)\left(-h^2(\mu_{12}-1)+\mu_{12}\,(2h-1)-4h\right)} \\
C_2 &= \frac{-6h\,(\mu_{12}-1)}{\left(-h^2(\mu_{12}-1)+\mu_{12}\,(2h-1)-4h\right)}
\end{aligned} \tag{E.1}$$

The ratio of the average velocity of phase 1 to phase 2 (ω) is a function of μ_{12} and h:

$$\omega = \frac{h\left(h^2(\mu_{12}-1)+2h\mu_{12}-3\mu_{12}\right)}{(1-h)\mu_{12}\left(-h^2(\mu_{12}-1)+2h(\mu_{12}-2)-\mu_{12}\right)} \tag{E.2}$$

The expressions for $f_1(y)$ and $f_2(y)$, used in the OEA model are given below:

$$\begin{aligned}
f_1\,(y) = {} & \frac{-(1-h)K\omega}{120(hK+1-h)(h\omega K+1-h)} \\
& \times \begin{bmatrix} 2A_1\left(h^5(K-5)+5h^4-5h(K-1)y^4-5y^4\right) \\ +5B_1\left(h^4(K-4)+4h^3-4h(K-1)y^3-4y^3\right) \\ +20C_1\left(h^3(K-3)+3h^2-3h(K-1)y^2-3y^2\right) \end{bmatrix} \\
& - \frac{kD_{12}(1-h)^3}{120(hK+1-h)(h\omega K+1-h)} \begin{pmatrix} A_2\left(8h^3+6h^2+4h-18\right) \\ +B_2\left(15h^2+10h-25\right) \\ +40\left(\omega hK+1-h-C_2\,(1-h)\right) \end{pmatrix}
\end{aligned} \tag{E.3}$$

$$f_2(y) = \frac{-(1-h)}{120(hK+1-h)(h\omega K+1-h)} \times \left[\begin{array}{l} 2A_2 \left\{ \begin{array}{l} h^5(5K-1)+h^2(10-20K) \\ -5h(K-1)y\left(y^3-4\right)-5y^4+20y-9 \end{array} \right\} \\ +5B_2 \left\{ \begin{array}{l} h^4(4K-1)+h^2(6-12K) \\ -4h(K-1)y\left(y^2-3\right)-4y^3+12y-5 \end{array} \right\} \\ -20 \left(\begin{array}{l} \frac{\omega hK}{(1-h)} \\ +1-C_2 \end{array} \right) \left\{ \begin{array}{l} h^3(3K-1)+h^2(3-6K) \\ -3h(K-1)(y-2)y \\ -3y^2+6y-2 \end{array} \right\} \end{array} \right] + \frac{\omega(1-h)h^3K(h(8A_1h+15B_1)+40C_1)}{120\beta(hK+1-h)(h\omega K+1-h)} \quad \text{(E.4)}$$

The expressions for $s_1(y)$,$s_2(y)$ and $q_2(y)$, used in the TEA model are given below:

$$s_1(y) = \frac{1}{120h}\left[2A_1\left(h^4-5y^4\right)+5B_1\left(h^3-4y^3\right)+20C_1\left(h^2-3y^2\right)\right] \quad \text{(E.5)}$$

$$s_2(y) = \frac{1}{120(1-h)}\left[\begin{array}{l} -2A_2\left(h^4+h^3+h^2-9h-5y^4+20y-9\right) \\ -5B_2\left(h^3+h^2-5h-4y^3+12y-5\right) \\ -20C_2\left(h^2-2h-3y^2+6y-2\right) \end{array} \right] \quad \text{(E.6)}$$

$$q_2(y) = \frac{1}{120}\left[\begin{array}{l} -2A_2\left(h^4+h^3+h^2-9h-5y^4+20y-9\right) \\ -5B_2(h^3+h^2-5h-4y^3+12y-5) \\ -20(C_2-1)(h^2-2h-3y^2+6y-2) \end{array} \right] \quad \text{(E.7)}$$

E.2 Expressions for Chapter 4

The expression for $G(n,m)$ is given below:

$$\begin{aligned} G(n,m) = {} & m^7+(6m^7-2m^6)n+(32m^5-9m^6)n^2+(344m^5-120m^6)n^3 \\ & +(408m^4+821m^5-88m^6)n^4+(224m^3+1642m^4+1426m^5)n^5 \\ & +(1240m^3+3667m^4+1096m^5)n^6 \\ & +(224m^2+3424m^3+3424m^4+224m^5)n^7 \\ & +(1096m^2+3667m^3+1240m^4)n^8+(1426m^2+1642m^3+224m^4)n^9 \\ & +(-88m+821m^2+408m^3)n^{10}+(344m^2-120m)n^{11} \\ & +(32m^2-9m)n^{12}+(6-2m)n^{13}+n^{14} \end{aligned} \quad \text{(E.8)}$$

REFERENCES

1. **Aljbour, S.**, **H. Yamada**, and **T. Tagawa** (2010). Sequential reaction-separation in a microchannel reactor for liquid–liquid phase transfer catalysis. *Top. Catal.*, **53**, 694–699.

2. **Andereck, C. D.**, **S. S. Liu**, and **H. L. Swinney** (1986). Flow regimes in a circular Couette system with independently rotating cylinders. *J. Fluid Mech.*, **164**, 155–183.

3. **Aota, A.**, **M. Nonaka**, **A. Hibara**, and **T. Kitamori** (2007). Countercurrent Laminar Microflow for Highly Efficient Solvent Extraction. *Angew. Chem. Int. Edit.*, **46**(6), 878–880.

4. **Aris, R.**, *Vectors, Tensors, and the Basic Equations of Fluid Mechanics*. Dover Publications, New York, 1989.

5. **Assmann, N.**, **A. Ładosz**, and **P. Rudolf von Rohr** (2013). Continuous Micro Liquid-Liquid Extraction. *Chem. Eng. Technol.*, **36**(6), 921–936.

6. **Baier, G.** and **M. D. Graham** (1998). Two-fluid Taylor-Couette flow: Experiments and linear theory for immiscible liquids between corotating cylinders. *Phys. Fluids*, **10**(12), 3045.

7. **Baier, G.** and **M. D. Graham** (2000). Two-fluid Taylor-Couette flow with countercurrent axial flow: Linear theory for immiscible liquids between corotating cylinders. *Phys. Fluids*, **12**(2), 294–303.

8. **Baier, G.**, **M. D. Graham**, and **E. N. Lightfoot** (2000). Mass transport in a novel two-fluid taylor vortex extractor. *AIChE J.*, **46**(12), 2395–2407.

9. **Balakotaiah, V.** (2004). Hyperbolic Averaged Models for Describing Dispersion Effects in Chromatographs and Reactors. *Korean J. Chem. Eng.*, **21**(2), 318–328.

10. **Balakotaiah, V.** and **S. Chakraborty** (2003). Averaging theory and low-dimensional models for chemical reactors and reacting flows. *Chem. Eng. Sci.*, **58**(21), 4769–4786.

11. **Balakotaiah, V.** and **R. R. Ratnakar** (2010). On the use of transfer and dispersion coefficient concepts in low-dimensional diffusion-convection-reaction models. *Chem. Eng. Res. Des.*, **88**(3), 342–361.

12. **Bandaru, S. V. S. R. K.** and **P. Rajendra** (2002). Pressure drop for single and two-phase flow of non-newtonian liquids in helical coils. *Can. J. Chem. Eng.*, **80**(April), 315–321.

13. **Barmak, I.**, **A. Gelfgat**, **H. Vitoshkin**, **A. Ullmann**, and **N. Brauner** (2016). Stability of stratified two-phase flows in horizontal channels. *Phys. Fluids*, **28**(4).

14. **Beals, R.** (1981). Partial-range completeness and existence of solutions to two-way diffusion equations. *J. Math. Phys.*, **22**, 954–960.

15. **Bender, C. M.** and **S. A. Orszag**, *Advanced Mathematical Methods for Scientists and Engineers: Asymptotic Methods and Perturbation Theory*. Springer, Berlin, 1999.

16. **Berger, S. A.**, **L. Talbot**, and **L. S. Yao** (1983). Flow in Curved Pipes. *Annu. Rev. Fluid Mech.*, **15**(1), 461–512.

17. **Blyth, M. G.**, **H. Luo**, and **C. Pozrikidis** (2007). Surfactant-driven instability in two-fluid pipe and channel flows. *Proc. Appl. Math. Mech.*, **7**, 1100601–1100602.

18. **Blyth, M. G.** and **C. Pozrikidis** (2004*a*). Effect of inertia on the Marangoni instability of two-layer channel flow, Part II: normal-mode analysis. *J. Eng. Math.*, **50**(2-3), 329–341.

19. **Blyth, M. G.** and **C. Pozrikidis** (2004*b*). Effect of surfactant on the stability of film flow down an inclined plane. *J. Fluid Mech.*, **521**, 241–250.

20. **Boomkamp, P. A. M.**, **B. J. Boersma**, **R. H. M. Miesen**, and **G. V. Beijnon** (1997). A Chebyshev collocation method for solving two-phase flow stability problems. *J. Comput. Phys.*, **132**(2), 191–200.

21. **Boomkamp, P. A. M.** and **R. H. M. Miesen** (1996). Classification of instabilities in parallel two-phase flow. *Int. J. Multiphas. Flow*, **22**, 67–88.

22. **Boyd, J. P.**, *Chebyshev and fourier spectral methods*. Dover, New York, 2001, 2nd edition.

23. **Carlo, D. D.** (2009). Inertial microfluidics. *Lab Chip*, **9**(21), 3038–46.

24. **Chakraborty, S.** and **V. Balakotaiah** (2002). Low-dimensional models for describing mixing effects in laminar flow tubular reactors. *Chem. Eng. Sci.*, **57**, 2545–2564.

25. **Chakraborty, S.** and **V. Balakotaiah** (2003). A novel approach for describing mixing effects in homogeneous reactors. *Chem. Eng. Sci.*, **58**(3-6), 1053–1061.

26. **Chakraborty, S.** and **V. Balakotaiah**, Spatially Averaged Multi-Scale Models for Chemical Reactors. *In* **G. B. Marin** (ed.), *Advances in Chemical Engineering Multiscale Analysis*, volume 30 of *Advances in Chemical Engineering*. Academic Press, 2005, 205–297.

27. **Chandrasekhar, S.**, *Hydrodynamic and Hydromagnetic Stability*. Clarendon Press, Oxford, 1961.

28. **Charles, M. E.** and **L. U. Lilleleht** (1965). An experimental investigation of stability and interfacial waves in co-current flow of two liquids. *J. Fluid Mech.*, **22**, 217–224.

29. **Chomaz, J.** (2005). Global instabilities in spatially developing flows: non-normality and nonlinearity. *Annu. Rev. Fluid Mech.*, **37**, 357–392.

30. **Conte, S. D.** (1966). The Numerical Solution of Linear Boundary Value Problems. *SIAM Review*, **8**(3), 309–321.

31. **Cornish, R. J.** (1928). Flow in a pipe of rectangular cross-section. *Proc R. Soc. Lond. A*, **120**(786), 691–700.

32. **Crawford, J. D.** and **E. Knobloch** (1991). Symmetry and symmetry-breaking bifurcations in fluid dynamics. *Annu. Rev. Fluid Mech.*, **23**, 341–387.

33. **Cross, M.** and **H. Greenside**, *Pattern Formation and Dynamics in Nonequilibrium Systems*. Cambridge University Press, New York, 2009.

34. **Cross, M. C.** and **P. C. Hohenberg** (1993). Pattern formation outside of equilibrium. *Rev. Mod. Phys.*, **65**(3), 851–1112.

35. **Cubaud, T.** and **T. G. Mason** (2008). Capillary threads and viscous droplets in square microchannels. *Phys Fluids*, **20**(5), 053302.

36. **Cuming, H. G.**, *The Secondary Flow in Curved Pipes*. Aeronautical Research Council, Her Majesty's Stationery Office, London, 1952.

37. **Cussler, E. L.**, *Diffusion: Mass Transfer in Fluid Systems*. Cambridge University Press, New York, 2009, 3rd edition.

38. **Davis, S. H.**, Interfacial fluid dynamics. *In* **G. K. Batchelor**, **H. K. Moffat**, and **M. G. Worster** (eds.), *Perspectives in Fluid Dynamics*. Oxford University Press, Cambridge, 2000, 1–49.

39. **Dean, W. R.** (1927). Note on the motion of fluid in a curved pipe. *Phil. Mag.*, **7**(4), 208–223.

40. **Dean, W. R.** (1928*a*). Fluid Motion in a Curved Channel. *Proc. R. Soc. Lond. A*, **121**(787), 402–420.

41. **Dean, W. R.** (1928*b*). The stream-line motion of fluid in a curved pipe. *Phil. Mag.*, **7**(5), 673–695.

42. **Dietze, G. F.** and **C. Ruyer-Quil** (2013). Wavy liquid films in interaction with a confined laminar gas flow. *J. Fluid Mech.*, **722**, 348–393.

43. **Dietze, G. F.** and **C. Ruyer-Quil** (2015). Films in narrow tubes. *J. Fluid Mech.*, **762**, 68–109.

44. **Donaldson, A. A.**, **D. Kirpalani**, and **A. Macchi** (2011). Curvature induced flow pattern transitions in serpentine mini-channels. *Int. J. Multiphas. Flow*, **37**(5), 429–439.

45. **Drazin, P. G.** and **W. H. Reid**, *Hydrodynamic Stability*. Cambridge University Press, New York, 2004, 2nd edition.

46. **Dutta, N. N.** and **G. S. Patil** (1993). Effect of Phase Transfer Catalysts on the Interfacial Tension of Water / Toluene System. *Can. J. Chem. Eng.*, **71**, 802–804.

47. **Ellenberger, J.**, **J. Hart**, and **P. J. Hamersma** (1988). Single- and two-phase flow through helically coiled tubes. *Chem. Eng. Sci.*, **43**(4), 775–783.

48. **Evans, A. W.** (1937). The effect of uni-univalent electrolytes upon the interfacial tension between normal-hexane and water. *Trans. Faraday Soc.*, **33**, 794–800.

49. **Fisch, N. J.** and **M. D. Kruskal** (1980). Separating variables in twoway diffusion equations. *J. Math. Phys.*, **21**(4), 740–750.

50. **Fitt, V.**, **J. R. Ockendon**, and **M. Shillor** (1985). Counter-current mass transfer. *International Journal of Heat and Mass Transfer*, **28**(4), 753–759.

51. **Frenkel, A. L.** and **D. Halpern** (2002). Stokes-flow instability due to interfacial surfactant. *Phys. Fluids*, **14**(7), L45—-L48.

52. **Frenkel, A. L.** and **D. Halpern** (2005). Effect of inertia on the insoluble-surfactant instability of a shear flow. *Phys. Rev. E*, **71**(1), 16302.

53. **Fries, D. M.**, **T. Voitl**, and **P. R. von Rohr** (2008). Liquid Extraction of Vanillin in Rectangular Microreactors. *Chem. Eng. Technol.*, **31**(8), 1182–1187.

54. **Garg, P.**, **J. R. Picardo**, and **S. Pushpavanam** (2015). Chaotic mixing in a planar, curved channel using periodic slip. *Phys. Fluids*, **27**, 032004.

55. **Gelfgat, A. Y.** (2001). Two and three dimensional instabilities of confined flows: numerical study by a global galerkin method. *Comput. Fluid Dyn. J.*, **9**, 437.

56. **Gelfgat, A. Y.**, **P. Z. Bar-Yoseph**, and **A. L. Yarin** (1999). Stability of multiple steady states of convection in laterally heated cavities. *J. Fluid Mech.*, **388**, 315–334.

57. **Gelfgat, A. Y.** and **I. Tanasawa** (1994). Numerical analysis of oscillatory instability of buoyancy convection with the galerkin spectral method. *Numer. Heat Tr. A-Appl.*, **25**, 627–648.

58. **Gelfgat, A. Y.**, **A. L. Yarin**, and **P. Z. Bar-Yoseph** (2001). Three-dimensional instability of a two-layer Dean flow. *Phys. Fluids*, **13**(11), 3185.

59. **Gelfgat, A. Y.**, **A. L. Yarin**, and **P. Z. Bar-Yoseph** (2003). Dean vortices-induced enhancement of mass transfer through an interface separating two immiscible liquids. *Phys. Fluids*, **15**(2), 330–347.

60. **Ghosh, S.**, **G. Das**, and **P. K. Das** (2011). Simulation of core annular in return bends—A comprehensive CFD study. *Chem. Eng. Res. Des.*, **89**, 2244–2253.

61. **Gibson, R. D.** and **A. E. Cook** (1974). The stability of curved channel flow. *Q. J. Mech. Appl. Math.*, **27**(2), 149–160.

62. **Golubitsky, M.** and **W. F. Langford** (1988). Pattern formation and bistability in flow between counterrotating cylinders. *Physica D*, **32**, 362–392.

63. **Golubitsky, M.** and **D. G. Schaeffer**, *Singularities and Groups in Bifurcation Theory Vol 1*. Springer, Berlin, 1984.

64. **Golubitsky, M.** and **I. Stewart** (1986). Symmetry and stability in Taylor-Couette flow. *SIAM J. Math. Anal.*, **17**(2), 249–288.

65. **Goussis, D. A.** and **R. E. Kelly** (1990). On the thermocapillary instabilities in a liquid layer heated from below. *Int. J. Heat Mass Tran.*, **33**(10), 2237–2245.

66. **Govindarajan, R.** and **K. C. Sahu** (2014). Instabilities in viscosity-stratified flow. *Annu. Rev. Fluid Mech.*, **46**, 331–353.

67. **Gumerman, R. J.** and **G. M. Homsy** (1974). Convective instabilities in concurrent two phase flow: Part i. Linear stability. *AIChE J.*, **20**(5), 981–988.

68. **Hagan, P. S.** and **J. R. Ockendon** (1991). Half-range analysis of a counter-current separator. *Journal of Mathematical Analysis and Applications*, **160**(2), 358–378.

69. **Halpern, D.** and **A. L. Frenkel** (2003). Destabilization of a creeping flow by interfacial surfactant: linear theory extended to all wavenumbers. *J. Fluid Mech.*, **485**, 191–220.

70. **Harkins, W. D.** and **E. C. Humphery** (1916). The surface tension at the interface between two liquids, and the effect of acids, salts and bases upon the interfacial tension. *J. Am. Chem. Soc.*, **38**(2), 242–246.

71. **Hennenberg, M.**, **T. S. Sorensen**, and **A. Sanfeld** (1977). Deformational instability of a plane interface with transfer of matter. Part 1 - non-oscillatory critical states with a linear concentration profile. *J Chem. Soc. Faraday II*, **73**, 48–66.

72. **Hinch, E. J.**, *Perturbation Methods*. Cambridge University Press, 1991.

73. **Hooper, A. P.** (1989). The stability of two superposed viscous fluids in a channel. *Phys Fluids*, **1**(7), 1133.

74. **Hotokezaka, H.**, **M. Tokeshi**, **M. Harada**, **T. Kitamori**, and **Y. Ikeda** (2005). Development of the innovative nuclide separation system for high-level radioactive waste using microchannel chip–extraction behavior of metal ions from aqueous phase to organic phase in microchannel. *Prog. Nucl. Energ.*, **47**, 439–447.

75. **Huang, Y.**, **T. Meng**, **T. Guo**, **W. Li**, **W. Yan**, **X. Li**, **S. Wang**, and **Z. Tong** (2013). Aqueous two-phase extraction for bovine serum albumin (BSA) with co-laminar flow in a simple coaxial capillary microfluidic device. *Microfluid. Nanofluid.*.

76. **Huerre, P.**, Open shear flow instabilities. *In* **G. K. Batchelor**, **H. K. Moffat**, and **M. G. Worster** (eds.), *Perspectives in Fluid Dynamics*. Cambridge University Press, Cambridge, 2000, 159–224.

77. **Huerre, P.** and **P. A. Monkewitz** (1990). Local and global instabilities in spatially developing flows. *Annu. Rev. Fluid Mech.*, **22**, 473–537.

78. **Huerre, P.** and **M. Rossi**, Hydrodynamic instabilities in open flows. *In Hydrodynamics and Nonlinear Instabilities*. Cambridge University Press, 1998, 81–294.

79. **Itoh, N.** (1996). Development of spiral and wavy vortices in circular Couette flow. *Fluid Dyn. Res.*, **17**, 87–105.

80. **Javed, K. H.**, **J. D. Thornton**, and **T. J. Anderson** (1989). Surface phenomena and mass transfer rates in liquid–liquid systems: Part 2. *AIChE J.*, **35**(7), 1125–1136.

81. **Johns, L. E.** and **R. Narayanan**, *Interfacial Instability*. Springer-Verlag, New York, 2002.

82. **Joseph, D. D.** (1975). Domain perturbations: the higher order theory of infinitesimal water waves. *Arch. Rational Mech. Anal.*, **51**, 295–303.

83. **Kalliadasis, S.**, **C. Ruyer-Quil**, **B. Scheid**, and **M. G. Velarde**, *Falling Liquid Films*, volume 176 of *Applied Mathematical Sciences*. Springer-Verlag, London, 2012.

84. **Kashid, M. N.**, **A. Renken**, and **L. Kiwi-Minsker** (2011). Influence of Flow Regime on Mass Transfer in Different Types of Microchannels. *Ind. Eng. Chem. Res.*, **50**, 6906–6914.

85. **Kirpalani, D.**, **T. Patel**, **P. Mehrani**, and **A. Macchi** (2008). Experimental analysis of the unit cell approach for two-phase flow dynamics in curved flow channels. *Int. J. Heat Mass Tran.*, **51**(5-6), 1095–1103.

86. **Kovalchuk, N. M.** and **D. Vollhardt** (2006). Marangoni instability and spontaneous non-linear oscillations produced at liquid interfaces by surfactant transfer. *Adv. Colloid Interfac.*, **120**, 1–31.

87. **Ku, D. N.** (1997). Blood Flow in Arteries. *Annu. Rev. Fluid Mech.*, **29**(1), 399–434.

88. **Kuban, P.**, **P. K. Dasgupta**, and **K. A. Morris** (2002). Microscale continuous ion exchanger. *Analytical chemistry*, **74**, 5667–5675.

89. **Kumar, P.**, **M. Franchek**, **K. Grigoriadis**, and **V. Balakotaiah** (2011). Fundamentals-Based Low-Dimensional Combustion Modeling of Spark-Ignited Internal Combustion Engines. *AIChE J.*, **57**(9), 2472–2492.

90. **Kumar, V.**, **S. Vashisth**, **Y. Hoarau**, and **K. Nigam** (2007). Slug flow in curved microreactors: hydrodynamic study. *Chem. Eng. Sci.*, **62**(24), 7494–7504.

91. **Langford, W. F.**, **R. Tagg**, **E. J. Kostelich**, **H. L. Swinney**, and **M. Golubitsky** (1988). Primary instabilities and bicriticality in flow between counterrotating cylinders. *Phys Fluids*, **31**(4), 776.

92. **Leal, L. G.**, *Advanced Transport Phenomena: Fluid Mechanics and Convective Transport Processes*. Cambridge University Press, New York, 2007.

93. **Lin, S. P.** and **J. N. Chen** (1998). Role played by the interfacial shear in the instability mechanism of a viscous liquid jet surrounded by a viscous gas in a pipe. *J. Fluid Mech.*, **376**, 37–51.

94. **Malengier, B.** and **S. Pushpavanam** (2012). Comparison of co-current and counter-current flow fields on extraction performance in micro-channels. *Adv. Chem. Eng. Sci.*, **02**, 309–320.

95. **Malengier, B.**, **J. Tamalapakula**, and **S. Pushpavanam** (2012). Comparison of laminar and plug flow-fields on extraction performance in micro-channels. *Chem. Eng. Sci.*, **83**, 2–11.

96. **Meleshko, V. V.** (1996). Steady Stokes flow in a rectangular cavity. *Proc. R. Soc. Lond. A*, **452**(1952), 1999–2022.

97. **Meleshko, V. V.** (1998). Biharmonic Problem in a Rectangle. *Appl. Sci. Res.*, **58**, 217–249.

98. **Muradoglu, M.** and **H. A. Stone** (2007). Motion of large bubbles in curved channels. *J. Fluid Mech.*, **570**, 455–466.

99. **Nandakumar, K.** and **J. H. Masliyah** (1982). Bifurcation in steady laminar flow through curved tubes. *J. Fluid Mech.*, **119**, 475–490.

100. **Novak, U.**, **A. Pohar**, **I. Plazl**, and **P. Žnidaršič Plazl** (2012). Ionic liquid-based aqueous two-phase extraction within a microchannel system. *Sep. Purif. Technol.*, **97**, 172–178.

101. **Okubo, Y.**, **T. Maki**, **N. Aoki**, **T. Hong Khoo**, **Y. Ohmukai**, and **K. Mae** (2008). Liquid–liquid extraction for efficient synthesis and separation by utilizing micro spaces. *Chem. Eng. Sci.*, **63**, 4070–4077.

102. **Ooms, G.**, **M. J. B. M. Pourquie**, and **J. Westerweel** (2015). Numerical study of laminar core-annular flow in a torus and in a 90 ° pipe bend. *AIChE J.*, **61**(7), 2319–2328.

103. **Peng, J.** and **K.-Q. Zhu** (2010). Linear instability of two-fluid Taylor–Couette flow in the presence of surfactant. *J. Fluid Mech.*, **651**, 357–385.

104. **Peterson, S. D.** (2010). Steady flow through a curved tube with wavy walls. *Physics of Fluids*, **22**(2), 023602.

105. **Picardo, J. R.** and **S. Pushpavanam** (2013). Core-Annular Two-Phase Flow in a Gently Curved Circular Channel. *AIChE J.*, **59**(12), 4871–4886.

106. **Picardo, J. R.**, **T. G. Radhakrishna**, **B. V. Anil**, **R. Sundari**, and **S. Pushpavanam** (2015). Modelling Extraction in Microchannels with Stratified Flow: Channel Geometry, Flow Configuration and Marangoni Stresses. *Indian Chemical Engineer*, **57**(3-4), 322–358.

107. **Poincare, H.**, *Science and Method*. Thomas Nelson and Sons, 1914.

108. **Pozrikidis, C.**, Instability of multi-layer channel and film flows. volume 40 of *Advances in Applied Mechanics*. Elsevier, 2004, 179–239.

109. **Priest, C.**, **J. Zhou**, **S. Klink**, **R. Sedev**, and **J. Ralston** (2012). Microfluidic Solvent Extraction of Metal Ions and Complexes from Leach Solutions Containing Nanoparticles. *Chem. Eng. Technol.*, **35**(7), 1312–1319.

110. **Ramkrishna, D.** and **N. R. Amundson** (1974). Transport in composite materials: reduction to a self adjoint formalism. *Chem. Eng. Sci.*, **29**, 1457–1464.

111. **Ramkrishna, D.** and **N. R. Amundson**, *Linear Operator Methods in Chemical Engineering with applications to transport and chemical reaction systems.*. Prentice-Hall, New Jersey, 1985.

112. **Ramkrishna, D.** and **R. Aris** (1999). The beauty of self-adjoint symmetry. *Ind. Eng. Chem. Res.*, **38**(3), 845–850.

113. **Ratnakar, R. R.** and **V. Balakotaiah** (2011). Exact averaging of laminar dispersion. *Phys. Fluids*, **23**(2), 023601.

114. **Ratnakar, R. R.** and **V. Balakotaiah** (2014). Coarse-graining of diffusion–reaction models with catalyst archipelagos. *Chem. Eng. Sci.*, **110**(c), 44–54.

115. **Ratnakar, R. R.**, **M. Bhattacharya**, and **V. Balakotaiah** (2012). Reduced order models for describing dispersion and reaction in monoliths. *Chem. Eng. Sci.*, **83**, 77–92.

116. **Reid, W. H.** (1958). On the stability of viscous flow in a curved channel. *Proc. R. Soc. Lond. A*, **244**(1237), 186–198.

117. **Renardy, Y.** and **D. D. Joseph** (1985). Couette flow of two fluids between concentric cylinders. *J. Fluid Mech.*, **150**(1), 381–394.

118. **Roberts, A. J.**, *Model Emergent Dynamics in Complex Systems*. SIAM, Philadelphia, 2015.

119. **Ruyer-Quil, C.** and **P. Manneville** (2000). Improved modeling of flows down inclined planes. *Eur. Phys. J. B*, **15**(2), 357–369.

120. **Samanta, A.** (2013). Effect of surfactant on two-layer channel flow. *J. Fluid Mech.*, **735**, 519–552.

121. **Sarkar, P. S.**, **K. K. Singh**, **K. T. Shenoy**, **A. Sinha**, **H. Rao**, and **S. K. Ghosh** (2012). Liquid–Liquid Two-Phase Flow Patterns in a Serpentine Microchannel. *Ind. Eng. Chem. Res.*, **51**(13), 5056–5066.

122. **Schmid, P. J.** and **D. S. Henningson**, Appendix A: Numerical issues and computer programs. *In Stability and Transition in Shear Flows*. Springer-Verlag, New York, 2001, 479–483.

123. **Schwarzenberger, K.**, **T. Köllner**, **H. Linde**, **T. Boeck**, **S. Odenbach**, and **K. Eckert** (2014). Pattern formation and mass transfer under stationary solutal Marangoni instability. *Adv. Colloid Interfac.*, **206**, 344–371.

124. **Scriven, L. E.** and **C. V. Sternling** (1964). On cellular convection driven by surface-tension gradients: effects of mean surface tension and surface viscosity. *J. Fluid Mech.*, **19**(03), 321–340.

125. **Smith, K. A.** (1966). On convective instability induced by surface-tension gradients. *J. Fluid Mech.*, **24**(2), 401–414.

126. **Sparrow, E. M.** (1964). On the onset of flow instability in a curved channel of arbitrary height. *ZAMP*, **15**, 638–642.

127. **Sternling, C. V.** and **L. E. Scriven** (1959). Interfacial turbulence: hydrodynamic instability and the Marangoni effect. *AIChE J.*, **5**(4), 514–523.

128. **Stewart, I.** and **M. Golubitsky**, *Fearful Symmetry: Is God a Geometer?*. Blackwell Publishers, Oxford, 1992.

129. **Sun, Z. F.** and **M. Fahmy** (2006). Onset of Rayleigh-Benard-Marangoni convection in gas-liquid mass transfer with two-phase flow: Theory. *Ind. Eng. Chem. Res.*, **45**(9), 3293–3302.

130. **Tadmouri, R.**, **N. M. Kovalchuk**, **V. Pimienta**, **D. Vollhardt**, and **J. Micheau** (2010). Transfer of oxyethylated alcohols through water/heptane interface: Transition from non-oscillatory to oscillatory behaviour. *Colloid Surface A*, **354**, 134–142.

131. **Tagg, R.**, **W. S. Edwards**, **H. L. Swinney**, and **P. S. Marcus** (1989). Nonlinear standing waves in Couette-Taylor flow. *Phys. Rev. A*, **39**(7), 3734–3737.

132. **Thangam, S.** and **N. Hur** (2006). Laminar secondary flows in curved rectangular ducts. *J. Fluid Mech.*, **217**, 421–440.

133. **Theofilis, V.** (2003). Advances in global linear instability analysis of nonparallel and three-dimensional flows. *Prog. Aerosp. Sci.*, **39**, 249–315.

134. **Topakoglu, H. C.** (1967). Steady Laminar Flow of an Incompressible Viscous Fluid in Curved Pipes. *J. Math. Mech.*, **16**(12), 1321–1337.

135. **Treybal, R.**, *Mass-Transfer Operations*. Mc-Graw Hill, Singapore, 1980, 3 edition.

136. **Valluri, P.**, **L. Ó. Naraigh**, **H. Ding**, and **P. D. M. Spelt** (2010). Linear and nonlinear spatio-temporal instability in laminar two-layer flows. *J. Fluid Mech.*, **656**, 458–480.

137. **Van Dyke, M.**, *Perturbation Methods In Fluid Mechanics*. The Parabolic Press, Stanford, California, 1975, annotated edition.

138. **Vashisth, S.**, **V. Kumar**, and **K. D. P. Nigam** (2008). A Review on the Potential Applications of Curved Geometries in Process Industry. *Ind. Eng. Chem. Res.*, **47**(10), 3291–3337.

139. **Vir, A. B.**, **A. S. Fabiyan**, **J. R. Picardo**, and **S. Pushpavanam** (2014*a*). Performance comparison of liquid-liquid extraction in parallel microflows. *Ind. Eng. Chem. Res.*, **53**(19), 8171–8181.

140. **Vir, A. B.**, **S. R. Kulkarni**, **J. R. Picardo**, **A. Sahu**, and **S. Pushpavanam** (2014*b*). Holdup characteristics of two-phase parallel microflows. *Microfluid. Nanofluid.*, **16**, 1057–1067.

141. **Šinkovec, E.**, **A. Pohar**, and **M. Krajnc** (2013). Phase transfer catalyzed esterification: modeling and experimental studies in a microreactor under parallel flow conditions. *Microfluid. Nanofluid.*, **14**, 489–498.

142. **Wang, P.** and **A. Anderko** (2013). Modeling Interfacial Tension in Liquid âĹŠ Liquid Systems Containing Electrolytes. *Ind. Eng. Chem. Res.*, **52**, 6822–6840.

143. **Wei, H.** (2005). On the flow-induced Marangoni instability due to the presence of surfactant. *J. Fluid Mech.*, **544**, 173–200.

144. **Wei, H.** (2006). Shear-flow and thermocapillary interfacial instabilities in a two-layer viscous flow. *Phys. Fluids*, **18**, 064109.

145. **Wei, H.** (2007). Role of base flows on surfactant-driven interfacial instabilities. *Phys. Rev. E*, **75**, 036306.

146. **Winters, K. H.** (1987). A bifurcation study of laminar flow in a curved tube of rectangular cross-section. *J. Fluid Mech.*, **180**, 343–369.

147. **Yiantsios, S. G.** and **B. G. Higgins** (1988). Linear stability of plane Poiseuille flow of two superposed fluids. *Phys Fluids*, **31**(11), 3225.

148. **Yih, C.** (1967). Instability due to viscosity stratification. *J. Fluid Mech.*, **27**(2), 337–352.

149. **You, X.**, **L. Zhang**, and **J. Zheng** (2014). Marangoni instability of immiscible liquid–liquid stratified flow with a planar interface in the presence of interfacial mass transfer. *J. Taiwan Inst. Chem. E.*, **45**(3), 772–779.

150. **Zaisha, M.**, **L. Ping**, **Z. Guangji**, and **Y. Chao** (2008). Numerical Simulation of the Marangoni Effect with Interphase Mass Transfer Between Two Planar Liquid Layers. *Chinese J. Chem Eng.*, **16**(2), 161–170.

151. **Zhao, Y.**, **G. Chen**, and **Q. Yuan** (2006). Liquid-liquid two-phase flow patterns in a rectangular microchannel. *AIChE J.*, **52**(12), 4052–4060.

152. **Znidarsic-Plazl, P.** and **I. Plazl** (2007). Steroid extraction in a microchannel system–mathematical modelling and experiments. *Lab Chip*, **7**, 883–889.

LIST OF PAPERS

The following articles are based on chapters 2 to 6 of this thesis:

1. **J.R. Picardo**, S. Pushpavanam, **2015**, “Low-dimensional modeling of transport and reactions in two-phase stratified flow", *Ind. Eng. Chem. Res.*, (Ramkrishna Festschrift) 54 (42): 10481-10496
2. **J.R. Picardo**, S. Pushpavanam, **2013**, “On the conditional superiority of counter-current over co-current extraction in microchannels", *Microfluid. Nanofluid.*, 15, 5: 701-713.
3. **J.R. Picardo**, Radhakrishna, T. G., S. Pushpavanam, **2015**, “Solutal-Marangoni instability in layered two-phase flows", *J. Fluid Mech.*, 793: 280-315
4. **J.R. Picardo**, S. Pushpavanam, **2015**, “Laterally stratified flow in a curved microchannel", *Int. J. Multiphas. Flow*, 75: 39-53.
5. **J.R. Picardo**, P. Garg, S. Pushpavanam, **2015**, “Centrifugal instability of stratified two-phase flow in a curved channel", *Phys. Fluids*, 27: 054106.

As this thesis evolved, it raised several interesting questions, a few of which have been addressed in the following articles:

1. **J.R. Picardo**, Radhakrishna T.G., Anil B. Vir, Sundari Ramji, S. Pushpavanam, **2015**, “Modeling Extraction in Microchannels with Stratified Flow: Channel Geometry, Flow Configuration and Marangoni Stresses", *Indian Chemical Engineer*, 57 (3-4): 322-358
2. **J.R. Picardo** and S. Pushpavanam, **2015**, “Understanding the Shape of Ant Craters: A Continuum Model", *Bull. Math. Bio.*, 77: 470-487.
3. **J.R. Picardo** and S. Pushpavanam, **2013**, “Core-annular two-phase flow in a gently curved circular channel", *AIChE J.*, 59, 12: 4871-4886.
4. P. Garg, **J.R. Picardo** and S. Pushpavanam, **2014**, “Vertically stratified two-phase flow in a curved channel: Insights from a domain perturbation analysis", *Phys. Fluids*, 26: 073604.
5. P. Garg, **J.R. Picardo** and S. Pushpavanam, **2015**, “Chaotic mixing in a planar, curved channel using periodic slip", *Phys. Fluids*, 27: 032004.
6. D. S. Pillai, **J.R. Picardo** and S. Pushpavanam, **2014**, “Shifting and breakup instabilities of squeezed elliptic jets", *Int. J. Multiphas. Flow*, 67: 189-199.
7. A.B. Vir, A.S. Fabiyan, **J.R. Picardo** and S. Pushpavanam, **2014**, “Performance Comparison of Liquid-Liquid Extraction in Parallel Microflows", *Ind. Eng. Chem. Res.*, 53, 19: 8171-8181.

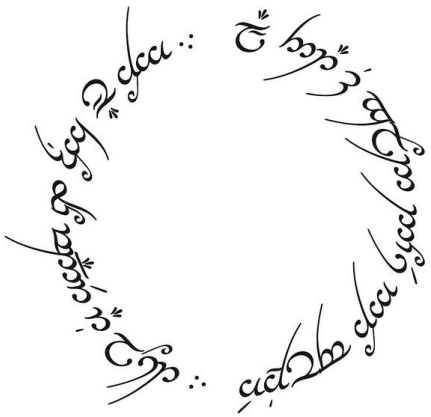

All that is gold does not glitter,
not all those who wander are lost

Tolkien